

Contributions to a Microkinetic Understanding of the Steam Reforming of Methanol (SRM) and the Oxidative Dehydrogenation of Propane (ODP)

vorgelegt von
Diplom-Ingenieur
Benjamin Frank
aus Aachen

von der Fakultät II - Mathematik und Naturwissenschaften
der Technischen Universität Berlin
zur Erlangung des akademischen Grades

Doktor der Ingenieurwissenschaften
Dr. Ing.

genehmigte Dissertation

Promotionsausschuss

Vorsitzender:	Prof. Dr. Andreas Grohmann, TU Berlin
Berichter:	Prof. Dr. Reinhard Schomäcker, TU Berlin
Berichter:	Prof. Dr. Robert Schlögl, Fritz-Haber-Institut, Berlin

Tag der wissenschaftlichen Aussprache: 03. September 2007

Berlin 2007

D 83

You may be interested to know that global warming, earthquakes, hurricanes, and other natural disasters are a direct effect of the shrinking numbers of pirates since the 1800s.

Bobby Henderson

Vorwort und Danksagung / Preface

Die vorliegende Arbeit wurde in der Zeit von April 2004 bis Juni 2007 im Institut für Chemie der Technischen Universität Berlin angefertigt. Für ausgewählte Experimentalreihen konnte die technische Ausstattung des Fritz-Haber-Instituts (FHI) der Max-Planck-Gesellschaft in Dahlem und des Leibniz-Instituts für Katalyse (LIKAT) in Adlershof genutzt werden.

Mein besonderer Dank gilt HERRN PROF. DR. REINHARD SCHOMÄCKER für die Betreuung der Arbeit, sowie FRAU DR. FRIEDERIKE JENTOFT und HERRN DR. EVGUENY KONDRATENKO für die Betreuung der Versuchsreihen im FHI und im LIKAT. Bei HERRN PROF. DR. ROBERT SCHLÖGL bedanke ich mich für die Übernahme der zweiten Begutachtung.

Eine erfolgreiche Arbeit wäre allerdings auch ohne die Unterstützung einer Vielzahl anderer Personen unmöglich gewesen (in alphabetischer Reihenfolge):

ARNE DINSE	VIOLA KLAUS	ANJA RUCH
DR. EGBERT FEIKE	MICHAEL KNUTH	PROF. DR. JOACHIM SAUER
DR. REMY FORTRIE	JUTTA KRÖHNERT	AXEL SCHIELE
WIEBKE FRANDSEN	ROLF KUNERT	PROF. DR. HELMUT SCHUBERT
DETLEF GRIMM	PATRICK KURR	OLIVER SCHWARZ
DR. DANIELA HABEL	DR. ÁGNES MASTALIR	HARY SOERIJANTO
DR. CHRISTIAN HESS	DR. OLGA OVSITSER	GABRIELE VETTER
DETLEF KLABUNDE	DR. XAVIER ROZANSKA	ALPARSLAN YILDIZ

Ihnen allen, die mir im Laufe der drei Jahre mehr oder weniger tatkräftig zur Seite gestanden, auf jeden Fall aber zum Gelingen der Arbeit beigetragen haben, sei an dieser Stelle herzlich gedankt. Weiterer Dank gebührt der gesamten Arbeitsgruppe von HERRN PROF. DR. SCHOMÄCKER. Die angenehme Arbeitsatmosphäre werde ich stets in Erinnerung behalten.

Die in den Laboratorien der Technischen Chemie genutzten Apparaturen wurden überwiegend von der ZEIT-Stiftung sowie von der Deutschen Forschungsgemeinschaft (DFG) über Drittmittelprojekte bereitgestellt. Die finanzielle Unterstützung meines Studiums geschah über Doktorandenstipendien der DFG sowie des Fonds der Chemischen Industrie (FCI). Die DECHEMA unterstützte meine Arbeit mit der Einladung zu zwei Fachkonferenzen im Rahmen der Verleihung des DECHEMA-Studentenpreises 2005. Den genannten Institutionen, insbesondere dem FCI, möchte ich für diese Unterstützung ebenfalls meinen Dank aussprechen.

Meinen Eltern

Abstract

By means of steam reforming of methanol (SRM) and oxidative dehydrogenation of propane (ODP) various macro- and microkinetic aspects of heterogeneously catalyzed reactions, whose industrial application fails due to insufficient selectivity, were investigated.

For SRM it was shown by kinetic modeling and a DRIFTS study at 493 K that the reaction pathway over selected, differently supported copper-catalysts is independent of the support material and obeys the mechanism on Cu/ZnO/Al₂O₃ catalysts proposed in literature. The dehydrogenation of adsorbed methoxy groups is rate-determining, consequently the reaction rate is dominated by the partial pressure of methanol. The impact of the water concentration on the reaction rate is rather low, hydrogen and carbon dioxide both act as inhibiting agents. Differences were observed in activity (TOF) and relative rates of elementary reaction steps. Using a Cr₂O₃/Fe₂O₃ support the stability of formate groups is noticeably enhanced, which affects reaction orders of the reactants, activation energy, and selectivity of the reaction towards CO.

For the investigation of the ODP, a low loaded VO_x/γ-Al₂O₃ model catalyst was prepared and comprehensively characterized with regard to nature, distribution, and red-ox properties of VO_x surface species. By means of an intrinsic formal kinetic model the impact of mass and heat transport inside the catalyst particle as well as in the catalytic fixed bed was modeled. The reaction network can be reduced to main and consecutive reaction, formation and deep oxidation of propene. This simplification was confirmed by transient experiments in vacuum (TAP), where further on CO and CO₂ sorption behaviour as well as CO oxidation were investigated in detail. Whereas temperature gradients are irrelevant, concentration gradients in large particles lead to a decrease in propene selectivity due to its accumulation and enhanced deep oxidation rate in the particle center. Hence, a tool for design and quantitative evaluation of microkinetic measurements is available. For the reoxidation of reduced VO_x species a microkinetic model, which predicts a substantial impact of water, was derived. From transient experiments in a gradient-free Berty-type reactor it was concluded that the reoxidation of hydrated and hydroxylated VO_x species occurs remarkably faster than the reaction of "naked" V^{+III} centers with oxygen. The proposed reaction pathways are in agreement with theoretical calculations. For, so far, unknown reason the reoxidation of V^{+III} to V^{+V} remains incomplete below 673 K although the activation energy of this reaction is low. With regard to the reaction pathway of ODP, an investigation of the dehydration of 2-propanol over the VO_x/γ-Al₂O₃ model catalyst indicated that a vanadium-bonded propoxy group is a possible intermediate. However, its decomposition yielding propene is not rate-determining, which was proven by estimation of TOF values and activation energy of this ODP-related reaction.

Zusammenfassung

Anhand der Dampfreformierung von Methanol (SRM) und der oxidativen Dehydrierung von Propan (ODP) wurden makro- und mikrokinetische Aspekte heterogen katalysierter Reaktionen, deren industrielle Anwendung bislang an einer unzureichenden Selektivität scheitert, untersucht.

Bei der SRM wurde über kinetische Modellierung und DRIFTS-Messungen gezeigt, dass der Reaktionspfad auf ausgewählten, verschieden geträgerten Kupferkatalysatoren unabhängig vom Trägermaterial ist und mit dem in der Literatur gängigen Mechanismus für Cu/ZnO/Al₂O₃-Katalysatoren übereinstimmt. Die Dehydrierung von Methoxygruppen ist geschwindigkeitsbestimmend, demnach wird die Reaktionsgeschwindigkeit maßgeblich vom Partialdruck von Methanol bestimmt. Unterschiede zeigen sich lediglich in Aktivität (TOF) und Kinetik der Einzelschritte. Auffällig ist bei Verwendung eines Cr₂O₃/Fe₂O₃-Trägers die erhöhte Stabilität von Formiat auf dem Katalysator, was sich sowohl auf Reaktionsordnungen der Reaktanden, Aktivierungsenergie und Selektivität der Reaktion gegenüber CO auswirkt.

Für die Untersuchungen zur ODP wurde ein gering beladener VO_x/γ-Al₂O₃-Modellkatalysator präpariert und umfassend in Bezug auf Beschaffenheit, Verteilung und Redox-Eigenschaften der VO_x-Oberflächenspecies charakterisiert. Mithilfe einer intrinsischen Formalkinetik wurde der Einfluss von Stoff- und Wärmetransport sowohl im Katalysatorpartikel als auch im katalytischen Festbett modelliert. Das Reaktionsnetzwerk lässt sich mit guter Genauigkeit auf Haupt- und Folgereaktion, die Bildung und Verbrennung von Propen, reduzieren. Diese Erkenntnis wurde durch Transientenexperimente im Vakuum (TAP) bestätigt. Während Temperaturgradienten nur eine untergeordnete Rolle spielen, wirken sich Konzentrationsgradienten in großen Partikeln vor allem auf eine verminderte Selektivität zu Propen aus, was aus dessen Akkumulation im Partikelinnern und der dadurch begünstigten Folgeoxidation resultiert. Es steht somit ein Werkzeug zur Verfügung, mit dem mikrokinetische Messungen an der ODP frei von Transportlimitierungen ausgelegt und quantitativ bewertet werden können. Für die Reoxidation reduzierter VO_x-Species wurde ein mikrokinetisches Modell abgeleitet, was einen substantiellen Einfluss von adsorbiertem Wasser aufzeigt. Aus Transientenexperimenten im gradientenfreien Berty-Reaktor wurde geschlossen, dass die Reoxidation hydratisierter und hydroxylierter VO_x-Species deutlich schneller abläuft, als die Reaktion "nackter" V^{+III} Zentren mit Sauerstoff. Die vorgeschlagenen Reaktionspfade wurden durch theoretische Berechnungen bestätigt. Aus bislang noch ungeklärter Ursache verläuft die Oxidation von V^{+III} zu V^{+V} unterhalb von 673 K nur unvollständig, obwohl die Aktivierungsenergie der Reaktion klein ist.

Table of Contents

Abstract	i
Zusammenfassung	ii
Table of Contents	iii
List of Publications	v
Symbols and Abbreviations	vi
1. Introduction and Motivation	1
2. Fundamentals and State of the Literature	5
2.1 Rate Laws and Kinetic Modeling	5
2.2 Impact of Mass and Heat Transport Limitations	9
2.2.1 External Transport	10
2.2.2 Internal Transport	11
2.3 Steam Reforming of Methanol over Cu Catalysts	13
2.3.1 Catalysts and Reaction Conditions	13
2.3.2 Reaction Network and Pathways	15
2.3.3 Thermodynamic Considerations	20
2.4 Oxidative Dehydrogenation of Propane over $\text{VO}_x/\gamma\text{-Al}_2\text{O}_3$ Catalysts	25
2.4.1 Catalytic Performance of $\text{VO}_x/\gamma\text{-Al}_2\text{O}_3$ Catalysts	25
2.4.2 Reaction Network and Pathways	29
3. Experimental Methods	37
3.1 Physicochemical Catalyst Characterization	37
3.1.1 Nitrogen Physisorption	38
3.1.2 X-ray Powder Diffractometry (XRD)	39
3.1.3 Temperature Programmed Reduction/Oxidation (TPR/TPO)	40
3.1.4 UV-Vis Diffuse Reflectance Spectroscopy (UV-Vis DRS)	40
3.1.5 Laser Raman Spectroscopy (LRS)	41
3.1.6 X-ray Photoelectron Spectroscopy (XPS)	42
3.1.7 Scanning and Transmission Electron Microscopy (SEM and TEM)	42
3.2 Microkinetic Modeling	43
3.2.1 Diffuse Reflectance Infrared Spectroscopy (DRIFTS)	44
3.2.2 Rate Data Acquisition and Kinetic Modeling	45
3.2.2.1 Experimental Set-up for SRM Kinetic Measurements	47

3.2.2.2	Experimental Set-up for ODP Kinetic Measurements	48
3.2.3	Temporal Analysis of Products (TAP)	48
4	Steam Reforming of Methanol	51
4.1	Catalyst Preparation and Physicochemical Characterization	51
4.2	Catalytic Catalyst Characterization	53
4.2.1	Mass Transport Limitations	53
4.2.2	Catalyst Aging	54
4.2.3	Identification of the SRM Active Phase in CCF	55
4.3	DRIFTS Study	56
4.4	Kinetic Modeling	61
4.4.1	Contact Time	61
4.4.2	Microkinetic Model	62
4.4.3	Formal Kinetics and Comparison of Activity	68
5.	Oxidative Dehydrogenation of Propane	73
5.1	Catalyst Preparation and Characterization	73
5.2	Analysis of Mass Transport Limitation Effects	84
5.2.1	Intrinsic Kinetics and Reactor Modeling	84
5.2.2	Modeling of Mass and Heat Transport Effects	89
5.3	TAP Study	93
5.3.1	Single Pulse Experiments	94
5.3.2	Sequential Pulsing Experiments	98
5.3.3	Modeling of CO _x Sorption and CO Oxidation	98
5.4	Reoxidation Kinetics of VO _x Species	105
5.4.1	Kinetic Modeling of Experimental Results	106
5.4.2	Theoretical Investigation of the Proposed Reaction Pathway	114
5.5	Dehydration of Propanol - an ODP Related Reaction?	119
6.	Concluding Remarks	127
7	Appendices	131
7.1	Supporting Information	131
7.2	Curriculum Vitae	138

Publications with Substantial Contribution to this PhD Thesis

- (1) B. FRANK, F.C. JENTOFT, H. SOERIJANTO, J. KRÖHNERT, R. SCHLÖGL, R. SCHOMÄCKER
Steam reforming of methanol over copper-containing catalysts: influence of support material on microkinetics
Journal of Catalysis **2007** Vol. 246 pp. 177
- (2) B. FRANK, A. DINSE, O. OVSITSER, E.V. KONDRATENKO, R. SCHOMÄCKER
Mass and heat transfer effects on the oxidative dehydrogenation of propane (ODP) over a low loaded VO_x/Al₂O₃ catalyst
Applied Catalysis A: General **2007** Vol. 323 pp. 66
- (3) B. FRANK, R. FORTRIE, X. ROZANSKA, J. SAUER, C. HESS, R. SCHLÖGL, R. SCHOMÄCKER
Reoxidation kinetics of a low loaded VO_x/Al₂O₃ catalyst under "non-ideal" conditions - a mechanistic approach
Journal of Catalysis **2007**, submitted

Publications with Minor Contribution to this PhD Thesis

- (4) Á. MASTALIR, B. FRANK, A. SZIZYBALSKI, H. SOERIJANTO, A. DESHPANDE, M. NIEDERBERGER, R. SCHOMÄCKER, R. SCHLÖGL, T. RESSLER
Steam reforming of methanol over Cu/ZrO₂/CeO₂ catalysts: a kinetic study
Journal of Catalysis **2005** Vol. 230 pp. 464
- (5) B. FRANK, D. HABEL, R. SCHOMÄCKER
N-alkylation of aniline with ethanol over an industrial niobic acid catalyst – influence of water formation on kinetics and selectivity
Catalysis Letters **2005** Vol. 100 pp. 181
- (6) L. GRÖSCHEL, R. HAIDAR, A. BEYER, H. CÖLFEN, B. FRANK, R. SCHOMÄCKER
Hydrogenation of propyne in palladium-containing polyacrylic acid membranes and its characterization
Industrial & Engineering Chemistry Research **2005** Vol. 44 pp. 9064
- (7) B. FRANK, A. YILDIZ, E. FEIKE, H. SCHUBERT, R. SCHOMÄCKER
Preparation and characterization of a solid acid catalyst from commercial niobia hydrate
Chemical Engineering & Technology **2006** Vol. 29 pp. 519
- (8) O. SCHWARZ, B. FRANK, C. HESS, R. SCHOMÄCKER
Characterisation and catalytic testing of VO_x/Al₂O₃ catalysts for microstructured reactors
Catalysis Communications **2007**, accepted (DOI: 10.1016/j.catcom.2007.06.009)
- (9) A. DINSE, B. FRANK, C. HESS, D. HABEL, R. SCHOMÄCKER
The influence of the support material on the kinetics and selectivity of propane oxidative dehydrogenation
Applied Catalysis A: General **2007**, in preparation
- about 15 Posters at national and international conferences and symposia over the period of 2004–2007

Symbols and Abbreviations

a	m^{-1}	Specific surface area
	mol	Amount of adsorbed gas in the BET equation
A	m^2	Surface area
	-	Dimensionless constant in the Antoine equation
	-	Coefficient for calculation of contact time (SRM)
B	K	Constant in the Antoine equation
	-	Coefficient for calculation of contact time (SRM)
c	mol m^{-3}	Concentration
	-	Dimensionless Constant in the BET equation
C	K	Constant in the Antoine equation
d	m	Spacing, distance, diameter
D	$\text{m}^2 \text{s}^{-1}$	Diffusion coefficient
E	J	Energy
E_A	J mol^{-1}	Activation energy
G	J mol^{-1}	Gibbs free energy
h	$\text{J m}^{-2} \text{s}^{-1} \text{K}^{-1}$	Heat transfer coefficient
	$6.626 \times 10^{-34} \text{J s}$	Planck's constant
H	J mol^{-1}	Enthalpy
k	$\text{g}^{-1} \text{s}^{-1} (\text{m}^3 \text{mol}^{-1})^{m-1}$	Rate constant (with m the reaction order)
	m s^{-1}	Mass transfer coefficient
k_0	$\text{g}^{-1} \text{s}^{-1} (\text{m}^3 \text{mol}^{-1})^{m-1}$	Preexponential factor (with m the reaction order)
K	$\text{Pa}^{-1}; \text{m}^3 \text{mol}^{-1}$	Adsorption equilibrium constant
	-	Dimensionless constant in the Scherrer equation
L	m	Crystallite size, characteristic length
m	-	Reaction order
	g	Mass
M	g mol^{-1}	Molar mass
n	mol	Mole number
	-	Diffraction order
N_A	$6.022 \times 10^{23} \text{mol}^{-1}$	Avogadro's or Loschmidt's number
p	Pa	Pressure
Q	J	Heat
r	$\text{mol m}^{-3} \text{s}^{-1};$ $\text{mol g}^{-1} \text{s}^{-1}$	Reaction rate per catalyst volume or per catalyst mass
	m	Radius
R	$8.314 \text{J mol}^{-1} \text{K}^{-1}$	Gas constant
	m	Radius
	-	Reflectance
S	$\text{J mol}^{-1} \text{K}^{-1}$	Entropy
	%	Selectivity
t	s	Time
	m	Thickness
T	$^{\circ}\text{C}; \text{K}$	Temperature
V	m^3	Volume
x	m	Reactor length in the mass balance
	-	Molar fraction
X	%	Conversion
Y	%	Yield

β	K min ⁻¹	Heating rate
		Full width at half maximum intensity
ε	%	Porosity
η	%	Effectiveness factor
Θ	%	Coverage
	°	Diffraction angle
λ	J m ⁻¹ s ⁻¹ K ⁻¹	Heat conductivity
	nm	Wavelength
	-	Molar ratio
ν	-	Stoichiometric coefficient
	m ³ mol ⁻¹	Molar volume
	cm ⁻¹	Wavenumber
π	3.1416	Ludolph's number
ρ	g m ⁻³	Density
σ	J m ⁻²	Surface tension
τ	-	Tortuosity
	s	Contact time
	g s m ⁻³	Modified contact time
Φ	J	Work function of spectrometer in XPS analysis
χ	-	Criterion for extraparticle heat transfer limitation
Ψ	-	Thiele modulus
Ψ''	-	Weisz modulus
ω	-	Criterion for extraparticle mass transfer limitation

AMU	Atomic Mass Unit
BET	Brunauer Emmet Teller
BJH	Barrett Joyner Halenda
EPR	Electron Paramagnetic Resonance Spectroscopy
CCF	Cu/Cr ₂ O ₃ /Fe ₂ O ₃
CS	Cu/SiO ₂
CZA	Cu/ZnO/Al ₂ O ₃
CZC	Cu/ZrO ₂ /CeO ₂
DFT	Density Functional Theory
DRIFTS	Diffuse Reflectance Infrared Fourier Transformed Spectroscopy
EDAX	Energy Dispersive Analysis of X-rays
EDX	Energy Dispersive X-ray Spectroscopy
HPLC	High-Pressure Liquid Chromatography
ICP-OES	Inductively Coupled Plasma Optical Emission Spectroscopy
LHHW	Langmuir Hinshelwood Hougen Watson
LRS	Laser Raman Spectroscopy
MFC	Mass-Flow Controller
MvK	Mars-van Krevelen
ODP	Oxidative Dehydrogenation of Propane
QMS	Quadrupol Mass Spectrometer
RDS	Rate-Determining Step
SEM	Scanning Electron Microscopy
SRM	Steam Reforming of Methanol
SSITKA	Steady-State Isotope Transient Kinetics Analysis
TAP	Temporal Analysis of Products
TEM	Transmission Electron Microscopy
TOF	Turn-Over Frequency
TPR/TPO	Temperature-Programmed Reduction/Oxidation
UV-Vis DRS	UV-Vis Diffuse Reflectance Spectroscopy
XPS	X-ray Photoelectron Spectroscopy
XRD	X-Ray Diffractometry

1 Introduction and Motivation

Kinetic modeling of a chemical reaction is a standard procedure and indispensable for scale-up and process design in chemical industry. The accurate prediction of rates of product and heat formation allows for adequate dimensioning of process equipment and refining capacities. With regard to existing catalysts and process equipment, kinetic studies can help to identify a certain potential of improvement by a specific modification of process parameters. However, for the description of chemical reactions, empirical rate expressions are in most cases sufficient. These rate laws allow the description of the process often within a narrow range of concentrations and temperatures, maybe include the effect of catalyst deactivation.

Against that, microkinetic modeling of heterogeneously catalyzed reactions is a powerful tool for a better understanding of catalysis and can substantially contribute to the clarification of molecular reaction pathways. The aspired microkinetic model contains specific data with chemical and physical meaning. Unfortunately a successful and coherent modeling at atomic level has been achieved only for one reaction so far, the ammonia synthesis. Most catalyst systems are by far too complex to be described by relatively simple Hougen-Watson or Mars-van Krevelen microkinetic approaches. Attempts for various reactions resulted in useful proposals and suggestions for the reaction pathway. Those in general have to be confirmed by non-kinetic techniques, e.g., spectroscopy or quantum-chemical calculations. The common problem is that simplified kinetic models in general provide data, which is not consistent with physicochemical or theoretically calculated data. Against that, highly complex models suffer from a lack of reliability because of a high number of constants, which have then been used for experimental data fitting. Independent methods, e.g., DRIFTS or TAP, can provide helpful input for the development of microkinetic models, which are not reliable if based on steady-state kinetic data only.

For this thesis two reactions have been chosen for microkinetic investigations: (i) steam reforming of methanol (SRM) over copper-catalysts, and (ii) oxidative dehydrogenation of propane over vanadia/ γ -alumina catalysts. Both reactions have an enormous industrial perspective but suffer from significant selectivity problems which permit their application so far. During the last decades SRM has been anticipated to be a promising alternative for gasoline in automobiles. Compared to gasoline, methanol can be easily synthesized from natural gas or coal. Their importance as alternative fossil fuels will raise in the coming decades due to the foreseeable depletion and increasing costs of crude oil. Hydrogen produced on-board by SRM can be used in fuel cells providing a relatively clean source of energy in metropolitan areas due to a higher H:C ratio of 4 compared to 2.25 in octane, and no production of particulate soot and nitric or sulphur oxides. The replacement of combustion engines by electrical motors furthermore provides advantages

with respect to energy-efficiency and generation of noise. Unfortunately, carbon monoxide is formed as a by-product under SRM reaction conditions, which acts as poison for Pt-anodes commonly used in fuel cells. The required concentration limit is about 20 ppm (proton-exchange membrane fuel cell, PEM-FC) which is about two orders of magnitude lower than the amount formed over typical copper catalysts at full methanol conversion. This requires expensive clean-up units for the product gas and is the main reason against a commercial application of this technique so far. Additionally commercial copper catalysts provide a poor long term stability and are susceptible to deactivation at load changes. Thus, actual projects of research are optimized and more selective catalysts, development of more effective clean-up units, and fuel cell electrodes more resistant to carbon monoxide. The alternative of using pure hydrogen as fuel, which is then produced at centralized gas stations, is problematic due to a safe handling of liquid or compressed hydrogen. Pressure tanks providing appropriate safety, are relatively heavy and the process of liquefaction or compression is very expensive. The perspective of a methanol based economy in comparison to a hydrogen based one beyond fossil fuels was recently given by Nobel laureate George A. Olah¹.

Oxidative dehydrogenation of propane (ODP) towards propene is a promising alternative to conventional processes based on non-oxidative dehydrogenation. Advantageously this reaction is not thermodynamically limited and there is no catalyst deactivation by coking. The typical reaction temperature is much lower than for the non-oxidative pathway, which, in addition to its exothermicity, leads to a drastic reduction of processing costs. However, due to consecutive combustion in the oxidizing environment, the propene yield is too low for a economically viable application up to now (at least 50% is required). Possible solutions by means of novel process engineering are the use of oxygen ion conductive Perovskite type membranes to separate the reactants and thereby lower the local oxygen concentration. Another starting-point is an alternated operation mode of the reactor with consecutive feed of oxygen and propane. Both methods minimize the deep oxidation and can increase the propene yield drastically. Propene is an important building block of the petrochemical industry and up to now mainly produced by steam-cracking of naphtha or alternatively by catalytic cracking/dehydrogenation. However, the main product of the first process is ethylene. As the world demand for propene increases faster than the demand for ethylene, and the desired ratio of these alkenes cannot be adjusted boundlessly, an independent process for propene production is desirable. Propane is a component of natural gas and also a by-product of petrochemical cracking processes. Its present application is mainly cooking, heating, or vehicle fuel and a remarkable value enhancement can be achieved by its

¹ G.A. Olah, A. Goeppert, G.K. Surya Prakash, *Beyond Oil and Gas: The Methanol Economy*, Wiley-VCH, Weinheim, 2005.

conversion into propene. The alkene is the starting material for the synthesis of important large-scale products like polypropylene, acetone, acrylic nitrile/acid, or propylene oxide.

Both investigated reactions, SRM and ODP, state complex networks of parallel and consecutive reactions, in which the rate of each individual reaction depends very sensitively on chemical composition, oxidation state and structure of the catalyst. A huge amount of copper and vanadia catalysts have been investigated so far, differing in support material, loading of active component and preparation method. Many studies do not get beyond rudimentary conversion-selectivity relationships or simple kinetic models. An optimized catalyst design requires detailed knowledge and understanding of structure-activity relationships for which these results are useless as long as there is no clarity on the molecular reaction pathway. However, a comparison of microkinetic data has been performed only in a few studies and very often these reports then fail in an appropriate structural characterization of the catalyst. Moreover, a comparison between different reports often fails or suffers from different reaction conditions in these studies. Kinetic data of SRM is relatively simple accessible by experiments in conventional tubular reactors. In case of ODP the high exothermicity of the reaction can cause severe experimental problems. Catalytic performance in conventional tubular reactors can suffer from disturbing radial and axial temperature gradients, which hinder a clear assignment of reaction conditions and experimental results. Clearly defined experimental conditions are ensured by a gradient-free differential reactor, in which the reaction rate can be measured directly under isothermic conditions. This reactor set-up is also appropriate for the kinetic investigation of the catalyst reoxidation, which is difficult due to the irreversibility and rapidness of this process. The entirety of oxidation reactions over vanadia catalysts is supposed to obey the two-step model by Mars and van Krevelen of catalyst reduction by substrate oxidation and its reoxidation by gas phase oxygen. Thus, the analysis of the reoxidation step is of fundamental interest in the field of vanadia catalysis.

Financial support for the experimental equipment required for a substantial part of this thesis was received by two organisations: (i) The ZEIT-foundation promoted the research project "Nanochemistry for the automobiles of the future - copper catalysts for the on-board production of hydrogen by steam reforming of methanol" with the objective to develop optimized copper catalysts with enhanced long-term stability and minimized CO formation; (ii) the German research foundation (DFG) granted the collaborative research centre "Structure, dynamics and reactivity of transition metal oxide aggregates" (Sonderforschungsbereich 546), where the ODP catalyzed by vanadium oxide clusters is a model reaction for the desired accord of detailed characterization of catalytic material, microkinetic modeling of experimental data, and quantum chemical calculations with the aim of an understanding of structure-activity relationships.

2 Fundamentals and State of the Literature [2.1–2.5]

Catalysis is the acceleration of a chemical reaction by means of a substance, which takes part in the reaction, but is not consumed or changed by the reaction. This substance provides an alternative route of reaction where the activation energy is lower than in the original chemical reaction. The catalyst can be dissolved in the reaction mixture which is referred to as homogeneous catalysis. It can also form its own separate phase, yielding heterogeneous catalysis. The latter will be introduced here on the basis of derivation of kinetic rate laws [2.6] and impact of transport processes [2.7] resulting from the heterogeneity of the reaction system. A simple model for heterogeneous catalysis involves the catalyst providing a surface for the temporary adsorption of the reactants. Chemical bonds thereby become weakened sufficiently for the creation of new bonds. Each step of the chemical reaction can be described by an elemental kinetic rate law including an Arrhenius-like temperature-dependent rate constant and the concentrations of participating species. In general, one of these steps is much slower than the entirety of the others and thereby becomes rate-determining. However, regarding heterogeneous catalysis, transport processes have to be considered for the kinetic description of the process. Two reactions, providing the basis for this thesis, namely steam reforming of methanol (SRM) and oxidative dehydrogenation of propane (ODP) will be presented in this chapter by a review of actual literature focussed on kinetically relevant topics.

2.1 Rate Laws and Kinetic Modeling

Chemical rate equations separate into mainly two groups: (i) empirical relations, and (ii) mechanistic rate laws. The first reflect the reaction rate as a function of temperature and the reactant's concentrations, mostly by means of a power-law approach. For a simple reaction scheme of an irreversible heterogeneously catalyzed reaction (Eq. 2.1),



a power rate law approach (Eq. 2.2) will describe the product formation in a well-defined, but often narrow range of experimental conditions.

$$r_C = \frac{dc_C}{dt} = k(T) \prod_{i=A,B,C} c_i^{m_i} \quad (2.2)$$

$$k(T) = k_0 \exp\left(-\frac{E_A}{R T}\right) \quad (\text{Arrhenius equation}) \quad (2.3)$$

The rate constant k is defined by the preexponential factor k_0 and the activation energy E_A (Eq. 2.3), given by intercept and slope in the Arrhenius plot (log. rate vs. reciprocal temperature), respectively. Reaction orders m_i of reactants and products can be derived by the slope in the log-

log plot of rate vs. concentration c_i of the respective component. However, this equation contains nearly no information about the surface mechanism. Reaction orders allow only assumptions about the rate-determining step (RDS) or indicate product inhibition. In return it is easy to handle and often used in chemical engineering for design of experiments and processes. Mathematical problems can arise in case of zero concentration of one component with negative reaction order, e.g., at initial conditions and inhibiting reaction product.

The mechanistic rate law is the essence of microkinetic modeling. It contains specific parameters with physical and chemical meanings, i.e., the rate constants of the rate-determining elementary reaction and equilibrium constants K of adsorption and surface reactions (Eqs. 2.4 and 2.5).

$$K = \frac{k_f}{k_r} = \prod_i c_{i,eq}^{\nu_i} = \exp\left(-\frac{\Delta G}{R T}\right) = \exp\left(\frac{\Delta S}{R}\right) \exp\left(-\frac{\Delta H}{R T}\right) \quad (2.4)$$

$$\frac{d \ln K}{dT} = \frac{\Delta H}{R T^2} \quad (\text{van't Hoff equation}) \quad (2.5)$$

where the indices f and r stand for forward and reverse reaction, ν is the stoichiometric weighting factor, and ΔG , ΔS , and ΔH are Gibbs free enthalpy, entropy and enthalpy change of the reaction, respectively. The latter can be derived from an Arrhenius type plot of the equilibrium constants, ΔS from the intercept and ΔH from the slope.

The solution of mechanistic rate equations also contains catalyst specific data dependent on the reaction conditions like coverages of distinct adsorbates or oxidation state of active species in red-ox reactions. Their derivation mostly proceeds via the Langmuir-Hinshelwood/Hougen-Watson (LHHW) formalism, which is described in detail elsewhere [2.5], based on the Langmuir adsorption isotherm. Although the underlying assumptions may not always be completely fulfilled, it is generally accepted that this approach is the most suitable and reliable way of rationalizing observed catalytic rate data. Typical LHHW-rate laws consist of the product of a rate factor and the driving force in the numerator and an inhibition term in the denominator (Eq. 2.6). For the reaction scheme mentioned above, several kinetic rate laws can be derived, dependent on the RDS of the overall reaction (Tab. 2.1, Eqs. 2.7–2.9).

A schematic comparison of the resulting shapes for initial reaction rates ($X = 0$) is presented in Fig. 2.1 for an arbitrary set of rate, adsorption and equilibrium constants and binary feed composition A and B without diluent. For reactions with reactant adsorption as RDS, the reaction rate is strongly dependent on the concentration of the respective reactant, whereas in case of a relatively slow surface reaction, the concentrations of both reactants contribute to the overall rate. Product desorption as RDS causes a broad range of experimental conditions, where the reaction rate is nearly independent from the feed composition.

Table 2.1 Mechanistic rate equations for the heterogeneously catalyzed reaction $A + B \rightarrow C$, differing in the RDS of the overall reaction.

RDS	Mechanistic rate law
LHHW general	$r = \frac{\text{rate factor} \times \text{driving force}}{\text{inhibition term}} \quad (2.6)$
Adsorption of A	$r = \frac{k_* c_{\text{tot}} \left(c_A - \frac{1}{K} \frac{c_C}{c_B} \right)}{1 + \frac{K_A c_C}{K c_B} + K_B c_B + K_C c_C} \quad (2.7)$
Surface reaction	$r = \frac{k_* c_{\text{tot}} \left(c_A c_B - \frac{1}{K} c_C \right)}{1 + K_A c_A + K_B c_B + K_C c_C} \quad (2.8)$
Desorption of C	$r = \frac{k_* c_{\text{tot}} K K_C \left(c_A c_B - \frac{1}{K} c_C \right)}{1 + K_A c_A + K_B c_B + K K_C c_A c_B} \quad (2.9)$

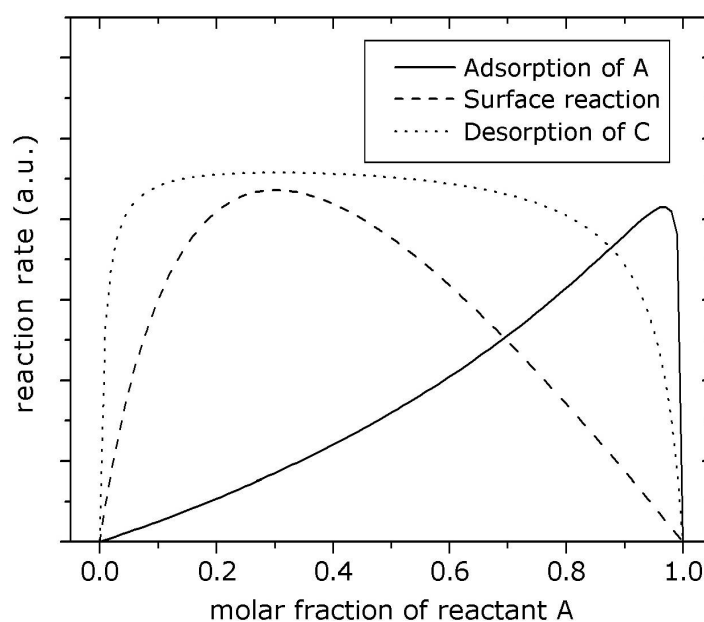


Figure 2.1 Schematic trends of rate equations assembled in Tab. 2.1 and their dependency of the molar composition of the reactant mixture.

Microkinetic modeling appears to be a powerful tool for the investigation of the RDS of a reaction. However, the investigation of the remaining elementary steps is difficult because minor variations in the inhibition term result in very similar curve shapes and congruence can often be achieved by varying the kinetic parameters in a small range. Some examples for the kinetic modeling of heterogeneously catalyzed reactions, performed by the author, are presented in

Tab. 2.2. Whereas both power-law approaches [2.8,2.9] were used predominantly for the determination and comparison of rate constants, the mechanistic studies [2.10,2.11] provided additional information about the RDS and the number of active sites involved therein.

Table 2.2 Examples for kinetic modeling in heterogeneous catalysis

Reaction	Rate law	Ref.
Steam reforming of methanol	$r_{\text{SRM}} = k p_{\text{MeOH}}^{0.6} p_{\text{H}_2\text{O}}^{0.4}$	[2.8]
Partial hydrogenation of propyne	$r_{\text{PHP}} = k p_{\text{C}_3\text{H}_4}^0 p_{\text{H}_2}^1$	[2.9]
N-alkylation of aniline with ethanol	$r_{\text{NAE}} = \frac{k K_{\text{EtOH}} (p_{\text{EtOH}} p_{\text{AnNH}_2} - p_{\text{H}_2\text{O}} p_{\text{MP}} / K)}{1 + K_{\text{EtOH}} p_{\text{EtOH}} + K_{\text{H}_2\text{O}} p_{\text{H}_2\text{O}}}$	[2.10]
Esterification of acetic acid with ethanol	$r_{\text{EAE}} = \frac{k K_{\text{EtOH}} K_{\text{AcOH}} p_{\text{EtOH}} p_{\text{AcOH}}}{(1 + K_{\text{EtOH}} p_{\text{EtOH}})(1 + K_{\text{AcOH}} p_{\text{AcOH}})}$	[2.11]

A special model for oxidation reactions involving lattice oxygen of metal oxide catalysts was developed by Mars and van Krevelen [2.12]. They observed that the substrate molecules in oxidation reactions over vanadia catalysts rather react with lattice oxygen than with adsorbed oxygen species. The feature of microkinetic modeling is a strict separation of these types of reaction into substrate oxidation by the oxidized catalyst and catalyst reoxidation by an oxidizing agent. Under steady-state conditions, both of these two steps occur with equal rate. The following model oxidation with gas phase oxygen (Eq. 2.10)



then separates into the independent reactions (Eqs. 2.11 and 2.12)



where $[\text{O}]$ is a lattice oxygen atom bonded on the catalyst surface and $[]$ is an oxygen defect or vacancy. The general derivation of the corresponding Mars-van Krevelen type rate law r_{MvK} results in Eq. 2.13

$$r_{\text{MvK}} = \frac{r_{\text{red}} r_{\text{ox}}}{r_{\text{red}} + r_{\text{ox}}} \quad (2.13)$$

where r_{red} and r_{ox} are the independent rate laws of catalyst reduction (substrate oxidation) and catalyst reoxidation. These can be individual and depend on various factors and assumptions, e.g., like Eqs. 2.7–2.9 differ in the RDS of the surface mechanism. In most cases the reoxidation is much faster than the reduction and the overall rate is then determined by the reduction step.

However, if an influence of the oxygen concentration on the overall reaction rate is detectible, very sophisticated overall rate laws can result and the independent investigation of the oxidation is preferable for a detailed kinetic analysis.

The decision towards one specific kinetic model is usually done by data regression and the estimation of the minimum square mean error. Different models are tested for their capability to describe the experimental kinetic data and at the end only a few are left which distinguish in details. The final decision and accurate parameter estimation requires specific experiments or statistical methods. However, data regression is not trivial because of the high number of parameters, which can appear in a mechanistic rate law, so the physical significance of the parameters is an important criterion. Physicochemical constraints and guidelines are collected in Tab. 2.3.

Table 2.3 Physicochemical constraints and guidelines for microkinetic modeling.

Rate constant	$k > 0$
Activation energy	$E_A > 0$
Adsorption entropy	$0 < -\Delta S_{\text{ads}}^0 < \Delta S_{\text{gas}}^0$ $\Delta S_{\text{ads}}^0 \approx 40 \text{ J mol}^{-1} \text{ K}^{-1}$
Adsorption enthalpy	$-\Delta H_{\text{ads}}^0 > 0$

It should be emphasized that LHHW kinetic rate expressions are derived with several assumptions, e.g., energetic uniformity of adsorption sites. In case of their violation these constraints should be used with caution. The rate constant should be in the range of 10^9 – 10^{17} s^{-1} , mainly determined the entropy change of the RDS. Relatively small preexponentials of about 10^{11} s^{-1} can be expected in case of dissociation as RDS. For surface recombination the typical order of magnitude is 10^{13} s^{-1} , and desorption as RDS results in preexponentials in the range of 10^{15} s^{-1} . These ranges are in agreement with transition-state rate theory calculations.

However, kinetic modeling will not deliver a complete description of the reaction mechanism. But any mechanism which is considered, should be consistent with the kinetic data [2.13].

2.2 Impact of Mass and Heat Transport Limitations

The application of solid porous catalysts in heterogeneous catalysis requires inevitably a view on transport processes during the reaction. These can result in the appearance of external and internal mass and heat transfer limitations and thereby affect the overall reaction rate. If the rate of mass transport is slow compared to the chemical reaction rate, concentration gradients can

appear in the laminar layer surrounding the catalyst pellet as well as inside of the catalyst pores. Consequently, a reduced reaction rate will be experimentally observed, the kinetic evaluation can provide solely apparent parameters. In case of strongly exothermic reactions the impact of heat transfer resistance can additionally influence the catalytic performance by the formation of intraparticle temperature gradients. Besides these effects on kinetic parameters the appearance of diffusional limitation can also affect selectivities in complex reaction networks due to product accumulation inside of the catalyst pores [2.14].

Thus, in experimental studies of heterogeneously catalyzed reactions, one of the first objectives should be the determination (and elimination) of the influences of transport phenomena on the measured rate data. Several criteria have been derived for the estimation of mass and heat transfer effects in heterogeneous catalysis. Each must be applied with due caution and understanding in order to achieve a more rigorously defined experimental system.

2.2.1 External Transport

The external transport includes reactant diffusion and heat conduction through the boundary layer or film around the particle. In case of steady state conditions and plane geometry these are defined as follows (Eqs. 2.14 and 2.15):

$$\dot{n}_i = \mathcal{A} k_g (c_{i,b} - c_{i,s}) \quad (\text{Fick's 1st law}) \quad (2.14)$$

$$\dot{Q} = \mathcal{A} h (T_b - T_s) \quad (\text{Fourier's law}) \quad (2.15)$$

where \dot{n} is the mass transport by diffusion, \mathcal{A} is the surface area, k_g is the gas-particle mass transfer coefficient, \dot{Q} is the heat transport by conduction, and h is the heat transfer coefficient. Indices b and s stand for bulk phase of the reactant gas and external catalyst surface, respectively. k_g and h are mainly determined by their inverse dependence from the thickness of the boundary layer. In order to achieve gradientless conditions, concentration and temperature differences should be close to zero. It can be clearly seen from these equations that sufficient mass and heat transfer can then be achieved by adjusting the surface area \mathcal{A} by reduction of the particles diameter or by optimizing the perturbation and thereby minimize the thickness of the boundary layer. Evidently the probability of mass transfer resistances will decrease with decreasing reaction rate and effects of heat transfer resistance will be less pronounced at low reaction enthalpy. The following criteria have been derived in order to estimate mass and heat transfer through the boundary layer (Eqs. 2.16 and 2.17):

$$\omega = \frac{r^{\text{eff}} r_p}{c_b k_g} < 0.15 \frac{1}{m} \quad (2.16)$$

$$\chi = \left| \frac{-\Delta_R H r^{\text{eff}} r_p}{h T_b} \right| < 0.15 \frac{R T_b}{E_A} \quad (2.17)$$

where $\Delta_R H$ is the reaction enthalpy, r^{eff} is the effective reaction rate, r_p is the catalyst particle radius, R is the gas constant, E_A is the activation energy, and m is the reaction order. Comparison of Eqs. 2.16 and 2.17 shows that for typical cases heat transfer across the film causes excessive deviations long before mass transfer becomes limiting.

If external mass transport affects the reaction rate, the apparent rate constant k^{app} is a function of the true kinetics and mass transfer (Eq. 2.18).

$$\frac{1}{k^{\text{app}}} = \frac{1}{k} + \frac{1}{k_g a} \quad (2.18)$$

where k is the intrinsic rate constant and a is the specific external surface area of the catalyst particles. In case of a total rate control by mass transport, temperature dependence is solely determined by diffusion, i.e. in the range of 5 kJ mol^{-1} , whereas the reaction will transform to first order concerning the reactants concentrations.

2.2.2 Internal Transport

The intraparticle transport includes mass transport by pore diffusion and heat transport by conduction through the catalyst pellet. Both can affect the overall reaction rate, if reaction rate and/or heat production is too fast. Mass and heat transfer can be described by the respective balances, i.e., for spherical particle geometry and steady-state conditions (Eqs. 2.19 and 2.20).

$$\frac{d}{dR} c_i + \frac{2}{R} \frac{d}{dR} c_i = \frac{\rho_{\text{cat}}}{D_i^{\text{eff}}} \sum_j r_{ij} \quad (2.19)$$

$$\frac{d}{dR} T + \frac{2}{R} \frac{d}{dR} T = \frac{\rho_{\text{cat}}}{\lambda^{\text{eff}}} \sum_j r_{ij} \Delta_R H_j \quad (2.20)$$

where ρ_{cat} is the catalyst density, D^{eff} is the effective diffusion coefficient, and λ^{eff} is the effective heat conductivity. The solution of Eq. 2.19 provides Thiele modulus Ψ and effectiveness factor η , the most common criteria for estimation of mass transfer resistances. This mass balance, however, requires the knowledge of the true kinetic behaviour and intrinsic rate constants. Weisz and Prater presented a criterion for the absence of significant diffusion effects ($\eta \geq 0.95$) which is independent of the true rate constant (Eq. 2.21).

$$\Psi' = \eta \Psi^2 = L^2 \frac{m+1}{2} \frac{r_p^{\text{eff}} r_p^2}{c_s D^{\text{eff}}} < 0.1 \quad (2.21)$$

where Ψ' is the dimensionless Weisz modulus and L the characteristic length of the particle.

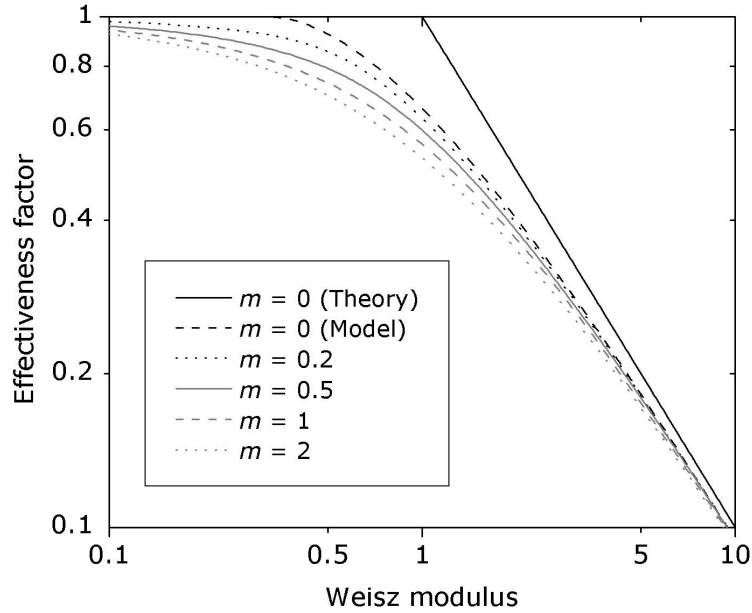


Figure 2.2 Dependency of effectiveness factor η on Weisz modulus Ψ' and reaction order m , calculated by numerical integration of concentration profiles inside of spherical catalyst particles.

As expected, Eq. 2.21 predicts a lower impact of pore diffusion on the overall reaction rate at small particle radii, low reactivity and high effective diffusion coefficients, i.e., high porosity and large pore diameter of the catalyst. In the mesoporous range pore diffusion is mainly determined by Knudsen diffusivity. The effectiveness factor as a function of Weisz modulus and reaction order is presented in Fig. 2.2. This figure, in accordance with Eq. 2.21, illustrates the border of significant impact of mass transfer on the reaction rate at $\Psi' > 0.1$.

A significant deviation between modeled and theoretical values is present only in case of zero'th reaction order and raises from mathematical handling of extremely low concentrations [2.1].

Intraparticle temperature gradients that result in a change of the observed reaction rate of less than 5%, can be neglected in case of (Eq. 2.22)

$$\left| \frac{\Delta_R H r_p^{\text{eff}} r_p^2}{\lambda^{\text{eff}} T_s} \right| < 0.75 \frac{R T_s}{E_A} \quad (2.22)$$

This criterion is valid whether diffusional limitation exists in the particle or not but requires the knowledge of the true activation energy E_A . The activation energy itself is strongly affected by diffusional limitation and for $\Psi' > 1$ approaches to the value of (Eq. 2.23)

$$E_{\Lambda}^{\text{eff}} = \frac{E_{\Lambda}}{2} \quad (2.23)$$

whereas the apparent rate constant is reduced by the effectiveness factor (Eq. 2.24)

$$k^{\text{eff}} = \eta k \quad (2.24)$$

and formal reaction orders transform in the following way (Eq. 2.25)

$$m^{\text{eff}} = \frac{m+1}{2} \quad (2.25)$$

As it has been demonstrated in this chapter, transport resistances have various impact on the apparent kinetic parameters.

2.3 Steam Reforming of Methanol over Cu catalysts

The reaction of methanol with water has been published for the first time in 1921. Christiansen found quantitative conversion into hydrogen and carbon dioxide in the ratio 3:1 as well as traces of carbon monoxide in the temperature range of 230–250 °C over a Cu catalyst [2.15]. The reaction was immediately associated with the hydrolysis of formaldehyde and the decomposition of formic acid, which both occur under similar reaction conditions. Up to now Cu-based catalysts are the most active and selective known for SRM, and also for the reverse reaction, the methanol synthesis. A second group of well investigated catalysts are Pd-based systems which provide acceptable performance in SRM [2.16], but will not be discussed here.

2.3.1 Catalysts and Reaction Conditions

Cu/ZnO and Cu/ZnO/Al₂O₃ systems are best investigated in terms of SRM, probably due to a long research history leading to their industrial application in the related methanol synthesis reaction [2.17]. Typical catalysts for SRM consist of copper as active component deposited on an oxidic support material. Activity and distribution of the active copper species can be enhanced drastically by addition of promoters. Most common methods of catalyst preparation are co-precipitation and impregnation [2.18,2.19]. The microstructure and thereby the catalytic performance of the catalyst strongly depends on wet chemical parameters, e.g., pH and temperature during precipitation or aging time of the precipitate, but also washing, drying, and calcination processes have to be considered [2.20,2.21]. The calcined catalyst usually provides Cu in the form of oxides and carbonates and has to be reduced to reach high activity. The activation method, either with a diluted hydrogen gas mixture or in situ using the SRM reactant mixture at temperatures > 200 °C, can also affect the catalytic performance [2.22]. Beyond kinetic studies SRM is typically carried

out at temperatures between 200 and 300 °C and ambient pressure. The reactant mixture is equimolar up to a 1.5 fold surplus of water. Under these reaction conditions copper catalysts suffer a rapid deactivation and loose up to 50% of their initial activity (see Ch. 4.2.2). The catalyst is furthermore susceptible to continuous deactivation due to load alternations and cooling/heating procedures [2.23].

The influence of various promoters and support materials on the catalytic performance of Cu-catalysts has been studied extensively. However, there exists no strict border in distinguishing between promoter and support characteristics. As a common problem, comparable data among different studies is difficult to find due to different preparation methods and reaction conditions or insufficient catalyst characterization. Thus, a meaningful comparison is in most cases ensured solely by catalytic systems and experimental design of one specific study. Widely investigated promoter materials for copper catalysts are ZnO and CeO₂ [2.24–2.26], but also oxides of Mn, Cr, and others have been investigated so far [2.22,2.27,2.28]. All of them, at least to a certain extent, improved the activity of the non-promoted catalyst for SRM. Ceria as redox active ceramic substance with high oxygen mobility and storage capacity combines both of them [2.29–2.31]. It is thereby in the focus of actual research, as is the combination CeO₂/ZrO₂ as support material [2.8,2.30,2.33]. Defects in the oxides of cerium and also zinc are supposed to stabilize active copper centres in a catalytically active state by their integration in the respective crystal structure. In case of zinc oxide this is due to the identical electronic structure of Zn²⁺ and Cu⁺ ions, whereas copper atoms in the ceria lattice are assumed to get stabilized by electron transfer [2.34]:



Eq. 2.26 reflects the enduring discussion about the active site of copper catalysts in methanol chemistry. Although it was proven that under SRM conditions most of the copper is reduced to Cu⁰, it was also shown that pure copper metal particles are inactive in SRM. Furthermore, it has been shown that the active phase of a Cu/ZnO catalyst consists of Cu⁰ containing small amounts of Cu^I and Zn, whereas an oxidized Cu^{II}/Cu^I mixture is completely inactive for SRM [2.35,2.36]. ZnO thereby becomes an integral part of the Cu/ZnO catalytic system by causing structural disorder in the bulk structure of copper particles. However, decades of investigation could not clearly identify the active site of Cu/ZnO in methanol synthesis [2.37]. Moreover, this active site is assumed to transform depending on the reaction conditions, i.e., is different in methanol synthesis and SRM. With respect to more complex systems, e.g., ternary catalysts, only assumptions can be made for the nature and surrounding of active copper species so far.

The classic function of a support material is to ensure high dispersion of the catalytically active phase by providing a high specific surface area. The common support materials SiO₂ and γ-Al₂O₃

in general meet these demands. However, Cu-particles deposited on their surface, tend to agglomerate under SRM conditions [2.38]. The Cu surface thereby decreases and so does the catalytic activity with ongoing time on stream, i.e., these support materials provide a poor long-term stability. ZrO₂ as support material has been reported to prevent sintering of Cu crystallites under reaction conditions and thus may be regarded as structural stabilizer [2.39–2.41]. Compared with the conventional ZnO- or Al₂O₃-supported Cu catalysts, ZrO₂-containing samples have shown increased activities and reduced CO levels for SRM [2.39–2.43]. The promoting effect of ZrO₂ has been attributed to an improved reducibility of CuO, which tends to increase the Cu dispersion [2.39]. Similarly, CeO₂ can positively affect the stability and catalytic performance of supported Cu catalysts. Long term stability is strongly enhanced by preventing copper crystallites from agglomeration and sintering. Copper particles are kept highly dispersed and relatively smaller compared to non-promoted Cu/Al₂O₃ catalysts, which at the end also affects the selectivity against CO formation positively [2.26]. The Cu/CeO₂ interfacial area is supposed to be the active site for SRM [2.44], which again makes it difficult to distinguish between support and promoter properties.

As a result of this survey it can be said that the catalytic systems, either being binary or ternary, differ strongly in their properties. These are determined by their chemical composition and by preparation parameters, which determine not only macroscopic characteristics of the catalyst but also, e.g., the dispersion of copper crystallites. The active site, neither for methanol synthesis nor for SRM, has not yet been clearly identified, only a rough localization at the interphase between a metallic copper and an oxidic phase has been proposed by several authors.

2.3.2 Reaction Network and Pathways

The formal reaction network of SRM over copper-based catalysts consists mainly of three reactions [2.8,2.45]. Steam reforming of methanol (Eq. 2.27) is an endothermic reaction that is as good as irreversible at temperatures above 200 °C and ambient pressure:



A less important side reaction is the decomposition of methanol (Eq. 2.28), which also is endothermic and nearly irreversible at temperatures above 200 °C and ambient pressure:



The reaction products of SRM suffer the consecutive endothermic reverse water-gas shift reaction (Eq. 2.29), which is also known to be catalyzed by copper-based catalysts:



Although this reaction is thermodynamically strongly disfavoured in the typical temperature range of SRM and due to the presence of water in the reactant mixture, it is important since it is the main reaction pathway for carbon monoxide formation [2.46]. Further by-products of this reaction are formaldehyde, methyl formate, and dimethyl ether. Although formed only in trace amounts, their existence provides important information on the reaction mechanism of SRM.

A detailed model of the reaction mechanism of SRM has been proposed by Peppley et al. for a Cu/ZnO/Al₂O₃ catalyst [2.47]. Based mainly on extensive investigations on methanol synthesis, the authors developed expressions for reaction rates of SRM, methanol decomposition, and water-gas shift reaction. The rate expressions include surface species and intermediates that were identified by diffuse reflectance infrared Fourier transform spectroscopy (DRIFTS). For SRM the dehydrogenation of surface methoxy groups was identified as RDS. Among several rate expressions assembled by Lee et al. [2.48], this model was used directly or with slight modifications in many other studies, in most cases providing results in excellent agreement with experimental data [2.49–2.52].

However, Peppley's comprehensive model gives no answer as to whether the reaction pathway occurs via methyl formate or dioxomethylene as an intermediate. Although the methyl formate route was predicted based on results of Jiang et al. [2.53], the corresponding adsorption term was deleted in the rate expression, because methyl formate was not detectable in Peppley's DRIFTS experiments. Indeed, exactly the same rate expression would be obtained assuming dioxomethylene as an intermediate and deleting its adsorption term. Because only a few research groups have detected methyl formate as trace by-product [2.29,2.54,2.55], mostly in cases of high methanol surplus, this step of the reaction pathway remains unclear. Takezawa and Iwasa [2.56] and Takahashi et al. [2.57] have proposed a second reaction pathway via dioxomethylene through the nucleophilic addition of surface hydroxyls to adsorbed formaldehyde for a Cu/SiO₂ catalyst. This attack occurs competitively to that of methoxy groups (Fig. 2.3), which can explain the formation of methyl formate observed only at high MeOH/H₂O ratios.

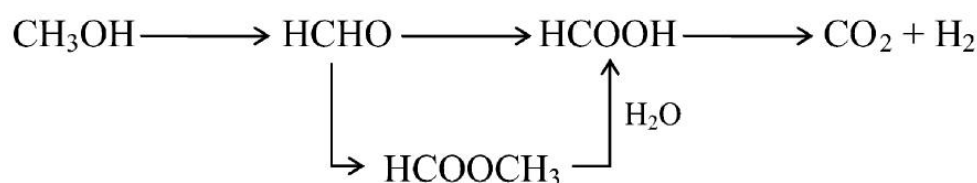


Figure 2.3 Reaction pathways of SRM over Cu/SiO₂ catalysts proposed by Takahashi et al. [2.57].

A further assumption by Peppley is the existence of two different kinds of active sites, one for oxygenate adsorption and one for hydrogen adsorption, based on a review by Skrzypek et al.

[2.54]. Because most of the other kinetic models found in the literature are based on a single active site, notable differences in the dependency of the reaction rate from the hydrogen partial pressure should be predicted from the rate laws, as discussed by Lee et al. [2.48]. Not taken into account in any model for SRM was the effect of hydrogen spillover. The existence of this elementary reaction step, although not rate-determining, was reported and proved for methanol synthesis [2.59,2.60]. Hydrogen adsorbs dissociatively on the copper surface, thereby providing a source of atomic hydrogen for methanol synthesis over oxidic phases. A possible relevancy of this process in SRM has been mentioned previously [2.41,2.47].

Up to now, only a few studies on surface species detected by DRIFTS during SRM have been published. One spectrum of a Cu/ZnO/Al₂O₃ catalyst has been given by Peppley et al. [2.47]; another for a CuO/ZnO/ZrO₂/Al₂O₃ catalyst has been reported by Breen et al. [2.61]. More detailed studies on Cu/ZnO/ZrO₂ samples have been published by Matter and Ozkan [2.62] and Vargas et al. [2.63]. All of these studies reported formate and methoxy groups as the predominant surface species. Hydroxyls and formaldehyde [2.61] were also detected, as was gas-phase or weakly bonded carbon dioxide [2.47]. Neither methyl formate nor carbon monoxide was found over copper-containing catalysts in these studies. In contrast, Jacobs and Davis [2.64] identified carbonate and carbon monoxide in SRM over a Pt/CeO₂ catalyst, but little data are available for a comparative evaluation, because the spectra were obtained under different reaction conditions.

The development of a possible microkinetic model for SRM over a commercial Cu/ZnO/Al₂O₃ catalyst has been described in detail by Peppley et al. [2.47]. As will be shown in Ch. 4, most of the experimental data gained in the present study can be explained using this proposed reaction mechanism. Thus, it was taken as basis of our investigations. The catalytic cycle begins with the dissociative adsorption of methanol on the catalyst surface, which is assumed to include two distinct types of active sites: one responsible for hydrogen adsorption (type 1a) and the other responsible for the adsorption of all other intermediates (type 1), which are exclusively oxygen-bonded. In this study, the adsorption sites are designated type A and type B instead of 1 and 1a, respectively. Jung and Bell [2.60], in their study of methanol synthesis, assigned the adsorption of hydrogen to the metallic copper surface, whereas the oxygenate chemistry occurs on the ceramic support (in this case, ZrO₂). A similar assignment in case of SRM is possible due to the principle of microreversibility. Matter and Ozkan [2.62] proposed methanol adsorption over hydroxylated surfaces via water formation. From kinetic experiments, this cannot be excluded, because at the end a similar reaction rate law would result. However, a methoxy group exhibiting dehydrogenation as the RDS of the overall reaction was also found by Lee et al. [2.48] and Jiang et al. [2.65] in their kinetic studies. Formaldehyde thus formed is immediately attacked by a methoxy group,

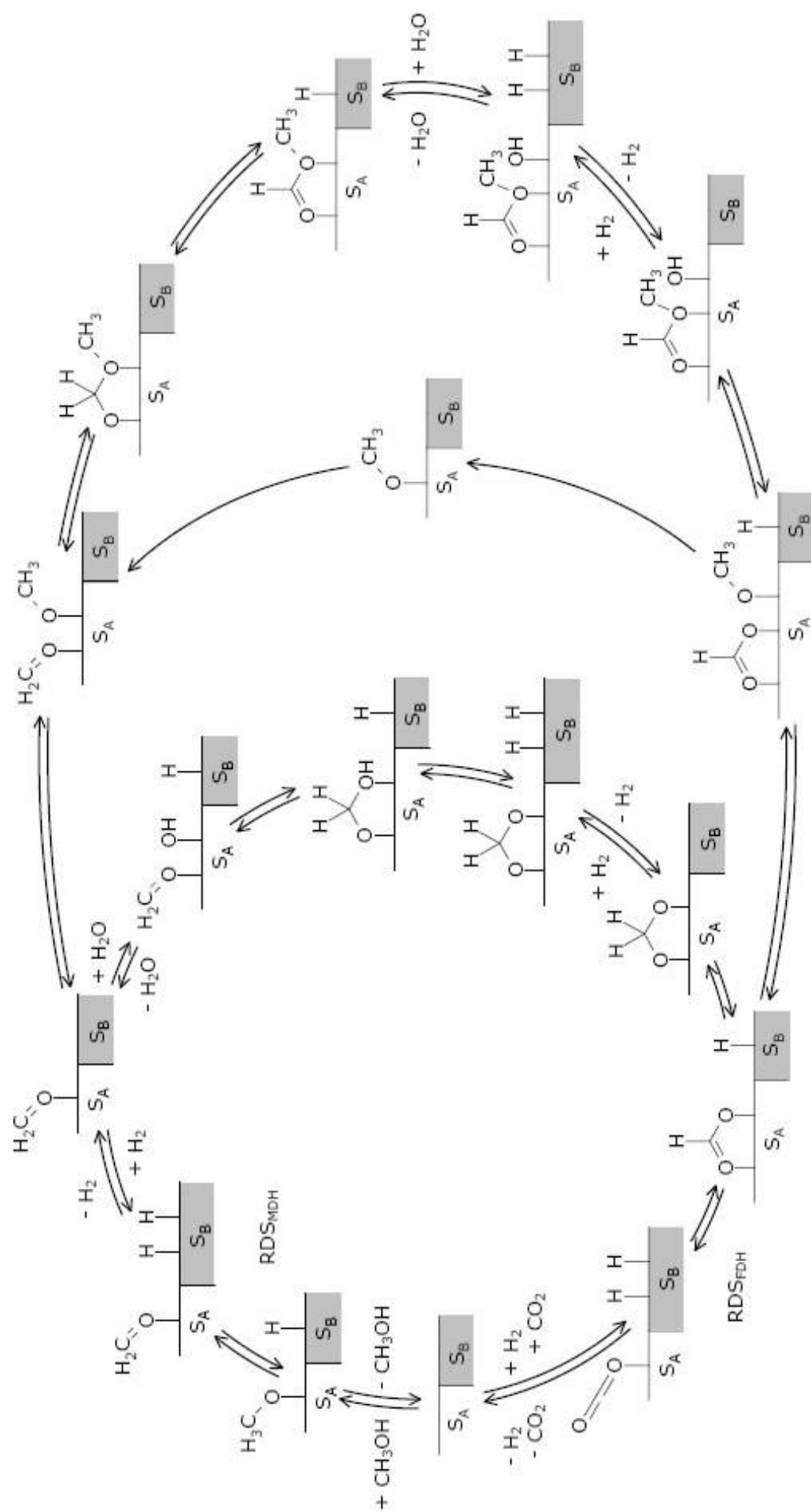


Figure 2.4 Catalysis cycle of methanol steam reforming on the basis of the investigations of Jiang et al. [2.53], Peppley et al. [2.47] and Takezawa and Iwasa [2.56], including different kinds of reactive surface sites A (□) and B (■).

resulting in the intermediate methyl formate [2.66,2.67], which was observed in several SRM studies as a by-product in trace amounts, exclusively in case of methanol surplus in the reactant mixture. One other reaction pathway towards methyl formate is described by the reaction of methanol with formate groups, as identified by Busca et al. [2.68] over VO_x/TiO_2 catalysts during methanol decomposition and partial oxidation. This reaction pathway appears less feasible over partly reduced copper catalysts due to the limited (and doubtful) ability to assign kinetic data from these greatly different catalyst systems and reaction conditions. However, methyl formate decomposes when in contact with hydroxyl groups to methoxy and formate groups. One other reaction mechanism was given by Takezawa and Takahashi et al. [2.56,2.57], who proposed the attack of formaldehyde by surface hydroxyls, resulting in the formation of dioxomethylene as a reaction intermediate. Dioxomethylene, the intermediate of the reverse methanol synthesis reaction, is supposed to dehydrogenate into a formate group. However, neither methyl formate nor dioxomethylene was observed in the DRIFTS study (Ch. 4.3) and thus will not appear in the adsorption term of the microkinetic rate law, which in this case then appears identical for both reaction mechanisms. The formate group dehydrogenates again to release carbon dioxide from the type A surface; the accumulated hydrogen desorbs molecularly from the type B surface.

The entire catalysis cycle of SRM is given schematically in Fig. 2.4. Adopting the Hougen–Watson formalism, based on the Langmuir adsorption isotherms, the kinetics of this catalysis cycle can be formulated using the following assumptions:

- (1) The dehydrogenation of methoxy group is rate-determining, all other elemental reactions are in thermodynamic equilibrium.
- (2) Oxygenates adsorb competitively and maximum in one monolayer on surface A, whereas hydrogen adsorbs dissociatively on surface B.
- (3) Only adsorbates observed in the DRIFTS study are considered in the adsorption term; in addition, adsorption of carbon dioxide is taken into account.
- (4) Measuring in the low-conversion regime, the reverse reaction is negligible.

The microkinetic rate equation of SRM is then given by Eq. 2.30, in which the index MDH means methoxy dehydrogenation:

$$\begin{aligned}
r_{\text{MDH}} &= -\frac{dp_{\text{MeOH}}}{dt} = k_{\text{MDH}} \epsilon_{\text{CH}_3\text{O}^{(\text{A})}} \epsilon_{\text{H}^{(\text{B})}} \\
&= \frac{k_{\text{MDH}} K_{\text{CH}_3\text{O}^{(\text{A})}}^* \left(p_{\text{CH}_3\text{OH}}/p_{\text{H}_2}^{1/2} \right) \left(1 - \left(p_{\text{H}_2}^3 p_{\text{CO}_2}/k_{\text{R}} p_{\text{CH}_3\text{OH}} p_{\text{H}_2\text{O}} \right) \right) C_{\text{S}_\text{A}}^{\text{T}} C_{\text{S}_\text{B}}^{\text{T}}}{\left(1 + K_{\text{CH}_3\text{O}^{(\text{A})}}^* \left(p_{\text{CH}_3\text{OH}}/p_{\text{H}_2}^{1/2} \right) + K_{\text{HCOO}^{(\text{A})}}^* p_{\text{CO}_2} p_{\text{H}_2}^{1/2} + K_{\text{OH}^{(\text{A})}}^* \left(p_{\text{H}_2\text{O}}/p_{\text{H}_2}^{1/2} \right) + K_{\text{CO}_2^{(\text{A})}}^* p_{\text{CO}_2} \right)} \\
&\quad \times \frac{1}{\left(1 + K_{\text{H}^{(\text{B})}}^{1/2} p_{\text{H}_2}^{1/2} \right)} \tag{2.30}
\end{aligned}$$

Here k_{MDH} is the rate constant and $C_{\text{S}_\text{A}}^{\text{T}}$ and $C_{\text{S}_\text{B}}^{\text{T}}$ are the total concentrations of type A and type B adsorption sites, respectively. Because these three values cannot be determined individually by parameter fitting, their product k^* (Eq. 2.31) was taken for this process:

$$k^* = k_{\text{MDH}} C_{\text{S}_\text{A}}^{\text{T}} C_{\text{S}_\text{B}}^{\text{T}} \tag{2.31}$$

The combined adsorption constants K^* given in the adsorption term of Eq. 2.30 are defined as Eqs. 2.32–2.34:

$$K_{\text{CH}_3\text{O}^{(\text{A})}}^* = \frac{K_{\text{CH}_3\text{OH}^{(\text{A,B})}}}{K_{\text{H}_2^{(\text{B})}}^{1/2}} \tag{2.32}$$

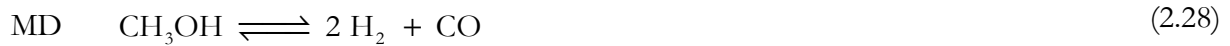
$$K_{\text{HCOO}^{(\text{A})}}^* = \frac{K_{\text{CO}_2^{(\text{A})}} K_{\text{H}_2^{(\text{B})}}^{1/2}}{K_{\text{HCOO}^{(\text{A,B})}}} \tag{2.33}$$

$$K_{\text{OH}^{(\text{A})}}^* = \frac{K_{\text{H}_2\text{O}^{(\text{A,B})}}}{K_{\text{H}_2^{(\text{B})}}^{1/2}} \tag{2.34}$$

with the temperature dependence of rate and adsorption constants given by the Arrhenius (Eq. 2.3) and van't Hoff (Eq. 2.5) equations, respectively:

2.3.3 Thermodynamic Considerations

To get an overview over the thermodynamically favoured product spectrum of the reactant mixture as a function of processing conditions, the reaction free Gibbs energy and equilibrium constants were calculated on the basis of materials data [2.69,2.70]. Hereby, gases were considered perfect, i.e., fugacity coefficients were set to 1. Calculations were performed by means of Maple V Release 4.00c software version. For the determination of the product spectrum of SRM including CO selectivity as a function of steam-to-carbon ratio and temperature only components have been taken into account that were observed experimentally, i.e., CH_3OH , H_2O , H_2 , CO_2 , and CO . Equilibrium constants of SRM (Eq. 2.27), methanol decomposition (Eq. 2.28), and reverse water-gas shift reaction (Eq. 2.29) as a function of temperature were calculated (Fig. 2.5).



SRM and methanol decomposition are thermodynamically strongly favoured in the range of typical SRM reaction conditions (200–300 °C, 1 bar). Against that, the equilibrium constant of reverse water-gas shift is below 1 for all temperatures included in the calculation. To test the impact of non-ideal behaviour as falsifying factor on the results, the experimental equilibrium constant of the reverse water-gas shift reaction is given as reference [2.71]. The observed congruency for temperatures > 500 K indicates the suitability of the simplified calculation method. The decomposition of methanol corresponds to the formal sum of SRM and reverse water-gas shift reaction. Consequently its equilibrium constant is the product of those of the latter reactions.

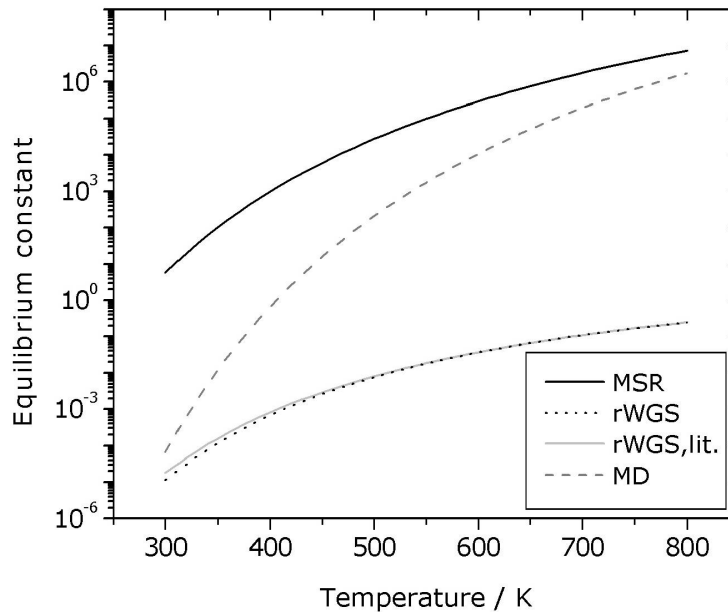


Figure 2.5 Equilibrium constants of SRM, reverse water-gas shift reaction (rWGS, including literature data as reference), and methanol decomposition (MD).

The resulting equilibrium conversion of CH₃OH and equilibrium partial pressure of CO on a wet basis (including water) in the temperature range of 400 up to 600 K is shown in Fig. 2.6. In accordance with other thermodynamic studies [2.72,2.73] independent from feed composition a conversion of > 99% can be achieved at temperatures > 470 K (Fig. 2.6 (a)). At stoichiometric feed ratio of 1:1 the temperature limit even decreases to 430 K and in case of water surplus full conversion can be achieved in the whole range of regarded temperatures. The hydrogen yield, however, decreases with increasing methanol content in the reactant mixture due to increasing participation of methanol decomposition as a result of a water deficit. At a methanol/water ratio

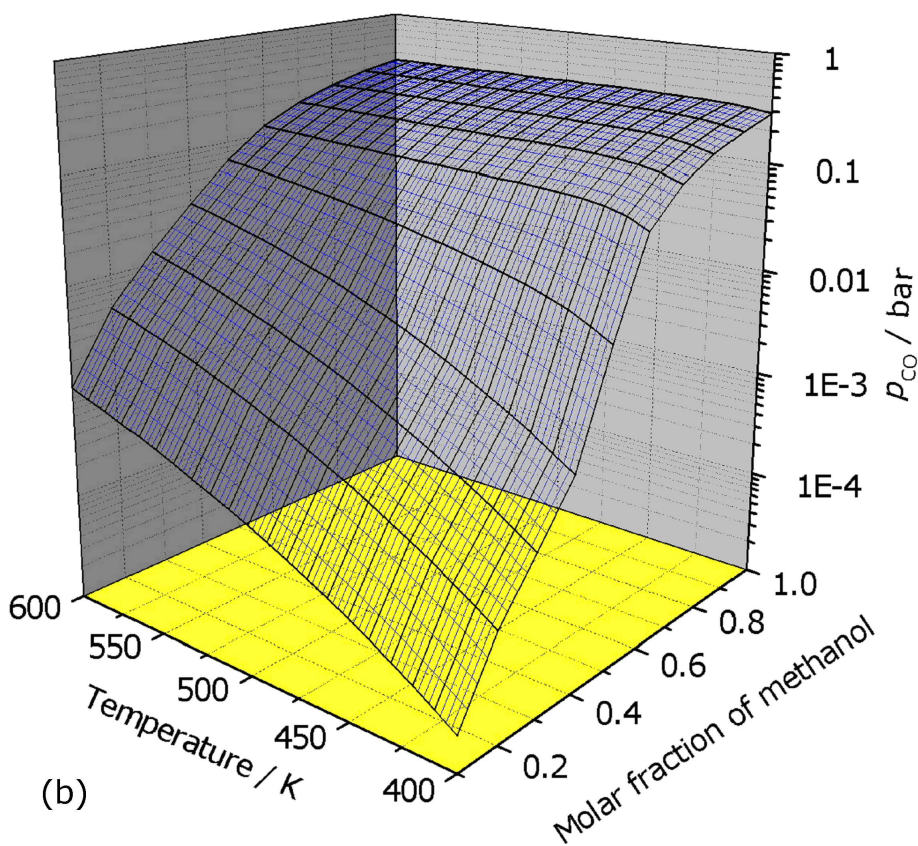
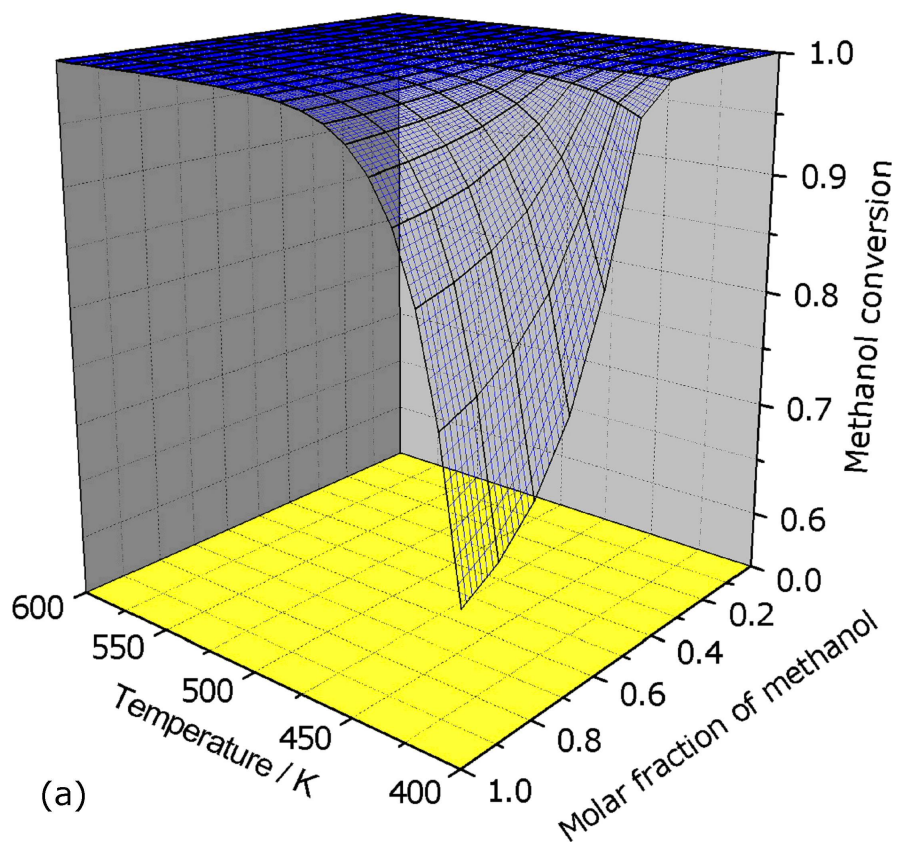


Figure 2.6 (a) Methanol conversion and (b) CO partial pressure in thermodynamic equilibrium considering SRM and reverse water-gas shift reactions and involved reactants.

of 1 and below, the hydrogen yield on a dry basis (exclusive water) is close to 75%, and decreases continuously down to 66.7% in case of pure methanol, as implied in Eqs. 2.27 and 2.28. Fig. 2.6 (b) shows the equilibrium concentration of CO on a wet basis (inclusive water). For pure methanol the CO yield is $> 33\%$ at $T > 460$ K (Eq. 2.28) and decreases strongly (note the logarithmic scale in Fig. 2.6 (b)) with increasing water content in the reactant mixture. Against that, the impact of temperature is relatively weak and causes an increasing CO content of one order of magnitude when raising the temperature from 400 to 600 K at stoichiometric reactant composition. However, a CO level tolerable for Pt electrodes of about 20 ppm is achieved only at the lowest regarded temperature of 400 K and a high water surplus [2.73]. Due to different scaling, these results are difficult to compare to diagrams presented in literature [2.72,2.73], however, tendencies are reflected in a satisfying manner. Formation of reaction products besides H_2 , CO_2 and CO has been observed only in a few studies. It was shown that this is due to thermodynamics and the formation of alkanes or higher alcohols is not favoured under SRM conditions [2.72,2.73]. Except methane and coke (graphite) formation no side reaction can have substantial contribution to the overall reaction network. The fact that neither coke nor methane was observed in most of the experimental studies found in literature can be referred to the high selectivity of Cu catalysts against these side products [2.73].

Unfortunately, Maple software failed in the determination of the product distribution with more than 6 reactants, so the thermodynamic equilibrium extended to several by-products (although in negligible quantities) cannot be given here. The reactions FA, F, DME, MF, C, and M describe the formation of formic acid, formaldehyde, dimethyl ether, methyl formate, coke (graphite), and methane, respectively (Eqs. 2.35–2.40).



Their equilibrium constants are given in Fig. 2.7. From Fig. 2.7 (a) it can be seen that the total oxidation of the carbon atom in methanol towards CO_2 (SRM) is strongly favoured compared to the partial oxidations yielding formic acid or formaldehyde. Since the latter reaction products are also disfavoured on the absolute scale ($\Delta_R G > 0$) they are not expected to have major influence on the product spectrum. Against that, dimethyl ether is a thermodynamically possible reaction

product under SRM conditions (Fig. 2.7 (b)). However, this component is hardly described in SRM related literature [2.55] but a common reaction product of acid catalyzed reactions of methanol. In the methanol to olefins (MTO) process, usually catalyzed by acidic zeolites, DME is a key intermediate. Methyl formate on the other hand is favoured at higher temperatures and methanol surplus. The fact, that this by-product was detected in a few studies mainly at lower temperatures of $< 250\text{ }^{\circ}\text{C}$ [2.29,2.54,2.55] may indicate a fast decomposition towards CO and H_2 or a kinetic barrier. The latter reason must also hold for the absence of coke and methane in the typical SRM product spectrum, since these components are thermodynamically strongly favoured compared to the SRM reaction (Fig. 2.7 (c)).

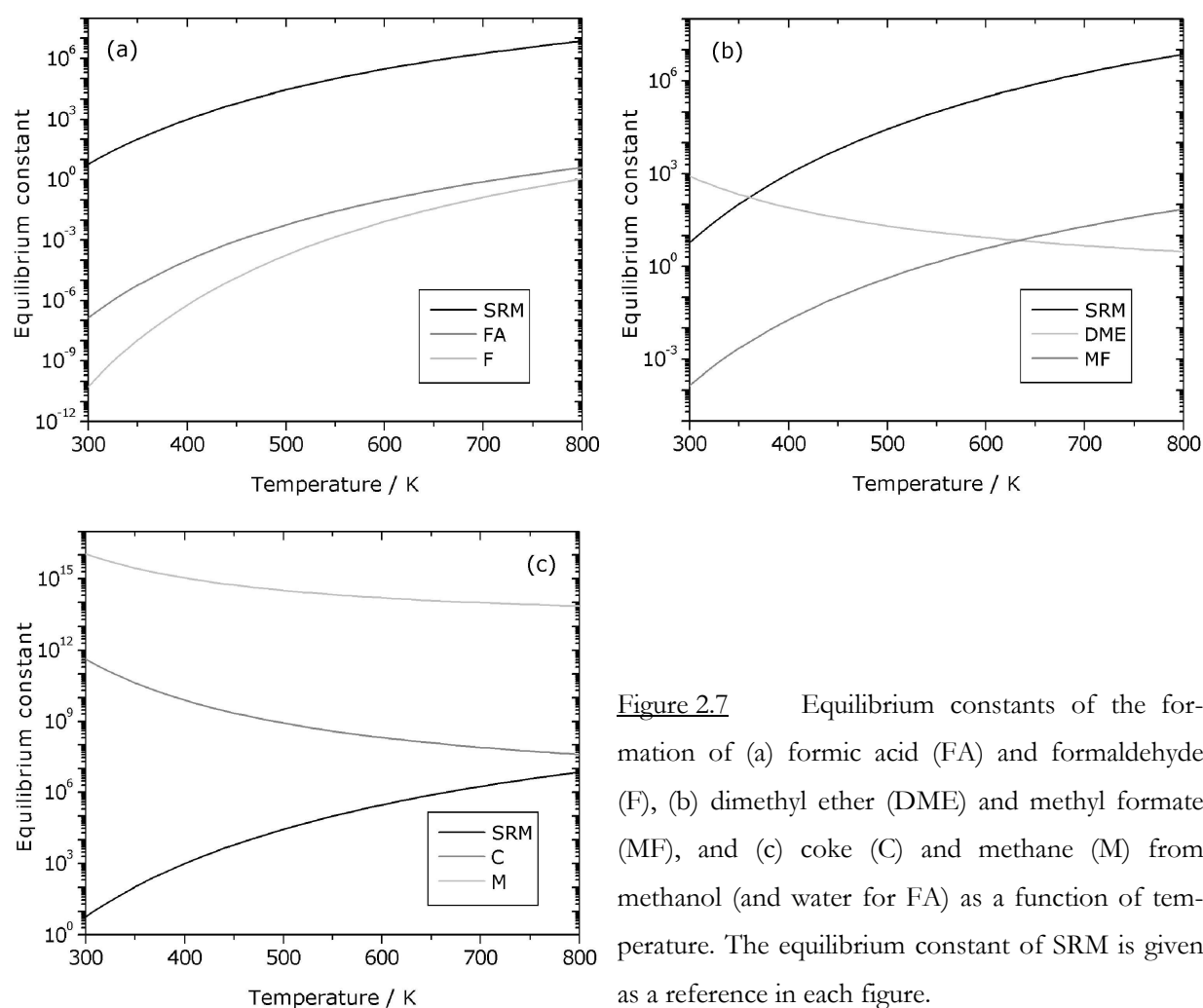


Figure 2.7 Equilibrium constants of the formation of (a) formic acid (FA) and formaldehyde (F), (b) dimethyl ether (DME) and methyl formate (MF), and (c) coke (C) and methane (M) from methanol (and water for FA) as a function of temperature. The equilibrium constant of SRM is given as a reference in each figure.

The thermodynamic evaluation regarding the equilibrium composition, however, should be performed with severe caution. As shown by Faungnawakij et al., the prediction of coke-formed and coke-free regions strongly depends on the chosen set of components in the model [2.72]. The calculated equilibrium constants should thereby only serve as a guideline for a possible reaction product composition under SRM conditions.

2.4 Oxidative Dehydrogenation of Propane over $\text{VO}_x/\gamma\text{-Al}_2\text{O}_3$ Catalysts

Oxidative dehydrogenation of lower alkanes ($\text{C}_2\text{--C}_4$) to the corresponding alkenes moved into the focus of research in the 1970s. Vanadia, molybdena, and also chromia catalysts were found to be outstandingly efficient in these reactions leading to the first patent of the Union Carbide Corp. for the oxidative dehydrogenation of ethane over various molybdena-containing mixed metal oxide catalysts [2.74]. However, due to low selectivity in most reactions, the conversion of n-butane to maleic anhydride is the only successful industrial practice in selective oxidation of alkanes. Vanadia catalysts being the most active and selective for oxidative dehydrogenation reactions compared to molybdena [2.75] or chromia based systems [2.76], which will not be considered here. Although there exist several studies on the catalytic performance of pure vanadia [2.77–2.79], these experiments have often been used only as a reference for those performed with supported vanadia species. Pure vanadia shows poor selectivity and is an inappropriate catalyst due to low surface area and Tamman temperature of 482 K ($\approx \frac{1}{2} T_m$) [2.75], which is below the typical reaction temperature of ODP. Catalytic performance can be drastically enhanced by deposition on an appropriate support, e.g., silica, alumina, titania, or zirconia.

Typical reaction conditions of the ODP in laboratory scale are temperatures of 300–500 °C and ambient pressure. Homogeneous gas phase reactions can be observed at temperatures above this range [2.80]. The feed composition is in general stoichiometric with respect to the ODP reaction, i.e., a molar ratio of $\text{C}_3\text{H}_8:\text{O}_2 = 2$. The feed is usually diluted with inert gases like He or N_2 to weaken the temperature increase due to high exothermicity.

2.4.1 Catalytic Performance of $\text{VO}_x/\gamma\text{-Al}_2\text{O}_3$ Catalyst

Supported vanadia catalysts are commonly prepared by the incipient wetness impregnation method. NH_4VO_3 is the most commonly used precursor, its low solubility in water can be enhanced by the addition of oxalic acid [2.81]. However, because solvent evaporation mainly occurs at the outer catalyst particle surface, the distribution of vanadia species provides a low homogeneity, i.e., higher degree of VO_x polymerization even at low vanadia loadings. An improvement in vanadia distribution can be achieved by the grafting or saturation-impregnation method, as applied in this study (Ch. 5.1.). Chemical anchoring of V onto the support is here achieved by ligand exchange of the precursor, e.g., acetyl acetonate or chloride, with surface hydroxyl groups. This prevents formation of double-layers and results in a high dispersion of vanadia species. Higher vanadia loadings can be achieved by repeated impregnation. Further suitable methods are spray drying [2.82], chemical vapour deposition [2.83], and thermal spreading [2.84].

$\text{VO}_x/\gamma\text{-Al}_2\text{O}_3$ catalysts have been extensively described in literature [2.85–2.89]. These studies imply their detailed characterization as well as catalytic testing in oxidative dehydrogenation of ethane and propane. Vanadia supported on $\gamma\text{-Al}_2\text{O}_3$ forms highly dispersed, amorphous phases whose structure changes from isolated vanadia tetrahedra at low loadings to polyvanadate species at medium loadings. At high loadings, crystalline V_2O_5 appears in addition to amorphous vanadia phases [2.81,2.85,2.86]. Klose et al. suggest the presence of $[\text{V}_3\text{O}_8]^{3-}$ as smallest unit present on the $\gamma\text{-Al}_2\text{O}_3$ support. Possible surface species are schematically depicted in Fig. 2.8.

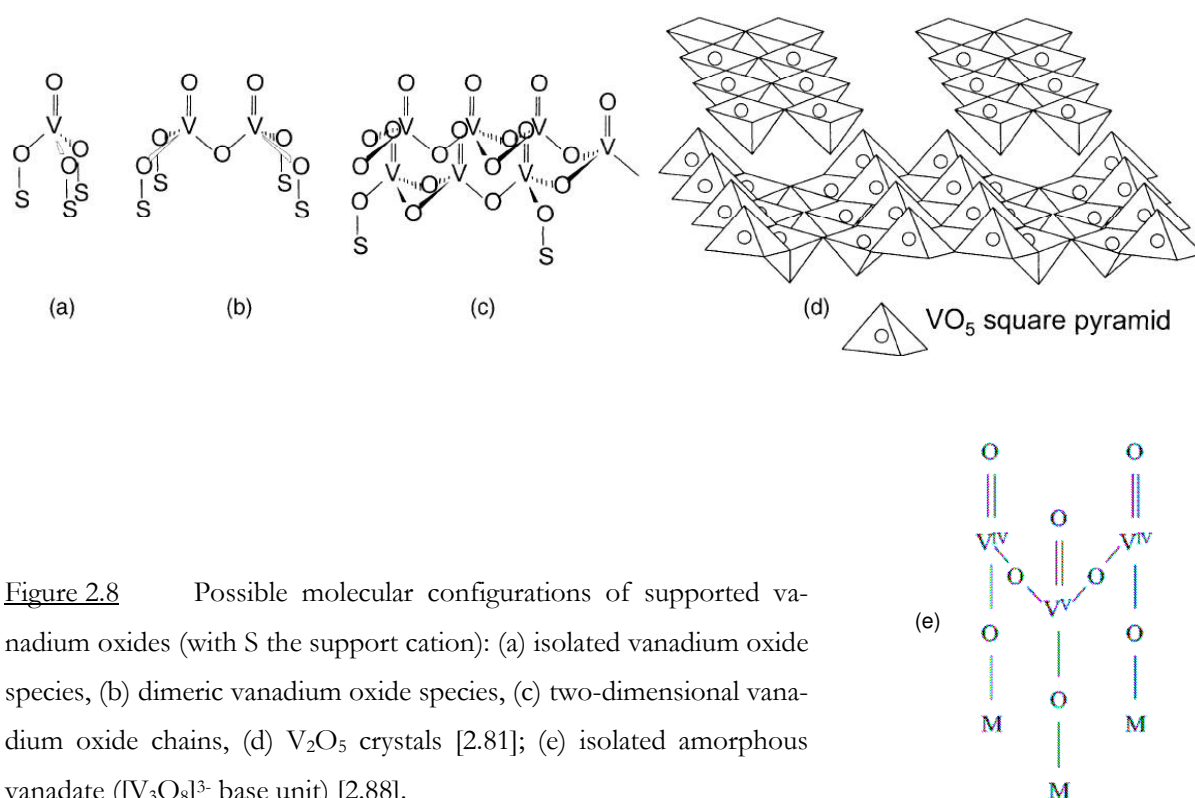


Figure 2.8 Possible molecular configurations of supported vanadium oxides (with S the support cation): (a) isolated vanadium oxide species, (b) dimeric vanadium oxide species, (c) two-dimensional vanadium oxide chains, (d) V_2O_5 crystals [2.81]; (e) isolated amorphous vanadate ($[\text{V}_3\text{O}_8]^{3-}$ base unit) [2.88].

The maximum amount of vanadia, that can be deposited on a $\gamma\text{-Al}_2\text{O}_3$ surface without formation of crystalline V_2O_5 , depends on support properties and preparation method and was found to be in the range of 5 up to 10 V atoms nm^{-2} [2.81,2.90]. Concentration ranges in which the formation of V_2O_5 bulk phase has been observed in recent studies are given in Fig. 2.9. Formation of crystalline V_2O_5 can be observed even below the theoretical value of 10 V atoms nm^{-2} , which originates from the crystal structure of pure V_2O_5 . Besides a heterogeneous distribution on the surface, one should also consider bond lengths and angles of the support material, which can lead to strains in the VO_x species and thereby also affect the maximum loading. This may explain the observation of V_2O_5 on silica even at relatively low loadings of 1 V atom nm^{-2} and below [2.81]. Formation of V_2O_5 is often accompanied by a drastic loss of surface area due to pore plugging. Additionally the induction of changes in the crystallinity of $\gamma\text{-Al}_2\text{O}_3$ has been reported [2.88,2.91].

The calculated value for an ideal coverage with monovanadates is 2.3–2.5 V atoms nm⁻². However, the distinguishment between monomeric and dispersed polymeric species appears difficult by spectroscopic methods. Differences of Brønstedt acidity or a slight shift in the Raman spectrum have been investigated for this purpose [2.87,2.88]. Tian et al. reported a method for quantification of monomeric species by UV-Vis spectroscopy [2.92]. This attempt is highly questionable due to severe methodological errors, even though a average value of V-O-V bonds per V atom can be derived from the UV-Vis edge energy [2.93].

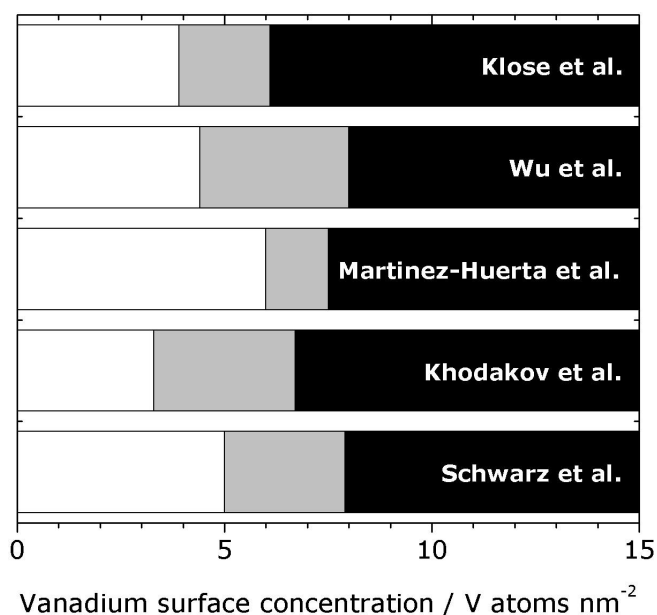


Figure 2.9 Absence (white) and presence (black) of crystalline V₂O₅ in VO_x/γ-Al₂O₃ catalysts as a function of the apparent vanadium surface concentration. Grey area indicates the range between two analyzed samples covering the critical concentration. The following reports are cited: Klose et al. [2.88], Wu et al. [2.87], Martínez-Huerta et al. [2.94], Khodakov et al [2.95], and Schwarz et al. [2.96].

In addition to VO_x species of various degrees of polymerization, mixed metal oxide phases (AlVO₄) have been observed in case of high vanadia loadings and under reaction/calcination temperatures above 570 °C [2.88,2.94]. These phases are the main reason for, although moderately pronounced, deactivation of VO_x/Al₂O₃ catalysts with time-on-stream.

Structurally different VO_x species provide different catalytic activity. This was investigated in several studies on the catalytic performance of differently loaded VO_x/γ-Al₂O₃ catalysts in the oxidative dehydrogenation of ethane and propane. The results are quite congruent as shown in Fig. 2.10, where activity in terms of turn-over frequency (TOF) is plotted against the vanadia loading. Due to different reaction conditions, data is displayed with normalized activity. One can see that highest TOFs can be achieved near theoretical monolayer coverage of 5–10 V atoms nm⁻². This indicates that polymeric dispersed species provide the highest activity for oxidative

dehydrogenation of propane and ethane. A decreased activity at lower loadings can be interpreted in the way that V-O-V bridging oxygen atoms play an important role in oxidation catalysis, whereas bridging V-O-Al atoms, as proposed by Wachs et al. [2.86], seem to be less active. This result is in agreement with the higher TPR maximum for monomeric species compared to dispersed agglomerates [2.94]. As soon as monolayer coverage is achieved and higher loadings lead to the formation of V_2O_5 , the TOF decreases again. This can indicate a lower activity of V_2O_5 bulk species but is more likely due to the inaccessibility of interior VO_x units, which are included in the TOF calculation, but do hardly get in contact with gas molecules and thereby do not participate in the reaction. The determination of the "real" TOF of surface VO_x units from V_2O_5 crystallites appears to be quite difficult.

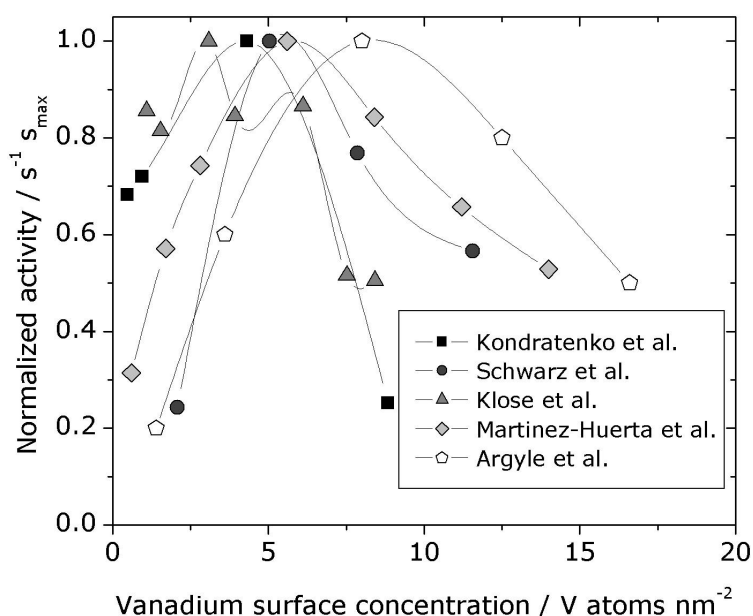


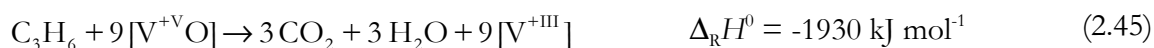
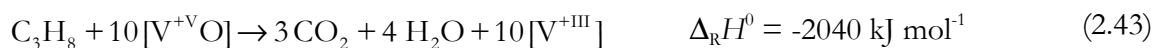
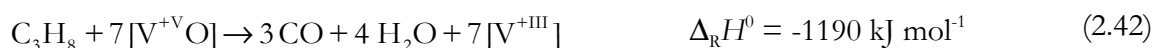
Figure 2.10 Normalized activity (TOF) of $VO_x/\gamma-Al_2O_3$ catalysts in the oxidative dehydrogenation of propane and ethane as a function of the apparent vanadium surface concentration. The following reports are cited: Kondratenko et al. [2.91], Schwarz et al. [2.96], Klose et al. [2.88], Martinez-Huerta et al. [2.94], and Argyle et al. [2.89].

Besides the discussed impact on activity, the vanadia loading also strongly affects the alkene selectivity in oxidative dehydrogenation reactions. The general trend is: the higher the vanadia loading, the lower the alkene selectivity at isoconversion [2.88,2.89], which is also observed for other support materials [2.97,2.98]. Either polymeric species are less selective a priori, or consecutive oxidation of the activated alkene is favoured due to the high surface concentration of active sites, i.e., the higher statistical probability of the alkene being directly further oxidized, at higher vanadia loadings. Kondratenko et al. observed a decreased selectivity at extremely low vanadia loadings [2.91], which may be explained by the fact that in this case the activity of the

support material cannot be neglected anymore. Although monomeric vanadia species are supposed to react highly selective due to the availability of only one active oxygen atom, the formed propene is supposed to non-oxidatively decompose on the acidic γ -alumina support yielding lower hydrocarbons and soot.

2.4.2 The reaction network and reaction pathways

The main reaction products of ODP are C_3H_6 , H_2O , CO , and CO_2 . Trace amounts of CH_4 , C_2H_4 , and C_2H_6 can be referred to cracking processes and have solely been observed at higher temperatures. Gas phase species get oxidized corresponding to the Mars-van Krevelen mechanism [2.12], the participation of lattice oxygen atoms of VO_x species was proven in several studies [2.100–2.103]. Regarding monomeric VO_x species as catalytically active sites, this is accompanied with their reduction from V^{+V} to V^{+III} and leads to the following reaction network of ODP including oxidation reactions only (Eqs. 2.41–2.47):



Due to the formation of water and/or carbon oxides and the resulting high reaction enthalpy, all of these reactions are close to irreversible in the typical range of ODP reaction conditions.

However, most of the reported kinetic studies of the ODP include only a selection of these reactions, whereas others were found to not occur or have negligible influence on the overall conversion. Some examples are assembled in Fig. 2.11. Andersson et al. only considered direct oxidation pathways starting from C_3H_8 but did not distinguish between CO and CO_2 [2.104]. Against that Creaser et al. took only consecutive combustion of C_3H_6 as a source of CO_x formation into account [2.105], which is the most common set of reactions for the description of ODP. Barsan et al. proposed a strictly consecutive reaction scheme including also CO oxidation yielding CO_2 [2.106]. The most comprehensive study, although based only on a formal kinetic model, was reported by Bottino et al., including the complete set of reactions [2.107]. However,

* Given reaction enthalpies include catalyst reoxidation with gas phase oxygen (Eq. 2.47).

one also has to consider different catalysts and reaction conditions here, i.e., range of reaction temperatures and partial pressures of the reactants.

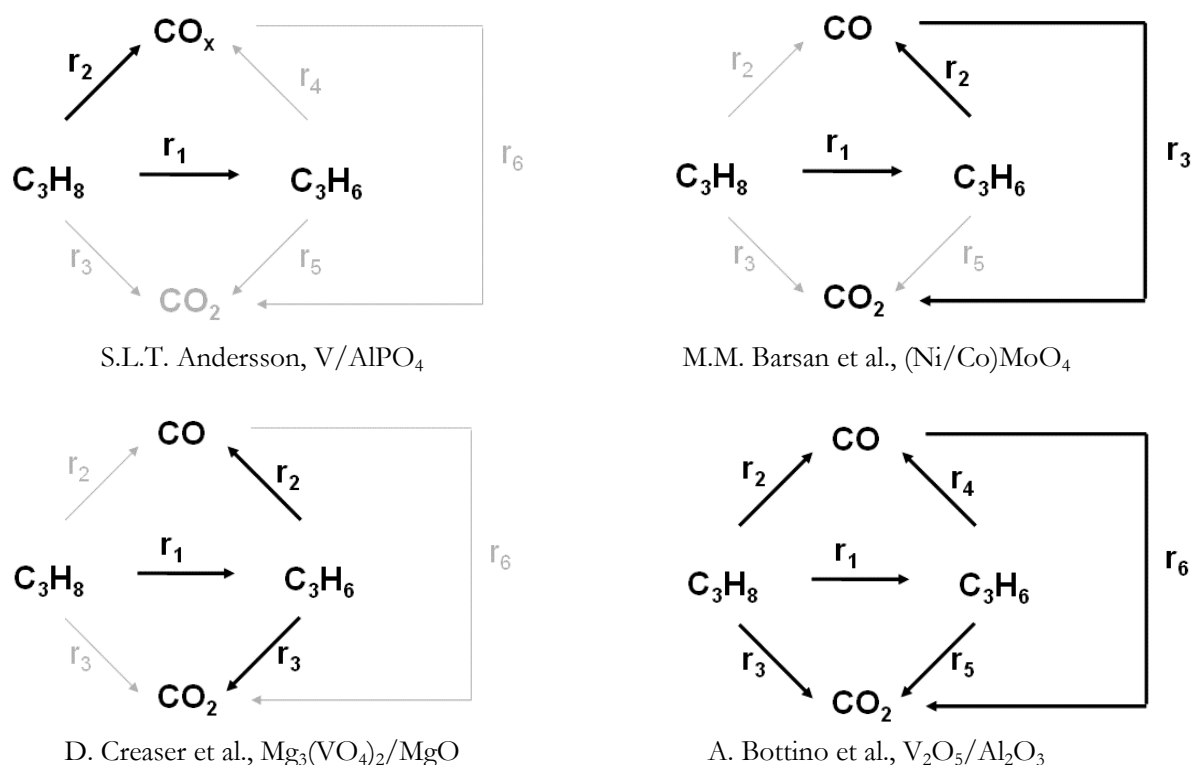
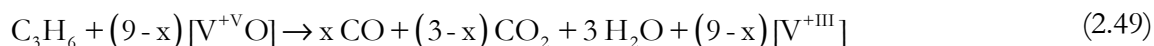
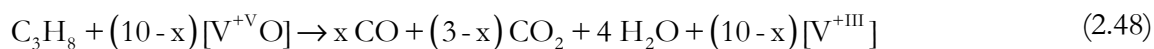


Figure 2.11 Reaction networks of ODP proposed for different catalysts and reaction conditions. The following reports are cited: S.L.T. Andersson [2.104], M.M. Barsan et al. [2.106], D. Creaser et al. [2.105], and A. Bottino et al. [2.107].

As the strictly independent formation of CO and CO₂ appears unlikely, Eqs. 2.42 and 2.43, as well as Eqs. 2.44 and 2.45. have been combined in several studies (Eqs. 2.48 and 2.49).



Since CO oxidation in general is rather slow, a dimensionless coefficient, defined as the ratio of CO and CO₂ or vice versa, is then used to describe the formation of both carbon oxides. Another important aspect for the description of the catalytic system is the degree of reduction of the catalyst, which fundamentally controls activity and selectivity in the ODP. This characteristic is part and parcel of steady-state models developed by Grabowski et al. or Deo et al. [2.108, 2.109]. It allows for the explanation of the apparent contradiction between (i) higher activation energy of propene combustion compared to the selective ODP reaction from independent experiments, and (ii) increasing selectivity of the overall ODP reaction with increasing temperature, as observed by Dinse et al. [2.110] for differently supported vanadia catalysts. It appears that

during pure propene combustion the catalyst is nearly fully reduced (V^{+II}) and the apparent activation energy can be attributed to the catalyst reoxidation, which is rate-determining in this case. Against that during ODP the catalyst is for the most part oxidized, resulting in apparent activation energies which can be referred to the C-H activation step of both substrates.

From the microkinetic point of view, only the selective pathway of propene formation has been investigated so far. The proposed catalysis cycle starts with the dissociative adsorption of C_3H_8 on an active site, i.e., a $[V^{+V}O]$ species, resulting in a propoxy intermediate and a hydroxyl group. Propene is then formed by decomposition of the propoxy group, again leaving a vanadium-bound hydroxyl group. Finally, the latter dehydrate under release of water. In the second part of the catalysis cycle the reduced active site is reoxidized by gas phase oxygen. This reaction pathway (Fig. 2.12) was first published for a V_2O_5/ZrO_2 catalyst by Chen et al. [2.111]. Weak propane adsorption and water desorption are here assumed to be reversible, whereas the consecutive dehydrogenation of propane and the propoxy group as well as the catalyst reoxidation are irreversible.

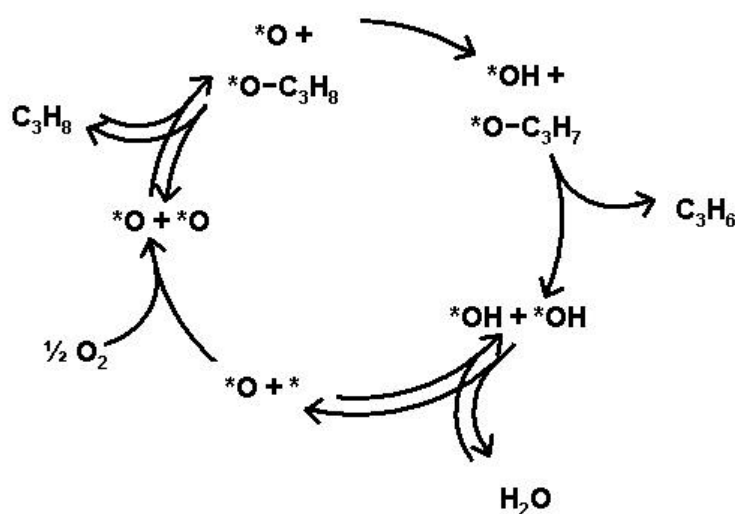


Figure 2.12 Catalysis cycle of the oxidative dehydrogenation of propane over a VO_x/ZrO_2 catalyst, proposed by Chen et al. [2.111].

From this mechanism a complex rate equation r_{MvK} can be derived (Eq. 2.50), which provides typical Mars-van Krevelen properties: (i) in case of a fast catalyst reoxidation (general case), the rate simplifies to a 1st order rate law depending only on the propane partial pressure, and (ii) in case of slow reoxidation, the rate depends with 0.5th order on the oxygen partial pressure, whereas the impact of propane partial pressure decreases to 0.5th order. Water as V^{+III} adsorbing agent then inhibits the reaction with a negative reaction order of -1.

$$r_{\text{MvK}} = \frac{k_{\text{red}} K_{\text{C}_3\text{H}_8} p_{\text{C}_3\text{H}_8}}{\left\{ 1 + \left(K_{\text{H}_2\text{O}} p_{\text{H}_2\text{O}} \right)^{0.5} \times \left(\frac{k_{\text{red}} K_{\text{C}_3\text{H}_8} p_{\text{C}_3\text{H}_8}}{2 k_{\text{ox}} p_{\text{O}_2}} \right)^{0.25} \right\}^2} \quad (2.50)$$

where k_{ox} and k_{red} are rate constants of catalyst oxidation and reduction, respectively, K_i are adsorption constants and p_i the partial pressures of the reactants. However, this model, as the entirety of published Mars-van Krevelen rate laws, does not consider re-adsorption of reaction products (except water) and fitted constants should be discussed with severe caution or only as guidelines for the comparison among different catalysts [2.112]. The above mechanism was developed for a 10 wt% $\text{V}_2\text{O}_5/\text{ZrO}_2$ catalyst, i.e., the presence of monomeric VO_x species can be excluded. Rozanska et al. in an exclusively theoretical study based on density functional theory proposed a similar mechanism for neighboured "cooperating" active sites but suggest a propyl radical as an intermediate for ODP over monomeric VO_x/SiO_2 sites [2.113]. This propyl radical desorbs after a first dehydrogenation at a vanadyl oxygen atom and is further dehydrogenated in a second step forming propene. Instead of the reduction of $\text{V}^{+\text{V}}$ to $\text{V}^{+\text{III}}$ this pathway would produce two hydroxylated $\text{V}^{+\text{IV}}$ sites.

Compared to this selective part of the reaction network, mechanistic studies of unselective reactions yielding CO_x are hardly described in literature. The total absence of oxygenated by-products indicates that the first step of the deep oxidation is rate-determining. Possible intermediates, e.g. carboxylic acids, aldehydes, or alcohols, appear to strongly adsorb and get oxidized quickly yielding exclusively CO_x . In general three reasons have been proposed for the appearance of selective and unselective reactions starting from propane: (i) a different orientation of the propane molecule in the first dehydrogenation step, (ii) a different oxygen atoms of the vanadyl group, and (iii) different active sites. Grabowski et al. proposed that propane reacts towards propene if the C_3H_8 molecule is orientated perpendicular to the surface and the reaction yields CO_x if the alkane adopts planar configuration of the carbon chain, parallel to the catalyst surface. The latter case allows for concurrent interaction of several lattice oxygen atoms with two neighbouring C-atoms in the alkane molecule which leads to a C-C bond breakage, the first step in unselective combustion. Against that Chen et al. suggest that C_3H_8 adsorption at the vanadyl oxygen yields exclusively C_3H_6 , whereas CO_x is the favoured reaction product if C_3H_8 gets in contact with the bridging oxygen atom between vanadium and support atoms [2.111]. Kondratenko et al. proposed highly active peroxovanadates to be responsible for unselective propane oxidation [2.114]. These peroxovanadates are the intermediate in the reoxidation process of $\text{V}^{+\text{III}}$ with gas phase dioxygen. Consequently the reaction provides much higher selectivity if N_2O is used as oxidant instead of pure oxygen. A similar theory was proposed previously based on TAP experiments

[2.100]. Electrophilic oxygen forms (e.g. O_2 , O_2^- , O^\cdot) have been claimed to perform total oxidation, whereas nucleophilic, lattice oxygen the selective [2.115,2.116]. In case of consecutive propene combustion this differentiation is needless since both configurations as well as both kinds of active sites lead to CO_x formation.

References of Chapter 2

- [2.1] M. Baerns, H. Hofmann, A. Renken, *Chemische Reaktionstechnik*, Thieme, Stuttgart, **1999**.
- [2.2] R.J. Wijngaarden, A. Kronberg, K.R. Westerterp, *Industrial Catalysis*, Wiley-VCH, Weinheim, **1998**.
- [2.3] I. Chorkendorff, J.W. Niemantsverdriet, *Concepts of Modern Catalysis and Kinetics*, Wiley-VCH, Weinheim, **2003**.
- [2.4] G. Ertl, H. Knözinger, J. Weitkamp (Eds.), *Handbook of Heterogeneous Catalysis*, Vol. 3, Wiley-VCH, Weinheim, **1997**.
- [2.5] J.R. Anderson, M. Boudart (Eds.), *Catalysis – Science and Technology*, Vol. 2, Springer, Berlin, **1982**.
- [2.6] G.F. Froment, *AIChE J.* **1975** 21 1041.
- [2.7] D.E. Maers, *Ind. Eng. Process. Des. Develop.* **1971** 10 541.
- [2.8] A. Mastalir, B. Frank, A. Szizybalski, H. Soerijanto, A. Deshpande, M. Niederberger, R. Schomäcker, R. Schlögl, T. Ressler, *J. Catal.* **2005** 230 464.
- [2.9] L. Gröschel, R. Haidar, A. Beyer, H. Cölfen, B. Frank, R. Schomäcker, *Ind. Eng. Chem. Res.* **2005** 44 9064.
- [2.10] B. Frank, D. Habel, R. Schomäcker, *Catal. Lett.* **2005** 100 181.
- [2.11] B. Frank, A. Yildiz, E. Feike, H. Schubert, R. Schomäcker, *Chem. Eng. Technol.* **2006** 29 519.
- [2.12] P. Mars, D.W. van Krevelen, *Chem. Eng. Sci. Spec. Suppl.* **1951** 3 41.
- [2.13] F.C. Jentoft, *Modern Methods in Heterogeneous Catalysis*, Lecture Series, **2002**, <http://w3.rz-berlin.mpg.de/~jentoft/lehre/jentoft_kinetics_011102.ppt>, 15.03.2007.
- [2.14] A. Wheeler, *Adv. Catal.* **1951** 3 250.
- [2.15] J.A. Christiansen, *J. Amer. Chem. Soc.* **1921** 43 1670.
- [2.16] N. Iwasa, N. Kudo, H. Takahashi, S. Masuda, N. Takezawa, *Catal. Lett.* **1993** 19 211.
- [2.17] K.C. Waugh, *Catal. Today* **1992** 15 51.
- [2.18] B. Bems, PhD Thesis, Technical University of Berlin, Berlin, **2003**.
- [2.19] H. Agarás, G. Cerrella, *Appl. Catal.* **1988** 45 53.
- [2.20] D.M. Whittle, A.A. Mirzaei, J.S.J. Hargreaves, R.W. Joyner, C.J. Kiely, S.H. Taylor, G.J. Hutchings, *Phys. Chem. Chem. Phys.* **2002** 4 5915.
- [2.21] B.L. Kniep, T. Ressler, A. Rabis, F. Girgsdies, M. Baenitz, F. Steglich, R. Schlögl, *Angew. Chem. Int. Ed.* **2003** 43 112.
- [2.22] R.O. Idem, N.N. Bakhshi, *Can. J. Chem. Eng.* **1996** 74 288.
- [2.23] P.J. de Wild, M.J.F.M. Verhaak, *Catal. Today* **2000** 60 3.
- [2.24] M.S. Spencer, *Top. Catal.* **1999** 8 259.
- [2.25] Y. Nitta, O. Suwata, Y. Ikeda, Y. Okamoto, T. Imanaka, *Catal. Lett.* **1994** 26 345.
- [2.26] X. Zhang, P. Shi, *J. Mol. Catal. A* **2003** 194 99.
- [2.27] B. Lindström, L.J. Petterson, *Int. J. Hydrogen Energy* **2001** 26 923.
- [2.28] H. Kobayashi, N. Takezawa, C. Minochi, *J. Catal.* **1981** 69 487.
- [2.29] Y. Liu, T. Hayakawa, K. Suzuki, S. Hamakawa, T. Tsunoda, T. Ishii, M. Kumagai, *Appl. Catal. A* **2002** 223 137.
- [2.30] H.S. Roh, K.W. Jun, W.S. Dong, S.E. Park, Y.S. Baek, *Catal. Lett.* **2001** 74 31.
- [2.31] M.F. Luo, J. Chen, L.S. Chen, J.Q. Lu, Z. Feng, C. Li, *Chem. Mater.* **2001** 13 197.
- [2.33] B. Frank, Diploma Thesis, Technical University of Berlin, Berlin, **2004**.
- [2.34] Y. Liu, T. Hayakawa, K. Suzuki, S. Hamakawa, *Catal. Commun.* **2001** 2 195.
- [2.35] B.E. Goodby, J.E. Pemberton, *Appl. Spectrosc.* **1988** 42 754.
- [2.36] M.M. Günter, T. Ressler, R.E. Jentoft, B. Bems, *J. Catal.* **2001** 203 133.
- [2.37] K.-O. Hinrichsen, J. Strunk, *Nachr. Chem.* **2006** 54 1080.
- [2.38] M.V. Twigg, M.S. Spencer, *Top. Catal.* **2003** 22 191.
- [2.39] P.H. Matter, D.J. Braden, U.S. Ozkan, *J. Catal.* **2004** 223 340.

- [2.40] X.R. Zhang, P. Shi, J. Zhao, M. Zhao, C. Liu, *Fuel Process. Technol.* **2003** 83 183.
- [2.41] J. Agrell, H. Birgersson, M. Boutonnet, I. Melian Cabrera, R.M. Navarro, J.L.G. Fierro, *J. Catal.* **2003** 219 389.
- [2.42] J.P. Breen, J.R.H. Ross, *Catal. Today* **1999** 51 521.
- [2.43] H. Purnama, F. Girgsdies, T. Ressler, J.H. Schattka, R.A. Caruso, R. Schomäcker, R. Schlögl, *Catal. Lett.* **2004** 94 61.
- [2.44] Y. Men, H. Gnaser, R. Zapf, V. Hessel, C. Ziegler, *Catal. Commun.* **2004** 5 671.
- [2.45] B.A. Peppley, J.C. Amphlett, L.M. Kearns, R.F. Mann, *Appl. Catal. A* **1999** 179 21.
- [2.46] H. Purnama, T. Ressler, R.E. Jentoft, H. Soerijanto, R. Schlögl, R. Schomäcker, *Appl. Catal. A* **2004** 259 83.
- [2.47] B.A. Peppley, J.C. Amphlett, L.M. Kearns, R.F. Mann, *Appl. Catal. A* **1999** 179 31.
- [2.48] J.K. Lee, J.B. Ko, D.H. Kim, *Appl. Catal. A* **2004** 278 25.
- [2.49] S.A. Asprey, B.W. Wojciechowski, B.A. Peppley, *Appl. Catal. A* **1999** 179 51.
- [2.50] M.P. Harold, B. Nair, G. Kolios, *Chem. Eng. J.* **2003** 58 2551.
- [2.51] A. Morillo, A. Freund, C. Merten, *Ind. Eng. Chem. Res.* **2004** 43 4624.
- [2.52] F. Gallucci, L. Paturzo, A. Basile, *Ind. Eng. Chem. Res.* **2004** 43 2420.
- [2.53] C.J. Jiang, D.L. Trimm, M.S. Wainwright, N.W. Cant, *Appl. Catal. A* **1993** 97 145.
- [2.54] K. Takahashi, N. Takezawa, H. Kobayashi, *Appl. Catal.* **1982** 2 363.
- [2.55] Y. Choi, H.G. Stenger, *Appl. Catal. B* **2002** 38 259.
- [2.56] N. Takezawa, N. Iwasa, *Catal. Today* **1997** 36 45.
- [2.57] K. Takahashi, N. Takezawa, H. Kobayashi, *Chem. Lett.* **1985** 759 (cited in [2.43]).
- [2.58] J. Skrzypek, J. Sloczynki, S. Ledakowicz, Methanol Synthesis, ISBN 83-01-11490-8, Polish Scientific Publishers, Warsaw, **1994** (cited in [2.33]).
- [2.59] R.J. Burch, S.E. Golunski, M.S. Spencer, *Catal. Lett.* **1990** 5 55.
- [2.60] K.D. Jung, A.T. Bell, *J. Catal.* **2000** 193 207.
- [2.61] J.P. Breen, F.C. Meunier, J.R.H. Ross, *Chem. Commun.* **1999** 2247.
- [2.62] P.H. Matter, U.S. Ozkan, *J. Catal.* **2005** 234 463.
- [2.63] M.A. Larrubia Vargas, G. Busca, U. Costantino, F. Marmottini, T. Montanari, P. Patrono, F. Pinzari, G. Ramis, *J. Mol. Catal. A* **2006** 266 188.
- [2.64] G. Jacobs, B.H. Davis, *Appl. Catal. A* **2005** 285 43.
- [2.65] C.J. Jiang, D.L. Trimm, M.S. Wainwright, N.W. Cant, *Appl. Catal. A* **1993** 93 245.
- [2.66] R. Zhang, Y. Sun, S. Peng, *Fuel* **2002** 11–12 1619.
- [2.67] G.J. Millar, C.H. Rochester, K.C. Waugh, *J. Chem. Soc. Faraday Trans.* **1991** 87 2795.
- [2.68] G. Busca, A.S. Elmi, P. Fortazzi, *J. Phys. Chem.* **1987** 91 5263.
- [2.69] G.H. Aylward, T.J.V. Findlay, *Datensammlung Chemie in SI-Einheiten*, 3rd Edition, ISBN 3-527-29468-6, Wiley-VCH, Weinheim, **1999**.
- [2.70] NIST Chemistry WebBook, Standard Reference Database of the National Institute of Standards and Technology, <<http://webbook.nist.gov/chemistry/>>, 30.04.2007.
- [2.71] G. Ertl, H. Knözinger, J. Weitkamp (Editors), *Handbook of Heterogeneous Catalysis*, Vol. 4, Wiley-VCH, Weinheim, **1997**.
- [2.72] K. Faungnawakij, R. Kikuchi, K. Eguchi, *J. Power Sources* **2006** 161 87.
- [2.73] Y. Lwin, W.R.W. Daud, A.B. Mohamed, Z. Yakoob, *Int. J. Hydrogen Energy* **2000** 25 47.
- [2.74] US Patent 4250346, to Union Carbide Corp., **1980**.
- [2.75] K. Chen, A.T. Bell, E. Iglesia, *J. Phys. Chem. B* **2000** 104 1292.
- [2.76] B.Y. Jibril, *Appl. Catal. A* **2004** 264 193.
- [2.77] J. Le Bars, J.C. Védrine, A. Auroux, B. Pommier, G.M. Pajonk, *J. Phys. Chem.* **1992** 96 2217.
- [2.78] L. Owens, H.H. Kung, *J. Catal.* **1993** 144 202.
- [2.79] S.T. Oyama, G.A. Somorjai, *J. Phys. Chem.* **1990** 94 5022.
- [2.80] R. Burch, E.M. Crabb, *Appl. Catal. A* **1993** 100 111.
- [2.81] B.M. Weckhuysen, D.E. Keller, *Catal. Today* **2003** 78 25.
- [2.82] J.B. Stelzer, J. Caro, D. Habel, E. Feike, H. Schubert, M. Fait, G. Hidde, *Chem. Eng. Technol.* **2004** 27 839.
- [2.83] K. Inumaru, M. Misono, T. Okuhara, *Appl. Catal. A* **1997** 149 133.
- [2.84] G. Centi, E. Giamello, D. Pijnelli, F. Trifiro, *J. Catal.* **1991** 130 220.
- [2.85] E.A. Mamedov, V. Cortés Corbéran, *Appl. Catal. A* **1995** 127 1, and references therein.
- [2.86] I.E. Wachs, *Catal. Today* **2005** 100 79.
- [2.87] Z. Wu, H.-S. Kim, P.C. Stair, S. Rugmini, S.D. Jackson, *J. Phys. Chem. B* **2005** 109 2793.

- [2.88] F. Klose, T. Wolff, H. Lorenz, A. Seidel-Morgenstern, Y. Suchorski, M. Piórkowska, H. Weiss, *J. Catal.* **2007** 247 176.
- [2.89] M.D. Argyle, K. Chen, A.T. Bell, E. Iglesia, *J. Catal.* **2002** 208 139.
- [2.90] M. Baltes, PhD Thesis, University of Antwerp, Belgium, **2001** (cited in [2.78]).
- [2.91] E.V. Kondratenko, M. Baerns, *Appl. Catal. A* **2001** 222 133.
- [2.92] H. Tian, E.I. Ross, I.E. Wachs, *J. Phys. Chem. B* **2006** 110 9593.
- [2.93] X. Gao, I.E. Wachs, *J. Phys. Chem. B* **2000** 104 1261.
- [2.94] M.V. Martínez-Huerta, X. Gao, H. Tian, I.E. Wachs, J.L.G. Fierro, M.A. Bañares, *Catal. Today* **2006** 118 279.
- [2.95] A. Khodakov, B. Olthof, A.T. Bell, E. Iglesia, *J. Catal.* **1999** 181 205.
- [2.96] O. Schwarz, B. Frank, C. Hess, R. Schomäcker, *Catal. Commun.* **2007** (accepted), DOI: 10.1016/j.catcom.2007.06.009.
- [2.97] P. Viparellia, P. Ciambelli, L. Lisi, G. Ruoppolo, G. Russo, J.C. Volta, *Appl. Catal. A* **1999** 184 291.
- [2.98] E.V. Kondratenko, M. Cherian, M. Baerns, D. Su, R. Schlögl, X. Wang, I.E. Wachs, *J. Catal.* **2005** 234 131.
- [2.100] A. Pantazidis, S.A. Bucholz, H.W. Zanthoff, Y. Schuurman, C. Mirodatos, *Catal. Today* **1998** 40 207.
- [2.101] K. Chen, A. Khodakov, J. Yang, A.T. Bell, E. Iglesia, *J. Catal.* **1999** 186 325.
- [2.102] E.V. Kondratenko, M. Cherian, M. Baerns, *Catal. Today* **2005** 99 59.
- [2.103] N. Ballarín, F. Cavani, M. Ferrara, R. Catanic, U. Cornaro, *J. Catal.* **2003** 213 95.
- [2.104] S.L.T. Andersson, *Appl. Catal. A* **1994** 112 209.
- [2.105] D. Creaser, B. Andersson, *Appl. Catal. A* **1996** 141 131.
- [2.106] M.M. Barsan, F.C. Thyron, *Catal. Today* **2003** 81 159.
- [2.107] A. Bottino, G. Capannelli, A. Comite, S. Storace, R. Di Felice, *Chem. Eng. J.* **2003** 94 11.
- [2.108] R. Grabowski, J. Słoczyński, *Chem. Eng. Proc.* **2005** 44 1082.
- [2.109] K. Routray, G. Deo, *AIChE J.* **2005** 51 1733.
- [2.110] A. Dinse, B. Frank, C. Hess, D. Habel, R. Schomäcker, *Appl. Catal. A*, in preparation.
- [2.111] K. Chen, E. Iglesia, A.T. Bell, *J. Catal.* **2000** 192 197.
- [2.112] M.A. Vannice, *Catal. Today* **2007** 123 18.
- [2.113] X. Rozanska, R. Fortrie, J. Sauer, *J. Phys. Chem. C* **2006** 111 6041.
- [2.114] E.V. Kondratenko, X. Rozanska, O. Ovsitser, R. Fortrie, U. Dingerdissen, J. Sauer, *J. Catal.* **2007**, submitted.
- [2.115] A. Bielanski, J. Haber, *Oxygen in Catalysis*, Marcel Dekker, New York, **1991**.
- [2.116] M. Che, A.J. Tench, *Adv. Catal.* **1982** 31 77 and *Adv. Catal.* **1983** 32 1.

3 Experimental Methods [3.1-3.4]

3.1 Physicochemical Catalyst Characterization

The performance of a catalyst depends on various factors, of which the chemical composition is unquestionably most important. However, physical properties determining the accessibility of active sites as well as the transport of the reactants through porous catalyst pellets, may have a significant impact on effective reaction rates. In order to ensure the determination of true micro-kinetics, these influences have to be identified and eliminated. On the other hand a detailed characterization is the key to a clear assignment of catalytic performance to a defined type of active site (structure-activity relationship). The state of the art for several spectroscopic characterization techniques is the in situ analysis of the catalyst under reaction conditions. Properties of active sites can be determined directly by correlation of the specific data with reaction data like conversion or selectivity. However, since most characterization techniques require defined conditions, i.e., inert atmosphere, vacuum or low temperature, this attempt appears difficult in many cases.

The catalyst particle itself is characterized macroscopically by its diameter and pore structure. The particle size fraction or distribution can be determined by screening or light scattering methods. Information about the specific surface area, pore size distribution, and porosity of the catalysts can be gained from nitrogen physisorption. For industrial application, information about catalyst grain and bed density, void fraction or mechanical strength of the pellets are also important.

The chemical composition of a catalyst, respectively the soluble components, can be determined by inductively coupled plasma spectroscopy (ICP-OES). If the elemental composition is well-known, also specific methods can be applied, e.g., gravimetric or titration analysis. Identified and quantified elements may then be attributed to crystalline phases detected by X-ray diffractometry (XRD). However, these methods provide volume averaged data and thereby predominantly give information about the catalyst bulk composition, which may be quite different from the state at the catalyst surface. The most common technique for the investigation of the surface chemical composition is X-ray photoelectron spectroscopy (XPS). Titration methods using adsorbates or reducing/oxidizing agents, which can interact only with the catalyst surface and in the ideal case exclusively with the active component, give further information about redox or acid-base properties of the catalyst surface. These procedures may be applied in combination with defined temperature profiles, i.e., temperature programmed reduction, oxidation, or desorption (TPR, TPO, and TPD, respectively), or under isothermic conditions (e.g., N_2O or pyridine titration). Active component deposited on the surface can further differ in cluster size (dispersion) and oxidation state. Both can be extracted from UV-Vis diffuse reflectance spectroscopy (UV-Vis DRS), the first also by XRD, the latter additionally by XPS. Clusters and deposits in the nanometer range

can be visualized by electron microscopy in scanning or transmission mode (SEM, TEM). Among various other techniques which have been developed and applied for the analysis of the catalyst texture, this listing is focused on the most common methods. Those applied in the present study will be described in detail below.

3.1.1 Nitrogen Physisorption

The adsorption isotherm of nitrogen at the temperature of liquid nitrogen (77 K) provides information about the internal catalyst structure. The total surface area S_t can be calculated by measuring the amount of gas adsorbed in a monolayer a_m , using the cross-sectional area of one adsorbed nitrogen molecule of $s_0 = 0.162 \text{ nm}^2$ (Eq. 3.1).

$$S_t = a_m N_A s_0 \quad (3.1)$$

The empirical equation of Brunauer, Emmet and Teller (BET equation, Eq. 3.2) describes multi-layer adsorption in the range of relative pressures $p/p_0 = 0.05\text{--}0.30$.

$$\frac{p/p_0}{a(1 - p/p_0)} = \frac{1}{a_m c} + \frac{(c-1)}{a_m c} \frac{p}{p_0} \quad (3.2)$$

where c is a dimensionless constant, dependent on the heat of adsorption and evaporation of the adsorbent and defining the isotherm shape.

Pore size distribution and micro- and mesopore volume can be estimated from the adsorption branch of the physisorption isotherm using the equation of Barrett, Joyner, and Halenda (BJH equation, Eq. 3.3).

$$V_{\text{ads}}(p/p_0) = \sum_{i=1}^k \Delta V_{p,i} (r_i \geq r_k(p/p_0)) + \sum_{i=k+1}^n \Delta S_{p,i} t_{\text{ads},i} (r_i < r_k(p/p_0)) \quad (3.3)$$

This computational method is based on the Kelvin equation of capillary condensation (Eq. 3.4) and equals the volume of (liquid) adsorbent V_{ads} at a certain relative pressure to the sum of the pore volume of pores smaller than the Kelvin radius r_k and the adsorbed layer volume inside the pores larger than the Kelvin radius. The latter is given by the product of pore surface area S_p and the thickness of the adsorbed layer t_{ads} .

$$r_k = \frac{2 \sigma v}{R T \ln(p/p_0)} \quad (3.4)$$

where σ is the surface tension of the condensed liquid and v is its molar volume. The BJH method holds for pore radii in the range of 1.5–100 nm but is bound to several simplifying assumptions concerning pore size and geometry.

Nitrogen physisorption measurements were conducted using a Micromeritics 2375 BET device equipped with a Vacprep 061 degasser. Before measurement, the catalyst samples of about 150 mg each were degassed for 1 h at 120 °C (copper catalysts), respectively 300 °C (vanadia catalysts), and 0.15 mbar to ensure a clean and dry surface. Adsorption and desorption branch were divided into 50 iso-distant intervals, respectively, in the range of p/p_0 from zero to one.

3.1.2 X-ray Powder Diffractometry (XRD)

XRD is a routine technique for the analysis of bulk phases of solids and particles that provide long-range order (crystalline) structures. Focusing an X-ray beam of the wavelength λ under a certain range of angles 2Θ on the sample, a complex pattern is obtained by diffraction at crystallographic phases. The position of a diffraction line is given by the Bragg relation (Eq. 3.5):

$$n\lambda = 2d \sin \Theta \quad (3.5)$$

where n is the diffraction order and d the spacing between two planes. Phase identification is based on the comparison of the experimental pattern with that of pure reference phases, or with a database. Furthermore, the diffraction pattern can be evaluated quantitatively since the peak intensity is directly proportional to the volume fraction of the phase.

The width of the diffraction lines contains information on the crystallite size in the specimen. This is an important information especially for supported catalysts, which often tend to agglomerate and thereby decrease in their catalytic performance. The Scherrer equation (Eq. 3.6) allows a rough estimation of the mean crystallite size $\langle L \rangle$.

$$\langle L \rangle = \frac{K\lambda}{\beta_{1/2} \cos \Theta_{\max}} \quad (3.6)$$

where K is a constant dependent on the shape of the crystallites, $\beta_{1/2}$ is the full width at half maximum intensity and Θ_{\max} is the angular position of the peak maximum.

Powder X-ray diffraction measurements were performed using a Siemens D500 instrument with monochromatic Cu K_α radiation ($\lambda = 0.154$ nm), a scanning speed of $8.3 \times 10^{-4} \text{ }^\circ \text{ s}^{-1}$ and a voltage and current of 40 kV and 30 mA, respectively. For the phase identification the Bruker AXS database EVA was applied.

3.1.3 Temperature Programmed Reduction/Oxidation (TPR/TPO)

TPR and TPO are sensitive tools for the investigation of red-ox properties and thermal behaviour of catalytic materials. A red-ox active solid specimen is kept in a reducing/oxidizing atmos-

phere (usually 5% H₂ or O₂ in Ar) as the temperature is linearly increased. The dynamic analysis of the gas phase composition provides insight into the interactions between gas and solid phase, i.e., reductant/oxidant consumption or reaction product formation, at distinct temperatures. The temperature of maximum consumption permits information, e.g., on the agglomeration state of red-ox active species. An integration of the resulting concentration profiles allows quantitative conclusions on the oxidation state of the sample. Furthermore, these profiles can be evaluated kinetically by numerical integration using a power law kinetic approach (Eq. 3.7).

$$\frac{dc_{\text{RS}}}{dt} = \beta \frac{dc_{\text{RS}}}{dT} = -k_0 \exp\left(-\frac{E_A}{R T}\right) \langle c_{\text{RS}} \rangle^{m_1} \langle c_{\text{gas}} \rangle^{m_2} \quad (3.7)$$

where $\langle c_{\text{RS}} \rangle$ and $\langle c_{\text{gas}} \rangle$ are the mean concentrations of red-ox active species (RS) and reductant/oxidant gas, respectively, β is the heating rate, k_0 and E_A are the preexponential factor and the activation energy, and m is the reaction order. However, a feasible kinetic evaluation of the transient response depends strongly on heating rate and reductant concentration.

Temperature programmed reactions were performed in a quartz tubular reactor (6 mm i.d.) in a programmable furnace. For each experiment 200 mg of fresh catalyst sample, fixed on a quartz frit, were oxidized and partially dehydrated in a stream of 20% O₂ in He at 500 °C (50 ml_n min⁻¹) for at least 30 min. For TPO the sample was then reduced in 20% H₂ in Ar for 30 min. The reactor was then flushed with He (47.5 ml_n min⁻¹) and cooled down. At a temperature of 25–50 °C, a reducing/oxidizing agent was added to the feed (5% $\hat{=}$ 2.5 ml_n min⁻¹) and as soon as the outlet concentration reached constancy, TPR as well as TPO were started with a heating rate of 10 K min⁻¹ up to a temperature of 820 °C. The whole procedure was monitored by mass spectrometry (InProcess GAM 200).

3.1.4 UV-Vis Diffuse Reflectance Spectroscopy (UV-Vis DRS)¹

Electromagnetic radiation in the UV-Vis range (190–800 nm) can induce electronic transitions in supported catalysts and between catalysts and adsorbed species. The energy-uptake from metal-centered (MC) and charge transfer (CT) transitions is then released in terms of vibrational relaxation. Absorption at distinct bands thereby provides information on the direct environment of catalytically active species, i.e., coordination and dispersion, as well as on their oxidation state. In heterogeneous catalysis, UV-Vis DRS can also be applied in situ and can give insight into reaction mechanisms. Quantification from the resulting reflectance spectra can be achieved by its transformation using the Kubelka-Munk function (Eq. 3.8).

¹ UV/Vis DRS measurements were performed by Dr. Evgueny Kondratenko, LIKAT, Berlin-Adlershof.

$$F(R_{\infty}) = \frac{(1 - R_{\infty})^2}{2 R_{\infty}} \quad (3.8)$$

where R_{∞} is the reflectance at "infinite thickness" of the reflecting layer (catalyst bed), which is generally obtained at about 1–2 mm.

The UV-Vis analysis was performed using a AVASPEC fiber optical spectrometer (Avantes) equipped with a DH-2000 deuterium-halogen light source and a CCD array detector. A high-temperature reflection probe consisting of 6 radiating and 1 reading optical fibers was located inside the furnace perpendicular to the reactor. The sensor was connected to the spectrometer and the light source by fiber optical cables (length 2 m) consisting of a core of pure silica surrounded with polyimide.

3.1.5 Laser Raman Spectroscopy (LRS)²

In opposite to the typical infrared (IR) spectroscopy, which is based on the analysis of absorbed radiation in the transmission mode or from elastically scattered light (DRIFTS, see Ch. 3.2.1), LRS provides information from inelastically scattered photons. Both methods analyze vibrational properties of the sample and complement one another. Since Raman scattering probabilities are very low particularly for common catalyst support materials as silica or alumina, this technique enables detailed spectra of surface species in the low-wavenumber region of 50–1200 cm^{-1} which are impossible to extract from IR spectroscopy due to heavy overlapping by support material bands. All characteristic vibrational features of the oxides of, e.g., Mo, W, Cr, V, or Re, fall into the frequency range of $< 1100 \text{ cm}^{-1}$ so a detailed structural characterization of these compounds can be achieved. However, in general, LRS has a relatively poor sensitivity due to the low probability of inelastic scattering of about $1:10^7$, thus the detection limit is quite high and monomeric species are often invisible. A significant increase in sensitivity can be observed in case of Raman resonance effects. Absolute quantification of detected species from Raman peak intensities, especially for polydisperse materials, is regarded to be presumably impossible due to the complexity of factors affecting the Raman scattering cross-section. Relative quantification could be done by reference to support bands or addition of an inert standard such as BN.

For the Raman experiments the powder samples were introduced into a stainless steel sample holder with a 0.6 mm deep rectangular well covering an area of $(12 \times 8) \text{ mm}^2$. Raman spectra were measured using 514 nm excitation (3 mW) at 5 cm^{-1} spectral resolution (Kaiser Optical). Raman

² LRS measurements were performed by Dr. Christian Hess, FHI, Berlin-Dahlem.

spectra under dehydrated conditions were recorded at room temperature after treating the samples in flowing air at 300 °C for 30 min. Sampling times were typically 60 min.

3.1.6 X-ray Photoelectron Spectroscopy (XPS)³

XPS is a surface sensitive method with a penetration depth of about 10 nm for the determination of the chemical composition, oxidation states and chemical state (ESCA) of a catalyst (in atom-%). The sample is impinged by X-ray photons of the energy $h\nu$ which results in the ejection of photoelectrons from the core of surface atoms. The kinetic energy E_k of these ejected electrons provides information about its former binding energy E_b (Eq. 3.9).

$$E_h = h\nu - E_k - \Phi \quad (3.9)$$

where Φ is the work function of the spectrometer. The binding energy is characteristic for each element and a slight shifting can be caused by the influence of neighboured atoms on the net atomic charge. This enables the determination of the direct surrounding of the respective element and its oxidation state.

The measurements were carried out using a modified LHS/SPECS EA200 MCD system equipped with a Mg K α source (1253.6 eV, 168 W). The binding energy scale of the system was calibrated using Au 4f_{7/2} = 84.0 eV and Cu 2p_{3/2} = 932.67 eV from foil samples. The powder samples were placed as prepared in a stainless steel sample holder with a 0.6 mm deep rectangular well covering an area of (12×8) mm². The base pressure of the ultra-high vacuum (UHV) chamber was 1×10⁻¹⁰ mbar. Data acquisition time was 100 min. Charging of the powder samples was accounted for by setting the peak of the Al 2p signal to 74 eV. Further data reduction included satellite deconvolution and subtraction of a Shirley background. Quantitative data analysis was performed on the basis of peak areas by fitting with 30/70 Gauss-Lorentz product functions. Atomic ratios were calculated using empirical cross-sections.

3.1.7 Scanning and Transmission Electron Microscopy (SEM and TEM)⁴

Electron microscopy can be applied for the measurement and visualization of morphology, particle size and pore size of a catalyst particle. Due to the shorter wavelength of electrons compared to visible light a higher resolution up to 1 nm can be achieved (SEM). During SEM a narrow electron beam is rastered over the sample surface and the yield of secondary and/or backscattered electrons is detected in order to calculate a two-dimensional image of the sample.

³ XPS measurements were performed and evaluated by Dr. Christian Hess, FHI, Berlin-Dahlem.

⁴ TEM images were taken by Wiebke Frandsen, FHI, Berlin-Dahlem.

To prevent electrostatic charging of non-conductive samples, these have to be sputtered with a thin layer of conductive material, e.g. gold or graphite.

TEM images originate from transmitting electrons, which are detected beyond the specimen. The resolution is in the range of 0.1 nm and compared to SEM, contrast is mainly produced by diffraction at crystal planes. The TEM technique can thereby provide information about the composition, size and orientation of crystallites. However, the sample has to be extremely thin (0.1–1 μm) to be electron transparent which requires difficult and thorough sample preparation.

Both techniques can be coupled with Energy Dispersive X-ray Spectroscopy (EDX) an elemental analysis of the visualized sample area. Compared to XPS (see Ch. 3.1.6) this technique has a higher penetration depth of about 1 μm thus the obtained "mapping" of elemental distribution can not in general be referred to the surface composition, particularly in case of porous samples.

Sample preparation for TEM analysis was the following: The finely powdered catalyst sample was dispersed in chloroform by means of ultrasonic treatment for 2 min. One drop of the dispersion was then given on a copper grid covered with a holey carbon film and dried for 10 min. TEM images were taken using a Philips CM200 FEG field emission transmission electron microscope operating with an acceleration voltage of 200 kV in vacuum (2.7×10^{-5} Pa) and with a point resolution of 0.19 nm.

3.2 Microkinetic Modeling

The modeling of a catalytic reaction on the molecular level is the state of the art in describing its kinetics. A microkinetic model includes elementary steps of the overall reaction as well as information about their individual rates. A high number of unknown kinetic constants can arise in a detailed model and several simplifying assumptions have to be made in order to derive a manageable rate equation. It thereby appears difficult and is generally not accepted to create a new model solely on kinetic measurements. For its validation, information about the reaction has to be gained from independent experiments. Insight into complex reaction networks can be achieved, e.g., by the independent investigation of single reactions. Intermediates of reaction pathways and their further transformation can also be investigated apart from the overall reaction, if these intermediates are creatable by other reactions. If there is a certain amount of information collected by steady-state experiments, the next step is a dynamic disturbance of the system, which can be sophisticated in its evaluation. However, the information density is enormous compared to conventional steady-state experiments. Besides these kinetic approaches, diverse in situ methods have come in the focus of microkinetic modeling in the past decades.

Diffuse reflectance IR spectroscopy (DRIFTS) is a powerful tool for the investigation of surface intermediates during the reaction. Reaction pathways of complex reactions can be extracted by temporal analysis of products (TAP) experiments. Helpful for the analysis of reaction pathways is the use of isotopic tracer substances. The preparation of a, e.g., ^{18}O labelled oxidic catalyst provides insight into the exchange of oxygen atoms during the reaction. A further method is the steady state isotope transient kinetics analysis (SSITKA), where isotopically labelled feed components are pulsed into the continuously working system. Relatively new in the field of heterogeneous catalysis research is the application of computational methods. Theoretical ab initio and density functional theory (DFT) calculations both provide a powerful tool for the prediction or confirmation of reaction pathways on the molecular level including transition states and their energetic position. The following chapters will describe the methods used in this study in detail.

3.2.1 Diffuse Reflectance Infrared Spectroscopy (DRIFTS)

The interaction of electromagnetic radiation in the infrared range (NIR: $5000\text{--}1000\text{ cm}^{-1}$) with chemical bonds can be used for the in situ vibrational analysis of surface functional groups on catalyst surfaces. Adsorption at distinct bands of the scattered radiation depends on the kind of surface species and the adsorption site. By the detection of intermediates and surface adsorbates DRIFTS can thereby provide direct information about reaction pathways and the coverage of the catalyst. However, this data has to be interpreted thoroughly because observed species can also act as spectators or poisons instead of intermediates. The signal-to-noise ratio depends strongly on the reflectance of the catalyst sample. DRIFTS can be evaluated quantitatively by transformation of the reflectance spectrum into the Kubelka-Munk function (Eq. 3.8).

In situ DRIFTS was conducted using the Graseby Specac Diffuse Reflectance Optics “The Selector” and an “Environmental Cell” (zinc selenide window). This unit operates with a Bruker ifs 66 FTIR-spectrometer equipped with a mercury cadmium telluride (MCT) detector. This technique was applied solely for the investigation of methanol steam reforming. Both reactants were dosed via saturators (water: $30\text{ }^{\circ}\text{C}$, methanol: $4\text{ }^{\circ}\text{C}$) in a helium stream. Their concentrations in the combined stream were controlled by the adjustment of three mass flow controllers, the calculations were based on the Antoine equation (Eq. 3.10)

$$\ln p_{\text{sat}} = A - \frac{B}{T + C} \quad (3.10)$$

which is an empirical relation of the saturation pressure p_{sat} to temperature and component specific constants A , B , and C . The reactants overall concentration was 4 vol% in a total flow of $10\text{--}15\text{ ml min}^{-1}$. The sample holder was filled with $15\text{--}50\text{ mg}$ of the $< 25\text{ }\mu\text{m}$ catalyst powder,

depending on its density. Each catalyst was reduced for 2 h in a 4% methanol flow at 250 °C, then cooled to 220 °C and kept in the methanol flow overnight in order to remove the high amount of adsorbed water on the catalyst surface via SRM reaction and reach steady state conditions. DRIFTS measurements were conducted beginning at 4:1 methanol excess and decreasing methanol to water ratio. Reaction products were analyzed on-line by MS (Pfeiffer Omnistar). DRIFT spectra were collected after steady-state conditions were achieved. Typically, 1000 scans were averaged at a resolution of 4 cm⁻¹ due to a low signal-to-noise ratio of the reduced copper catalysts. The single channel sample spectra were divided by a KBr background spectrum, which was taken prior to in situ measurements. The resulting spectra were transformed into the Kubelka-Munk function.

3.2.2 Rate Data Acquisition and Kinetic Modeling

Kinetic experiments concerning heterogeneous catalytic reactions are generally carried out in tubular type reactors. One data point consists of a measured product gas composition which is attributed to a distinct reaction temperature, feed composition and contact time. In case of differential conversion the reaction rate r is then given by Eq. 3.11:

$$r_i = \frac{\Delta c_i \dot{V}_{\text{tot}}}{m_{\text{cat}}} \quad (3.11)$$

To measure the true chemical reaction rate, several precautions have to be taken. The influence of intraparticle mass and heat transfer limitations has been discussed in detail in Ch. 2.2. Further disturbing factors can arise from non-ideal flow conditions. A sufficiently small tube diameter ensures a minimization of extraparticle mass transfer limitation due to a high flow velocity as well as the reduction of radial concentration and temperature profiles, which can falsify the measured data. Against that the tube-to-particle diameter ratio should be at least 10 to avoid channelling along the wall. Furthermore, the effect of catalyst aging and deactivation due to poisoning or coking should be appreciated. Tubular reactors can be operated both in a differential and integral way. However, their application for microkinetic analysis is limited in case of highly exothermic reactions. Up to a certain extent, one can reduce axial temperature profiles by catalyst or reactant dilution. However, the determination of the functional form of a rate equation is convenient only on the basis of isothermal data.

A series of so-called *differential reactors* has been developed in order to solve these problems [3.5]. Internal temperature and concentration gradients get minimized by a complete mixing of the gas phase inside the vessel and catalyst bed. The reaction rate for these types of reactors is also given by Eq. 3.11. Most common models are the Carberry reactor with a spinning catalyst basket per-

turbating the gas phase and the Berty reactor with a stationary catalyst basket and a vane type blower. Due to the low density of gaseous media their rotation speed even at high reaction temperatures is quite high (up to 5000 min^{-1}), which requires special precautions and thorough manufacture of the whole reactor device. An insufficient mixing enlarges the risk of by-pass flows and dead zones in the vessel.

For a meaningful model discrimination especially between similar mechanistic rate laws a huge amount of kinetic data is required. This data should differ strongly in its experimental parameters, i.e., especially the feed composition. The addition of product components to the feed is helpful to investigate their impact on the reaction rate. Usually the model discrimination occurs by comparison of the measured data with a set of mechanistic rate equations. Based on general shapes and dependencies most of theoretically possible equations can be rejected. The remaining rival models mostly differ solely in details and the decision is made by the goodness of fit. Positive kinetic and adsorption constants are a necessary fitting criterion as well as a positive activation energy and a negative adsorption enthalpy. Statistical tests can further confirm a decision towards one model. Once a model has been chosen, its applicability for integral modeling of the reactor can be tested.

3.2.2.1 Experimental Set-up for SRM Kinetic Measurements

Steam reforming of methanol was studied in a fixed bed tubular reactor (stainless steel, i.d. = 10 mm). Liquid reactants were introduced by a HPLC pump (Dionex HPLC 580), gases were dosed by a mass flow controller (MFC) into the reactor. The MFC was calibrated with nitrogen, conversion factors of 1.010 and 0.784 were used for hydrogen and carbon dioxide, respectively, calculated from the ratios of their heat capacities. Before feeding into the reactor, the methanol/water mixture and the gases were preheated separately up to the intended reaction temperature. The reactor and the evaporator/preheater were surrounded by an aluminium heating block in order to achieve an efficient heat transfer. Two thermocouples were used for temperature measurement, one was located in the heating block and the other one in the catalyst bed. The catalyst was supported inside the reactor by a stainless steel grid and placed between two layers of inert Pyrex beads of the catalyst's size for better flow conditioning and heat transfer. The product mixture leaving the reactor passed two condensers at 0 and $-20\text{ }^{\circ}\text{C}$, respectively, in order to remove water and methanol. The dry product gas mixture then passed a mass flow meter calibrated with a 3:1 hydrogen/carbon dioxide mixture for conversion measurement. The condensed liquid was analyzed gas chromatographically in order to detect by-products like methyl formate or dimethyl ether. Therefore an Intersmat gas chromatograph (GC) separating with a

50 m \times 0.53 mm CP-Wax column at 90 °C using He as carrier gas and equipped with a thermal conductivity detector (TCD) was applied. The composition of the dry product gas was monitored with a Varian 3800 GC also equipped with a TCD. Helium was applied as a carrier gas, and separation was achieved with a 25 m \times 0.53 mm CarboPLOT P7 column at 31 °C.

The liquids used in this study were methanol (Roth, HPLC grade, >99.9% purity) and deionized water. Both were degassed at 20 kPa before use. For the fine adjustment of the molar ratio of the liquid reactant mixture the Intersmat GC described above was used. By using an exact calibration curve, surplus reactant mixture could be recycled and the production of waste liquid drastically reduced. The gases used had the following minimum purities: N₂ 99.99%; H₂ 99.999%; CO₂ 99.995%. They were obtained by Air Liquide.

After determination of mass transfer limitations and the aging period of about one week (reaction conditions are described in the respective Chs. 4.2.1 and 4.2.2), kinetic measurements were conducted. The molar ratio of the reactants was varied with and without addition of nitrogen, hydrogen, and carbon dioxide as follows:

- CH₃OH/H₂O molar ratio from 1:9 to 9.5:1
- N₂ and H₂ addition from 20 to 80%
- CO₂ addition from 20 to 60%

To keep the conversion of the minor component below 10%, the liquid flow rate was adjusted between 0.05 and 0.5 ml min⁻¹, and gases were added at a flow rate of 50–250 ml_n min⁻¹. The molar ratios were changed not systematically (e.g., increasing water content), but rather randomly, to avoid tendencies originating from the experimental process or misinterpretation of catalyst aging effects. However, the gases were added to the given CH₃OH/H₂O composition in increasing concentrations (20/40/60/80%) in the order N₂, H₂, CO₂.

3.2.2.2 Experimental Set-up for ODP Kinetic Measurements

For the detailed investigation of the oxidative dehydrogenation of propane two completely independent reactor set-ups were used.

The first is a 6-channel screening-apparatus with U-shaped fixed-bed quartz reactors (6 mm i.d.) connected in parallel. The reactants were dosed by 3 MFCs (C₃H₈/C₃H₆, O₂/syn. air, N₂/He) through a static mixer and pre-heated up to 150 °C prior to entering the reactors. The reactors, containing the diluted catalyst (1:1 with quartz particles) between two layers of quartz particles, were immersed into a fluidized bed of sand serving as a source of heat to provide near isothermal

operating conditions. The reaction temperature was measured in a separate quartz tube placed in a position of the sand bed, which is comparable to that of the catalyst. For the measurement of the temperature profile inside the catalyst bed during the reaction, a special reactor was designed, containing an axially movable thermocouple located in a quartz capillary in the center. The product mixture leaving the reactor was analyzed by an on-line gas chromatograph (GC, Satochrom 5873), equipped with Poraplot Q and Molsieve 5 columns. Light gases (O_2 , N_2 , CO , CH_4 , CO_2) were detected with a thermal conductivity detector, C_2 and C_3 hydrocarbons and oxygenates were quantified using a flame ionization detector. The duration of one GC analysis was about 20 min, which is longer than the time to achieve steady state conditions, as confirmed by repeated measurements in one channel. Using nitrogen as an internal standard, the reproducibility of conversion and selectivity measurement and calculation is sufficient (deviation < 5% for the ODP reaction).

Detailed microkinetic measurements were conducted in a Berty "Micro" reactor purchased from Autoclave Engineers[®]. The basket volume and the free vessel volume are 3.6 and 15.4 cm³, the reaction temperature is measured directly inside the catalyst basket. The device used in this study is made of inert HASTELLOY[®] C-276 and designed for temperatures up to 536 °C at a pressure of 345 bar. The reactor is connected with a "Control Tower" for adjustment of heating and mixing speed. Ideal mixing conditions inside the vessel were proven by measurement of the residence-time distribution. Reactants were dosed by 5 MFCs (C_3H_8/C_3H_6 , N_2/He , CO/CO_2 , O_2 , and H_2). For catalytic measurements the catalyst basket was filled with catalyst diluted with inert pyrex beads of the same size between two layers of pyrex beads. The reactants and products leaving the reactor were detected on-line by quadrupole mass spectrometry (QMS) using a GAM 200 (InProcess Instruments) device. Mass numbers in the range of 2–44 were detected with a time resolution of 1.0 s.

The overall ODP set-up was designed in order to use respectively two gas mixing units, three catalytic reactors (including TPR experimental set-up) and two analytical devices independently and in each combination with each other.

3.2.3 Temporal Analysis of Products (TAP)

Transient experiments are a promising method for the investigation of single reaction pathways of a complex reaction network. However, the time-resolution in conventional reactors at ambient conditions is in the range of one second. In contrast, the TAP reactor set-up allows fast transient experiments in the submillisecond time regime by working under vacuum conditions. This allows effective mass transport by Knudsen diffusion (Eqs. 3.12 and 3.13) and undergoes the problem

of relatively slow macroscopic mixing and perturbation. As a negative effect, the system suffers a loss of significance compared to "real" systems due to the pressure-gap.

$$\varepsilon_b \frac{d\bar{c}_i}{dt} = D_{K,i}^{\text{eff}} \frac{d^2 \bar{c}_i}{dx^2} \quad (3.12)$$

$$D_{K,i}^{\text{eff}} = \frac{d_c}{3} \frac{\varepsilon_b}{\tau} \sqrt{\frac{8 R T}{\pi M_i}} \quad (3.13)$$

where ε_b is the void bed fraction, $D_{K,i}^{\text{eff}}$ is the effective Knudsen diffusivity, d_c is the average interparticle distance, and τ is the tortuosity.

During one TAP experiment, a sharp and small pulse of reactants is given on the continuously evacuated catalyst sample. The product composition is monitored on-line by MS, which is positioned directly between the catalyst bed and vacuum pump. The high time-resolution allows the monitoring of only one atomic mass unit (AMU) per pulse. The signal shape of inert and non-reacting gases provides information about the Knudsen diffusivity and about surface interactions. Shape and delay of product signals contain information about the reaction pathway and rates of elementary reactions. The application of isotopic tracer components or sequential pulsing of different reactants can also be useful for this purpose. For microkinetic evaluation the whole set of signals has to be modeled by numerical integration using different mechanistic approaches, where the rate constant of each elementary reaction as well as the total number of active sites has to be fitted (Eqs 3.14 and 3.15).

$$\varepsilon_b \frac{d\bar{c}_i}{dt} = D_{K,i}^{\text{eff}} \frac{d^2 \bar{c}_i}{dx^2} + \varrho_b \sum_j r_{ij} \quad (3.14)$$

$$\frac{d\Theta_i}{dt} = \frac{1}{N_z} \sum_j r_{ij} \quad (3.15)$$

where ϱ_b is the catalyst bed density and N_z the total number of active sites per catalyst weight.

Temporal analysis of products experiments were performed for the oxidative dehydrogenation of propane with the TAP-2 reactor set-up, which is described in detail elsewhere [3.6]. A mass of 45.3 mg of the $\text{VO}_x/\text{Al}_2\text{O}_3$ catalyst VA-200 was pretreated in a flow of oxygen ($30 \text{ ml}_n \text{ min}^{-1}$) at 500°C for about 0.5 h. The interaction of O_2 , C_3H_8 , C_3H_6 , and CO with the oxidized surface were investigated independently by single-pulse experiments. Low intensity pulsing (pulse size $\approx 10^{15}$ molecules) of 1:1 mixtures of Xe and respectively C_3H_8 , C_3H_6 , and CO were performed in order to get insight into the reaction schemes and to test the catalyst ability for CO oxidation in the temperature range of $450\text{--}550^\circ\text{C}$. The role of adsorbed oxygen species and lattice oxygen on the product distribution was investigated for propane and propene oxidation. Therefore sequential pulsing of $^{18}\text{O}_2/\text{Ne}$ and $\text{C}_3\text{H}_6/\text{Xe}$ mixtures (1:1 respectively) with a time-delay of 0.5 s at

500 °C was performed. The sorption behaviour of CO and CO₂ on the catalyst surface was investigated by CO/Xe and CO₂/Xe pulsing in a somewhat lower temperature range (300–500 °C). For each AMU the signal of at least 20 pulses (10 for sequential pulsing) was averaged to reach a sufficient signal-to-noise ratio. Prior to each pulsing series, the catalyst was freshly oxidized with 20 pulses of a 1:1 ¹⁶O₂/Ne mixture.

References of Chapter 3

- [3.1] G. Ertl, H. Knözinger, J. Weitkamp (Eds.), *Handbook of Heterogeneous Catalysis*, Vol. 2, Wiley-VCH, Weinheim, **1997**.
- [3.2] J.F. Haw (Ed.), *In-Situ Spectroscopy in Heterogeneous Catalysis*, Wiley-VCH, Weinheim, **2002**.
- [3.3] J.R. Anderson, M. Boudart (Eds.), *Catalysis - Science and Technology*, Vol. 2, Springer, Berlin, **1981**.
- [3.4] B. Cornils, W.A. Herrmann, R. Schlögl, C.-H. Wong (Eds.), *Catalysis from A to Z*, Wiley-VCH, Weinheim, **2003**.
- [3.5] B. Hesselbarth, R. Adler, *Chem. Ing. Tech.* **2004** 76 914.
- [3.6] J.T. Gleaves, G.S. Yablonskii, P. Phanawadee, Y. Schuurman, *Appl. Catal. A* **1997** 160 55.

4 Steam Reforming of Methanol (SRM)

4.1 Catalyst Preparation and Physicochemical Characterization

For the microkinetic study, commercially available copper catalysts were used whenever possible to enable easier reproducibility of the experiments. One CuO/ZnO/Al₂O₃ low-temperature shift catalyst and one Cr₂O₃/Fe₂O₃ high-temperature shift catalyst containing a small amount of copper oxide were obtained by Süd-Chemie, denoted as C 18 HA and G-3 C, respectively. The (6×3) mm² pellets were ground and sieved to a defined particle diameter to eliminate mass transport limitation of the reaction rate.

Further CuO/Cr₂O₃/Fe₂O₃ catalyst samples were synthesized from metal sols, prepared from the appropriate amounts of the mixed precursors Cu(NO₃)₂ · 3 H₂O (a Ferak product of > 99.5% purity), Cr(NO₃)₃ · 9 H₂O (Fluka, > 97% purity), and Fe(NO₃)₃ · 9 H₂O (Merck, > 99% purity). The metal nitrates corresponding to 5 g oxidic catalyst were dissolved in 300 ml distilled water and co-precipitated as hydroxides by the addition of NaOH solution saturated with NaHCO₃ until the remaining solution became colorless. The co-precipitate was aged in the mother liquor overnight, then repeatedly washed with distilled water. The resulting catalyst precursor was dried (10 h at 80 °C) and calcined (3 h at 500 °C) in air, respectively.

CuO/ZrO₂/CeO₂ catalysts were investigated in a previous kinetic study. Detailed discussions of the preparation and characterization of these materials are available in the literature [4.1,4.2]. The CZC15 sample containing about 15 mol% CuO provided the best selectivity for SRM against CO formation, and thus it was chosen for this study.

A catalyst consisting of copper on a silica support was prepared as fourth sample by cation exchange of tetraammine Cu²⁺ complexes [4.3]. A mass of 2.5 g Cu(NO₃)₂ · 3 H₂O dissolved in 10 ml distilled water and 10 ml 25% ammonium hydroxide was slowly added to a stirred mixture of 5.0 g silica gel (Merck Kieselgel 100) and 30 ml distilled water, which corresponds to a CuO content of 14.1 wt%. The solution became nearly colorless due the complexation of copper on the silica surface. The deep-blue silica gel was washed several times with distilled water, then dried (15 h at 80 °C) and finally calcined (3 h at 500 °C) in air, respectively. The final copper content of this sample was determined gravimetrically after dissolution of the CuO with concentrated hydrochloric acid and repeated calcination of the colorless silica gel.

Hereinafter, the four samples Cu/ZnO/Al₂O₃, Cu/Cr₂O₃/Fe₂O₃, Cu/ZrO₂/CeO₂, and Cu/SiO₂ are designated as CZA, CCF, CZC, and CS, respectively. Chemical composition data and physical properties of the catalyst samples investigated in this study are listed in Tab. 4.1.

Table 4.1 Physicochemical properties of the catalysts

Sample	CZA ^a (C 18 HA)	CCF ^a (G-3 C)	CZC ^b (CZC15)	CS
composition / wt%	CuO	50–60	1.5–2.5	6.9
	ZnO	25–35	-	-
	Al ₂ O ₃	8–15	-	-
	Fe ₂ O ₃	-	bal.	-
	Cr ₂ O ₃	-	7–10	-
	C ^c	2-3	3.5–4.5	-
	ZrO ₂	-	-	39.2
	CeO ₂	-	-	53.9
	SiO ₂	-	-	88.4
BET surface area / m ² g ⁻¹	68.6	74.2	102	270
average pore diameter / nm	16.7	12.8	9.9	15.0
Particle size chosen for the microkinetic study / μm	200–300	200–300	100–300	63–200
Cu crystallite size / nm	6.3	-	-	20.3

a) Composition given by suppliers data sheet.

b) Mastalir et al. [4.1] reported the molar composition of CZC catalysts.

c) Synthetic graphite.

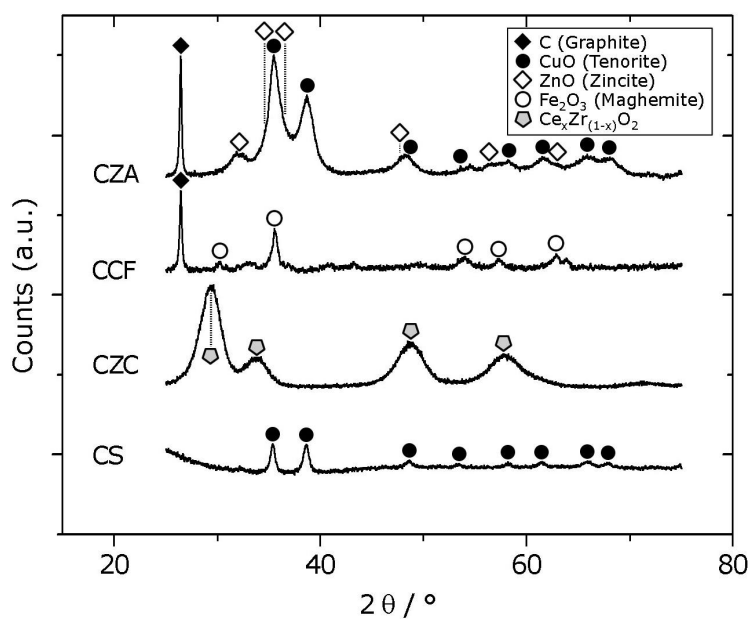


Figure 4.1 X-ray diffractograms of the investigated copper catalysts.

Furthermore, X-ray diffractograms were taken from each catalyst sample (Fig. 4.1). The presence of CuO crystallites (tenorite) can be confirmed for CZA and CS, whereas for CCF and CZC (diffractogram from [4.1]) either the amount appears to be too low or the crystallites are too small for detection by XRD, i.e., < 3 nm [4.4]. CZA and CCF show the characteristic peak of graphite, a common additive of several commercial catalysts. ZnO (zincite) can also be identified in CZA. The feature at $35\text{--}36^\circ$ in the pattern of CCF rather belongs to a Fe_2O_3 phase (maghemite) than to CuO due to the absence of other characteristic features. The presence of $\text{Fe}_x\text{Cr}_y\text{O}_z$ mixed phases in CCF, i.e., FeCr_2O_4 (chromite), cannot be excluded. The broad peaks of CZC belong to single mixed or separate phases of ceria and zirconia, which are difficult to determine.

4.2 Catalytic Catalyst Characterization

4.2.1 Mass Transport Limitations

Several authors reported diffusion limitations in SRM over $\text{Cu}/\text{ZnO}/\text{Al}_2\text{O}_3$ catalysts. In a previous study on a different commercial catalyst (MeOH1, Süd-Chemie), diluted with inert boron nitride, a reduced reaction rate was observed at a particle size of $0.71\text{--}1.00$ mm [4.5] and temperature of 250°C . Lee et al. [4.6] predicted mass transport limitations at 240°C for their catalyst (Synetix 33-5) from theoretical calculations; however, besides the larger particle diameter in both of the studies, their catalysts were about three to five times more active than the $\text{Cu}/\text{ZnO}/\text{Al}_2\text{O}_3$ catalyst investigated in the present study. In contrast, Jiang et al. [4.7] found no dependence of particle diameter of $150\text{--}190$ μm on the reaction rate in their studies using commercial catalysts (S3-85, BASF), even though they used a more active catalyst and worked at temperatures of $160\text{--}260^\circ\text{C}$. This result was also reported by Peppley et al. [4.8], investigating SRM over a $\text{Cu}/\text{ZnO}/\text{Al}_2\text{O}_3$ catalyst (K3-110, BASF) with a particle size of $710\text{--}850$ μm in the same temperature range.

The Weisz–Prater criterion (Eq. 2.21) using the Weisz modulus Ψ'' as dimensionless quantity is applied to estimate intraparticle diffusion limitations [4.9]. With a typical tortuosity value of $\tau = 3.5$ [4.10] and a measured porosity of $\varepsilon = 0.7$, the effective Knudsen diffusivity of methanol constitutes $D_{\text{K,M}}^{\text{eff}} = 6.4 \times 10^{-7} \text{ m}^2 \text{ s}^{-1}$. Since a reaction order of 0.5 for methanol results in Weisz moduli of $\Psi'' \ll 1$ for the chosen particle size fraction, the Weisz–Prater criterion predicts no mass transport limitation for the chosen reaction conditions and an effectiveness factor of $\eta \approx 1$. The results were confirmed with experimental determination of the influence of pore diffusion for the most active catalyst, CZA. Here, 0.5 g of sieved particle size fractions from $100\text{--}200$, $200\text{--}300$, and $300\text{--}450$ μm of the catalyst were placed into the reactor and fed with a 0.3 ml min^{-1}

equimolar methanol/water mixture at 220 °C. The initial conversion after a 30-min reduction period were calculated from the measured product gas flow rate. No change in reaction rate was observed when varying the particle diameter of CZA in this range, indicating no mass transport limitation at 220 °C. A previous study showed only insignificant mass transport limitation in CZC [4.1]. Using a small particle size fraction of 100–300 μm , an affect on the reaction rate can be excluded. The most active catalysts proved to be gradientless under the chosen reaction conditions. Similar tests with CCF and CS thus were omitted because of lower activity, similar pore diameter, smaller particle size (for CS), and very low copper content (for CCF).

4.2.2 Catalyst Aging

It is well known that copper catalysts used in methanol synthesis and in SRM deactivate rapidly during the initial period of operation. Irreversible alloy formation of the active copper species with support material and thermal sintering of small Cu particles, and thereby the reduction of the active surface area, are two possible reasons for this effect [4.11,4.12]. Zhang and Shi [4.13] reported a positive effect of ceria on the preservation of high copper dispersion and consequently enhanced long-term stability. The same effect was found by Szizybalski et al. [4.14] using zirconia as a support material.

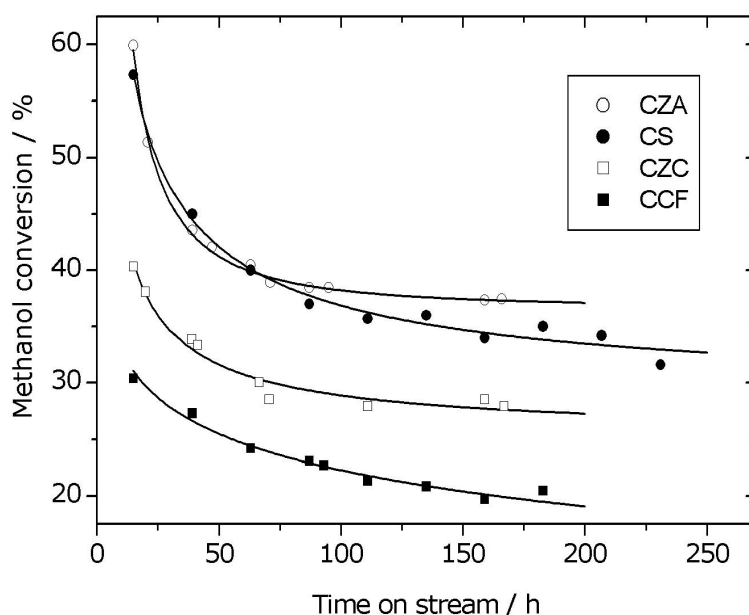


Figure 4.2 Initial catalyst deactivation of copper catalysts during SRM as a function of time on stream ($m_{\text{CZA}} = 0.5 \text{ g}$, $m_{\text{CCF}} = 2.5 \text{ g}$, $m_{\text{CZC}} = 1.0 \text{ g}$, $m_{\text{CS}} = 2.0 \text{ g}$, $T = 220 \text{ }^{\circ}\text{C}$, $p = 1 \text{ bar}$, $w = 0.05 \text{ ml min}^{-1}$, $\text{MeOH}/\text{H}_2\text{O} = 1$).

Another factor is the deposition of coke on the catalyst surface. Liu et al. [4.15] removed up to 1.7 wt% coke from their Cu/CeO₂ catalyst by repeated calcination in air and again reached the initial activity. Coke formation was observed by XPS and even fitted with a kinetic model for a Cu/ZnO/Al₂O₃ catalyst by Agarwal et al. [4.16]. As a fourth reason, a change in the oxidation state of copper from Cu^{+II} to Cu⁰ was found to be responsible for catalyst deactivation by Choi and Stenger [4.17], who observed copper reduction with XPS during the first 100 h of operation of their Cu/ZnO/Al₂O₃ catalyst.

Because kinetic measurements took about one week for each catalyst, a change in catalyst activity during this time period had to be excluded. Therefore, the catalysts were aged for several days under identical reaction conditions until they reached constant conversion in SRM. The deactivation of the samples after the reduction period of 15 h in a 50 ml_n min⁻¹ flow of 20% H₂ in N₂ at 220 °C is presented in Fig. 4.2. This figure clearly shows that each catalyst lost about 30–40% of its initial activity after 100 h time on stream. Whereas CZA, CCF, and CZC reached a constant activity, CS seemed to further deactivate and to not be a stable catalyst under SRM conditions. Concerning CZC, it is interesting that deactivation stopped earlier and the catalyst maintained a comparatively higher activity at 220 °C than at 250 °C [4.1]; at the latter temperature, this catalyst lost more than half of its initial activity and became stable after 200 h on stream. This result is in agreement with the observation of thermal sintering of the copper particles during SRM conditions, especially at higher temperatures.

4.2.3 Identification of the SRM Active Phase in CCF

For CZA, CZC, and CS there is general agreement that the support materials are inactive for SRM and the presence of copper is responsible for the catalytic activity. In contrast the oxides of iron and chromium, which form the support of CCF, are known to be active for water-gas shift catalysis and a certain activity in SRM may be considered possible. The proof that copper or a copper containing phase forms the only active species in this catalyst species appears necessary in order to keep the comparability between the chosen catalyst samples. To determine the activity as a function of copper content, catalyst samples with different compositions were synthesized. The ratio of Cr₂O₃ and Fe₂O₃ was kept constant at the value given by CCF, whereas the copper content was varied from 0–6 wt%. The activity in SRM was determined at 300 °C and an equimolar methanol/water feed of 0.5 ml min⁻¹. The conversions thus observed were related to the BET surface areas of the samples. This modified activity correlated linearly with the copper content of the sample, as shown in Fig. 4.3.

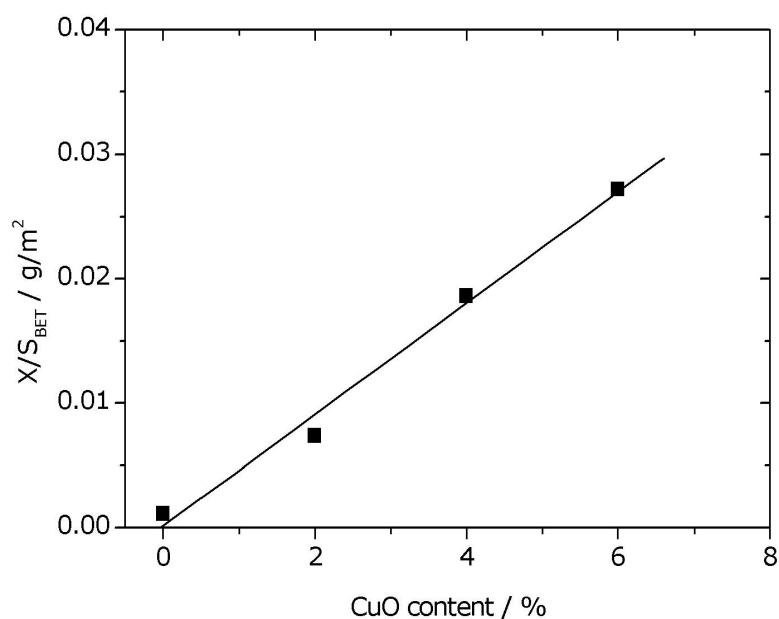


Figure 4.3 Dependence of the surface area related SRM activity of CuO/Cr₂O₃/Fe₂O₃ catalyst samples from their copper oxide content.

This result is a clear indication that copper or a copper-containing phase formed in these samples is responsible for the catalytic activity. Because the copper-free sample provided nearly no activity, the contribution of the Fe₂O₃/Cr₂O₃ catalyst support to the measured conversion can be neglected. The linear increase in this low-concentration range indicates the formation of uniform and uniformly sized copper particles.

4.3 DRIFTS Study

A series of DRIFT spectra were collected to obtain information about the surface reactions and intermediates during SRM. Based on previous studies [4.18–4.21] and the proposed mechanism over Cu/ZnO/Al₂O₃ catalysts, the appearance of hydroxyl, methoxy, and formate groups was expected, as was carbon dioxide as gas-phase or weakly bonded surface species. One aim of this study was to determine whether the reaction occurs mainly via dioxomethylene or via methyl formate by detecting one of these species on the catalyst surface. The reactant composition was varied from methanol excess to water excess in an effort to observe a dependence of the band areas on the reactant partial pressure and thereby support the mechanistic model as a basis for the kinetic model. The process of DRIFT spectra conversion and manipulation is reported elsewhere [4.36].

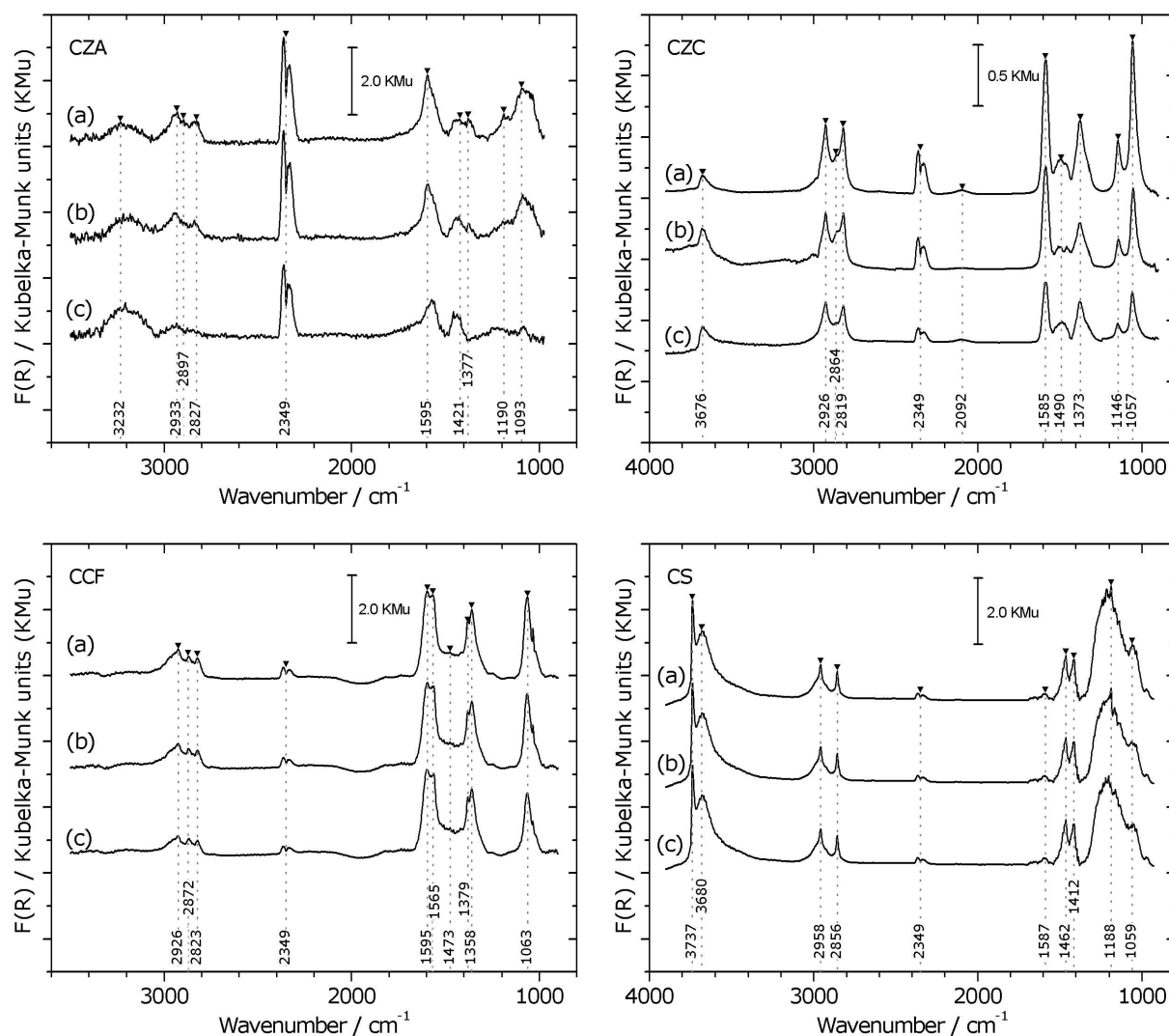


Figure 4.4 DRIFT spectra of the investigated catalysts CZA, CCF, CZC, and CS, collected at 220 °C, reactant overall concentration 4% in He. (a) MeOH/H₂O = 4:1, (b) MeOH/H₂O = 1:1, (c) MeOH/H₂O = 1:4.

The DRIFT spectrum of CZA is of relatively low quality, which may be ascribed to the high copper content of this catalyst. Peppley et al. [4.18] also reported a spectrum of a high Cu content Cu/ZnO/Al₂O₃ catalyst, with comparatively high signal-to-noise ratio. The reflectance, which was > 10% in a wide spectral range for the oxidized catalyst, sustained a drastic drop during the reduction period (see also [4.36], Figs. 3(a) and (b)), and the resulting spectra allow only cautious statements about the absence of surface intermediates. A dilution of the catalyst with inert α -alumina powder had no effect on the signal-to-noise ratio. Vargas et al. [4.21] also observed decreased intensity over a reduced Cu/ZnO/Al₂O₃ catalyst compared with the oxidized sample.

As can be seen from Fig. 4.4 and Tab. 4.2, the same intermediates were found on each investigated copper-based catalyst. Surface hydroxyls were present on the surface of all catalysts but CCF, with broad features at 3000–3800 cm⁻¹. Also identified on every surface was the characteristic

pattern of two methoxy bands bordering one formate band at 2800–3000 cm^{-1} from C–H stretching modes. The bands at around 2349 cm^{-1} can be attributed to the two branches of the rotation vibration spectrum of gaseous carbon dioxide. Surface copper carbonyls were observed only on CZC and CS, with a feature at 2092 cm^{-1} . Surprisingly, no CO was detected on the surface of CCF, although this catalyst demonstrated the worst selectivity in the on-line analysis based on the DRIFTS measurements as well as in the kinetic measurements. The region at 1000–1600 cm^{-1} contained bands of carbonates, as well as features from methoxy and formate C–O stretching and C–H bending modes. These bands are summarized and assigned to surface species and their vibrational modes (along with the references for these assignments) in Tab. 4.2. Over CCF, the asymmetric O–C–O stretching band and the C–H bending band of formate species appeared to be divided into two neighbouring bands at 1358/1379 and 1565/1595 cm^{-1} . This can indicate either monodentate and bidentate formate adsorption [4.22] or the parallel adsorption of formate on two different kinds of surfaces [4.21] that may be present in the CCF catalyst. On the other hand, a shoulder at about 1360 cm^{-1} was also seen on CZC. This feature, as well as the band at 1358 cm^{-1} on CCF, also may be attributed to symmetric O–C–O stretching. These spectra also can be evaluated semiquantitatively. Except for CS, the DRIFT spectra of which seem to be independent of the feed composition, the band areas of methoxy groups clearly increased with increasing methanol partial pressure. In contrast, the intensity of surface hydroxyls decreased because the overall concentration of the reactants was kept constant at 4%. Integration of the hydroxyl bands (3232 and 3676 cm^{-1} for CZA and CZC, respectively) and the bands of methoxy groups (1093, 1057, and 1063 cm^{-1} for CZA, CZC, and CCF, respectively) after fitting resulted in good linear correlations of the band areas with the methanol (methoxy groups) and water (hydroxyl groups) partial pressure in the feed. This confirms the appearance of the corresponding adsorption terms in the mechanistic rate equation from independent spectroscopic experiments. As expected, the signal of the gas-phase carbon dioxide correlated with the measured conversion in this experimental series and was stronger with higher methanol partial pressure. The latter indicates that the reaction rate depends more on the methanol than on water partial pressure, because other reaction parameters (e.g., temperature, contact time) were kept constant during this experimental series. However, bands of methyl formate, expected at 1666 and 1726 cm^{-1} [4.25], which was detected by MS only over CS in traces and only in the case of high methanol surplus in the feed, or dioxomethylene, expected at 1405 and 2765 cm^{-1} [4.22], were absent, as were bands of formaldehyde, expected at 1148 cm^{-1} [4.20], another "missing" intermediate in the assumed reaction pathway. It appears that these species either do not participate in the SRM reaction mechanism or transform too rapidly to enable detection with infrared spectroscopy; consequently, this part of the reaction network cannot be clarified using this technique.

Table 4.2 Observed bands from the DRIFT spectra of SRM over the reduced Cu catalysts and assignment to vibrational modes of surface species and gas phase species (indicated as such)

species	mode ^a	CZA	CCF	CZC	CS	Cu/ZnO/ZrO ₂	Cu/ZnO/Al ₂ O ₃	Fe ₂ O ₃ /SiO ₂	Pt/CeO ₂	Cu/SiO ₂	
						[4.20]	[4.21]	[4.23]	[4.24]	[4.25]	[4.22]
methoxy	$\nu(\text{CH})_a$	2933	2926	2926	2958	2926	2950		2920	2960	2951
	$\nu(\text{CH})_s$	2827	2823	2819	2856	2821	2830		2820	2859	2851
	$\delta(\text{CH})_a$				1462			1466 1438		1463	
	$\rho(\text{CH}_3)$	1190		1146	(1188)		1190				
	$\nu(\text{CO})$	1093	1063	1057	1059	1047	1081		1080		
hydroxy	$\nu(\text{OH})$				3737		3735			3738	
	$\nu(\text{OH} \cdots \text{O})$	3232		3676	3680		3445		3650	3650	
formate	$\nu(\text{CH})$	2897	2872	2864		2871	2896		2830		2902
	$\nu(\text{OCO})_a$	1595	1595 1565	1585	1587	1600	1594 1610	1567	1580		1564
	$\delta(\text{CH})$	1377	1379 1358	1373		1357	1390	1377	1350		
Gas phase or weakly adsorbed carbon dioxide						2359 2327					
Gas phase carbon dioxide		2349	2349	2349	2349		2341				
carbonyls				2092		2095					
carbonate		1421		1490	1412		1550 1395		1460		1415

a) ν : stretch; δ : bend; ρ : rock.

Another observation concerning the range of 2600–3200 cm^{-1} is the signal of the formate group, which was comparatively strong on CCF and nearly invisible on the other three catalysts. Because the absolute band area is not meaningful in itself without knowledge of the extinction and scattering coefficients, the ratio of the band areas from the symmetric $\nu(\text{CH})$ bands of the formate groups and the methoxy groups was calculated from the fits of the spectra; these values are given in Fig. 4.5 and Tab. 4.3.

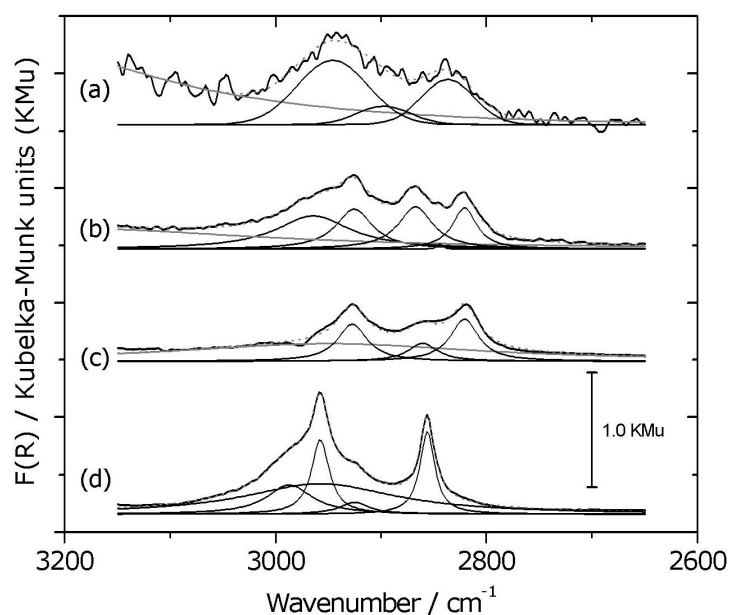


Figure 4.5 Fit of spectra (b) of each catalyst from Fig. 4.5; (a) CZA, (b) CCF, (c) CZC, (d) CS; feed: 4% reactants ($\text{MeOH}/\text{H}_2\text{O} = 1:1$), 220 °C.

Note that the wavenumbers given in the table result from the fits and may differ slightly from the values shown in Fig. 4.4.

Table 4.3 Band areas and ratios of the $\nu(\text{CH})_s$ bands of the formate and the methoxy groups.

Catalyst	$\nu(\text{CH})_s$ methoxy	band area	$\nu(\text{CH})_s$ formate	band area	ratio
CZA	2836	24.7	2897	10.1	2.5
CCF	2820	15.8	2867	23.2	0.7
CZC	2821	18.8	2860	8.3	2.3
CS	2855	19.4	2925	5.6	3.5

These ratios clearly indicate that the surface of CCF is relatively heavily covered with formate groups compared with that of the other catalysts. This means that formate groups on this catalyst are relatively stable, and their decomposition by dehydrogenation may affect the overall reaction rate. Along with the results of the kinetic model discrimination (which are discussed in more

detail later), these findings confirm the difference in the RDS of SRM over Cu/Cr₂O₃/Fe₂O₃ compared with already well-investigated Cu/ZnO/Al₂O₃ and Cu/SiO₂ systems. Further information from the fits included the presence of another methoxy-related band at 2987 cm⁻¹ on CS and 2964 cm⁻¹ on CCF. These bands, not observed on CZA and CZC, also may be attributed to C-H stretching vibrations.

4.4 Kinetic Modeling

4.4.1 Contact Time

For kinetic modeling, knowledge of the contact time is an essential condition. Determining contact time may be difficult, especially for isobaric gas-phase reactions with expanding or contracting volume due to a change in the total mole number. Measurements in the high-conversion regime require numerical integration, because the resulting deviation depends on the conversion and will cause a systematic error. This may be irrelevant for kinetics developed for technical application, but for mechanistic studies, the determination of contact time merits at least as much attention as the analysis of the product mixture. In the present study case, mainly differential conversions of < 10% have been measured, thus, conversion can be considered directly proportional to contact time. The molar ratio λ of the reactants and added gases such as N₂, H₂, and CO₂ also had to be considered. Measuring in the linear range, the contact time can be calculated from Eq. 4.1:

$$\tau = \frac{V_R}{\dot{V}_0} \frac{1}{B X} \ln \left(\frac{A + B + B X}{A + B} \right) \quad (4.1)$$

where V_R is the catalyst bed volume, \dot{V}_0 is the initial gas flow rate, and X is the conversion of the reactant present as a minor component. The coefficients A and B depend on the molar ratio of methanol and water, $\lambda = n_M/n_W$ (Tab. 4.4).

Table 4.4 Coefficients for calculation of the contact time referring to Eq. 4.1.

	A	B
$\lambda \leq 1$	$x_{\text{gas},0} + (1 - x_{\text{gas},0}) \frac{1 - \lambda}{1 + \lambda}$	$(1 - x_{\text{gas},0}) \frac{2\lambda}{1 + \lambda}$
$\lambda \geq 1$	$x_{\text{gas},0} - (1 - x_{\text{gas},0}) \frac{1 - \lambda}{1 + \lambda}$	$(1 - x_{\text{gas},0}) \frac{2}{1 + \lambda}$

where $x_{\text{gas},0}$ is the initial molar ratio of added gas. Fig. 4.6 shows the deviation of the contact time with increasing conversion in SRM calculated from Eq. 4.1 and from numerical integration as done in a previous study of the author [4.1].

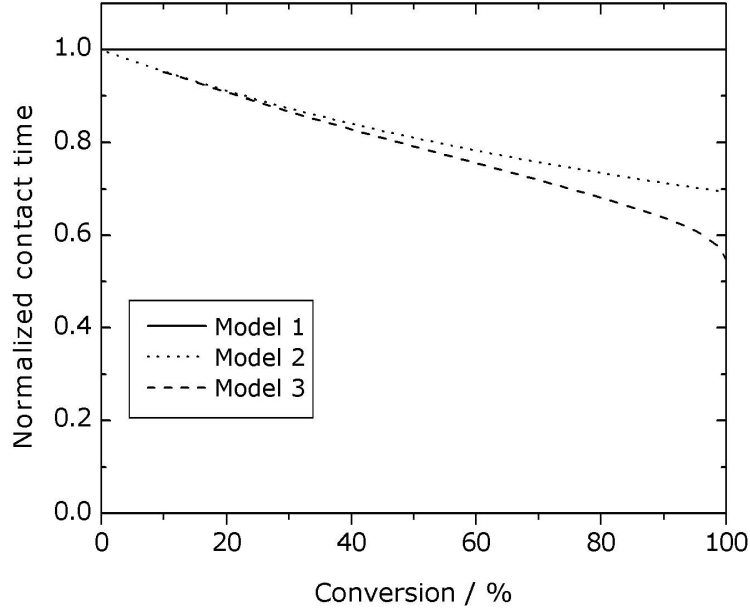


Figure 4.6 Predicted reduction of the contact time during SRM as a function of conversion due to increase of total mole number, calculations for equimolar reactant mixture. Model 1: contact time related to initial flow rate (no change in mole number, full line); model 2: contact time calculated from Eq. 4.1 (short dashed line); model 3: contact time from numerical integration [4.1] (long dashed line).

The most accurate calculation is of course the numerical integration (model 3), but, as can be seen from Fig. 4.6, model 2 (Eq. 4.1) reaches close approximation to the "real" contact time up to a conversion of 20%. In contrast, neglecting the increase in volume (model 1), the deviation is about 5% at a conversion of 10%.

4.4.2 Microkinetic Model

For microkinetic modeling the mechanism described in Ch. 2.3.2 was taken as basis, since most of the measured data can be explained by this model. The corresponding rate equation (Eq. 4.2)

$$r_R = \frac{k_R K_{\text{CH}_3\text{O}^{(A)}}^* \left(p_{\text{CH}_3\text{OH}}/p_{\text{H}_2}^{1/2} \right) \left(1 - \left(p_{\text{H}_2}^3 p_{\text{CO}_2} / k_R p_{\text{CH}_3\text{OH}} p_{\text{H}_2\text{O}} \right) \right) C_{\text{S}_A}^T C_{\text{S}_B}^T}{\left(1 + K_{\text{CH}_3\text{O}^{(A)}}^* \left(p_{\text{CH}_3\text{OH}}/p_{\text{H}_2}^{1/2} \right) + K_{\text{HCOO}^{(A)}}^* p_{\text{CO}_2} p_{\text{H}_2}^{1/2} + K_{\text{OH}^{(A)}}^* \left(p_{\text{H}_2\text{O}}/p_{\text{H}_2}^{1/2} \right) + K_{\text{CO}_2^{(A)}}^* p_{\text{CO}_2} \right)} \times \frac{1}{\left(1 + K_{\text{H}^{(B)}}^{1/2} p_{\text{H}_2}^{1/2} \right)} \quad (4.2)$$

predicts a SRM reaction rate that is determined mainly by the partial pressure of methanol. For water the rate shows a weak reverse dependence, expressed by a negative reaction order in a power law approach. The adsorption of carbon dioxide is competitive to that of methanol, water, and the oxygenate intermediates and thereby inhibits the overall reaction. Moreover, water and methanol adsorption occur dissociatively in combination with dehydrogenation, which should lead to strong inhibition by hydrogen. These predictions from the mechanistic rate law were compared with the experimental data.

Because the kinetic measurements were conducted under isothermal conditions at 220 °C, values for activation energy, E_A , and heat of adsorption ΔH_{ads} , could not be determined, except an apparent activation energy for the overall rate, as discussed in Ch. 4.4.3.

For each catalyst, the rate constant, as well as the adsorption constants of methanol, water, hydrogen, and carbon dioxide and the equilibrium constant of formate formation on the surface given in Eq. 4.2, were fitted to a total set of approximately 150 experimental rate data, calculated in the low-conversion regime from the ratio of methanol conversion and contact time (Fig. 4.7). The following rate and adsorption constants of SRM over the catalysts CZA, CZC, and CS were determined (Tab. 4.5) at a reaction temperature of 220 °C.

Table 4.5 Parameters of microkinetic modeling of SRM over supported copper catalysts CZA, CZC, and CS, given with confidence interval ($\pm 5\%$ of the absolute rate value) and stability index R^2 .

	CZA	CZC	CS	K3-110 [4.18]	Synetix 33-5 [4.6]
$k^* / \text{bar s}^{-1}$	0.537 ± 0.008	0.422 ± 0.012	0.0920 ± 0.003		
$K_{\text{CH}_3\text{O}^{(A)}}^* / \text{bar}^{-0.5}$	1.16 ± 0.06	0.86 ± 0.06	1.02 ± 0.08	0.862	4.93
$K_{\text{OH}^{(A)}}^* / \text{bar}^{-0.5}$	0.06 ± 0.01	0.035 ± 0.015	0.033 ± 0.017	0.623	-
$K_{\text{HCOO}^{(A)}}^* / \text{bar}^{-1.5}$	17 ± 4	6.71 ± 0.18	7.4 ± 0.6	0.058	-
$K_{\text{CO}_2^{(A)}} / \text{bar}^{-1}$	0.65 ± 0.07	7.2 ± 0.6	3.8 ± 0.4	-	-
$K_{\text{H}_2^{(B)}} / \text{bar}^{-1}$	0.41 ± 0.09	0.77 ± 0.02	0.288 ± 0.011	1.16	12.6
R^2 (see Fig. 4.7)	0.992	0.989	0.988		

CCF showed a particularly different catalytic behaviour than the other three catalysts and thus, could not be fitted with the model described above, its modeling is described later.

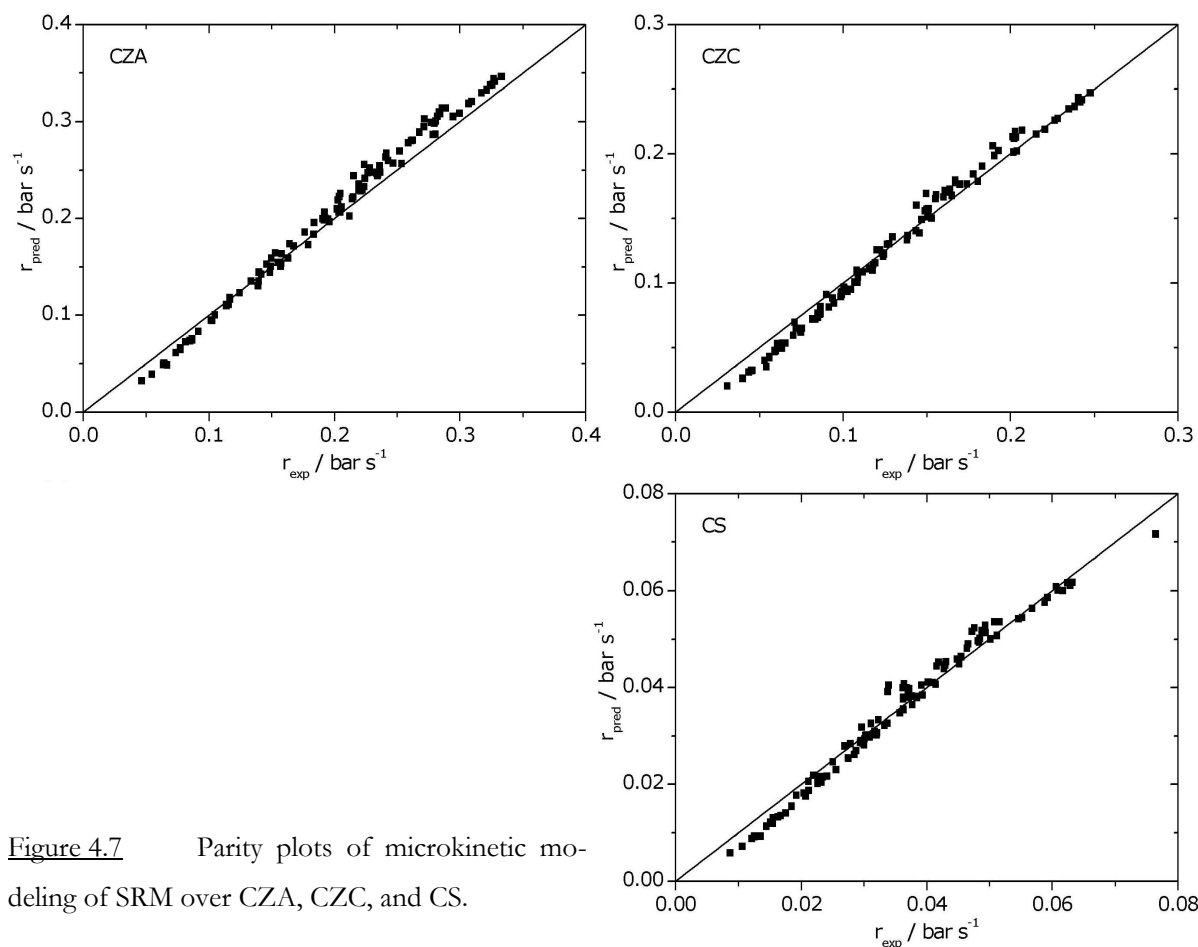


Figure 4.7 Parity plots of microkinetic modeling of SRM over CZA, CZC, and CS.

As can be seen from the confidence intervals, the rate constant k^* was determined with the highest accuracy, whereas the adsorption constants $K_{\text{CH}_3\text{O}^{(\text{A})}}^*$, $K_{\text{OH}^{(\text{A})}}^*$, and $K_{\text{H}_2^{(\text{B})}}$ could be fitted only with moderate exactness. Because $K_{\text{CO}_2^{(\text{A})}}$ and $K_{\text{HCOO}^{(\text{A})}}^*$ affect each other in the prediction of the surface inhibition caused by carbon dioxide, by either molecular adsorption or formate formation, their values have a relatively low accuracy. This also may explain the difference in the ratio of $K_{\text{HCOO}^{(\text{A})}}^*$ and $K_{\text{CO}_2^{(\text{A})}}$ regarding CZA on the one hand and CZC and CS on the other hand. Nevertheless, the elimination of one of these constants resulted in a significant loss of fitting quality, and so both of them were kept in the rate equation. However, the stability index R^2 is between 0.95 and 1.0 for the three catalysts, confirming the good agreement between the experimental data and the microkinetic model. To provide a better comparison of the rate constants and to obtain information about the intrinsic rate constants, the k^* values must be referred to the number of active sites on the catalyst surface. These surface concentrations are, of course, dependent on the copper content of the samples, but certainly are not linear functions

due to agglomeration effects related to higher copper content. However, because the absolute number of active sites remains unknown, a relatively rough comparison of the reaction rates related to the copper content is given in Ch. 4.4.3. Compared with previously published data, the fitted parameters $K_{\text{CH}_3\text{O}}^{(*)}$ and $K_{\text{H}_2}^{(*)}$ for CZA come closer to the corresponding constants that Peppley et al. [4.18] determined than to the adsorption constants that Lee et al. [4.6] measured for their Cu/ZnO/Al₂O₃ catalysts. The combined adsorption constant $K_{\text{HCOO}}^{(*)}$ is two orders of magnitude higher than the value published by Peppley et al. This discrepancy may be explained by the fact that this group did not observe carbon dioxide inhibition of SRM over their commercial catalyst. Lee et al. also did not observe this kind of inhibition and included neither a formate nor a carbon dioxide adsorption term in their kinetic model, indicating that even among Cu/ZnO/Al₂O₃ systems, the relationship between different surface species can differ strongly. However, because in the DRIFTS study no molecularly adsorbed CO₂ species could be observed, but an inhibiting influence of this product gas on the SRM reaction was detected, carbon dioxide adsorption via carbonate formation is assumed, in agreement with a recent study [4.21].

As mentioned above, the Cu/Cr₂O₃/Fe₂O₃ catalyst CCF exhibited different behavior in SRM than the other three catalysts tested. The dependence of the rate on the feed composition indicated an RDS beyond methoxy dehydrogenation and including the participation of water or hydroxyl groups. This is shown in Fig. 4.8 for SRM over CZA and CCF applying a varying binary feed composition of water and methanol without the addition of inert or product gases.

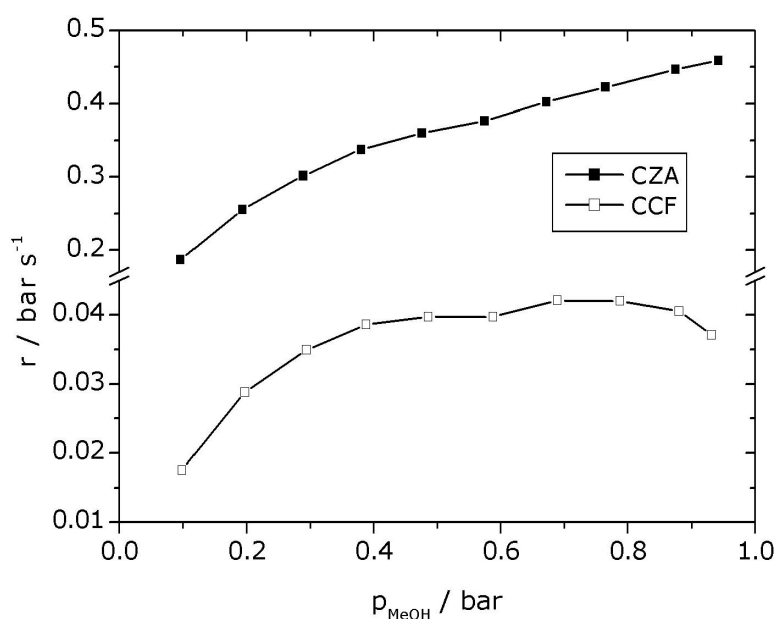


Figure 4.8 Comparison of the dependence of SRM reaction rate over CZA and CCF on the feed composition without addition of inert or product gases, $T = 220\text{ }^{\circ}\text{C}$.

The important difference between the curve shape for CCF and that of the other three catalysts is the plateau of the SRM reaction rate from 40 up to 80% methanol in the binary feed and the subsequent significant decrease. Because of this shape, the reaction could not be fitted sufficiently with the mechanistic rate law in Eq. 4.2. Against this, the rate of SRM over CZA steadily increased with increasing methanol partial pressure up to 90% methanol in the feed, which exactly fits the general shape of this function.

The DRIFTS experiments showed that especially CCF was covered with a relatively high amount of formate groups. These results lead to the conclusion that formate dehydration was noticeably slower on this catalyst than on the other catalysts, maybe singularly rate-determining but definitely involved in the total rate.

The mechanistic rate equation assuming formate dehydration (FDH) as the RDS in the catalysis cycle described in Fig. 2.4 is given by Eq. 4.3

$$r_{\text{FDH}} = \frac{k_{\text{FDH}} C_{\text{S}_A}^T (C_{\text{S}_B}^T)^6 \prod_i K_i^* (p_{\text{CH}_3\text{OH}} p_{\text{H}_2\text{O}} / p_{\text{H}_2}^{5/2})}{\left(1 + \underbrace{K_{\text{CH}_3\text{O}}^* (p_{\text{CH}_3\text{OH}} / p_{\text{H}_2}^{1/2})}_{\text{methoxy}} + \underbrace{K_{\text{OH}}^* (p_{\text{H}_2\text{O}} / p_{\text{H}_2}^{1/2})}_{\text{hydroxy}} + \underbrace{\prod_i K_i^* (p_{\text{CH}_3\text{OH}} p_{\text{H}_2\text{O}} / p_{\text{H}_2}^{5/2})}_{\text{formate}} + \underbrace{K_{\text{CO}_2}^* p_{\text{CO}_2}}_{\text{carbon dioxide}} \right)} \times \frac{1}{\left(1 + K_{\text{H}}^{1/2} p_{\text{H}_2}^{1/2} \right)^6} \quad (4.3)$$

where $\prod_i K_i^*$ represents the product of the equilibrium constants of all elemental reaction steps in the catalysis cycle from methanol adsorption up to dioxomethylene dehydrogenation. (The rate law following the methyl formate route is the same with respect to its algebraic form but with different meaning of its parameters.) Obviously, this product of six factors prevents meaningful fitting of experimental data, and thus the following discussion is only qualitative. As can be seen, this rate law describes in the differential conversion regime ($p_{\text{H}_2}, p_{\text{CO}_2} \approx 0$) a zero-order reaction over a wide range of feed compositions. However, against the rate law with methoxy dehydrogenation as the RDS, this rate law predicts a decreasing rate with the decrease of water in the feed, which is exactly the observed result. Applying Eq. 4.3 for fitting the rate data acquired from CCF could be better fitted than with Eq. 4.2, but still not in a sufficiently high quality. Because the experimental data, displayed in Fig. 4.8, seems to result from a combination of both fundamental rate equation shapes, a combined rate equation is proposed for the final description (Eq. 4.4),

$$\frac{1}{r} = \frac{1}{r_{\text{MDH}}} + \frac{1}{r_{\text{FDH}}} \quad (4.4)$$

which is the expression corresponding to Kirchhoff's law of electricity, implying that the total rate is affected mainly by the slowest of both elemental reactions, methoxy and formate dehydrogenation, the activation barriers of which may be comparable to electronic resistors. Unfortunately, only the general shape of the results can be explained using this model. The high reaction order of hydrogen in r_{FDH} predicts an immense inhibition of the reaction progress by its appearance, which actually is not observed to this extent in the experimental results. This produces unrealistically low values for the hydrogen adsorption constant $K_{\text{H}_2^{(B)}}$ and thereby high values for the product $\prod_i K_i^*$, although the rate data fit is sufficiently accurate. The values of the fitted parameters are not presented here. However, the assumption that SRM over CCF has a second barrier at formate dehydrogenation is also confirmed by its low selectivity. Compared with the other three catalysts, CCF produced a high amount of CO in the product stream, which must have formed from an intermediate preliminary to formate, because formate itself decomposes directly into the main reaction products H_2 and CO_2 . Millar et al. [4.26] and Fisher and Bell [4.27] reported CO formation from methyl formate in the absence of water. Although not observed in the DRIFTS studies, increased CO production may indicate a higher amount of methyl formate on the surface due to slower formate dehydrogenation.

In an early stage of this study, it was observed that the $\text{Cu/Cr}_2\text{O}_3/\text{Fe}_2\text{O}_3$ high-temperature-shift catalyst exhibited remarkably low activity and poor selectivity for SRM, and this combination will definitely never reach technical application for this reaction. However, this catalyst was not suspended from further experiments, because there is a pool of information about a reaction system that cannot be discovered by the analysis and investigation of good and optimized catalysts. The knowledge of reasons why particular systems (e.g., CCF as a catalyst for SRM) do not operate in the expected way sometimes provides deeper insight into and better understanding of the systems that work well.

Vargas et al. [4.21] proposed that methanol adsorption during SRM occurs on oxidized surface sites independent of the presence of oxygen in the feed. They posited that these sites in the absence of oxygen are formed via dissociative water adsorption, especially at low temperatures ($< 250\text{ }^\circ\text{C}$). A kinetic evaluation of this pathway inevitably should result in a much stronger influence of water concentration on the SRM reaction rate than was actually found in this study. From a kinetic standpoint, this mechanism could not be adapted to these experimental results. However, their DRIFT study was conducted at even higher temperatures, up to $450\text{ }^\circ\text{C}$. Despite these contradictions, Vargas et al. also identified the selectivity-determining step between methoxy and formate intermediates, which is in agreement with these results. Enhanced CO formation via

formate decomposition [4.21], as well as methyl formate decomposition [4.26,4.27], match well with the higher amount of formate on CCF and the resulting poor selectivity towards CO₂. Indeed, a recent kinetic study on the SRM reaction network over CCF (B. Frank, unpublished results) indicated that CO formation over this catalyst occurred mainly via methanol decomposition, whereas the main source of CO over CZA and CZC was the rWGS reaction [4.1,4.5].

4.4.3 Formal Kinetics and Comparison of Activity

Because of their easier handling, power rate laws are often used for sizing reactors in industrial and technical sciences [4.28–4.30]. An interesting difference among several power rate laws given in the literature is found in the inhibiting effect of carbon dioxide. Jiang et al. [4.7] and Lee et al. [4.6] could not measure any inhibition of carbon dioxide on SRM over Cu/ZnO/Al₂O₃ catalysts. In contrast, Idem and Bakhshi [4.31] and Samms and Savinell [4.32] found such an inhibition over their copper catalysts. For technical applications, this differentiation between two inhibiting species is of no importance, because hydrogen and carbon dioxide are formed at a strict stoichiometric ratio of 3, and their exponents can be transformed algebraically. But from a mechanistic standpoint, this finding may be very important, as was shown earlier.

Many kinetic studies reported in the literature are based on simple power rate laws, thus, this study was completed with a power law fit of the kinetic data, to allow a better comparison with the results of research groups who published only power law fits. The reaction orders of methanol (m_M), water (m_W), hydrogen (m_H), and carbon dioxide (m_C) were fitted to the complete dataset of about 150 data points for each catalyst with a rate expression of the following form (Eq. 4.5):

$$r = k^{\text{eff}} p_{\text{CH}_3\text{OH}}^{m_M} p_{\text{H}_2\text{O}}^{m_W} p_{\text{H}_2}^{m_H} p_{\text{CO}_2}^{m_C} \quad (4.5)$$

where r is the reaction rate of methanol consumption, k^{eff} is the effective rate constant, p is the partial pressure, and m is the reaction order of the reactant.

In agreement with mechanistic modeling, the reaction rate was found to be determined mainly by the methanol partial pressure, whereas the reaction order of water was very low for all catalysts. Both main reaction products were found to inhibit the reaction, which is expressed in negative reaction orders. The reaction order of nitrogen m_N was found to be 0 ± 0.02 , as expected, and the range of ± 0.02 may indicate the experimental error of this study. The results of the power law fit are given in Tab. 4.5.

Lee et al. [4.6] used a power expression for hydrogen of the type $(A + p_{\text{H}_2})^{m_H}$ to undergo infinite reaction rates at the reactor inlet, where the partial pressure of hydrogen is zero. For numerical

fitting, this mathematical problem has been solved by initializing the hydrogen partial pressure with an extremely small value of 10^{-5} bar. Indeed, the variation of this initialization parameter in the range of 10^{-4} – 10^{-7} bar causes a negligible deviation of the predicted methanol conversion of $< 0.1\%$. As shown in Tab. 4.6, the reaction order of water is the highest on CCF. This is in good agreement with the results of the mechanistic study, because on this catalyst, the effect of the water partial pressure is relatively high, due to the influence of formate dehydrogenation on the overall reaction rate. The water reaction orders are slightly positive on CZA, CZC, and CS compared to the slightly negative reaction order predicted by the pure application of Eq. 4.3. This also may indicate a minor influence of formate dehydrogenation on the SRM reaction rate on these catalysts.

Table 4.6 Rate constants and reaction orders of SRM over the investigated copper-containing catalysts measured at 220 °C.

catalyst	k [bar ^x s ⁻¹]	m_M	m_W	m_H	m_C	m_N	R ²
CZA	0.117	0.491	0.021	-0.31	-0.082	-0.021	0.963
	± 0.004	± 0.012	± 0.008	± 0.01	± 0.005	± 0.008	
CCF	0.034	0.521	0.115	-0.19	-0.09	-0.012	0.984
	± 0.003	± 0.012	± 0.003	± 0.01	± 0.01	± 0.004	
CZC	0.062	0.603	0.032	-0.319	-0.173	0.017	0.979
	± 0.002	± 0.010	± 0.006	± 0.007	± 0.005	± 0.005	
CS	0.0245	0.567	0.048	-0.266	-0.110	-0.01	0.980
	± 0.007	± 0.009	± 0.005	± 0.006	± 0.004	± 0.01	

From the temperature dependence of the reaction rate, the apparent activation energy was calculated from the slope of the dataset in an Arrhenius plot (Fig. 4.9). Linearity was observed for each catalyst, indicating no change in the RDS or diffusion limitation over the temperature range investigated. This figure also gives a clear comparison of the activities of the catalysts. The activation energies, E_A , determined from the Arrhenius plot and the reaction rate at 220 °C are given in Tab. 4.7.

The activation energies of SRM over CZC and CS were nearly identical, in agreement with the assumption of the same RDS. The temperature dependence over CZA was slightly lower, but this can be attributed to the high copper content of this sample, as shown in a previous study [4.1]. A clear difference in the activation energy was observed for CCF; this value was noticeably low, indicating a difference in the RDS as described in detail above. An extremely low value of E_A for SRM over a Cu/Cr₂O₃/Fe₂O₃ water-gas shift catalyst was also found by Löffler et al. [4.33].

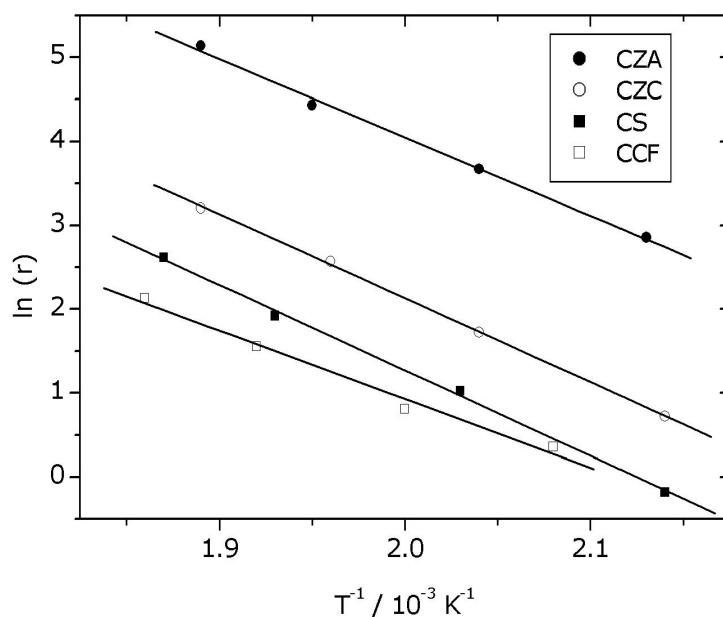


Figure 4.9 Arrhenius plot for SRM over the investigated copper catalysts in the temperature range of 200–250 °C ($m_{\text{CZA}} = 0.5$ g, $m_{\text{CCF}} = 2.5$ g, $m_{\text{CZC}} = 1.0$ g, $m_{\text{CS}} = 2.0$ g, $p = 1$ bar, $w = 0.3\text{--}2$ ml min⁻¹, MeOH/H₂O = 1, reaction rate r in mmol s⁻¹ kg⁻¹).

Table 4.7 Activation energies and reaction rates at 220 °C of copper-based catalysts expressed for overall catalyst amount and Cu-content.

Sample	E_A [kJ mol ⁻¹]	r_{220} [mmol kg _{cat} ⁻¹ s ⁻¹]	r_{220} [mmol kg _{Cu} ⁻¹ s ⁻¹]
CZA	76.9	44.1	80.3
CCF	67.4	2.0	100.2
CZC	84.9	6.4	92.2
CS	85.7	2.6	22.5

Because there are no comparable data on the influence of the catalyst support on the activity in SRM, the activities referred to the mass of copper have been compared with specific activities found for methanol synthesis given by Fujitani et al. [4.34]. Those authors found that the specific activity of copper-based catalysts depends on the support in the decreasing order $\text{Cr}_2\text{O}_3 > \text{ZrO}_2 \approx \text{Al}_2\text{O}_3 > \text{SiO}_2$ and observed a promoting effect of ZnO on each support. Taking into account that the chosen Cu/ZnO/Al₂O₃ catalyst was up to 5 times less active than other systems reported (see Ch. 4.2.1), these results are in good agreement. Although there are significant differences in the copper loading of the investigated catalysts, and the influence of Fe₂O₃ and CeO₂ was neglected in this comparison, this may indicate the similarity of the active sites of copper-based catalysts used in methanol synthesis and SRM.

References of Chapter 4

- [4.1] Á. Mastalir, B. Frank, A. Szizybalski, H. Soerijanto, A. Deshpande, M. Niederberger, R. Schomäcker, R. Schlögl, T. Ressler, *J. Catal.* **2005** 230 464.
- [4.2] A.S. Deshpande, N. Pinna, P. Beato, M. Antonietti, M. Niederberger, *Chem. Mater.* **2004** 16 2599.
- [4.3] L. Trouillet, T. Toupance, F. Villain, C. Louis, *Phys. Chem. Chem. Phys.* **2000** 2 2005.
- [4.4] D.S. Brands, E.K. Poels, T.A. Krieger, O.V. Makarova, C. Weber, S. Veer, A. Blik, *Catal. Lett.* **1996** 36 175.
- [4.5] H. Purnama, T. Ressler, R.E. Jentoft, H. Soerijanto, R. Schlögl, R. Schomäcker, *Appl. Catal. A* **2004** 259 83.
- [4.6] J.K. Lee, J.B. Ko, D.H. Kim, *Appl. Catal. A* **2004** 278 25.
- [4.7] C.J. Jiang, D.L. Trimm, M.S. Wainwright, N.W. Cant, *Appl. Catal. A* **1993** 93 245.
- [4.8] B.A. Peppley, J.C. Amphlett, L.M. Kearns, R.F. Mann, *Appl. Catal. A* **1999** 179 21.
- [4.9] M. Baerns, H. Hofmann, A. Renken, *Chemische Reaktionstechnik*, Thieme, Stuttgart, **1999**.
- [4.10] J.R. Katzer, dissertation, Massachusetts Institute of Technology, Cambridge, Massachusetts, 1969 (cited in [32]).
- [4.11] M. Kurtz, H. Wilmer, T. Genger, O. Hinrichsen, M. Muhler, *Catal. Lett.* **2003** 86 77.
- [4.12] M.V. Twigg, M.S. Spencer, *Top. Catal.* **2003** 22 191.
- [4.13] X. Zhang, P. Shi, *J. Mol. Catal. A* **2003** 194 99.
- [4.14] A. Szizybalski, F. Girgsdies, A. Rabis, Y. Wang, M. Niederberger, T. Ressler, *J. Catal.* **2005** 233 297.
- [4.15] Y. Liu, T. Hayakawa, K. Suzuki, S. Hamakawa, T. Tsunoda, T. Ishii, M. Kumagai, *Appl. Catal. A* **2002** 223 137.
- [4.16] V. Agarwal, S. Patel, K.K. Pant, *Appl. Catal. A* **2005** 279 155.
- [4.17] Y. Choi, H.G. Stenger, *Appl. Catal. B* **2002** 38 259.
- [4.18] B.A. Peppley, J.C. Amphlett, L.M. Kearns, R.F. Mann, *Appl. Catal. A* **1999** 179 31.
- [4.19] J.P. Breen, F.C. Meunier, J.R.H. Ross, *Chem. Commun.* **1999** Iss. 22 2247.
- [4.20] P.H. Matter, U.S. Ozkan, *J. Catal.* **2005** 234 463.
- [4.21] M.A. Larrubia Vargas, G. Busca, U. Costantino, F. Marmottini, T. Montanari, P. Patrono, F. Pinzari, G. Ramis, *J. Mol. Catal. A* **2007** 266 188.
- [4.22] D.B. Clarke, D.K. Lee, M.J. Sandoval, A.T. Bell, *J. Catal.* **1994** 150 81.
- [4.23] C.T. Wang, R.J. Willey, *J. Catal.* **2001** 202 211.
- [4.24] G. Jacobs, B.H. Davis, *Appl. Catal. A* **2005** 285 43.
- [4.25] D.M. Monti, N.W. Cant, D.L. Trimm, M.S. Wainwright, *J. Catal.* **1986** 100 17.
- [4.26] G.J. Millar, C.H. Rochester, K.C. Waugh, *J. Chem. Soc. Faraday Trans.* **1991** 87 2795.
- [4.27] I.A. Fisher, A.T. Bell, *J. Catal.* **1999** 184 357.
- [4.28] J. Agrell, H. Birgersson, M. Boutonnet, *J. Power Sources* **2002** 106 249.
- [4.29] P. Reuse, A. Renken, K. Haas-Santo, O. Görke, K. Schubert, *Chem. Eng. J.* **2004** 102 133.
- [4.30] L. Ma, C. Jiang, A.A. Adesina, D.L. Trimm, M.S. Wainwright, *Chem. Eng. J.* **1996** 62 103.
- [4.31] R.O. Idem, N.N. Bakhshi, *Chem. Eng. Sci.* **1996** 51 3697.
- [4.32] S.R. Samms, R.F. Savinell, *J. Power Sources* **2002** 112 13.
- [4.33] D.G. Löffler, S.D. McDermott, C.N. Renn, *J. Power Sources* **2003** 114 15.
- [4.34] T. Fujitani, M. Saito, Y. Kanai, T. Kakumoto, T. Watanabe, J. Nakamura, T. Uchijima, *Catal. Lett.* **1994** 25 271.
- [4.36] B. Frank, F.C. Jentoft, H. Soerijanto, J. Kröhnert, R. Schlögl, R. Schomäcker, *J. Catal.* **2007** 246 177.

5 Oxidative Dehydrogenation of Propane (ODP)

5.1 Catalyst Preparation and Characterization

Common methods of catalyst preparation are co-precipitation [5.1,5.2] and incipient wetness impregnation [5.3,5.4] of support material as powder. The resulting precursor is then calcined, compressed, crushed and sieved to get catalyst pellets with a defined size providing optimal flow conditions inside the reactor for catalytic testing. However, the compression of catalyst powder results in low porosity of the produced grains which adversely affects the mass transport by causing slow pore diffusion [5.5]. In order to avoid this, the use of highly porous support material in the form of commercially available extrudates may be appropriate. Compared to compressed powders, these extrudate-based grains are also expected to provide higher mechanical stability, which may be important with respect to its use in a Berty-type reactor. A moderate intraparticle heat production can be achieved by a low loading of the catalyst. The model catalyst to be prepared should furthermore exhibit identical active sites to allow a meaningful study of structure-activity relationships. To allow for these demands the following method of catalyst preparation was developed.

The $\text{VO}_x/\text{Al}_2\text{O}_3$ catalyst was prepared by wet saturation-impregnation of a porous γ -alumina catalyst support (Alfa Aesar, item no. 43857) according to [5.6,5.7]. Prior to the impregnation, the alumina pellets were crushed and sieved to the following particle size fractions: 0.1–0.3, 0.3–0.6, 0.6–1.0, 1.0–1.5 and 1.5–2.5 mm, denoted in the following as VA-200, VA-450, VA-800, VA-1250 and VA-2000, respectively. A 0.1 mol l^{-1} solution of vanadyl acetylacetonate (Sigma-Aldrich, > 97%) in toluene was heated under reflux until the boiling point was reached. For each catalyst sample, 2 g of the support were added slowly to 100 ml of the mixture and boiled under reflux for about 5 h. Impregnated particles were thoroughly washed with fresh toluene to remove unbound vanadyl species, then dried at 353 K for 12 h and finally, calcined in air at 773 K for 3 h. Calcined catalysts were sieved again to remove abrasion.

The preparation method was designed for the deposition of well-dispersed VO_x monomeric species on the alumina surface, which is known to be appropriate to highly dispersed deposition [5.8]. The organic ligand acetylacetonate is relatively bulky and was chosen in order to prevent the adsorption of directly neighboured vanadium atoms. The presence of at least one of the ligands on the uncalcined catalyst is assumed from the dark colour of the precursor compared to support and calcined catalyst. Since following experiments showed that the duration of impregnation from 15 min up to 8 h has no effect on the catalytic activity [5.9], the surface may be regarded as homogeneously covered and "saturated" with vanadia species corresponding to this preparation

method. This is advantageous to the highly reproducible preparation of adequate amounts of catalyst material for further studies.

When crushed and sieved to a particle diameter of 0.1–0.3 mm, all of the catalyst samples provided the same intrinsic activity and selectivity. The amount and the distribution of vanadia precipitated on the surface were thereby assumed to be identical in all of the particle size fractions. Further detailed catalysts characterization was curtailed to the sample VA-200.

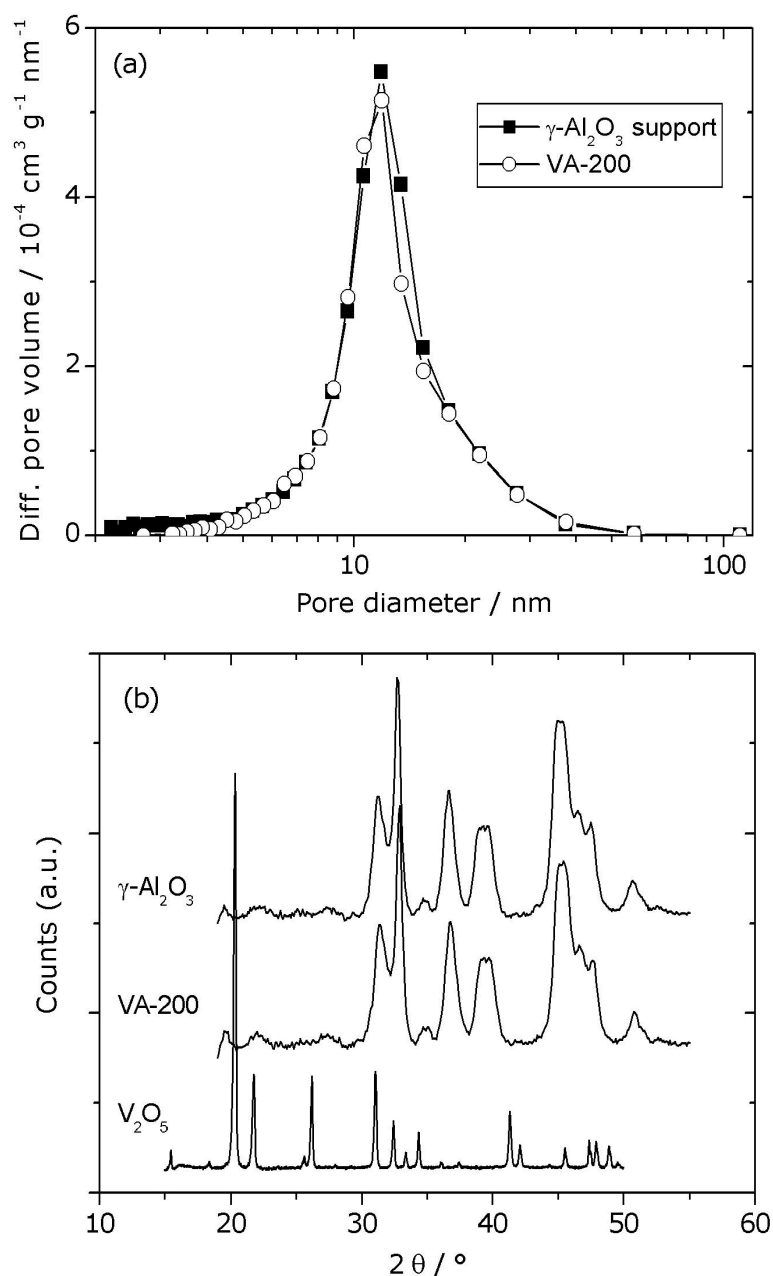


Figure 5.1 (a) Pore size distributions of $\gamma\text{-Al}_2\text{O}_3$ support and catalyst VA-200; (b) powder XRD spectra of catalyst VA-200, $\gamma\text{-Al}_2\text{O}_3$ support, and crystalline V_2O_5 .

The pale yellow catalyst grains had a BET surface of $106.6 \text{ m}^2 \text{ g}^{-1}$ and were found to be mesoporous with a medium pore diameter of 15.7 nm. These values are almost identical to that of the not impregnated catalyst support. The pore size distribution of both catalyst and support is given in Fig. 5.1 (a). As can be seen from the similar shapes of the curves, there is a little clogging of micropores $< 5 \text{ nm}$ observable but the support structure seems to be unaffected by the deposition of vanadia. Both catalyst and support material provided a high porosity of about 0.65 which was determined from the measured micropore volume.

The baseline-corrected XRD patterns of the powdered catalyst, the $\gamma\text{-Al}_2\text{O}_3$ support material, and crystalline V_2O_5 powder are presented in Fig. 5.1 (b). One can see that there is no difference in the XRD patterns of the catalyst and the support. Moreover, any reflexes related to crystalline bulk vanadia phase are absent. This may be understood either as the presence of small crystalline V_2O_5 nanoparticles ($< 4 \text{ nm}$) or as surface VO_x species that cannot be detected by XRD due to the absence of long-range order. Based on the below UV-Vis and H_2 -TPR results, the presence of small crystalline V_2O_5 nanoparticles can be excluded. For deriving insights into the distribution of surface VO_x species, apparent density of vanadium (V nm^{-2}) was calculated from the BET value and vanadium loading. The total vanadia surface concentration was calculated from the results of the ICP experiments, which gave a content of 1.4 wt% V in the catalyst. This leads to the apparent density of vanadium of $1.55 \text{ V atoms nm}^{-2}$ or 0.21 theoretical monolayers corresponding to the value of 7–8 $\text{VO}_x \text{ nm}^{-2}$ from Raman spectroscopy measurements [5.10,5.11]. This is in good agreement with the calculated value for a monolayer coverage with isolated monovanadates of $2.3 \text{ VO}_x \text{ nm}^{-2}$ [5.12].

The atomic ratio (%) of the detected elements at the catalyst surface that were obtained from the XPS analysis is O: 61.2%, V: 2.5%, C: 3.8%, and Al: 32.5%. Subtracting the contribution of some CO_x species adsorbed on the surface, this composition is in excellent agreement with that calculated with the results of BET and ICP analysis. Using ionic radii of Al^{3+} , V^{5+} , C^{4+} , and O^{2-} of 57, 59, 16, and 132 pm, respectively, a surface coverage of $1.50 \text{ VO}_x \text{ nm}^{-2}$ is derived. The XP spectrum of the V $2p_{3/2}$ region after subtraction of the X-ray induced satellites of the O 1s peak is presented in Fig. 5.2 (a). The deconvolution of this spectrum provides information about the oxidation states of surface vanadia species. By analogy with the literature, the bands at 517.4 (2.3 eV, 70%) and 516.4 eV (2.3 eV, 30%) can be assigned to V^{+V} and V^{+IV} , respectively [5.13]. The effect of UHV/X-ray induced changes on the XP spectra are accounted for by recording time-dependent XP spectra. The analysis shows that 80% V^{+V} and 20% V^{+IV} are present at $t = 0 \text{ min}$.

The partial reduction can be explained by catalyst aging e.g. the adsorption of water molecules from the ambient as observed recently for VO_x/SiO_2 catalysts [5.14]. The C 1s spectrum (not

shown) reveals three contributions at 284.1, 285.7, and 288.7 eV. The first two peaks are assigned to C-C or C-H bonds and to carbon atoms bound to single oxygen atoms resulting from residual or incompletely decomposed acetylacetonate molecules. The third peak is assigned to carbonate-type carbon atoms formed during calcination. The organic ligand acetylacetonate and also carbon oxides are indeed highly adsorptive on the acidic γ -Al₂O₃ surface.

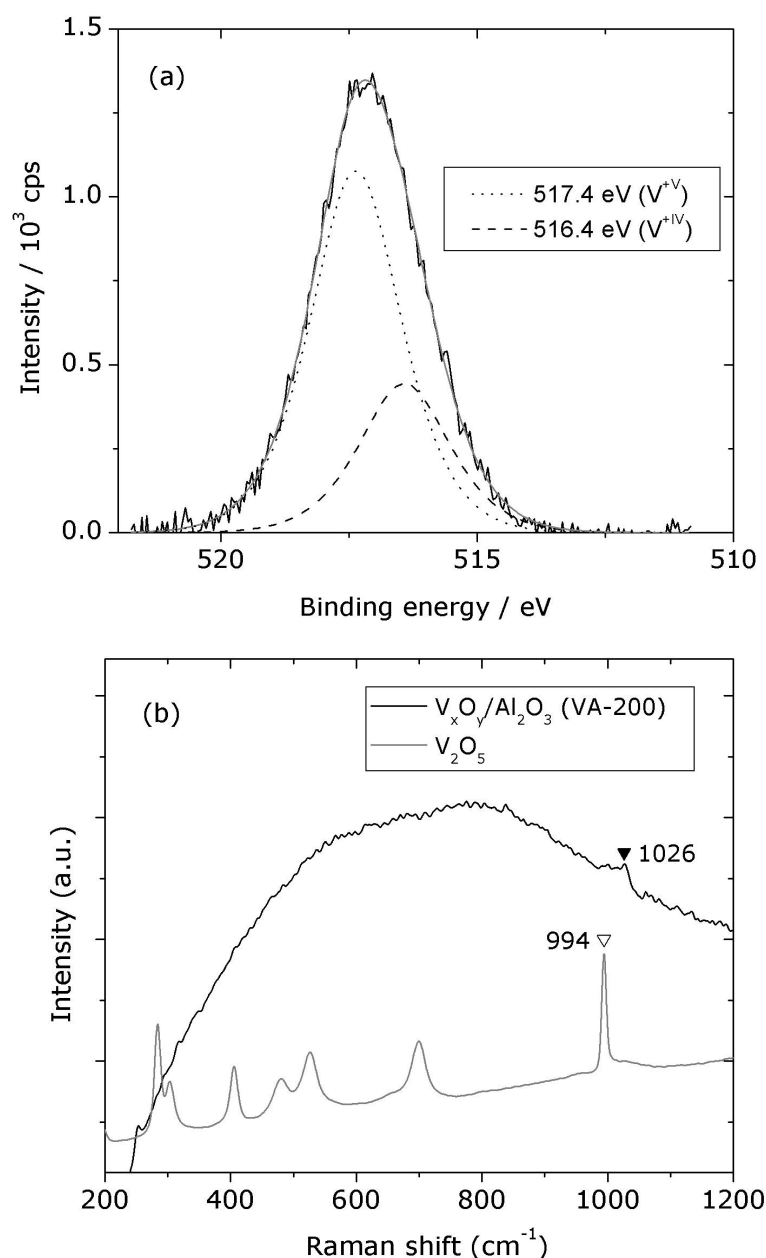


Figure 5.2 (a) XPS spectrum of the V 2p_{3/2} region of the VO_x/γ-Al₂O₃ catalyst VA-200; (b) Raman spectra of the VO_x/ γ-Al₂O₃ catalyst VA-200 and crystalline V₂O₅.

The Raman spectrum of VA-200 is presented in Fig. 5.2 (b) and compared to the spectrum of crystalline V₂O₅. The spectrum is dominated by a broad fluorescence band of the γ-Al₂O₃ support. The support does not give rise to Raman bands of significant intensity in the 950–

1050 cm^{-1} region [5.15]. Therefore, the band at 1026 cm^{-1} is due to a vanadium oxide related Raman band. In particular, it is assigned to the vanadyl stretch vibration of highly dispersed vanadia species [5.15]. The shoulder to the left hand side of this feature can result from the presence of a small amount of crystalline V_2O_5 , which has a strong feature at 993-994 cm^{-1} [5.16]. The Raman cross section of the vanadyl band of V_2O_5 crystalline species is, however, about 10 times larger than that of disperse VO_x species [5.17], and no further features of V_2O_5 could be detected at lower wavenumbers. Argyle et al. determined a V_2O_5 : monovanadate ratio of 0.085 from a Raman spectrum showing even more intensive V_2O_5 features [5.18] than the spectrum presented here. The Raman analysis confirms therefore the high dispersion degree of the vanadia species on the VA-200 surface.

Further insights into the degree of polymerization of surface VO_x species were derived from in situ UV-Vis analysis. The UV-Vis spectra of fresh and dehydrated (oxidized in an O_2 flow at 773 K) VA-200 catalyst are presented in Fig. 5.3 (a). Both samples exhibit charge-transfer (CT) bands below 500 nm. However, the intensity of these bands is higher for the oxidized sample as compared to the fresh one. The difference is due to the fact that the fresh sample contained reduced VO_x species, which were oxidized to V^{+V} during the O_2 pretreatment at 773 K for 0.5 h. Small amounts of V^{+IV} in the oxidized sample cannot be completely excluded. In order to derive insights into the structure/distribution of surface VO_x species in the oxidized VA-200 sample, its UV-Vis spectrum was compared to that of VO_x (2.7 wt%)/MCM-41, where isolated VO_4 units and small VO_x aggregates having V-O-V bonds are present on the surface [5.6]. The comparison is presented in Fig. 5.3 (b). It can be seen that the height-normalized UV-Vis spectrum of the oxidized VA-200 sample is slightly broader than that of the VO_x (2.7 wt%)/MCM-41 sample. This broadening of the UV-Vis spectra could be caused by an increase in the domain size of VO_x species in the former sample as compared to the latter one. It appears that the VA-200 sample possesses small amounts of VO_x species with a higher degree of polymerization or domain size. However, the main VO_x species are highly dispersed.

From the spectra a UV-Vis edge energy of 2.6 eV can be calculated for the oxidized VA-200 sample. With regard to a study by Gao et al. [5.19] this corresponds to an average value of about 3.5 V-O-V bonds per V atom which is hardly realistic for an apparent surface concentration of 1.5 V nm^{-2} . In deed, a repeated UV-Vis experiment using a different experimental set-up¹ (spectrum not shown here) resulted in an edge energy of close to 3 eV, which corresponds to an average value of 2 V-O-V bonds per V-atom. It appears that the determination of the UV-Vis edge energy depends on the type of spectrometer and experimental details, which can cause

¹ Presented spectra were taken by Dr. Evgueni Kondratenko (LIKAT, Adlershof), repeated measurements were performed by Dr. Christian Hess (FHI, Dahlem).

different offsets or shifts in the wavelength. The correlation reported by Gao et al. should thereby be used with caution.

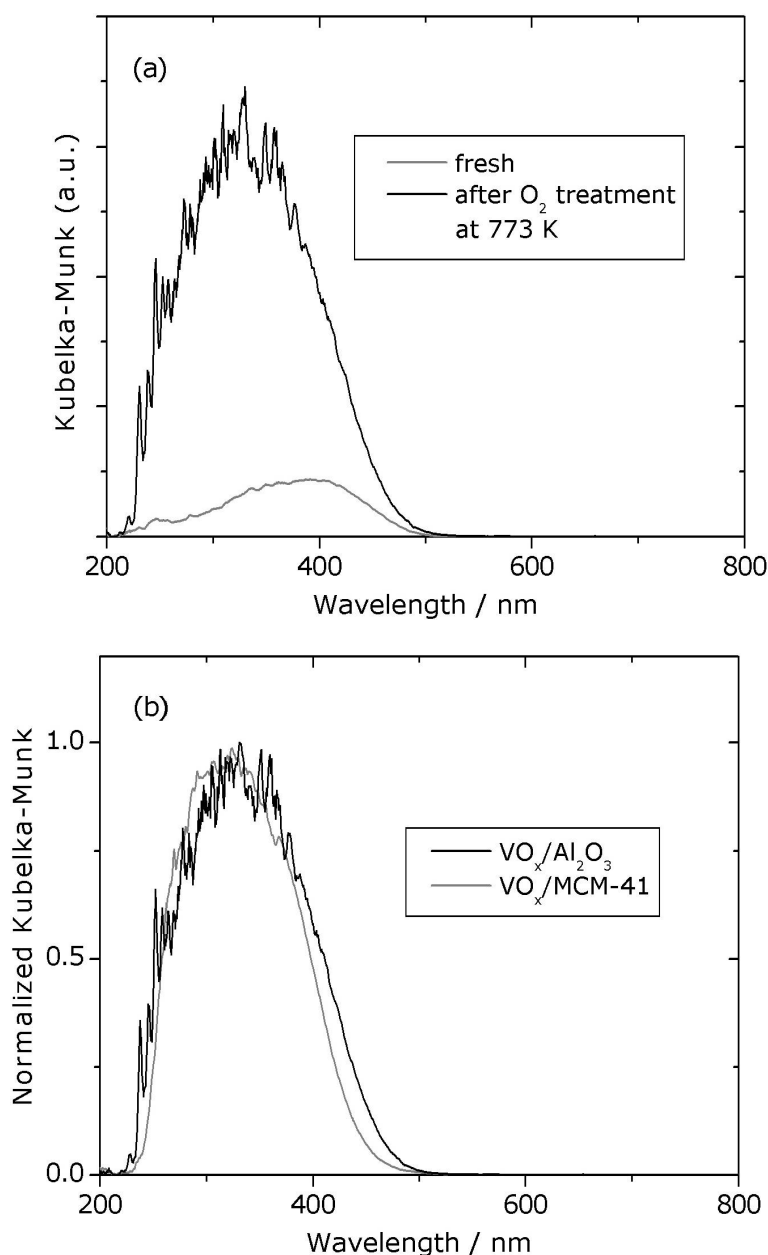


Figure 5.3 (a) UV-Vis DRS spectra of fresh and dehydrated VA-200 catalyst; (b) normalized UV-Vis DRS spectra of dehydrated VO_x (2.7 wt%)/MCM-41 and VA-200 catalysts.

To derive basic insights into the redox properties of surface VO_x species, the VA-200 material was tested by temperature programmed reduction (TPR) in a hydrogen (5% H₂ in Ar) flow. The respective concentration profiles of H₂ and formed H₂O are presented in Fig. 5.4. One peak of H₂ consumption was observed with maximum at ca. 800 K. One peak of H₂O is also observed in a somewhat higher temperature range. The presence of water indicates that H₂ is oxidized by lattice oxygen of VO_x species. In a study of Kondratenko [5.2], also only one maximum of H₂

consumption over VO_x (1 wt%)/ $\gamma\text{-Al}_2\text{O}_3$, which is similar to the VA-200 material, was detected at approx. 860 K. The discrepancy between these two studies can be related to the procedure of catalyst preparation; the VA-200 catalyst was prepared at 773 K, while the VO_x (1 wt%)/ $\gamma\text{-Al}_2\text{O}_3$ was calcined at 973 K. As shown by Steinfeldt et al. [5.20], the higher the calcination temperature, the higher the temperature of maximum of H_2 consumption. According to this previous work, it can be concluded that the VA-200 catalyst does not contain microcrystalline V_2O_5 , since no maxima of H_2 consumption were detected above 900 K.

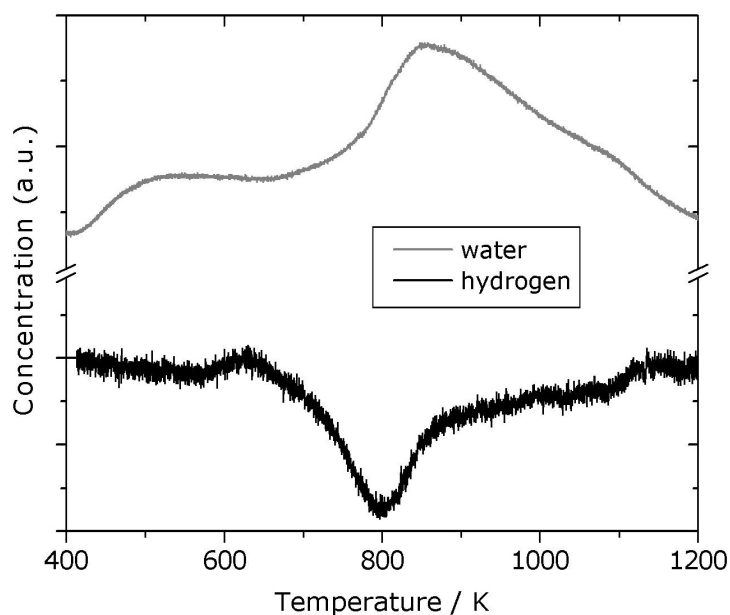


Figure 5.4 H_2 and H_2O concentration profiles during temperature-programmed reduction of oxidized VA-200 catalyst.

The quantitative evaluation of the TPR profiles in Fig. 5.4 indicates that almost all V^{+V} species were reduced to V^{+III} assuming that the VA-200 catalyst possessed V^{5+} before the TPR test. The hydrogen amount consumed during TPR was 55 ± 5 mmol. This fits well with the amount of vanadium atoms, which was 55 mmol in this experimental series. Recently an non-stoichiometric reduction during TPR of differently loaded $\text{VO}_x/\gamma\text{-Al}_2\text{O}_3$ catalysts has been reported [5.21] and referred to an incomplete oxidation of VO_x species. Although the XPS analysis indicated that the average oxidation state of the freshly oxidized VA-200 catalyst is somewhat below +V, this effect could not be observed here. In order to prove if the reduced VO_x species are reoxidized, O_2 pulse experiments were performed at 773 K after the TPR test. Only a part (ca. 40%) of reduced V^{3+} species was reoxidized to V^{+V} or V^{+IV} . The difference in the amount of lattice oxygen removed by H_2 in the temperature range of 423-1073 K and generated upon reoxidation of reduced VO_x species by O_2 at 773 K indicates that there are various VO_x species, which differ in their red-ox properties. However, the structure of VO_x species and their red-ox properties can significantly

change after TPR experiments due to the high temperature of 1073 K. V^{+III} species generated by vanadia reduction may diffuse into the alumina lattice, and hence become non-available for the reoxidation step.

For a detailed kinetic analysis of the TPR profile the reduction was performed with higher resolution, i.e. higher amount of catalyst and novel, optimized reactor set-up. In Fig. 5.5 the base-line corrected TPR profile using 450 mg VA-200 is shown, catalyst pre-treatment and TPR conditions were the same as in the previous experiment except the temperature ramp which was decreased to 8.4 K min^{-1} . For the fit of data a rate equation (Eq. 5.1) of the type

$$r_{\text{red}} = k_0 \exp\left(-\frac{E_A}{R T}\right) n_V c_{\text{H}_2} \quad (5.1)$$

was applied, where n_V is the number of freshly oxidized V atoms determined by ICP, and T is given by the temperature ramp of 8.4 K min^{-1} .

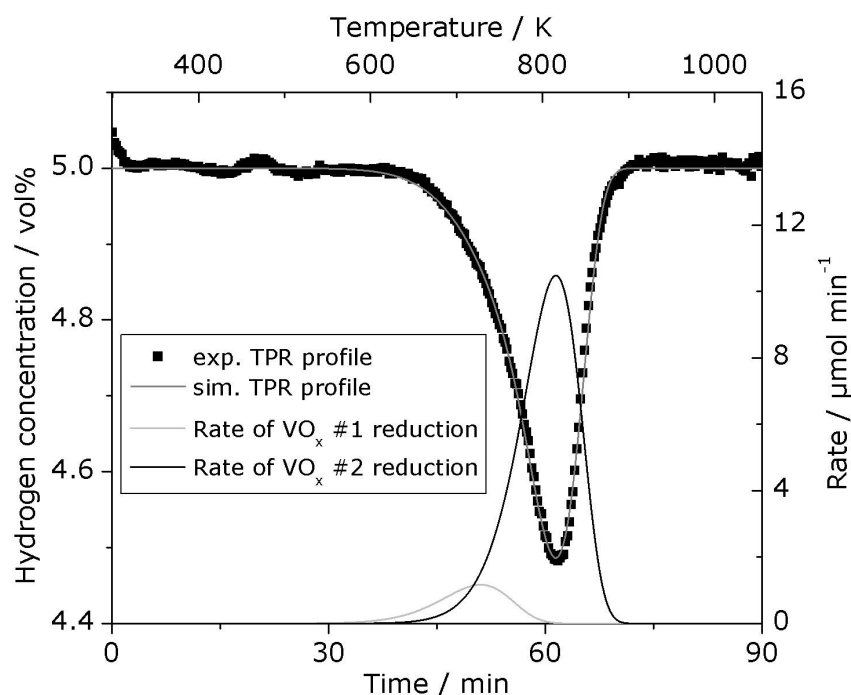


Figure 5.5 Experimental and simulated TPR profiles of $\text{VO}_x/\gamma\text{-Al}_2\text{O}_3$ catalyst VA-200, simulation of reduction rates using a 2-site kinetic model.

Due to the pronounced asymmetry of the profile a fit using this model failed. Thus, two methods have been tested to achieve a better description of the TPR data. Providing the number of V atoms in the TPR rate law (Eq. 5.1) with a reaction order between 0.3 and 0.6 can induce the observed asymmetry. Such a reaction order, however, is hardly to explain by a physico-chemical

meaning. It is more likely the fact that different types of VO_x species are present on the catalyst². These species can either differ in their degree of polymerization or be deposited on different surfaces of the $\gamma\text{-Al}_2\text{O}_3$ support. Such a 2-site model has been applied to the experimental data as shown in Fig. 5.5. The kinetic data gained from the fit of the TPR profile are listed in Tab. 5.1.

Table 5.1 Results of the kinetic evaluation of the TPR profile

	VO_x species #1	VO_x species #2
Molar fraction on VA-200	0.151	0.849
T_{max} / K	728	816
k_0 / $\text{mol m}^{-3} \text{min}^{-1}$	1.53×10^7	1.72×10^{10}
E_A / kJ mol^{-1}	121	186

Klose et al. [5.21] in their TPR study of differently loaded $\text{VO}_x/\gamma\text{-Al}_2\text{O}_3$ catalysts also observed two different temperature maxima in the similar temperature range even at low loadings. As the low-temperature reduction peak increases with the vanadia loading and inversely the high-temperature reduction peak decreases, the following assignment is derived: (i) the lower T_{max} peak (730–750 K) can be assigned to dispersed VO_x species with a high degree of polymerization, whereas (ii) the higher T_{max} peak (740–820 K) can be assigned either to monomeric vanadates or to VO_x species with a low degree of polymerization. From the detailed TPR analysis it appears that the VA-200 catalyst contains predominately highly dispersed VO_x species with a low degree of polymerization. The determined activation energies are quite high compared to the range reported by Klose et al. [5.21] (80–100 kJ mol^{-1}). Kanervo [2.22] reported a decreasing activation energy from TPR experiments with increasing vanadia content and an activation energy of 146 kJ mol^{-1} for a low loaded $\text{VO}_x/\text{Al}_2\text{O}_3$ catalyst. This confirms the assignments stated above. However, for more precise determination of T_{max} peaks and their assignment to different VO_x species, a more detailed study is required.

Finally a TEM study was performed for visualization of the collected information. The TEM and EDAX results are assembled in Fig. 5.6, the selected region is near the edge of the carbon support film (dark line in Fig. 5.6 (a)). The spectrum shown in Fig. 5.6 (b) is dominated by $\text{K}\alpha$ emission from aluminium and oxygen atoms. Vanadium atom emission is detectable very weakly, which is in agreement with the low vanadia loading of the VA-200 catalyst sample. Peaks of carbon and copper result from the sample holder (see Ch. 3.1.7). Element mapping, performed

² Two different types of V^{4+} on the VA-200 catalyst under reaction conditions have recently been identified by EPR (A. Dinse, unpublished results)

for aluminium and vanadium, is illustrated in Figs. 5.6 (c,d) and demonstrates a homogeneous distribution of vanadium on the catalyst surface on the chosen scale.

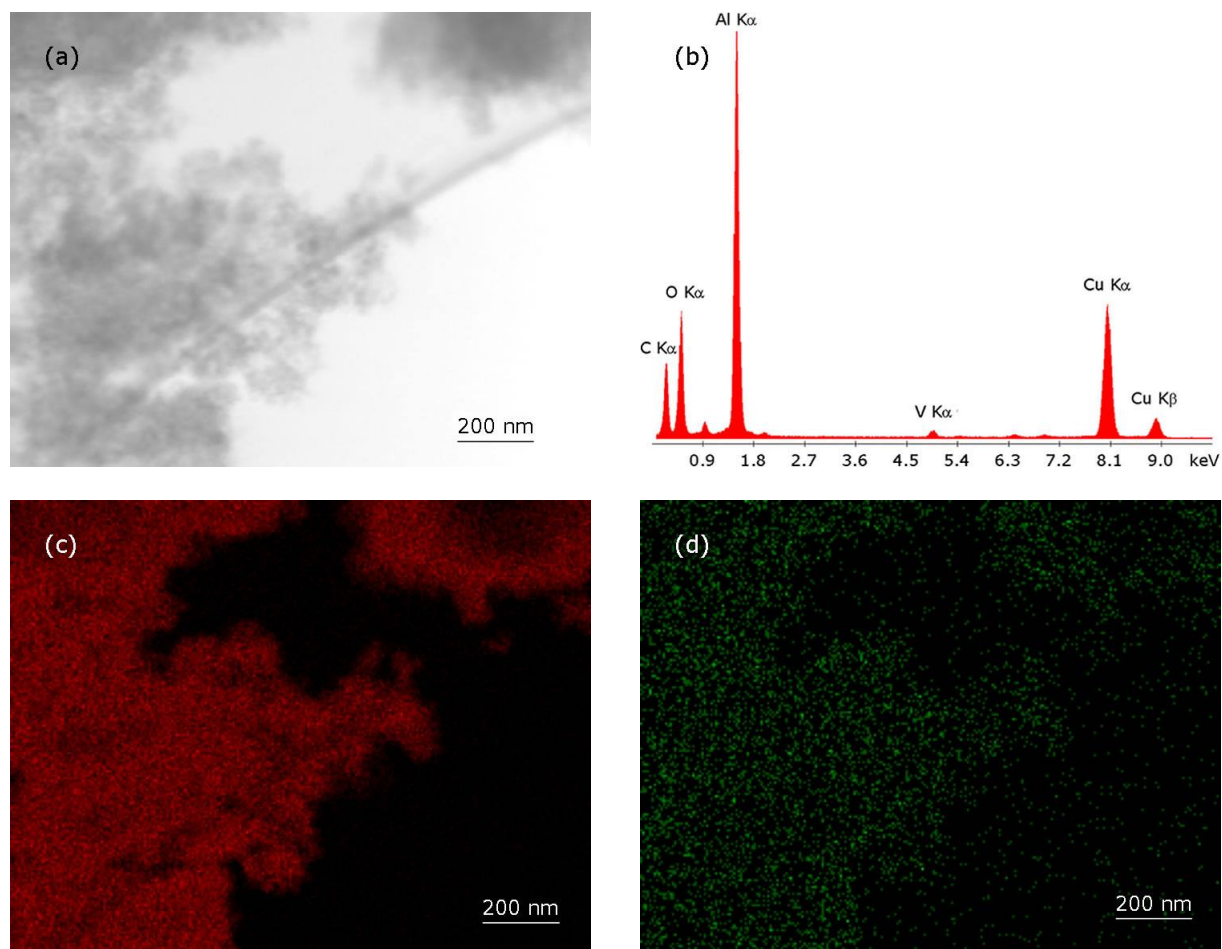


Figure 5.6 EDAX results of the TEM analysis of $\text{VO}_x/\gamma\text{-Al}_2\text{O}_3$ catalyst VA-200. (a) original TEM image, (b) corresponding EDAX spectrum, (c) and (d) element mapping of aluminium (red) and vanadium (green), respectively.

In Figs. 5.7 (a-d) the resolution of the TEM micrographs is enhanced. Different regions of the catalyst have been analyzed and the focus for EDAX is indicated with a grey circle (corresponding spectra not shown), respectively. One can see that the catalyst consists of agglomerated crystallites with a diameter in the range of 10 nm. With regard to the XRD pattern of the catalyst (Fig. 5.1 (b)), crystalline areas in these micrographs can be assigned to γ -alumina. Some measured distances between identifiable vertical layers are in agreement with the diffraction lines detected there (Bragg relation, Eq. 3.5). The signal of vanadium atoms in every analyzed TEM image is close to the detection limit as in Fig. 5.6 (b), confirming the high dispersion of vanadium also on the nanometer scale. However, one has to consider that the catalyst powder has been dispersed in chloroform during sample preparation for TEM analysis. Possibly some vanadia species have been dissolved during this process.

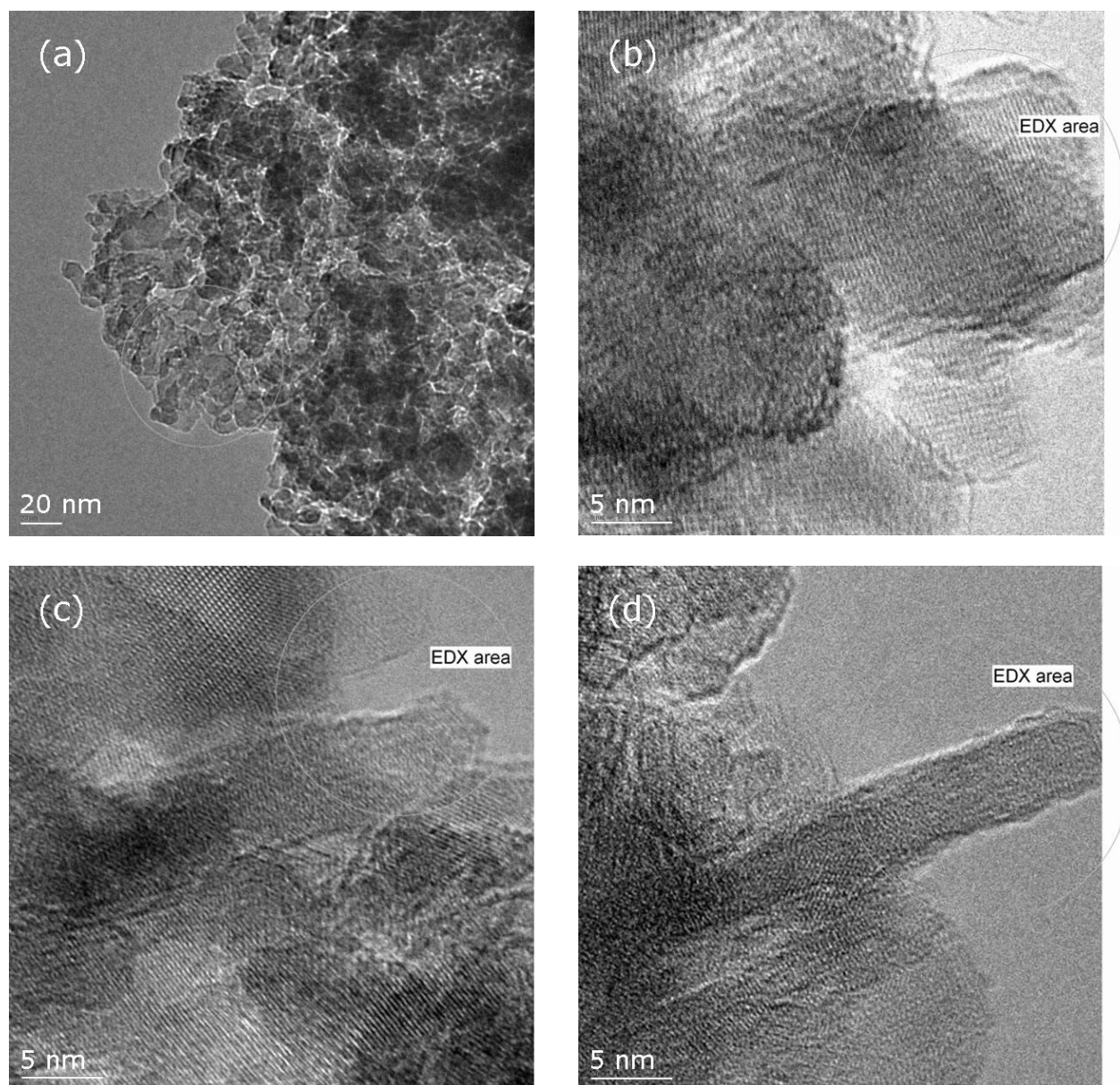


Figure 5.7 (a) Medium and (b-d) high resolution TEM images of $\text{VO}_x/\gamma\text{-Al}_2\text{O}_3$ catalyst VA-200; in (a-d) the area selected for EDAX is indicated with a grey circle.

Summarizing the results of catalyst characterization, it can be concluded that the $\text{VO}_x/\gamma\text{-Al}_2\text{O}_3$ catalyst VA-200 possesses predominantly highly dispersed VO_x species with a low degree of polymerization. These can either be isolated VO_x units or oligomeric species with up to two V-O-V bonds per V atom. However, the catalyst contains at least two different VO_x species, which either differ in their degree of polymerization or in the $\gamma\text{-Al}_2\text{O}_3$ support lattice face. All these VO_x species are redox active. The presence of trace amounts of crystalline V_2O_5 cannot be excluded.

5.2 Analysis of Mass Transport Limitation Effects

The modeling of intraparticle mass transfer limitation in the VA catalyst series by pore diffusion is described in the following chapter. Therefore an intrinsic formal kinetic model for ODP is developed, which is then used for modeling of the quartz tubular reactor as well as, in combination with mass transport by Knudsen diffusion, for modeling of intraparticle gradients indicating mass and heat transfer limitations.

5.2.1 Intrinsic Kinetics and Reactor Modeling

Experiments for kinetic modeling were performed using the catalyst VA-200 with the smallest particle size fraction of 0.1–0.3 mm. As will be shown in Ch. 5.2.2, this is an essential requirement to avoid mass transport limitation of the reaction rate. Propane conversion and propene selectivity were measured at temperatures of 673, 723, and 773 K with a catalyst amount of 600, 110, and 50 mg, respectively. In order to achieve different degrees of propane conversion, the total gas flow was varied between 30 and 240 ml_n min⁻¹. The resulting selectivity-conversion relationships are shown in Fig. 5.8 (a) together with the Arrhenius plot (b) from initial conversions measured with the highest flow rate of 240 ml_n min⁻¹.

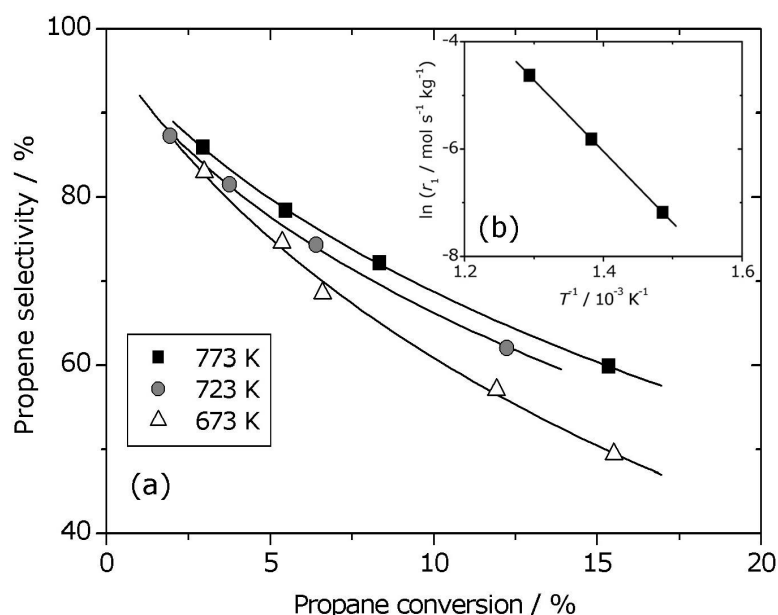
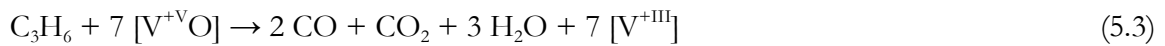
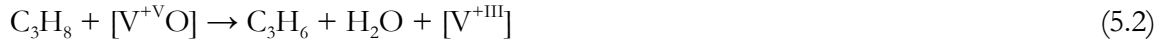


Figure 5.8 (a) Propene selectivity as a function of propane conversion over catalyst VA-200; $\text{C}_3\text{H}_8/\text{O}_2/\text{N}_2 = 29.1/14.5/56.4$ and a total gas flow of 30–240 ml_n min⁻¹; (b) Arrhenius plot from initial rates of the ODP reaction, i.e. lowest conversion data from (a).

For all temperatures, propene selectivity decreases with an increase in propane conversion. This is due to a consecutive C_3H_6 oxidation to CO and CO_2 . The ratio of CO/ CO_2 was found to be

1.8–2 and independent on temperature and degree of propane conversion. Increasing temperature results in increased propene selectivity at similar degrees of propane conversion. This positive influence of temperature on propene selectivity is in agreement with previously reported results of the oxidative dehydrogenation of propane (ODP) over alumina-supported vanadia catalysts [5.23] and over a mixed vanadium-containing alumina-supported catalyst [5.24].

The catalyst VA-200 shows a high selectivity towards propene compared to samples prepared by a conventional incipient wetness impregnation method [5.25] in the same vanadia concentration range. This may indicate a difference in the vanadia distribution on the support due to the preparation method on the one hand or be related to the high porosity of the catalyst support of about 0.7 on the other hand, which allows efficient mass transport by diffusion. Since the kinetic modeling presented here is required only to estimate the influence of mass and heat transport on the ODP reaction, a simplified power-law type kinetic model is applied, which contains no mechanistic information. The following simplifications concerning the reaction network in Eqs. 2.41–2.47 were made: (i) direct (not via consecutive propene oxidation) propane conversion to CO_x can be neglected, since near 100% propene selectivity at near zero propane conversion is expected from the selectivity–conversion relationships in Fig. 5.8; (ii) secondary oxidation of CO to CO_2 does not play any significant role, because the ratio of CO and CO_2 does not depend on the propane conversion. Taking the above simplifications into account the reaction network required for a sufficient fit simplifies to Eqs. 5.2–5.4:



with the following rate laws for the oxidative dehydrogenation of propane (Eq. 5.5) and consecutive propene combustion (Eq. 5.6):

$$r_1 = k_{0,1} \exp\left(-\frac{E_{A,1}}{R T}\right) c_{\text{C}_3\text{H}_8}^{m_1} c_{\text{O}_2}^{m_2} \quad (5.5)$$

$$r_2 = k_{0,2} \exp\left(-\frac{E_{A,2}}{R T}\right) c_{\text{C}_3\text{H}_6}^{m_3} c_{\text{O}_2}^{m_4} \quad (5.6)$$

The parameters to be determined reduce to two preexponential factors k_0 , two apparent activation energies E_A and four reaction orders m_i . The apparent activation energy of the ODP reaction can be calculated from the lowest conversions given in Fig. 5.8 (a), the value for propene combustion was measured in a somewhat lower temperature range of 633–678 K due to higher reaction rates. In case of gradientless reaction conditions for VA-200 up to 773 K (as will be shown in Ch. 5.2.2), this value can be adopted to the higher temperature range. Due to the enormous exothermicity of propene deep oxidation, the conversion of this reaction has to be adjusted at

very low values ($< 3\%$) in order to exclude falsification of the initial rate data by temperature arise along the catalyst bed. The Arrhenius plot then shows linear correlations of $\ln(r_2)$ versus T^{-1} with excellent accuracy. The preexponential factors were not taken from this plot because the intercept contains also the concentration terms of the rate equations Eqs. 5.5 and 5.6. The reaction orders were determined by varying the concentration of one reactant while keeping the other one constant at a temperature of 673 K. The composition ranges of $C_3H_8/O_2/N_2$ in vol% for the ODP reaction were varied between 40/2–40/balance and 20–60/20/balance, respectively. For propene combustion the following compositions of $C_3H_6/O_2/N_2$ in vol% were applied: 20–50/20/balance and 40/2–20/balance with a total gas flow of $100 \text{ ml}_n \text{ min}^{-1}$ in each of the four experimental series. The reaction order of component j in reaction i is then given by the slope of $\ln(r_i)$ versus $\ln(c_j)$ where j is the component which was varied in its concentration. However, although the results of the ODP reaction could be linearized in a sufficient manner, the accuracy of the propene combustion reaction orders suffered probably from the high reaction exothermicity, which caused relatively high error bars on the measured conversions and thereby on m_3 and m_4 . The resulting apparent activation energies and reaction orders are listed in Tab. 5.2.

Table 5.2 Kinetic parameters determined for the ODP reaction and propene combustion

Propene formation	$k_{0,1}$	$E_{A,1}$	m_1	m_2
	$1.97 \times 10^5 \frac{\text{mol}^{0.25}}{\text{m}^{-2.25} \text{ s kg}}$	111 kJ mol^{-1}	0.65 ± 0.01	0.1 ± 0.002
Propene combustion	$k_{0,2}$	$E_{A,2}$	m_3	m_4
	$9.43 \times 10^4 \frac{\text{mol}^{-0.70}}{\text{m}^{-5.10} \text{ s kg}}$	102 kJ mol^{-1}	0.7 ± 0.2	1.0 ± 0.2

It can be seen that the apparent activation energy of the ODP reaction is slightly higher than that of propene combustion. This may be related to the stronger C-H bond in the propane molecule than in the propene molecule. The absolute values of $E_{A,i}$ as well as their difference $E_{A,1} - E_{A,2}$ are dependent on the vanadia content and are in moderate agreement with comparable literature data [5.23]. Based on the positive difference of $E_{A,1} - E_{A,2}$, an increase of propene selectivity with temperature can be expected and was experimentally observed (Fig. 5.8 (a)).

For both, the ODP reaction and propene combustion, the reaction order with respect to propane and propene partial pressures is close to one. However, the reaction orders with respect to oxygen partial pressure are close to zero and to one for propane and propene oxidation, respectively. The reaction orders are in general comparable to another study [5.26], although this presented kinetic model could not reflect our measurements. A reason for the higher reaction order

of oxygen in the propene combustion relative to the ODP reaction may be the higher overall reaction rate of propene combustion. This enhances the impact of catalyst reoxidation, based on the assumption that the rate of this elementary reaction step is independent from the reducing agent. Against that, the ODP reaction is relatively slow and the reoxidation rate seems to be nearly negligible in the overall reaction rate, expressed in a reaction order of nearly zero. The last missing parameters, the preexponential factors, were not calculated from the Arrhenius plot, due to the relatively high inaccuracy of the reaction orders especially of the propene combustion. The resulting error in k_0 would be enhanced due to the exponential character of the Arrhenius plot, so these values were determined by the integral fit described in the following.

The U-shaped quartz reactor used in this study was modeled as ideal plug-flow tubular reactor (PFTR), which means that axial dispersion as well as radial temperature and concentration gradients were not taken into account. However, the calculated Bodenstein numbers in the range of 20–50 and Reynolds numbers in the range of 1–3 for this experimental study indicate the presence of residual backmixing effects and parabolic velocity profiles. Their influence on the measured reaction rate was estimated to be low and thereby was neglected in order to greatly simplify the kinetic evaluation. A narrow residence time distribution of the applied reactor set-up was tested and confirmed by independent tracer step marking before catalytic experiments (see Ch. 5.4).

Furthermore, the reaction mixture was set constant in volume, although the mole number of the reaction increases slightly with the conversion and so does the gas volume. This simplification is of no consequence because of the dilution of the reaction mixture with inert nitrogen, which weakens this effect. The following balances (Eqs. 5.7–5.10) were used for the one-dimensional modeling of the experimental data presented in Fig. 5.8 (a):

$$\frac{d}{dt} c_{\text{C}_3\text{H}_8} = -r_1 \quad (5.7)$$

$$\frac{d}{dt} c_{\text{C}_3\text{H}_6} = r_1 - r_2 \quad (5.8)$$

$$\frac{d}{dt} c_{\text{O}_2} = -0.5 r_1 - 3.5 r_2 \quad (5.9)$$

$$\frac{d}{dt} T = \frac{r_1 \Delta_R H_1 + r_2 \Delta_R H_2}{c_0 \bar{c}_p} - (T - T_w) \frac{k_w A_w}{V_R c_0 \bar{c}_p} \quad (5.10)$$

where $\Delta_R H_1 = 120 \text{ kJ mol}^{-1}$ and $\Delta_R H_2 = 1360 \text{ kJ mol}^{-1}$ are the enthalpies of reactions r_1 and r_2 , respectively, c_0 the total gas concentration with the medium heat capacity \bar{c}_p , estimated from literature data [5.27], and T_w is the temperature of the fluidized sand bed. The ratio of the heat transfer area A_w and the reactor volume V_R is given by the reactors dimensions and equal to $2/r_R$

for cylindrical geometry. k_w is the overall heat transfer coefficient of the quartz wall of the reactor. The estimated value of $k_w = 3.4 \text{ W m}^{-2} \text{ K}^{-1}$, given by the experimental set-up and mainly limited by the inner convection heat transfer coefficient h of the reactor wall due to laminar flow conditions [5.27], allows a fit of concentration and temperature profiles in an excellent quality. Using these equations, the preexponential factors of rates Eqs. 5.5 and 5.6 were determined as given in Tab. 5.2. The axial temperature and concentration profiles of the reactor are illustrated in Fig. 5.9 exemplarily for $T = 773 \text{ K}$.

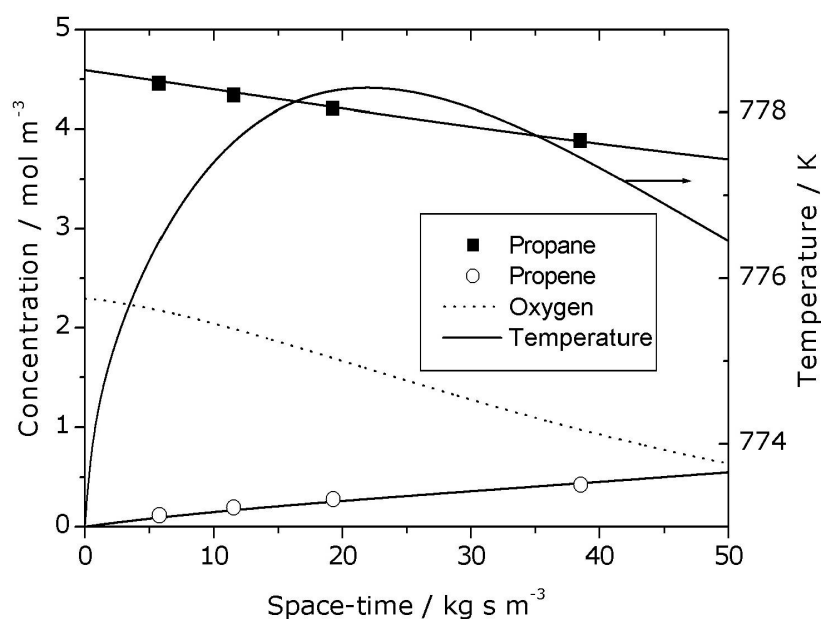


Figure 5.9 Temperature and concentration profiles of C_3H_8 , C_3H_6 and O_2 during the ODP reaction over VA-200 using conventional quartz reactors; $\text{C}_3\text{H}_8/\text{O}_2/\text{N}_2 = 29.1/14.5/56.4$, $T_{\text{in}} = 773 \text{ K}$ and a total gas flow of $30\text{--}200 \text{ ml}_n \text{ min}^{-1}$.

As can be seen from the fit there are no remarkable hotspots in the reactor during this experiment. The absence of relevant temperature gradients may be referred to the low activity of the catalyst VA-200 and the dilution of the catalyst particles with inert quartz particles. The temperature maxima increase to values of 0.4, 1.1, and 5.3 K above the temperature of the fluidized sand bed in the experimental series conducted at 673, 723, and 773 K, which indicates an efficient heat transfer. The more pronounced maxima at higher temperatures are the result of the local heat production due to higher catalyst activity. Measurements with the reactor equipped with a centred thermocouple resulted in temperature peaks of 3 K in a diluted 50 mg catalyst bed at 773 K. At both of the lower reaction temperatures no temperature increase was detectable. This is in good agreement with the model, confirming the assumption of a moderate and controllable heat production in this system.

5.2.2 Modeling of Mass and Heat Transport Effects

Mass transport effects are one of the most important error sources in a kinetic analysis of fast reactions and therefore have to be excluded before beginning a detailed investigation of reaction networks and microkinetics. Further microkinetic investigations of the ODP reaction are planned to be performed in a Bertly-type reactor. Since its gas-phase mixing quality is amongst others strongly dependent on the catalyst particle size, it is very essential to prove whether the ODP reaction is influenced by the size of catalyst particles. To this end, we studied the ODP reaction over differently sized $\text{VO}_x/\gamma\text{-Al}_2\text{O}_3$ samples (VA-200, VA-450, VA-800, VA-1250, and VA-2000) in the temperature range of 673–773 K. Fig. 5.10 illustrates the selectivity–conversion relationships obtained at 673, 723, and 773 K over these samples. Not depending on the size of catalyst particles propene selectivity decreases with an increase in the degree of propane conversion. However, the size of catalyst particles strongly influences the propene selectivity. The larger the particle size, the lower the propene selectivity. Moreover, the difference between differently sized catalyst particles in propene selectivity at a certain contact time depends on reaction temperature and increases with an increase in temperature. The observed effects of the particle size on the propene selectivity are explained by mass transport limitations inside of larger particles. The reaction product is accumulated inside of larger particles due to a longer path for pore diffusion, which causes an acceleration of consecutive reactions [5.28]. Since propene combustion is faster than the ODP reaction, this effect occurs at noticeably smaller particle sizes than the observation of mass transport effects on the ODP reaction. The influence of mass transport limitations on propene selectivity decreases with falling temperature, because the rate of chemical reaction depends stronger on temperature than diffusion inside catalyst particles. Thus, in opposition to the tendency for nearly intrinsic kinetics as shown in Fig. 5.8 (a), the selectivity then decreases with increasing temperature in case of mass transfer resistances.

Besides the effect on the overall propene selectivity, the initial (at near zero propane conversion) propene selectivity is also strongly influenced in the presence of diffusion limitations. It decreases significantly upon increasing size of catalyst particles. Compared to VA-200, where the intercept is near 100% propene selectivity, this pretends a change in the reaction network and a parallel combustion pathway of propane. This effect may be explained by the accumulation of propene inside the catalyst pores and thereby an enhanced consecutive propene combustion. The material balance at the particle surface then also contains a particle flux of CO_x leaving the particle even at differential propane conversion, which macroscopically may be misinterpreted as direct propane combustion. It should also be mentioned that the degree of propane conversion decreases with increasing particle diameter for a constant residence time. Reduced ODP reaction rates are the common effect of mass transport limitation.

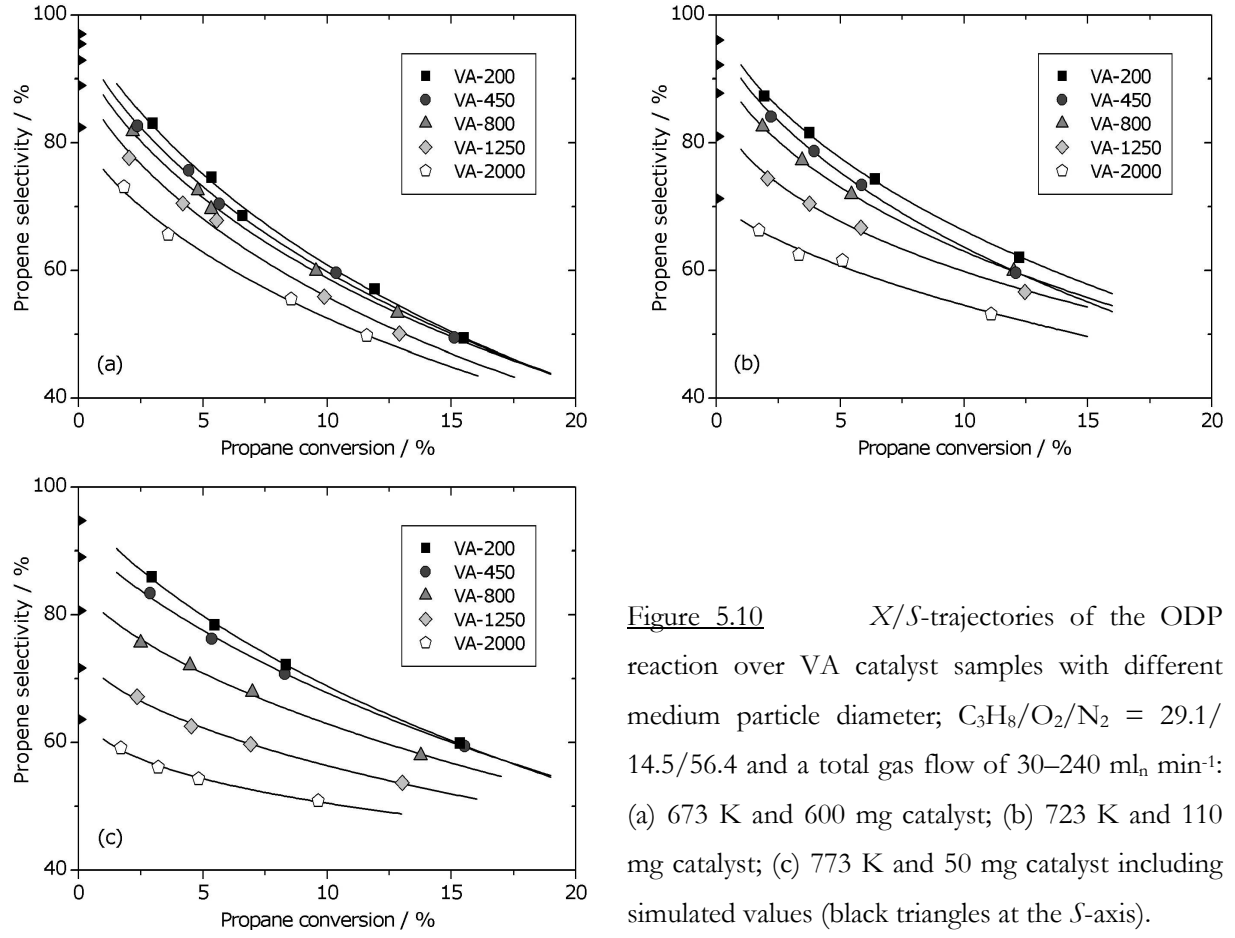


Figure 5.10 X/S -trajectories of the ODP reaction over VA catalyst samples with different medium particle diameter; $C_3H_8/O_2/N_2 = 29.1/14.5/56.4$ and a total gas flow of $30\text{--}240\text{ ml}_n\text{ min}^{-1}$: (a) 673 K and 600 mg catalyst; (b) 723 K and 110 mg catalyst; (c) 773 K and 50 mg catalyst including simulated values (black triangles at the S -axis).

In order to further analyze the effect of mass transport limitations on the ODP reaction, the interior balances for the catalyst particles were solved. The following conditions were assumed: (i) spherical geometry; (ii) gradients in the center of the particles are zero (symmetry criterion); (iii) reactant concentrations and temperature at the surface are equal to gas phase concentrations and temperature, respectively. The latter means no outer mass transport limitation, which is provided by high gas flow rates at differential conversion (Maers criterion). Balances Eqs. 5.11–5.14 were used for the intraparticle gradient simulation:

$$\frac{d^2}{dR^2} c_{C_3H_8} + \frac{2}{R} \frac{d}{dR} c_{C_3H_8} = \frac{\rho_{cat}}{D_{K,C_3H_8}} r_1 \quad (5.11)$$

$$\frac{d^2}{dR^2} c_{C_3H_6} + \frac{2}{R} \frac{d}{dR} c_{C_3H_6} = \frac{\rho_{cat}}{D_{K,C_3H_6}} (-r_1 + r_2) \quad (5.12)$$

$$\frac{d^2}{dR^2} c_{O_2} + \frac{2}{R} \frac{d}{dR} c_{O_2} = \frac{\rho_{cat}}{D_{K,O_2}} (0.5 r_1 + 3.5 r_2) \quad (5.13)$$

$$\frac{d^2}{dR^2} T + \frac{2}{R} \frac{d}{dR} T = \frac{\rho_{cat}}{\lambda_{eff}} (r_1 \Delta_R H_1 + r_2 \Delta_R H_2) \quad (5.14)$$

where R is the particle radius, ρ_{cat} the catalyst density, $D_{K,i}$ the Knudsen diffusivity Eq. 5.15 and λ^{eff} the effective heat conductivity of porous γ -alumina, estimated with $0.2 \text{ W m}^{-1} \text{ K}^{-1}$:

$$D_{K,i} = \frac{\varepsilon}{\tau} \frac{d_p}{3} \sqrt{\frac{8RT}{\pi M_i}} \quad (5.15)$$

where ε and τ are the catalysts porosity and tortuosity, d_p the pore diameter and M_i the molar mass of component i . A typical value of 3.5 was taken for the tortuosity, whereas porosity and pore diameter were determined by BET experiments. The resulting gradients for VA-2000 at 773 K are exemplarily shown in Fig. 5.11.

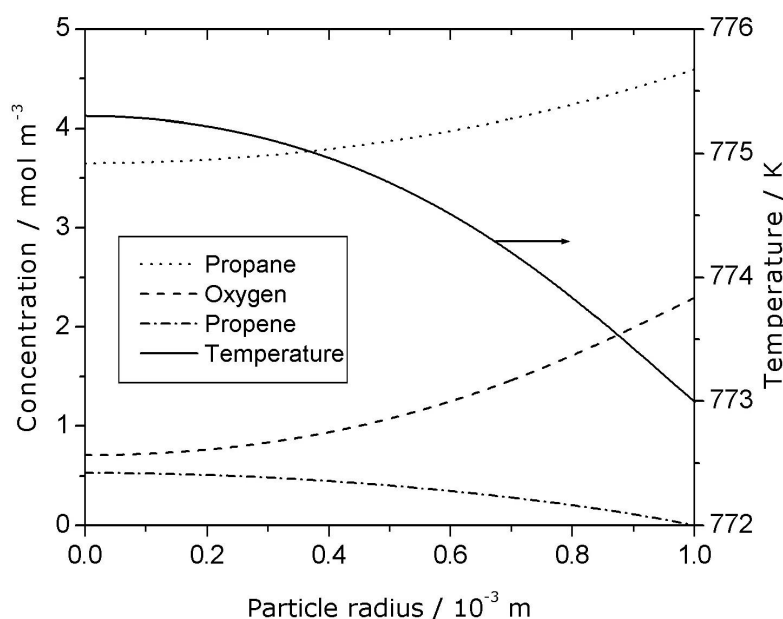


Figure 5.11 Intraparticle concentration and temperature profiles simulated for a VA-2000 catalyst particle; initial reaction conditions: $\text{C}_3\text{H}_8/\text{O}_2/\text{N}_2 = 29.1/14.5/56.4$, $T = 773 \text{ K}$.

This figure nicely illustrates that the lowest concentration of propane and oxygen is expected in the middle of the particle. It increases with a decrease in the distance to the outer surface of the catalyst particle. The profile of propene concentration shows an inversed trend as compared to propane and oxygen; i.e. the lowest propene concentration is expected at the outer surface of the catalyst particle. The concentration gradients become smaller when the size of catalyst particles decreases as exemplified in Fig. 5.12 (a) for O_2 concentration.

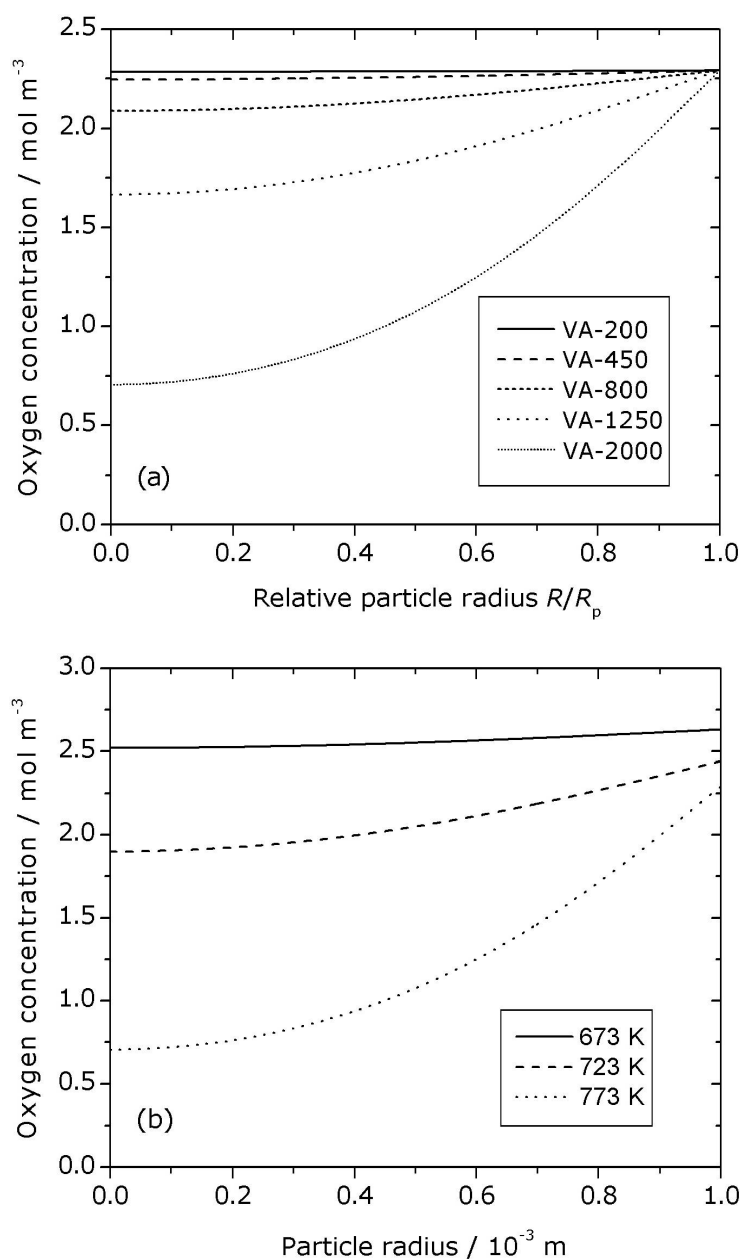


Figure 12 Simulated intraparticle gradients of the oxygen concentration: (a) for different particle diameters at 773 K; (b) for different temperatures using VA-2000; $C_3H_8/O_2/N_2 = 29.1/14.5/56.4$, initial reaction conditions.

This observation is due to an enhanced diffusion through the particle upon decreasing particle size. The smallest gradient were calculated for particles of 0.1–0.3 and 0.3–0.6 mm. This is in good correspondence to our experimental observations in Fig. 5.10. The measured propene selectivities over these two catalyst fractions were very similar in a broad range of propane conversions. Upon further increase in the size of catalyst particles, propene selectivity decreases (Fig. 5.10) and concentration gradient inside the catalyst particles significantly increases (Fig. 5.12 (a)). The effects of temperature on intraparticle gradients of reaction components were also calculated for the largest catalyst particles (1.5–2.5 mm). Fig. 5.12 (b) exemplifies O_2 concentra-

tion profiles. It can be seen that the highest gradients were calculated at 773 K. They decrease upon decreasing reaction temperature. The difference between large and small catalyst particles in propene selectivity decreases in a similar manner. This is due to the fact the reaction rate decreases stronger with temperature than the diffusion. Therefore, the influence of mass transport on the ODP reaction decreases and the kinetic regime is reached at gradientless conditions.

Besides the visualization of intraparticle gradients, more information can be extracted from the modeling. The initial propene selectivity S is given by the ratio of the propene and propane concentration gradients at the catalyst particle surface (Eq. 5.16):

$$S = - \frac{\frac{d}{dR} c_{C_3H_6} \big|_{R=R_p}}{\frac{d}{dR} c_{C_3H_8} \big|_{R=R_p}} \quad (5.16)$$

where R_p is the radius of the catalyst particles. The selectivities determined for VA-2000 at 673 and 723 K as well as for the whole VA-series at 773 K are assembled in Tab. 5.3. The predicted selectivities are in excellent agreement with the extrapolated values from Fig. 5.10, which are in the range of about 60–100%.

Table 5.3 Initial selectivities of the ODP reaction over the VO_x/Al_2O_3 catalyst, simulated (S_{sim}) with the spherical particle model and estimated (S_{est}) from extrapolation of experimental data given in Fig. 5.10 to zero propane conversion.

Sample	VA-2000	VA-2000	VA-2000	VA-1250	VA-800	VA-450	VA-200
T / K	673	723	773	773	773	773	773
S_{sim} / %	82.4	71.3	63.6	71.7	80.7	89.1	94.7
S_{est} / %	80	70	63	73	82	92	96

Summarizing, a manifold impact of mass transport limitation on activity, selectivity and the apparent reaction network could be identified in the present study. This conclusion is of high importance for deriving intrinsic kinetics of the ODP reaction and generally indicates the tremendous impact of this falsifying factor in kinetic studies.

5.3 TAP Study

The reaction pathways of the formation of C_3H_6 , CO, and CO_2 in the oxidative dehydrogenation of propane (ODP) have been investigated by means of the temporal analysis of products (TAP) technique. The interactions of C_3H_8 , C_3H_6 , CO, and O_2 with the catalyst VA-200 were investigated in the temperature range of 723–823 K by performing single and sequential pulse experi-

ments. A sorption study of CO and CO₂ in the somewhat lower temperature range of 573–773 K was also part of the experimental program. The range of monitored AMUs (atomic mass units) provided the detection of C₃H₈, C₃H₆, H₂CO (formaldehyde), CO₂, CO, H₂O, O₂, Xe, and Ne. Each AMU was assigned to a specific component and corrected for contributing parts of other components having fragments with the same AMU. The presented spectra show typical TAP response curves with a fast increase in concentration up to a temporal maximum followed by a relatively slow decay. In order to allow better comparison of signal shape and delay, the signals are displayed intensity-normalized. The ratio of the AMU signal areas from the integration of the original signal A_i prior to normalization is also displayed in each figure. These values, normalized relative to ¹³²Xe, allow for the calculation of conversion and selectivities.

5.3.1 Single Pulse Experiments

The oxidation of C₃H₈, C₃H₆, and CO on the catalyst surface was investigated by means of single pulse experiments. Since gas phase oxygen was not present in the pulses, it can be concluded that all of the reaction products were formed by interaction with lattice oxygen of the VO_x species. This is in agreement with the Mars-van Krevelen reaction mechanism. From Fig. 5.13 (a) it can be seen that pulsing of C₃H₈ results in the formation of C₃H₆, whereas neither CO and CO₂ nor H₂O could be detected. At 773 K the activity appears to be still too low for quantification of the C₃H₈ conversion. This is indicated by the high signal-to-noise ratio of the C₃H₆ response, which is clearly identified by the shift towards a longer residence time due to the surface reaction. The absence of CO and CO₂ is in accordance with the high selectivity determined under ambient conditions as well as with the simplified reaction scheme proposed in Ch. 5.2.2, where a parallel deep oxidation of propane was found to not occur.

In order to further investigate the origin of CO_x formation, C₃H₆ pulsing was performed over VA-200 (Fig. 5.13 (b)). A C₃H₆ conversion of about 60% at 773 K agrees well with the higher reactivity of propene in comparison to propane, which was also derived from the formal kinetic study in Ch. 5.2.2. The reaction products are CO and CO₂ in a close to equimolar ratio, whereas H₂CO and water could not be detected. As shown in the sorption study (Ch. 5.3.3) the extremely long tailing of the CO_x responses is not due to sorption processes on the acidic γ -alumina surface, but must have its origin in a relatively slow transformation of strongly adsorbing intermediates. This can be partly explained by the low loading and high dispersion of VO_x species on the catalyst surface. Reactive intermediates have to be relatively mobile to "collect" enough oxygen atoms for total oxidation since isolated VO₄ deposits just provide for one oxygen atom. Most of the potential intermediates from propene to CO_x usually contain at least one functional

group. A strong interaction with the acidic γ -alumina surface is thereby a plausible reason for their relatively low mobility and the resulting slow release of CO_x .

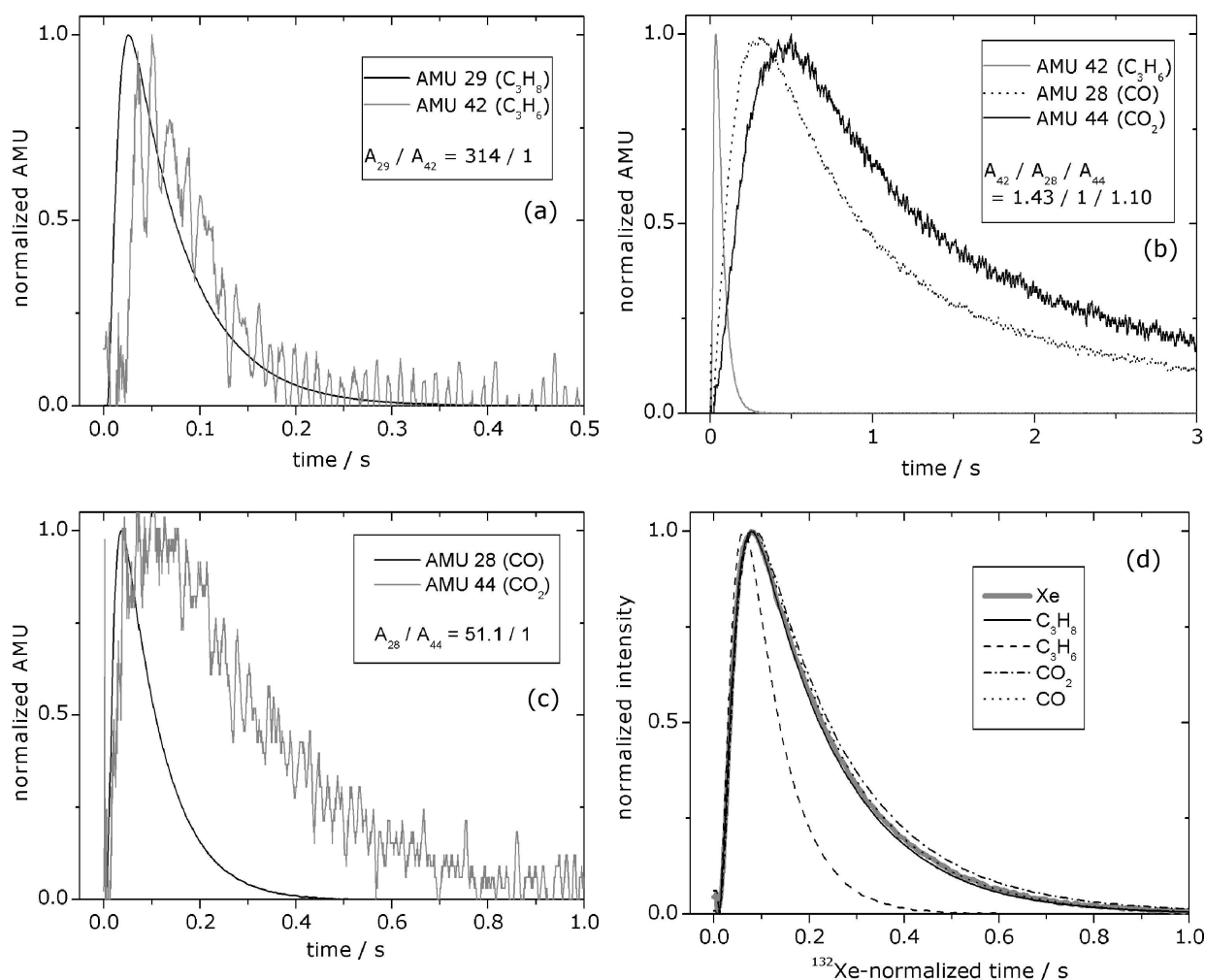


Figure 5.13 Intensity-normalized transient responses to (a) C_3H_8 , (b) C_3H_6 , and (c) CO pulsing over catalyst VA-200 at 773 K; (d) comparison of intensity- and time-normalized reactant responses with ^{132}Xe signal.

This explanation is in agreement with a result of Kondratenko et al [5.29] (Fig. 5.14) who performed C_3H_6 pulsing over a much higher loaded $\text{VO}_x(9.5 \text{ wt}\%)/\gamma\text{-Al}_2\text{O}_3$ catalyst. Although the reaction temperature is somewhat higher than in the experiments of this study (which may also explain higher H_2CO yields) the time-scale of CO_x responses is one order of magnitude smaller. As Kondratenko et al. identified crystalline V_2O_5 on the surface of this catalyst, time-delay of CO_x responses to propene pulsing may be regarded as a kind of indicator for the molecular dispersion of VO_x species on the catalyst surface.

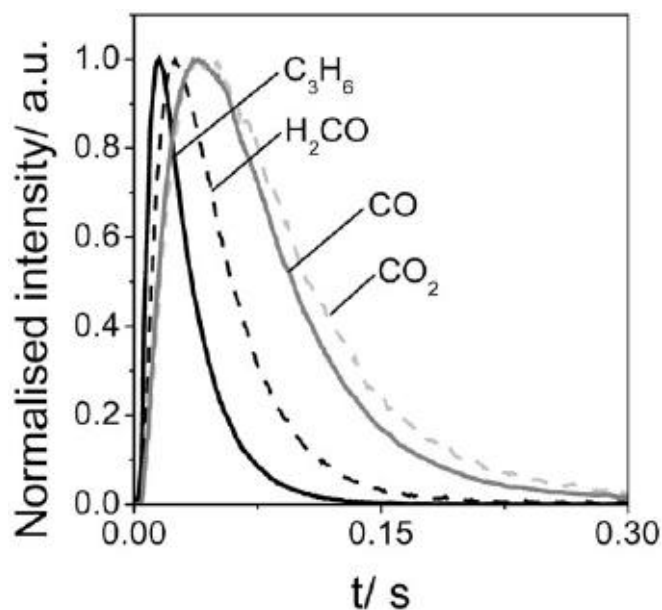


Figure 5.14 Transient responses to pulsing of C_3H_6 over $VO_x(9.5 \text{ wt}\%)/\gamma\text{-Al}_2O_3$ at 848 K [5.29].

Additionally, the yield of CO_x is only about one third of the converted C_3H_6 , which indicates that a certain amount of intermediates and products remains adsorbed irreversibly on the acidic surface. It is assumed that for the same reason water has never been detected in any of the experiments in this TAP study [5.30]. Different temporal maxima of the CO and CO_2 responses are only partly due to different diffusivities of these components. Also on time-normalized scale the CO response is slightly earlier compared to the CO_2 signal. This can indicate either a slower reaction pathway towards CO_2 or a contribution of a consecutive CO oxidation. A third reason could be a weak interaction of CO_2 with the catalyst surface via reversible sorption processes. C_3H_6 pulsing has been investigated at 723, 748, and 773 K, the CO and CO_2 yields are displayed in an Arrhenius plot (Fig. 5.15). Although C_3H_6 conversion was at about 60% at the highest temperature, the results may be used to estimate the activation energy.

The transient response to CO pulsing is displayed in Fig. 5.13 (c). It can be seen that close to 2% of the CO has been oxidized which is a higher conversion than in the C_3H_8 pulsing experiments. This is in contradiction to the formal kinetic study, where the CO oxidation was found to be negligible. The long delay of the CO_2 signal is due to the lower diffusivity and reduces drastically in the time-normalized scale. However, the remaining delay identifies CO_2 as a reaction product. CO pulsing has been investigated at 773, 798, and 823 K, the CO_2 yields are displayed in an Arrhenius plot (Fig. 5.15).

In order to identify reversible sorption processes of the investigated and detected components with the catalyst surface, the pulsing signals of C_3H_8 , C_3H_6 , CO_2 , and CO have been time-normalized and compared to the Xe response (Fig. 5.13 (d)). As can be seen, the responses of Xe,

C_3H_8 and CO are close to congruent which proves the absence of perturbing interactions at 773 K for these components. For C_3H_6 this comparison fails due to the high conversion at this temperature. For CO_2 the presence of sorption processes cannot be excluded, but their influence is rather weak. Dewaele and Froment in their sorption study of CO and CO_2 on γ -alumina [5.31] also found a stronger interaction of CO_2 with the surface. A more detailed investigation is presented in Ch. 5.3.3.

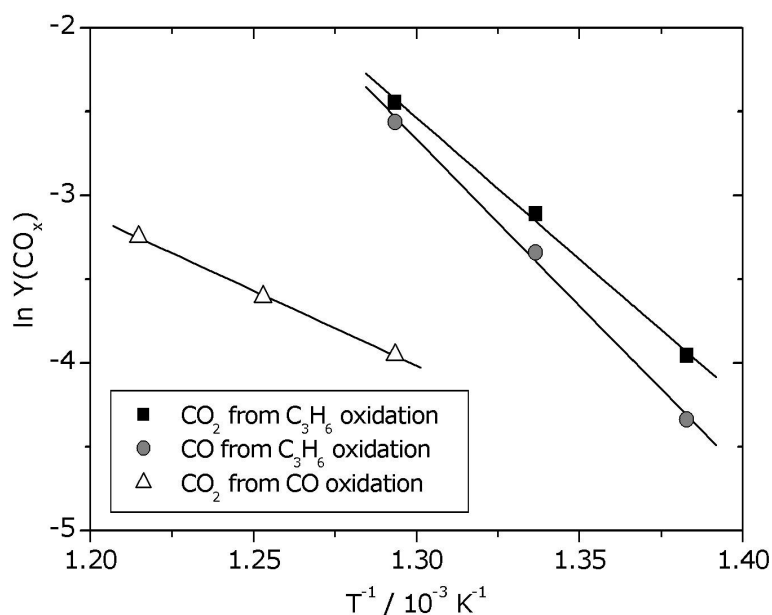


Figure 5.15 Arrhenius plot for CO and CO_2 yields from propene pulsing at 723–773 K and for CO_2 yield from CO pulsing from 773–823 K over catalyst VA-200.

From the Arrhenius plot of CO_x yields (Fig. 5.15) the activation energies of product formation can be determined (Tab. 5.4).

Table 5.4 Activation energies of CO_x formation from CO and C_3H_6 pulsing experiments over catalyst VA-200.

Formation of ...	Activation energy E_A / kJ mol^{-1}
... CO from C_3H_6 oxidation	165.5
... CO_2 from C_3H_6 oxidation	140.4
... CO_2 from CO oxidation	74.6

Activation energies determined from TAP experiments are drastically higher than those values determined under ambient conditions. The barrier of CO_x formation from C_3H_6 is about 50 kJ mol^{-1} higher than the value determined in Ch. 5.2 (102 kJ mol^{-1}), whereas the CO oxidation has an about 15 kJ mol^{-1} higher activation energy compared to the reaction under ambient

conditions (60 kJ mol^{-1} , B. Frank, unpublished results). This is a typical phenomenon for reactions under high-vacuum conditions. The absence of gas phase species and their collisions with adsorbed molecules and reaction intermediates lead to a stabilization of the latter. This missing energy uptake from these interactions results in higher activation energies. The high propene conversion of about 60% in the respective pulsing experiments at 773 K may explain the non-linearity and the slightly lower CO_x yield. The true activation energy is supposed to be about 10 kJ mol^{-1} higher than the fitted values from Tab. 5.4.

5.3.2 Sequential Pulsing Experiments

In order to investigate the role of adsorbed oxygen species in the ODP, sequential pulsing of $^{18}\text{O}_2$ followed by C_3H_8 or C_3H_6 was performed at 773 K. The time-delay of 0.5 s was adjusted to assure the removal of gas phase O_2 prior to hydrocarbon pulsing. As expected, sequential pulsing with C_3H_8 provided no further insight into the reaction mechanism due to the low conversion of ODP over the VA-200 catalyst sample, and the spectra are not discussed here. The response signals of sequential pulsing of $^{18}\text{O}_2$ and C_3H_6 , which provided evaluable spectra due to the higher reactivity of the alkene, are presented below (Fig. 5.16). Due to the small amount of pulsed $^{18}\text{O}_2$ molecules, the main products of C_3H_6 pulsing are C^{16}O and C^{16}O_2 and the response of these components in the range of 0.5–5 s is nearly identical to the spectrum presented in Fig. 5.13 (b). The upper diagrams (Fig. 5.16 (a,b)) present responses which refer to the $^{18}\text{O}_2$ pulsing in the time-frame of 0–0.5 s. The diagrams below (Fig. 5.16 (c,d)) present responses which refer to both the $^{18}\text{O}_2$ and the consecutive C_3H_6 pulsing.

The response of different oxygen isotopes to $^{18}\text{O}_2$ pulsing on $^{16}\text{O}_2$ pretreated VA-200 catalyst is shown in Fig. 5.16 (a). The consecutive responses of $^{18}\text{O}_2$, $^{18}\text{O}^{16}\text{O}$ and $^{16}\text{O}_2$ with decreasing intensity clearly indicate a reversible exchange of one oxygen atom at the VO_x surface species. The presence of cross-labelled O_2 can be related to the R^1 reaction mechanism of oxygen exchange corresponding to Doornkamp et al. [5.32] (Eqs. 5.17 and 5.18).



This is in accordance with the high distribution and low loading of VO_x surface species and the resulting low diffusivity of oxygen atoms between these active sites. Mechanistic information about the pathway of isotopic exchange can not be derived from the shapes except by modeling of the responses which was not performed. One plausible intermediate is a vanadium ozonide structure $\text{V}(\text{O}_3)$ formed by the addition of gas phase O_2 to a vanadyl group as found over magne-

sium oxide [5.33]. Furthermore, it can be seen from Fig. 5.16 (a) that after 0.5 s there is no more gas phase O₂ present which could interact with the following C₃H₆ pulse.

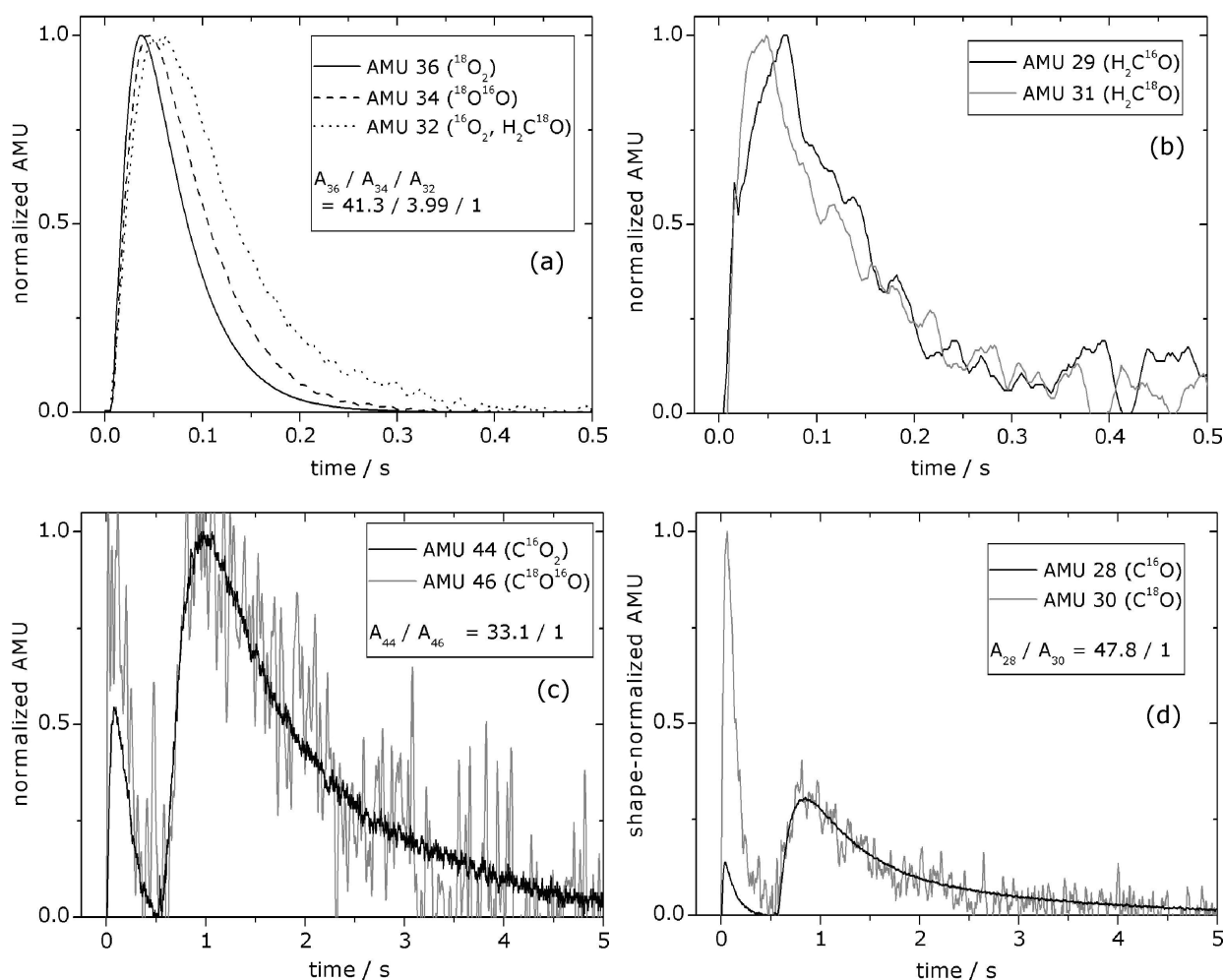


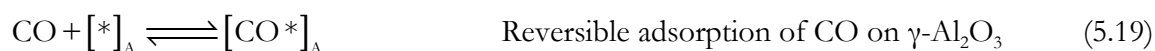
Figure 5.16 Transient responses to sequential pulsing of ¹⁸O₂ and C₃H₆ over catalyst VA-200 at 773 K; Figures show intensity-normalized (a) O₂, (b) H₂CO, (c) CO₂ and (d) CO signals of labelled and unlabelled compounds.

Trace amounts of labelled and unlabelled formaldehyde were detected as a response to the ¹⁸O₂ pulsing (Fig. 5.16 (b)), whereas during the C₃H₆ pulsing this component could not be detected. Their signals could not be quantified due to a missing calibration of this compound. In contrast Kondratenko et al. detected H₂CO after C₃H₆ pulsing on a higher loaded VO_x(9.5 wt%)/γ-Al₂O₃ catalyst at 848 K [5.29]. This can be explained by the presence of strongly adsorbing C_xH_yO_z soot species remaining on the catalyst surface after C₃H₆ pulsing. These either get oxidized by gas phase ¹⁸O₂ or receive energy from collisions with gas molecules to desorb or further oxidize. This explanation also holds for the presence of labelled and unlabelled CO and CO₂ (double-labelled C¹⁸O₂ could not be detected) as a response to ¹⁸O₂ pulsing. The relatively sharp decay of these compounds within 0.5 s compared to the long tailing observed during C₃H₆ pulsing (see Fig. 5.16

(c,d)) confirms the suggestion of desorption of residual molecules without reaction. Furthermore, from the latter figures it can be seen that the normalized shapes of $C^{16}O$ and $C^{18}O$ on the one hand and of $C^{16}O_2$ and $C^{18}O^{18}O$ on the other hand as a response to the C_3H_6 pulsing ($t > 0.5$ s) are nearly identical. This indicates that the exchange of labelled oxygen into the VO_x species is finished after 0.5 s and there is no preferred reaction with activated oxygen species, i.e., peroxo groups, detectable. The reaction proceeds exclusively via lattice oxygen, which is also confirmed by the absence of $C^{18}O_2$.

5.3.3 Modeling of CO_x Sorption and CO Oxidation³

Due to the complex sorption behaviour of the C_3H_6 deep oxidation intermediates the transient response of this reaction was not attempted to be described by a microkinetic model. Much more data should be collected for a meaningful description of this surface reaction. From balancing of response areas of C_3H_6 only the activation energy of the RDS can be derived as described in Ch. 5.3.1. Instead the relatively simple CO oxidation with two components and two types of sorption sites was estimated to give more reliable information from this basic study. The model included the following elementary steps (Eqs. 5.19-5.21):



Sorption of CO and CO_2 is less pronounced at temperatures above 773 K (see Fig. 5.13 (d)) and the determination of sorption heats appears difficult in this temperature range. Thus, CO and CO_2 pulsing was performed at lower temperatures of 300–500 °C, where a reaction can be neglected, but sorption was expected to affect the pulsing response. The results are depicted in Figs. 5.17 (a) and (b).

³ Kinetic modeling of CO/ CO_2 -sorption and CO-oxidation experiments was performed by Dr. Evgueny Kondratenko, LIKAT Adlershof.

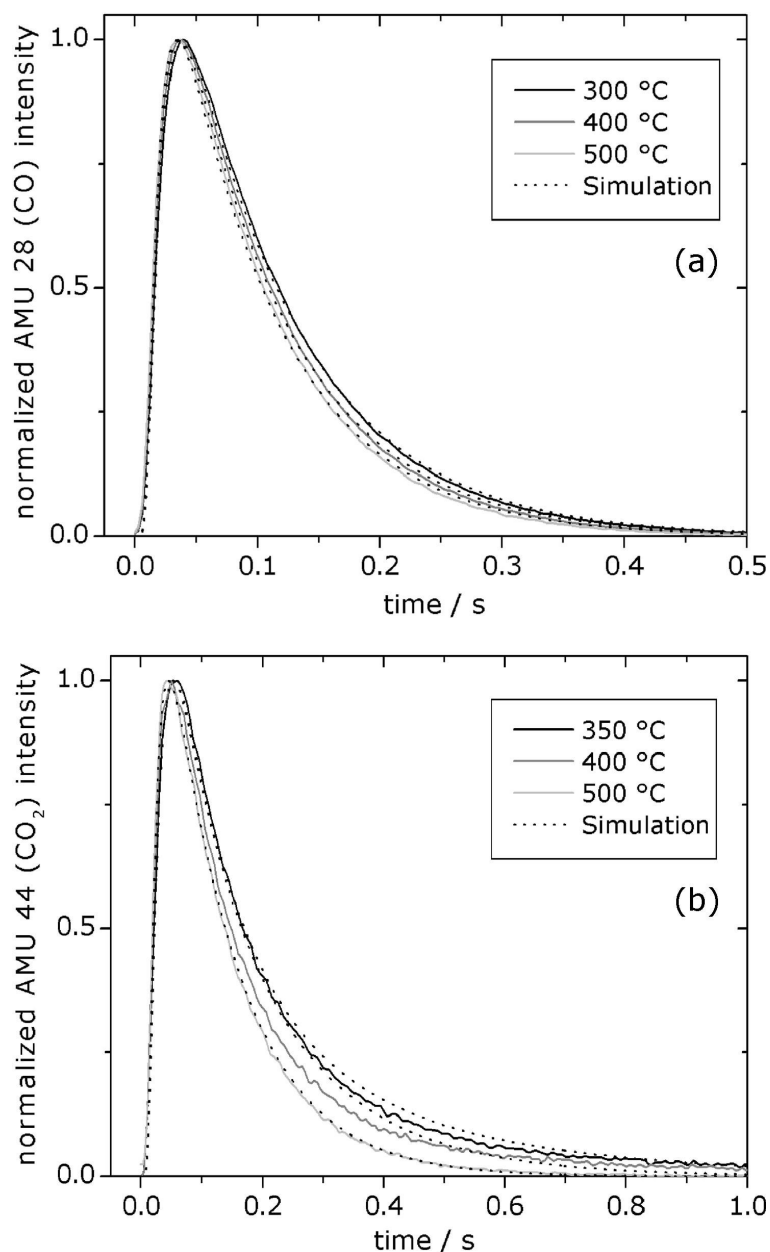


Figure 5.17 Transient responses to (a) CO and (b) CO₂ pulsing over catalyst VA-200 at 300-500 °C.

From the time-scale of these figures it can be seen that CO₂ interacts stronger with the catalyst surface than CO. This conclusion also holds for the comparison of the CO_x responses with mass-normalized Xe responses (not shown here). Whereas CO responses are close to congruent with these reference curves over the whole range of temperatures, for CO₂ responses this is not even the case at 500 °C. Below this temperature the interaction of CO₂ with the catalyst causes remarkable delay of the response. This is in agreement with already published data [5.31,5.34]. Furthermore the retention time increases with decreasing temperature. This is partly due to the dependency of the Knudsen diffusivity on temperature ($\sim T^{0.5}$) but moreover due to sorption processes which become significant at lower temperatures. Reversible adsorption of CO and CO₂ on γ -Al₂O₃ was modeled using rate-laws describing the catalyst coverage (Eq. 5.22). It should be

mentioned that within the fit the rate constant of adsorption was found to correlate with the total number of sorption sites and therefore the product of both was taken to determine the heat of adsorption in an Arrhenius-type plot.

$$\frac{d\Theta_i}{dt} = k_{\text{ads}} c_i (1 - \Theta_i) - k_{\text{des}} \Theta_i \quad (5.22)$$

The following parameters of sorption kinetics were derived from the fit of CO and CO₂ pulsing in the range of 300–500 °C (Tab. 5.5).

Table 5.5 Parameters of CO and CO₂ sorption from TAP data fitting in the range of 300–500 °C.

Adsorbate	CO	CO ₂
Concentration of sorption sites / mol m _{cat} ⁻³	6.51×10 ⁻²	7.14×10 ⁻³
E _A of adsorption / kJ mol ⁻¹	23.1	51.9
E _A of desorption / kJ mol ⁻¹	21.2	136
Heat of adsorption / kJ mol ⁻¹	2	-84

As can be seen the modeling of CO sorption kinetics provided very low values of activation energies and a positive value of the adsorption heat. This indicates a negligible interaction of CO with the catalyst in this temperature range, resulting in the impossibility to derive physically relevant parameters from these pulsing responses. Consequently this interaction can be neglected when describing the CO oxidation in a somewhat higher temperature range. Against that CO₂ sorption modeling provided more reliable kinetic data. However, the activation energy of desorption is quite high compared to an interval of 100 ± 20 kJ mol⁻¹ from previous studies [5.31, 5.35], whereas the adsorption heat is lower than published values in the range of 100–140 kJ mol⁻¹ [5.34,5.35]. This may be partly due to the strong heterogeneity of CO₂ sorption sites on the one hand and of adsorbed CO₂ species on the other hand which were identified over γ-Al₂O₃ [5.36]. Since the kinetic model chosen for data fitting was reduced to one type of CO₂ adsorption the resulting parameters can only serve as benchmarks, which is confirmed by the relatively low fitting quality of CO₂ pulsing responses.

In order to describe the CO oxidation with lattice oxygen of VO_x species, in the temperature range of 500–550 °C the shape of CO responses was applied for fitting and model discrimination. Because of the low resolution of CO₂ responses, numerical fitting of these data failed. However, CO conversions were calculated using the yield of CO₂ due to a higher accuracy of these values. A simple kinetic approach (Eq. 5.23) was applied successfully for description of the CO responses, which is displayed in Fig. 5.18 (a).

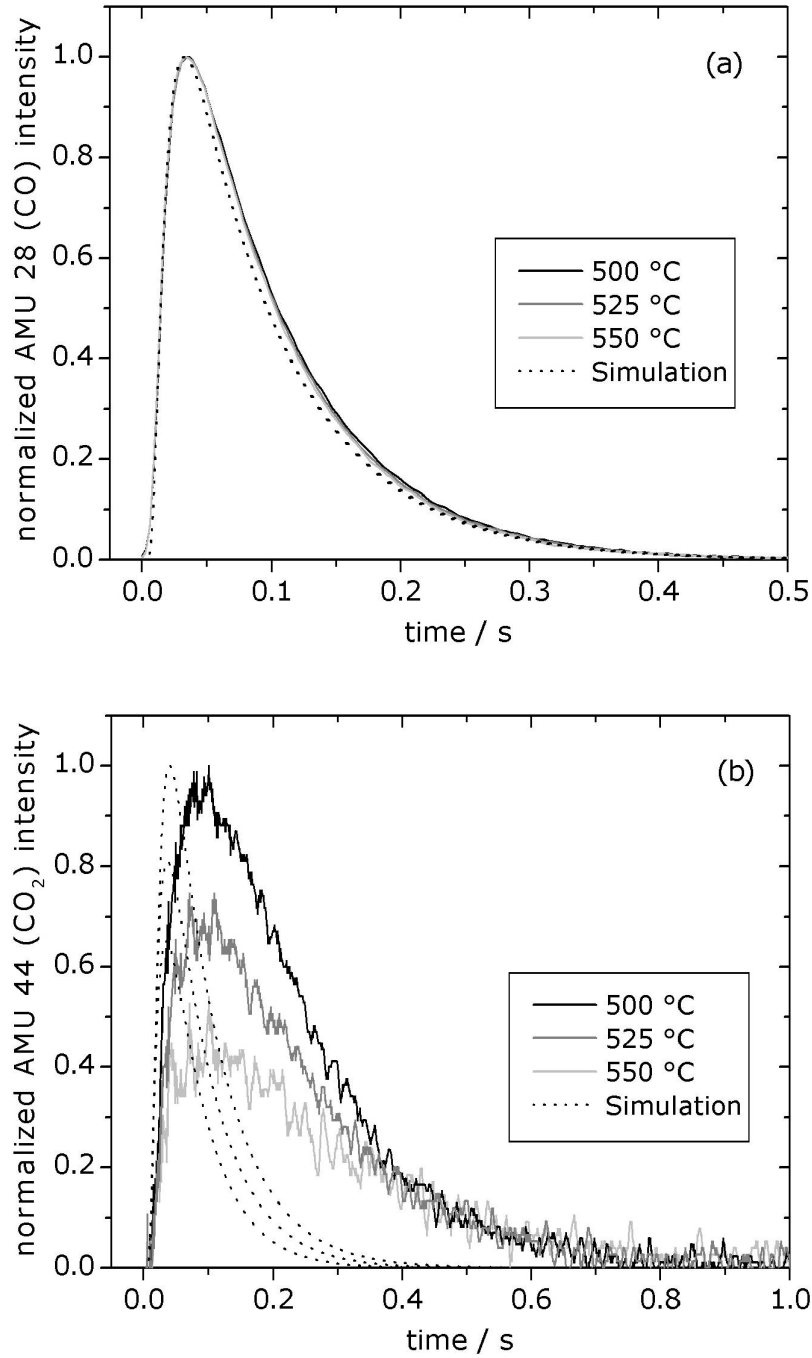


Figure 5.18 Microkinetic modeling of CO oxidation from TAP experiments in the temperature range of 500–550 °C, responses of (a) CO, and (b) CO₂.

$$\frac{d\epsilon_{\text{CO}}}{dt} = k \epsilon_{\text{CO}} \Theta_{\text{ox}} \quad (5.23)$$

The narrow temperature range and the normalization may be responsible for the nearly identical appearance of CO model responses. Since transient CO₂ responses could not be fitted, Fig. 5.18 (b) contains only simulated responses. These curves are based upon CO₂ formation via surface reaction on VO_x sites (Eq. 5.23, Tab. 5.6) and its reversible adsorption on γ -Al₂O₃ sites (Eq. 5.22, Tab. 5.5). CO₂ responses are displayed normalized with respect to the signal at 823 K, where the

highest conversion could be achieved. However, the model turned out to be insufficient for the prediction of product formation, the modeled response is too sharp indicating an underestimation of the interaction with the catalyst. It appears that the extrapolation of sorption kinetic data gained from Fig. 5.17 (b) to a somewhat higher temperature range is not trivial. On the other hand the model discrimination by means of the CO responses can be the reason for the insufficient prediction of CO₂ responses. A stable [VO...CO] intermediate could be the key for a more appropriate modeling, which, for any reason, failed in the fitting procedure. There is no doubt that also more complicated microkinetic models are capable for the description of CO responses, however, in this study the simplest one was chosen.

Table 5.6 Parameters of CO oxidation from TAP data fitting in the range of 500–550 °C.

Concentration of sorption sites / mol m ⁻³	6.38×10 ⁻⁴
Activation energy E_A / kJ mol ⁻¹	87.4
Preexponential factor k_0 / s ⁻¹	4.09×10 ¹⁰

The resulting activation energy is markedly higher than the value determined from the Arrhenius plot. This can be explained by the fact that experimental yields of up to 10% do not hold for the condition of differential conversion. Furthermore the number of active sites for CO oxidation is only about 1/10 of the value capable for CO₂ reversible sorption. This is in excellent agreement with the low vanadia loading of the catalyst VA-200. The XPS analysis resulted in a close to identical ratio of vanadium atoms to aluminium atoms at the surface.

5.4 Reoxidation Kinetics of VO_x Species

Reoxidation experiments were performed in the Berty reactor set-up. Ideal mixing conditions inside the vessel were proven by tracer step experiments switching the feed between N₂ and O₂. For this purpose the catalyst basket was filled with inert alumina grains with particle sizes similar to that of the catalyst (100–300 μm). The resulting concentration profiles for ambient conditions were detected by on-line mass spectrometry (MS) as shown in Fig. 5.19. A rotation speed of at least 4000 min⁻¹ is required for ideal gas phase mixing for flow rates up to 100 ml_n min⁻¹, below this value a weak bypass flow can be observed. The ideally mixed reactor volume determined this way is in the range of 13 ± 0.5 ml, which is in agreement with the data given by the supplier.

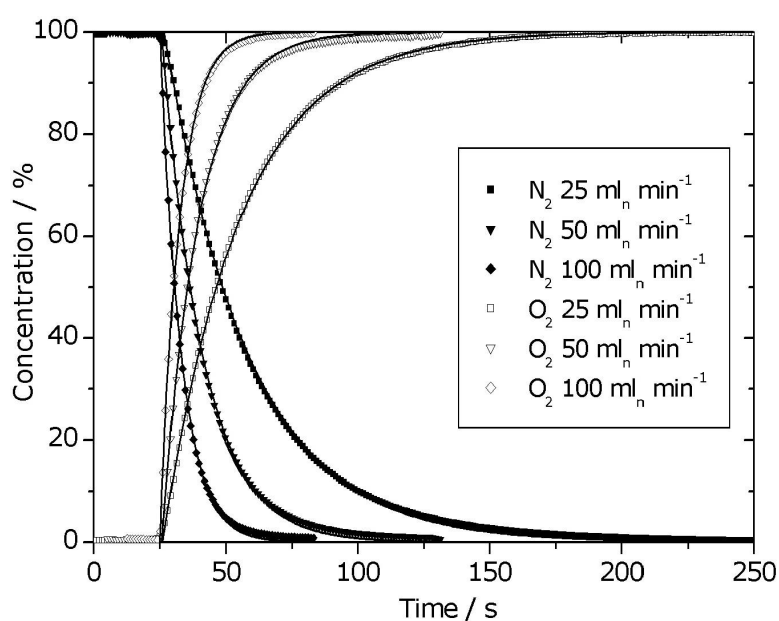


Figure 5.19 Residence-time distribution of the Berty reactor from tracer step experiments switching the feed from nitrogen to oxygen at different flow rates; fit of the data with exponential decay functions (full lines).

The signal functions represent nearly ideal exponential decays indicating a well mixed gas phase inside the vessel. The signal curves can also be used to quantify the deviations from exponential decay functions which may be caused by back-mixing in tubing, particle filter and valves of the experimental set-up. As can be seen, their influence on the overall residence time behavior is negligible.

For catalytic measurements the catalyst basket was filled with 1.0 g freshly calcined catalyst diluted with inert alumina particles of the same size and placed between two layers of this inert material. Catalyst reduction was achieved with 50 ml_n min⁻¹ of a H₂/N₂ mixture (20% H₂) at 713 K. Gas supply was changed to pure hydrogen as water concentration in the product flow

began to decrease. After 30 min, the feed was switched to $50 \text{ ml}_n \text{ min}^{-1}$ He for 1 h to flush the reactor and remove gas phase impurities of hydrogen and water at 713 K. This procedure was repeated strictly before each oxidation experiment to get a reproducible starting point. The reactor was then cooled down to the required reaction temperature afterwards. As soon as the required temperature was reached, the He flow was increased to $100 \text{ ml}_n \text{ min}^{-1}$ for 1 min, and the feed was switched to a $100 \text{ ml}_n \text{ min}^{-1}$ flow of a O_2/N_2 mixture (3–10% O_2) to initiate the catalyst re-oxidation. The reproducibility of the experiments is sufficient and confirms the suitability of the experimental set-up for dynamic experiments as well as the total reversibility of the redox cycles.

The modeling of catalytic experiments was performed with the “Berkeley Madonna” software using a 4th order Runge-Kutta algorithm and experimental data fitting by the method of least square error.

5.4.1 Kinetic Modeling of Experimental Results

A typical response signal of catalyst reoxidation after initiating a step function of $100 \text{ ml}_n \text{ min}^{-1}$ O_2/N_2 (3% O_2) at 479 K is shown in Fig. 5.20. Compared to the nitrogen signal, which describes an exponential curve, the oxygen concentration increases moderately due to the oxygen consumption for catalyst reoxidation. With proceeding reoxidation, the oxygen consumption decreases. This is accompanied with an increase of the oxygen concentration that finally approaches the oxygen concentration of the feed. A modeled oxygen signal for a tracer step without reaction is shown as reference.

The following characteristics are observed in the oxygen signal: there are (i) a short delay in oxygen appearance compared to nitrogen for about 3 s, which indicates an extremely fast reaction at the beginning of the reoxidation process (see also Fig. 24 (b)), (ii) a step in oxygen concentration increase at $t = 10 \text{ s}$, (iii) a bend at 0.4 mol m^{-3} oxygen concentration, and (iv) a sudden stop of the reaction at $t = 100 \text{ s}$ reflected in a relatively fast increase of the oxygen concentration to the inlet value. The appearance of water released during the reoxidation shows that the catalyst surface is not dry, although the reactor has been flushed with helium at 713 K for about one hour. Moreover, the well-structured shape of the signal indicates a significant role of water sorption processes on the reoxidation kinetics, since the water peaks at 20 and 125 s correlate with characteristics of the oxygen outlet signal. The water signal is detected in the ppm range and displayed in arbitrary units (a.u.). The sorption equilibrium on inert alumina reduces its intensity and maxima sharpness.

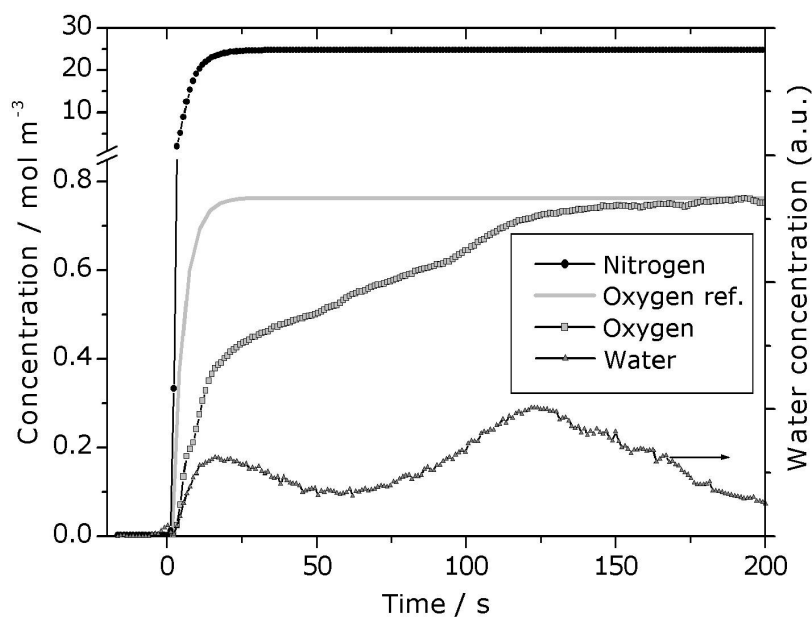


Figure 5.20 Experimental response signal of $\text{VO}_x/\text{Al}_2\text{O}_3$ catalyst reoxidation; $100 \text{ ml}_n \text{ min}^{-1} \text{ O}_2/\text{N}_2$ (3 vol% O_2), 479 K and 1 g catalyst containing 0.275 mmol V.

As a matter of fact, the detailed shape of the oxygen signal cannot be modeled using the simple reaction rate equations for catalyst reoxidation that are proposed in literature. Previously, only the reaction of gas phase dioxygen molecules with $\text{V}^{+\text{III}}$ sites was accounted for and the rate equations differed only in the reaction order of oxygen and vacancy concentrations. Then, the reoxidation of surface vanadia species was found to occur either directly in a dissociative mode [5.37] or by adsorption of molecular oxygen followed by dissociation [5.38]. Whereas the first mode is observed mainly in catalyst samples containing bulk vanadia phase, the latter kinetics can be ascribed to highly dispersed species e.g. supported on silica [5.39]. The following reaction rate laws for the formation of $\text{V}^{+\text{V}}$ sites $r_i = d\alpha([\text{V}^{+\text{V}}\text{O}])/dt$ (Eqs. 5.24-5.26) were derived for these mechanisms:

$$r_1 = k_1 c(\text{O}_2)^{0.5} c([\text{V}^{+\text{III}}]) \quad (5.24)$$

$$r_2 = k_2 c(\text{O}_2) c([\text{V}^{+\text{III}}])^2 \quad (5.25)$$

$$r_3 = k_3 c(\text{O}_2) c([\text{V}^{+\text{III}}]) \quad (5.26)$$

These rate laws are ascribed to the reactions (Eqs. 5.27-5.29):



where Eqs. 5.27 and 5.28 belong to rates r_1 (Eq. 5.24) and r_2 (Eq. 5.25), respectively [5.40]. In r_1 , the rate of oxygen adsorption is relatively slow compared to its dissociation and vice versa in r_2 ;

Eq. 5.29 describes the molecular adsorption of oxygen with consecutive dissociation (Eq. 5.30), as kinetically described in r_3 (Eq. 5.26), where the adsorption is the rate determining step.

For a better comparison of the curve shapes, the oxygen signal at the outlet of the Berty reactor was modeled using these relatively simple models. The result is shown in Fig. 5.21 for an oxygen concentration of 0.76 mol m^{-3} (3 vol% O_2) at 479 K. The response shapes of the signals are normalized by adjustment of the rate constants k_i with respect to the bend of the curve after the initial increase of the reaction from $t = 0$ –10 s (see arrow in Fig. 5.21) to allow a better comparison. When oxygen concentration is ca. 0.4 mol m^{-3} at $t = 10 \text{ s}$, a bend reflects the beginning of the reoxidation process, since oxygen concentration is too low for remarkable conversion at $t < 10 \text{ s}$. The resulting response curves are similar for the chosen modeling conditions. However, they strongly differ when the oxygen concentration, the flow rate, or total number of active sites varies because of the different reactant reaction orders.

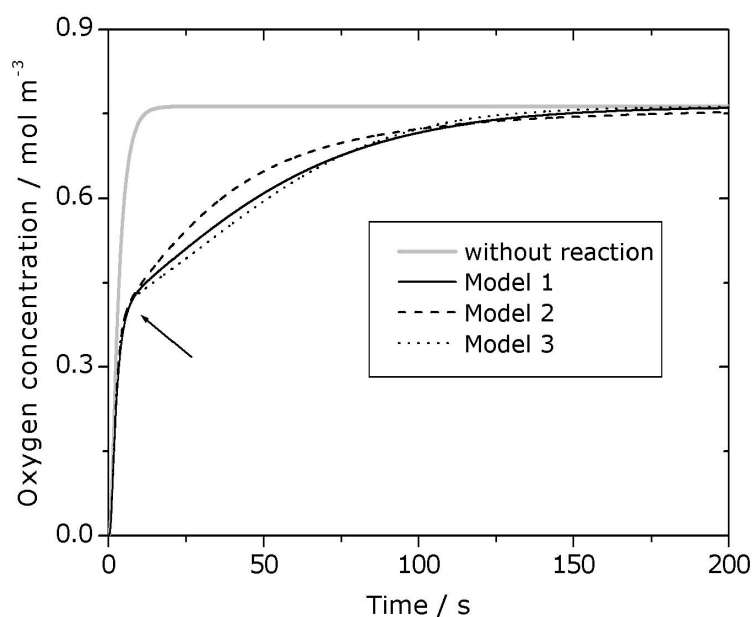
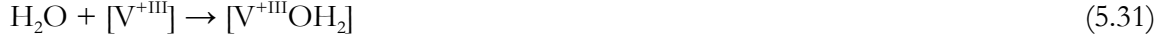


Figure 5.21 Simulation of the oxygen signals at the outlet of the reactor during the catalyst reoxidation process by models presented in literature (model 1-3 correspond to Eq. 5.24–5.26, respectively); arbitrary rate constants.

A simulated oxygen response curve without reaction is given as reference. The oxygen concentration calculated using the reoxidation models is below this curve for the whole simulation due to the oxygen consumption in the reactor. The total amount of oxygen used for the catalyst reoxidation is given by the difference between the two curves and is the same for models 1-3 (Eqs. 5.24-5.26).

Furthermore, a modeling of the experimental results including sorption processes of water on vanadia sites was done since water seems to have a strong influence on the reoxidation process. This requires a higher number of elementary reaction steps and additionally to Eqs. 5.27-5.30, the following reactions were included (Eqs. 5.31-5.38):



where [V] stands for a structurally undefined surface vanadia species as active site and $[\text{Al}_2\text{O}_3]$ for a γ -alumina surface site.

The addition of a second type of active site, which allows for a differentiation between monomeric and dimeric structures, was not found to improve the fitting of experimental data and is therefore avoided. However, a heterogeneous composition of vanadia species including vanadia monomers, dimers, and polymers cannot be excluded from spectroscopic analysis of the catalyst. The kinetic modeling, however, indicates a similar catalytic behaviour of these species. Other structural differences between reduced and oxidized active sites are also not taken into account. Furthermore, the model fails in quantitatively describing the complex response of water. This can be attributed to the water sorption on alumina (Eq. 5.38) that could not be included successfully into the modeling. The modeled values, however, may approximate the intraparticle water concentration or a pseudo-concentration due to migration of mobile water molecules on the catalyst surface between vanadia and alumina sites. After leaving the catalyst particle, most of the water is assumed to adsorb irreversibly on the alumina grains, especially at temperatures below the reduction temperature. The resulting outlet concentration, however, is too low for accurate handling in the numerical integration process of microkinetic modeling and could thereby not be described.

The set of reactions Eqs. 5.27 and 5.31-5.37 and the corresponding rate laws allow for a reasonable description of the experimental results (Fig. 5.22).

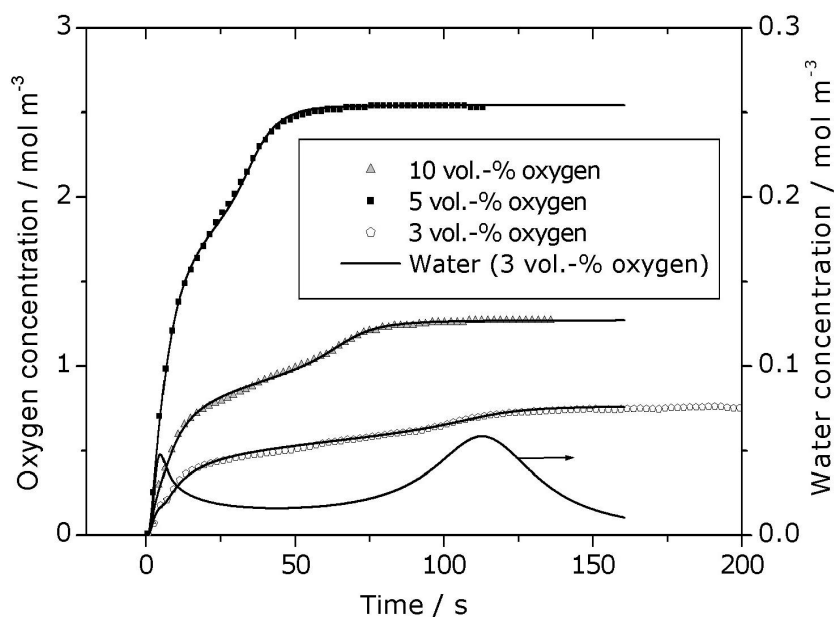


Figure 5.22 Experimental results and simulated response curves of oxygen to step-marking with different oxygen concentrations at 479 K, water response for 3 vol% O₂.

The fit of the rate constants of these elementary reactions was performed in parallel on three datasets measured at 479 K and oxygen concentrations of 3, 5, and 10 vol%. The essential characteristics of the oxygen and water signals are reflected. However, the direct oxidation of naked V^{III} to V^V (Eq. 5.27) is negligible compared to a reoxidation process via vanadia hydroxyls [V^{IV}OH] and hydrated vanadia [V^{III}OH₂] as intermediates. Moreover, a forced inclusion of direct oxidation reactions (Eqs. 5.27-5.30) with substantial contribution to the overall reaction resulted in a poor accuracy of the fit, which supports the negligible impact of the direct oxidation under oxidative dehydrogenation conditions. The calculated surface coverage with transition species [V^V(OH)₂], [V^VO(OH₂)], and [V^VO(OH)] was found to be negligible, which also means that their decomposition (Eqs. 5.33, 5.34, 5.37) is very fast and not rate determining for the overall reaction rate. Furthermore, the best fit was achieved with first order rate laws with respect to oxygen and surface species for the reactions including oxygen. This validates a consecutive adsorption-dissociation model as expected for the low loaded catalyst, and implies a peroxo species, which decomposes quickly, as precursor for the species [V^V(OH)₂], [V^VO(OH₂)], and [V^VO(OH)] [5.41]. This has recently been investigated and confirmed by means of TAP experiments over catalyst VA-200 [5.42] and drastically reduces the number of rate equations that are relevant in the description of the measured responses. The modeling suggests the reaction mechanism shown in Fig. 5.23.

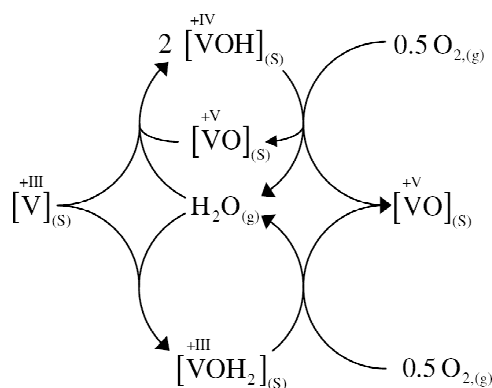


Figure 5.23 Proposed reaction network of oxidation of highly dispersed hydrated VO_x species supported on $\gamma\text{-Al}_2\text{O}_3$.

Small amounts of water in the system adsorb predominantly on the $\text{V}^{+\text{III}}$ sites (Eq. 5.31). It is concluded from the experiments that, compared to naked $\text{V}^{+\text{III}}$ sites, these hydrated species react more easily with gas phase oxygen. Since water is only weakly adsorbed on $\text{V}^{+\text{V}}$ sites, the reoxidation process finally results in the release of the adsorbed water (Eq. 5.34), which then adsorbs instantly on the next free $\text{V}^{+\text{III}}$ active site. When a certain amount of $\text{V}^{+\text{V}}$ sites is present at the surface, the reaction mechanism changes, and water adsorbs dissociatively on $\text{V}^{+\text{V}}$ and $\text{V}^{+\text{III}}$ sites to produce two hydroxylated $\text{V}^{+\text{IV}}$ sites (Eq. 5.35). Hydroxyls are also a favoured point of attack for reoxidation compared to naked $\text{V}^{+\text{III}}$ and get oxidized under release of water (Eq. 5.36). These consecutively occurring cycles are responsible for the sudden release of water and its batch-wise appearance in the reoxidation signal (Fig. 5.20). Since there is still some uncertainty about the absolute water concentration in particles and gas phase, the absolute values of the rate constants are not published here and the results are reported only semi-quantitatively. Furthermore, water released during the reoxidation might not be released in the gas phase but migrate on the alumina surface. Consequently, the reverse pathway, which is the migration of mobile water molecules from hydrated alumina sites onto naked $\text{V}^{+\text{III}}$ sites, should also be taken into account,

To further investigate the impact of water on the reoxidation, several experiments were conducted with addition of steam to the gas mixture. The lowest concentration that could be adjusted using a conventional saturator is ca. 0.6 vol% (water saturation pressure at 1 °C). However, even this concentration is too high and the detailed structures of both oxygen and water response curve disappear at temperatures lower than the reduction temperature. As expected, the reoxidation rate also becomes retarded. It can be concluded that when water is present in the feed, $\text{V}^{+\text{III}}$ sites and $\gamma\text{-Al}_2\text{O}_3$ surface are immediately fully saturated with water that inhibits the reaction and leads to signal-smearing.

The influence of the reaction temperature on the reoxidation process was then investigated. The oxygen response curves at temperatures between 479 and 712 K is depicted in Fig. 5.24 (a). A feed containing 3 vol% oxygen was used. Fig. 5.24 (b) is an enlargement of the initial phase of the reoxidation. Again, the nitrogen response indicates ideal residence-time distribution.

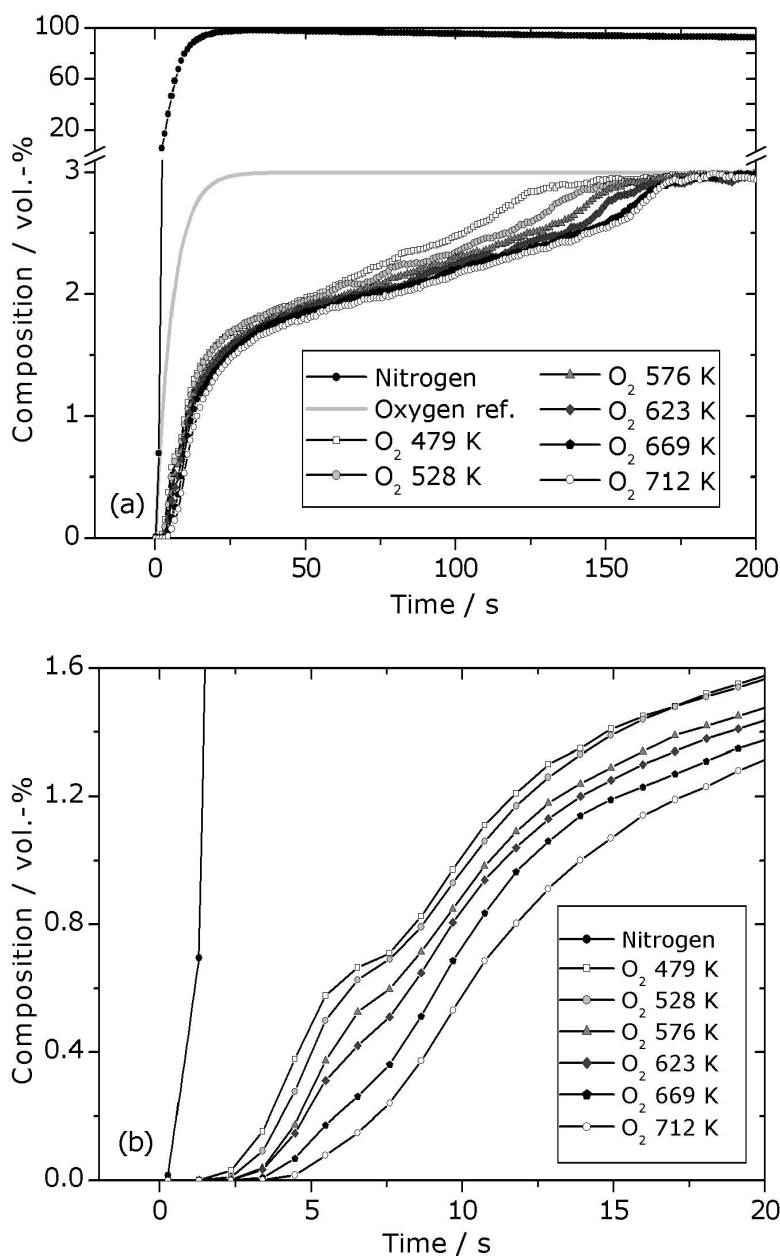


Figure 5.24 (a) Reoxidation responses to step-marking with 3 vol% O₂ in the temperature range of 479–712 K, (b) magnification of the initial period.

Two conclusions can be drawn from Fig. 5.24 (a): (i) the curve shapes are quite similar over a wide range of temperatures, which means that the activation energy of vanadia reoxidation occurring via water adsorption is relatively low, and (ii) the overall oxygen consumption increases with temperature.

The influence of temperature on the elementary steps of reoxidation can be observed in the initial phase of the reaction (Fig. 5.24 (b)). The shoulder in oxygen concentration at $t \approx 7$ s is relatively pronounced at low temperatures and absent at high temperatures with a fluent transition. The disappearance of this shoulder and the extension of the initial period where nearly no oxygen passes the reactor, is due to the acceleration of reaction Eq. 5.32. The impact of increasing temperature on reaction Eq. 5.36 results in a general decline of the oxygen concentration level in the range of 10 s up to the end of the reaction, respectively.

The oxygen consumption as a function of reoxidation temperature is illustrated by full squares in Fig. 5.25 (a) and is referred to the total amount of vanadia in the reactor. The resulting oxidation state of vanadium is plotted. The maximum oxidation state of +V is approached at high temperatures, the maximum change in oxidation state being $\Delta = +2$. It can be concluded that the starting point of each reoxidation experiment corresponds to a sample containing almost only V^{+III} species. However, the total oxygen consumption decreases below 700 K and the average change in oxidation state is only +1.3 (479 K).

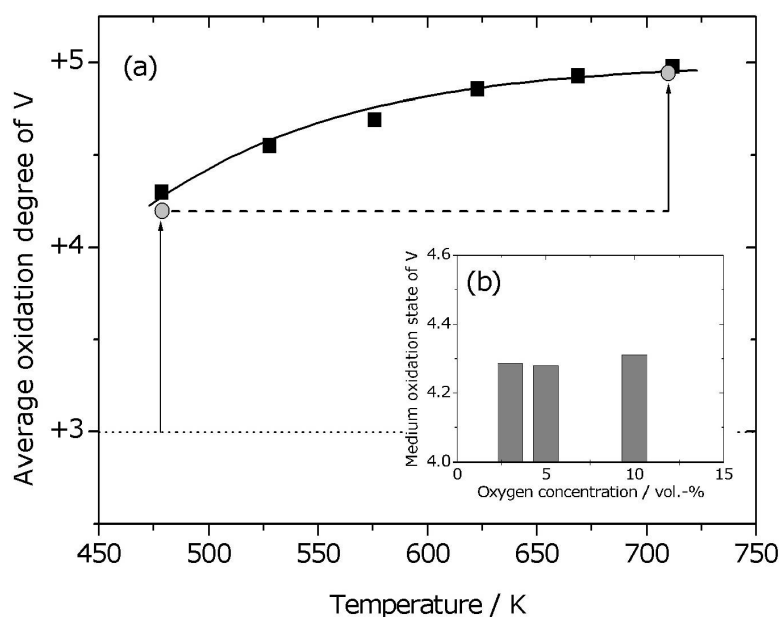


Figure 5.25 (a) Final average oxidation degree of VO_x species on catalyst VA-200 after reoxidation experiments with 3 vol% O_2 gas mixture, (b) variation of oxygen concentration at 479 K.

Fig. 5.25 (b) shows that the inlet oxygen concentration has no impact on the amount of consumed oxygen during reoxidation at 479 K. This indicates that the incomplete reoxidation is a kinetic rather than a thermodynamic effect. The catalyst can also be reoxidized step-wise (Fig. 5.25 (a), grey circles). After partial oxidation of V^{+III} sites to an average oxidation degree of +4.3 at 479 K, the reactor was heated up to 709 K under helium. A continued oxidation resulted in the

maximum oxidation state +V, which is also reached by total reoxidation in this temperature range. A lower number of V^{+V} active sites at lower temperatures can have an influence on the experimentally determined activation energy of each reaction that depends on the V^{+III}/V^{+V} redox cycle. This is not the case: to monitor this falsifying effect, which is observable up to about 623 K, the fraction of active sites V^{+V}/V_{tot} was plotted in an Arrhenius-type diagram (Fig. 5.26).

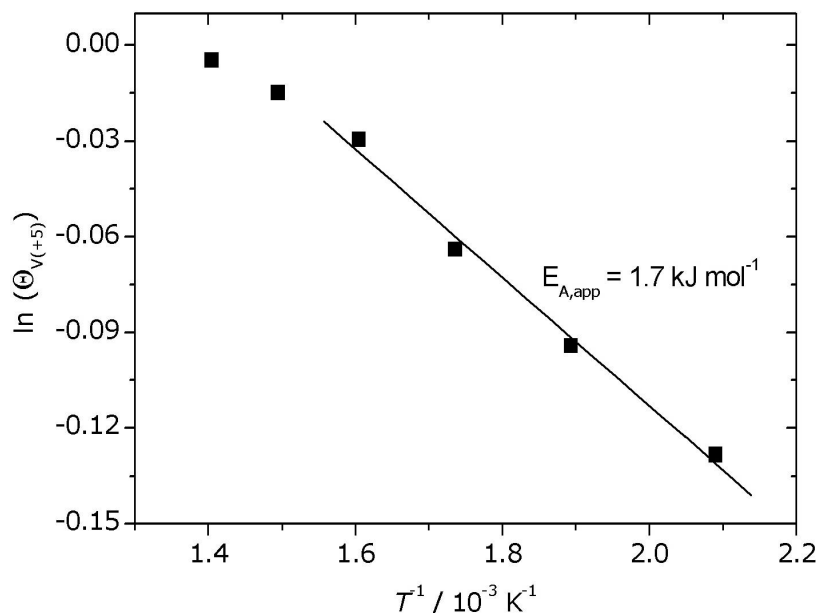


Figure 5.26 Arrhenius-type plot of final V^{+V} -fraction after reoxidation.

The slope in the range of 479–523 K gives a contribution to the apparent activation energy of 1.7 kJ mol^{-1} , caused solely by different fraction of V^{+V} sites. A falsifying impact in this order of magnitude is negligible especially of exothermic reactions. Above 523 K this contribution even decreases and approaches to zero at temperatures of about 773 K.

5.4.2 Theoretical Investigation of the Proposed Reaction Pathway⁴

To get insights in the thermodynamic feasibility of the elementary steps chosen for modeling the reoxidation reaction, reaction Gibbs free energies are calculated using density functional theory (DFT) at the B3LYP/TZVP level. Only isolated monomeric species are considered here, since they are most likely predominant for the low vanadia loading of VA-200 [5.23,5.44,5.45]. DFT calculations for vanadia species on γ -alumina have not been performed yet. Therefore, as a first approximation, very simple models derived from the $(\text{HO})_3\text{VO}$ molecule (compounds **3** to **6**) have been adopted. These were proven relevant for the calculation of thermodynamic properties

⁴ Theoretical calculations were performed by Dr. Remy Fortrie, Humboldt University Berlin.

of reactions that do not involve the bridging oxygen atoms between the (silica) support and the vanadia species [5.41]. In these models the bonds between the active vanadia site and the support are terminated by H atoms, i.e., the electronic effect of the support is not explicitly taken into account. The geometrical parameters of these compounds are reported in Fig. 5.27 and their electronic energies and Gibbs free energies are reported in Tab. 5.7. Further details can be found in literature [5.41]. The harmonic oscillator/rigid rotor/ideal gas approximation is used. Translations and rotations are not taken into account for surface species, i.e., for vanadium containing species. Gibbs free energies are given at standard conditions (1 bar) [5.46].

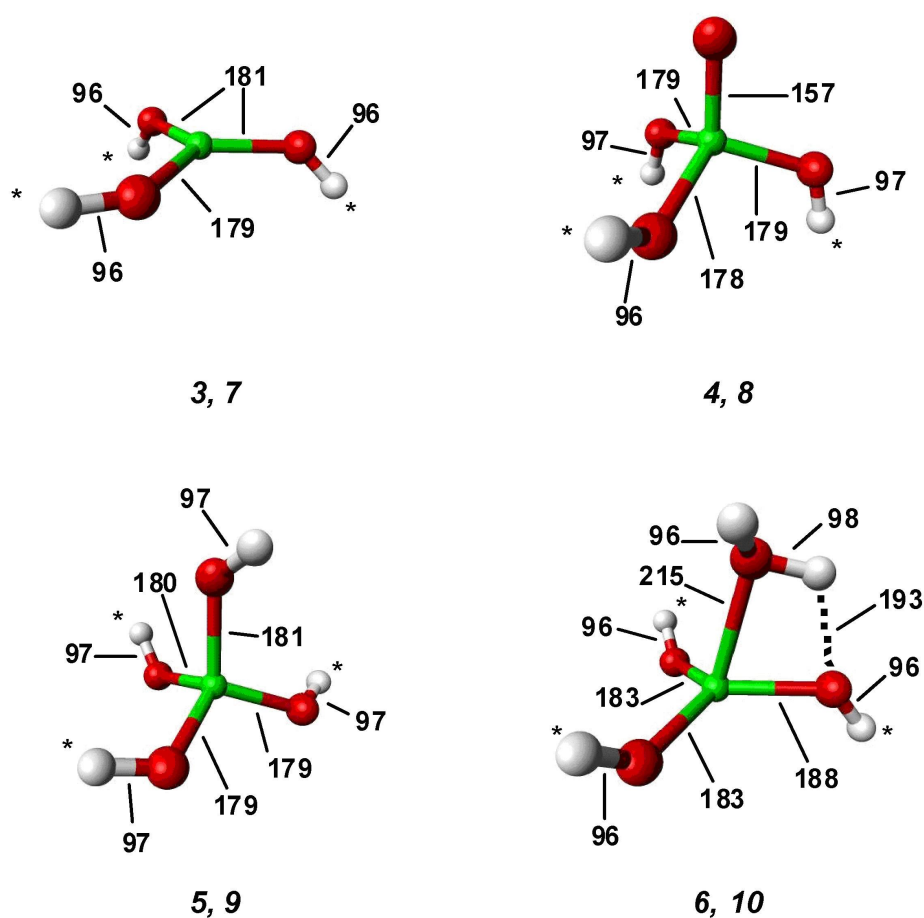


Figure 5.27 Geometric structures of models **3** to **10**. Green central spheres represent vanadium atoms, red spheres represent oxygen atoms and white spheres represent hydrogen atoms. Stars indicate which hydrogen atoms have been used for representing the support. Distances are given in pm. The dotted line denotes the presence of a hydrogen bond.

Table 5.7 Electronic energies and Gibbs free energies of compounds **1** to **10**. No particular treatment has been applied to soft vibrational modes.

Molecular compound			Electronic energy / Hartree	Standard Gibbs free energy / kJ mol ⁻¹ ^a		
Index	Chemical formula	Spin		0 K	300 K	700 K
1	0.5 O ₂	singlet	-75.2009	1	-28	-77
2	H ₂ O	singlet	-76.4607	56	9	-73
3	(HO) ₃ V ^b	triplet	0.0000	98	85	35
4	(HO) ₃ VO	singlet	-75.2994	114	107	64
5	(HO) ₃ VOH	doublet	-75.9068	140	129	76
6	(HO) ₃ VOH ₂	triplet	-76.4913	168	153	86
7	([Al]O) ₃ V ^c	triplet	0.0000	40	14	-64
8	([Al]O) ₃ VO	singlet	-75.2994	53	34	-38
9	([Al]O) ₃ VOH	doublet	-75.9068	79	56	-27
10	([Al]O) ₃ VOH ₂	triplet	-76.4913	108	79	-17

a) For all compounds, Gibbs free energies include spin and vibrational Gibbs free energies (including zero point energies) and additionally, for gas phase compounds, translational and rotational Gibbs free energies.

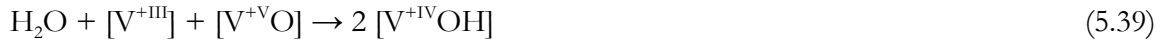
b) Electronic energy used as a reference for other vanadium containing compounds.

c) [Al] stands for an atom with the electronic properties of a hydrogen atom and the mass of an aluminium atom.

The calculations performed using the previously mentioned models are expected to provide reaction Gibbs free energies which are close to that of alumina supported VO_x species. This assumption is made even if neither the electronic nor the vibrational influence of the support is explicitly included. This appears acceptable, since none of the reactions investigated here involves bridging oxygen atoms between the support and the vanadium atom.

The vibrational influence of the support is estimated by replacing the mass of each terminating hydrogen atom by the mass of an aluminium atom, i.e., the support atom to which the active vanadia species is attached (compounds **7** to **10**). The results are shown in Tab. 5.7, where [Al] stands for the terminating H atoms with the mass of Al.

Changing the mass of the terminating atoms has a large influence on the calculated absolute Gibbs free energies (e.g., at 700 K, the Gibbs free energy is 99 kJ mol⁻¹ higher for (HO)₃V (**3**) than for ([Al]O)₃V (**7**), but only a small impact on reaction Gibbs free energies (Tab. 5.8). This supports the vibrational assumption. The results for reactions Eqs. 5.27 and 5.31, as well for the following reactions (Eqs. 5.39-5.41) are assembled in Tab. 5.8.



The redox disproportionation, Eq. 5.39, consists of reactions Eqs. 5.31 and 5.35, the oxidation reaction Eq. 5.40 consists of reactions Eqs. 5.36, 5.37 and 5.34, and the oxidation reaction Eq. 5.41 consists of reactions Eqs. 5.32-5.34. Most of them do not correspond to true elementary steps and involve most probably several of the latter. As a consequence, transition structures and activation energies are not directly theoretically accessible and only reaction Gibbs free energies are here considered for comparison with the experimentally derived kinetic model

Table 5.8 Standard Gibbs free energies of reactions Eqs. 5.27, 5.31, and 5.39–5.41 calculated from the values reported in Tab. 5.7 for Al and H masses (in parenthesis).

Reaction		Standard reaction Gibbs free energy / kJ mol ⁻¹		
Eq.	Description	0 K	300 K	700 K
5.27	$0.5 \text{ O}_2 + ([\text{Al}]\text{O})_3\text{V} \rightarrow ([\text{Al}]\text{O})_3\text{VO}$	-247 (-244)	-210 (-209)	-156 (-153)
5.31	$\text{H}_2\text{O} + ([\text{Al}]\text{O})_3\text{V} \rightarrow ([\text{Al}]\text{O})_3\text{VOH}_2$	-68 (-66)	-23 (-21)	41 (44)
5.39	$\text{H}_2\text{O} + ([\text{Al}]\text{O})_3\text{V} + ([\text{Al}]\text{O})_3\text{VO} \rightarrow 2 ([\text{Al}]\text{O})_3\text{VOH}$	-132 (-128)	-85 (-83)	-18 (-15)
5.40	$0.5 \text{ O}_2 + 2 ([\text{Al}]\text{O})_3\text{VOH} \rightarrow 2 ([\text{Al}]\text{O})_3\text{VO} + \text{H}_2\text{O}$	-115 (-116)	-125 (-126)	-137 (-138)
5.41	$0.5 \text{ O}_2 + ([\text{Al}]\text{O})_3\text{VOH}_2 \rightarrow ([\text{Al}]\text{O})_3\text{VO} + \text{H}_2\text{O}$	-179 (-179)	-187 (-187)	-196 (-197)

Two conclusions are drawn from these results. First, all considered reactions correspond to negative reaction Gibbs free energies at standard conditions. This means that the elementary steps which have been considered within the above kinetic model are thermodynamically favoured, which then supports the proposed reaction pathways.

The second conclusion concerns the hydration of the sample. Fig. 5.28 reports the Gibbs free energies of reactions Eqs. 5.31, 5.38, and 5.39 at the experimental relevant water pressure of 10⁻⁶ bar. The Gibbs free energy of hydration of γ -alumina (reaction Eq. 5.38) has been calculated for the (100) and (110) surfaces, using the DFT results of Digne et al. [5.47]. At each temperature, the most stable water coverage has been considered, and the average adsorption energy per water molecule has been calculated using the values reported in the Fig. 1 of reference [5.47]. The

final reaction Gibbs free energy has then been obtained by summing this value with the entropic contribution of water reported in Tab. 5.7.

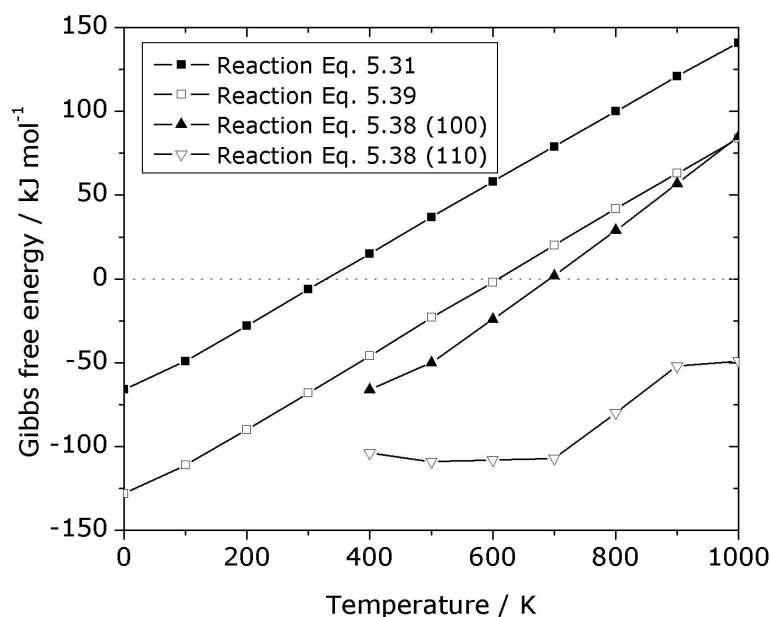


Figure 5.28 Gibbs free energies ($\Delta_R G$) of reaction Eqs. 5.31, 5.38 and 5.39 (water adsorptions) at 10^{-6} bar of water pressure. The reaction Gibbs free energies of reactions Eqs. 5.31 and 5.39 are reported in Tab. 5.8. The Gibbs free energy of reaction Eq. 5.38 has been calculated by combining the values reported in reference [5.47] for the (100) and (110) faces of γ -alumina with the entropic contribution of water reported in Tab. 5.7.

As can be seen in Fig. 5.28, the reactions corresponding to the adsorption of water and leading to $[V^{+III}OH_2]$ and $[V^{+IV}OH]$ are, at 10^{-6} bar of water pressure, thermodynamically favoured up to 300 K and 600 K, respectively. Given the uncertainty of the water pressure and the limited accuracy of the theoretical modeling, the above assumption of a possible presence of water adsorbed on the vanadium containing sites of the catalyst, even at the rather high temperature used for reducing the sample (713 K) appears reasonable. It is however more likely that most of the adsorbed water remaining on the catalyst at high temperature sits to alumina rather than on vanadia sites, which is thermodynamically much more favourable, as can be seen in Fig. 5.28, especially for the (110) surface.

5.5 The Dehydration of Propanol - an ODP Related Reaction?

The catalytic cycle of ODP described in Ch. 2.5.2 includes a propoxy species as intermediate, which decomposes under formation of C_3H_6 and release of a surface hydroxyl group. In the kinetic model proposed by Chen et al. the rate determining step (RDS) of the overall reaction is the first C-H bond breakage in C_3H_8 [5.48]. This means that the entirety of all other elementary reaction steps is fast compared to the RDS, which is confirmed by theoretical calculations [5.49]. In case of the decomposition of a propoxy intermediate this can be experimentally investigated by the dehydration reaction of propanol (Eq. 5.42).



This reaction is well investigated and a standard probe reaction for the determination of the surface properties of a solid acid catalyst. The formation of propene and di-isopropyl ether hereby occurs over acidic sites, whereas at basic and redox active sites the dehydrogenation towards acetone is favoured [5.50,5.51]. On acid sites the alcohol adsorbs in general dissociatively under formation of a propoxy group and a surface hydroxyl group, or by alcohol condensation with surface hydroxyl groups with water formation [5.52,5.53]. In case of both Brønsted and Lewis acid sites hydrogen exchange in a six-membered ring transition state then leads to the release of propene (Fig. 5.29).

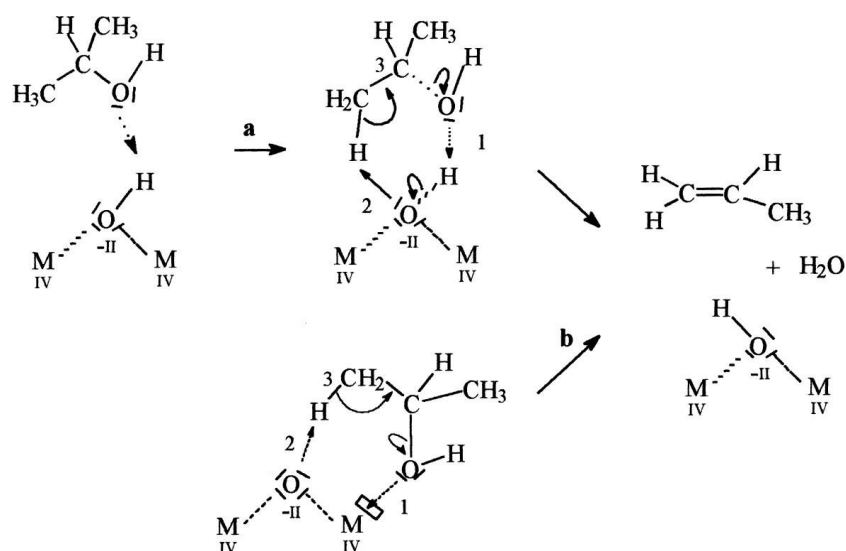


Figure 5.29 Reaction mechanism of propene formation via dehydration of 2-propanol over (a) Brønstedt and (b) Lewis acid sites, figure copied from literature [5.53].

In case of red-ox active surface species, as proposed by Rekoske and Barteau on oxidized TiO_2 , 2-propanol adsorbs dissociatively under formation of propoxy and hydroxyl groups bonded to the same cation (Fig. 5.30) [5.54]. Here, hydrogen exchange takes place in a five-membered ring

transition state, which results in the formation of adsorbed acetone and water. From titania, however, only acetone desorbs, whereas water decomposes under release of hydrogen and rearrangement of the oxidized active site. With respect to vanadia catalysts, which are easier to reduce, the desorption of both, acetone and water appears likely, which then is accompanied with a reduction of the active site.

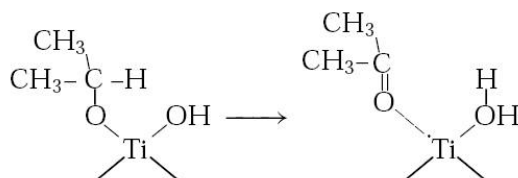


Figure 5.30 Reaction mechanism of acetone formation via dehydrogenation of 2-propanol over red-ox active oxidized titania catalyst, figure copied from literature [5.54].

Whatever the nature of the active site, from a schematic point of view the propoxy-species generated in these reactions and their decomposition appear similar to the intermediate in the ODP catalysis cycle.

The experimental set-up for experiments described in this chapter as well as details of their performance can be found elsewhere [5.9]. In order to investigate the catalytic activity of the VA-200 catalyst in the dehydrogenation of 2-propanol, the material was subjected to a TPR like experiment, i.e., a TPR using 2-propanol instead of H_2 as reducing agent. This experiment combines temperature programmed reaction of 2-propanol and the reduction of the catalyst. Reaction product analysis by on-line MS provided for the detection of H_2 , H_2O , N_2 , 2-propanol, and acetone. A $50\text{ ml}_n\text{ min}^{-1}$ feed of 1.67 vol% 2-propanol in N_2 was introduced into the TPR reactor containing 100 mg freshly oxidized VA-200 catalyst, which was then heated with 10 K min^{-1} . The resulting profile is shown in Fig. 5.31 (a). Conversion of 2-Propanol begins at $150\text{ }^\circ\text{C}$, whereas C_3H_6 formation starts with a short delay, indicating a period where only chemisorption of 2-propanol occurs but the temperature is still too low for driving the dehydration. The concentration of 2-propanol then continuously decreases and at $250\text{ }^\circ\text{C}$, full conversion is achieved. Against that, propene formation shows the inverse trend but passes a maximum before reaching the constant level of incoming 2-propanol concentration. This can be explained by the sudden reaction of 2-propanol molecules which have adsorbed already at lower temperatures. The concentration of water goes in parallel to that of propene except a small peak at $60\text{ }^\circ\text{C}$, indicating the desorption of water molecules adsorbed from the ambient after catalyst calcination.

At $290\text{--}350\text{ }^\circ\text{C}$ data acquiring was affected by an operational disturbance of the QMS. As the significant temperature range has been recorded successfully, this experiment has not been repeated.

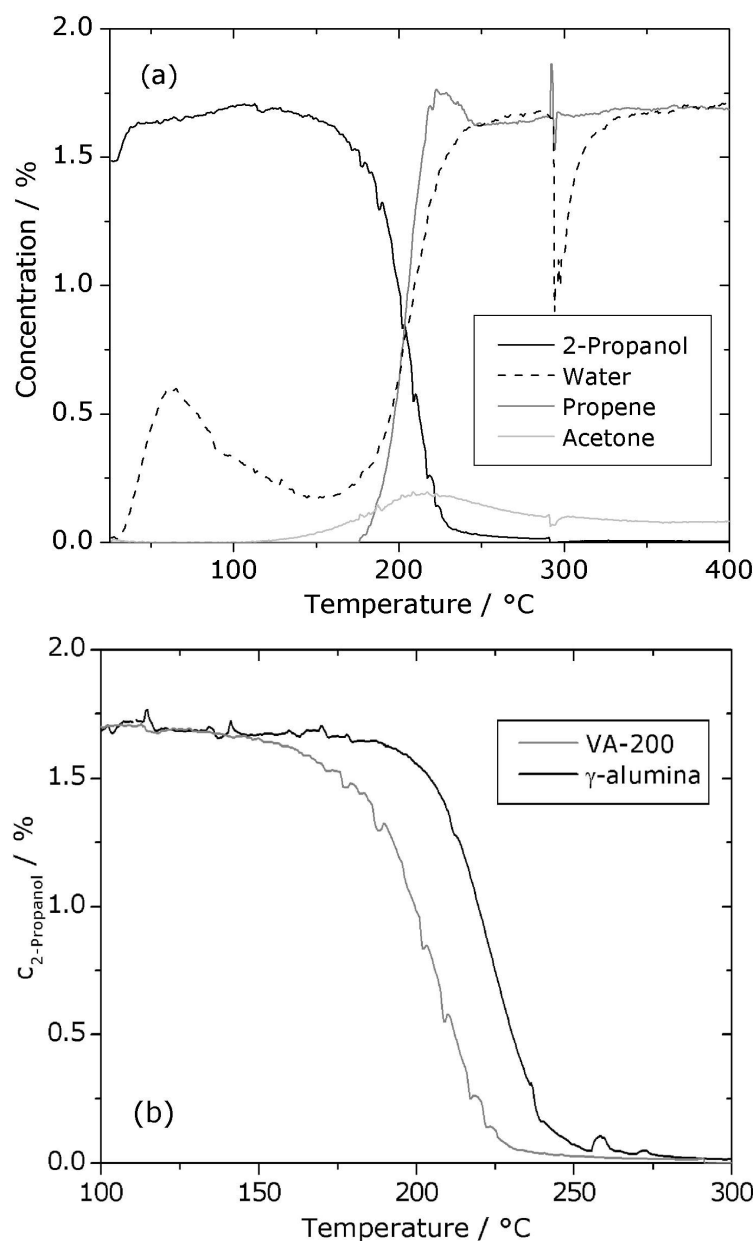


Figure 5.31 (a) Concentration profiles of temperature-programmed reduction/reaction with 2-propanol over VA-200, (b) comparison of 2-propanol concentrations during TPR over VA-200 and pure γ -alumina.

In the temperature range of 130–300 °C, the formation of acetone can be observed. The decrease of its concentration after passing a maximum may be interpreted in the way that this compound is a by-product of the reduction of the vanadia catalyst, which then is completed. The constant level of acetone at $T > 300$ °C may be referred to pure dehydrogenation of 2-propanol or, more likely, disturbance of the QMS calibration matrix by other decomposition products. The latter complicates the determination of the total amount of acetone formed, which corresponds to a reduction of vanadia species with $\Delta = 1.8 \pm 0.5$ in oxidation state, i.e., from V^{+V} to V^{+III} . The following reaction can be derived from this observation (Eq. 5.43):



As a matter of fact, γ -alumina also catalyzes the dehydration of alcohols very well due to its surface acidity [5.55,5.56] (Fig. 5.29). To prove that the observed dehydration reaction over VA-200 can be attributed to the catalytic activity of the vanadia species, a similar experiment was performed using the vanadia-free support material. The selectivity towards dehydration is here near 100%, i.e., no acetone formation was observed. For a better comparison the concentrations of 2-propanol monitored during TPR over VA-200 and pure γ -alumina are presented together in Fig. 5.31 (b). This figure nicely illustrates that VA-200 provides catalytic activity in a narrow range of temperature from 170 up to 210 °C, where over pure γ -alumina no conversion could be observed. This indicates catalytic activity of VO_x species in the dehydration reaction of 2-propanol. However, in a somewhat higher temperature range it cannot be excluded that the measured activity is affected by the catalytic activity of γ -alumina. Thus kinetic measurements were restricted to the mentioned range of 170–210 °C (443–483 K).

To allow for the reduction of V^{+V} during the initial time on stream, kinetic measurements were conducted after conversion has reached constancy. This procedure ensured the reaction rate data acquisition at similar, i.e., reduced, active sites and took at least several hours. Experimental series depicted in Fig. 5.32 were performed using 100 mg VA-200 catalyst and a feed of 50 ml_n min⁻¹ containing 1.67 vol% 2-propanol in N₂.

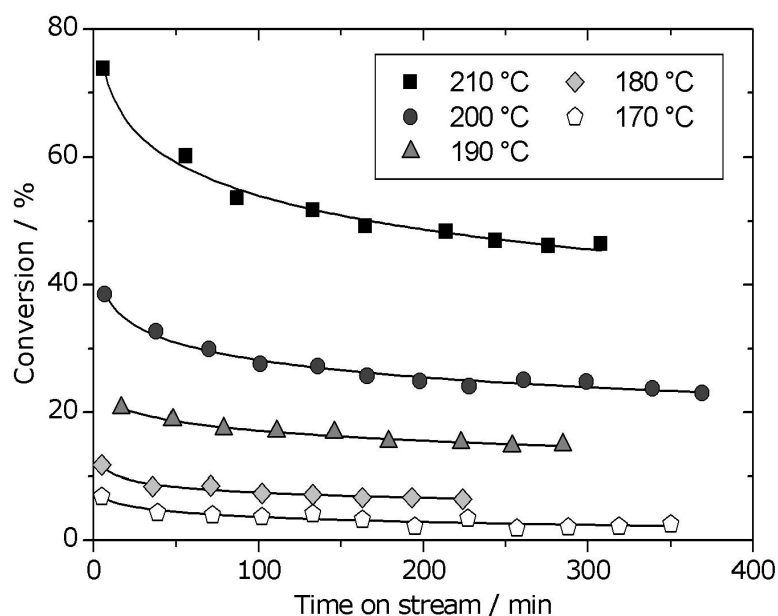


Figure 5.32 Initial reduction period of the VA-200 catalyst during dehydration of 2-propanol.

The slight decrease in activity can be referred to a lower activity of V^{+III} compared to V^{+V} in this reaction and/or to an inhibiting impact of water formed during the dehydration and covering

active sites. The latter is in accordance with results by Ruch [5.9], who investigated the effect of water addition to the feed. However, as soon as no more acetone was detectable in the product flow, its composition was taken to calculate the reaction rate of dehydration given in the Arrhenius plot (Fig. 5.33).

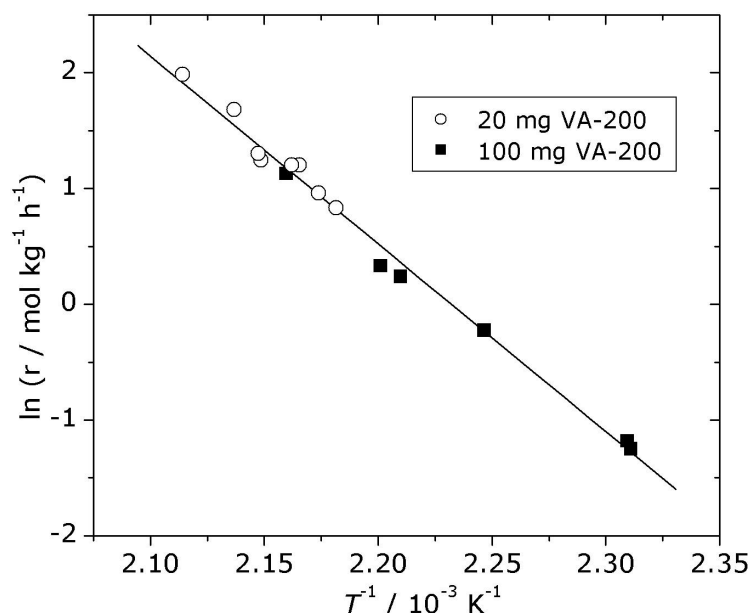


Fig. 5.33 Arrhenius plot of the dehydration of 2-propanol over $\text{VO}_x/\gamma\text{-Al}_2\text{O}_3$ catalyst VA-200.

From the slope an apparent activation energy of 135 kJ mol^{-1} can be derived. This value is rather high compared to literature data. Cunningham et al. determined the activation energy of the dehydration of 2-propanol over V_2O_5 to be 83.9 kJ mol^{-1} , whereas in the same study the activation energy over $\gamma\text{-Al}_2\text{O}_3$ was found to be 130 kJ mol^{-1} [5.57]. With respect to this it appears questionable that the measured reaction mainly takes place over VO_x sites although experimentally confirmed in Fig. 5.31 (b). On the other hand the determined value is lower than the theoretically calculated activation energy of a propoxy intermediate over a vanadyl silsesquioxane cluster. Rozanska et al. determined activation energies in the range of 170 kJ mol^{-1} for this model system, which represents a monomeric VO_x species on a silica support [5.49]. As for the comparison with activation energies determined under vacuum conditions (TAP, Ch. 5.3), the absence of collisions with gas phase molecules may be the reason for the markedly higher E_A compared to the value determined experimentally under ambient conditions. Furthermore, it has to be taken into account that the reaction here occurs over reduced VO_x species. However, the reactivity at 475 K relating to the surface area of V_2O_5 is more than two orders of magnitude higher than that of $\gamma\text{-Al}_2\text{O}_3$ [5.57]. The reported value of $1.2 \times 10^{18} \text{ molecules m}^{-2} \text{ s}^{-1}$ for V_2O_5 is in good agreement with the results of the present study ($1.5 \times 10^{18} \text{ molecules m}^{-2} \text{ s}^{-1}$) and supports the assignment of the active site to be the VO_x species.

To test if the decomposition of a 2-propoxy species bonded to a vanadium cation under release of propene is rate determining in the ODP reaction, the TOF (turn-over frequency) can be extrapolated to the temperature range where ODP has been investigated (see Ch. 5.2). At 673 K the TOF of ODP is about 0.05 s^{-1} on the VA-200 catalyst. The extrapolated kinetic data from Fig. 5.33 gives a TOF of 2-propanol dehydration in the range of 200 s^{-1} at this temperature. Using literature data with a drastically lower activation energy [5.57], the TOF reduces to about 5 s^{-1} . Whatever the true value is, one can see that this step is at least two orders of magnitude faster than the ODP at 673 K and can thereby assumed to be not rate determining.

Since from a statistical point of view the first C-H activation is expected to occur favourably at a methyl carbon atom of propane, similar experiments have been performed with 1-propanol. However, 1-propanol dehydrates much slower than 2-propanol and this reaction has a much lower activation energy. This confirms the assumption, that a 2-propoxy group is an intermediate of ODP rather than a 1-propoxy group, as shown by Rozanska et al. [5.49].

References of Chapter 5

- [5.1] K. Scheurell, E. Hoppe, K.-W. Brzezinka, E. Kemnitz, *Mater. Chem.* **2004** 16 2560.
- [5.2] E.V. Kondratenko, M. Baerns, *Appl. Catal. A* **2001** 222 133.
- [5.3] K. Routray, G. Deo, *AIChE J.* **2005** 51 1733.
- [5.4] A. Khodakov, J. Yang, S. Su, E. Iglesia, A.T. Bell, *J. Catal.* **1998** 177 343.
- [5.5] H. Purnama, T. Ressler, R.E. Jentoft, H. Soerijanto, R. Schlögl, R. Schomäcker, *Appl. Catal. A* **2004** 259 83.
- [5.6] E.V. Kondratenko, M. Cherian, M. Baerns, D. Su, R. Schlögl, X. Wang, I.E. Wachs, *J. Catal.* **2005** 234 131.
- [5.7] A. Bottino, G. Capannelli, A. Comite, S. Storace, R. Di Felice, *Chem. Eng. J.* **2003** 94 11.
- [5.8] J. Le Bars, A. Auroux, M. Forissier, J.C. Vedrine, *J. Catal.* **1996** 162 250.
- [5.9] A. Ruch, Diploma thesis, Technical University of Berlin, Berlin, **2007**.
- [5.10] I.E. Wachs, *Catal. Today* **1996** 27 437.
- [5.11] G. Deo, I.E. Wachs, *J. Catal.* **1994** 146 323.
- [5.12] A. Khodakov, B. Olthof, A.T. Bell, E. Iglesia, *J. Catal.* **1999** 181 205.
- [5.13] M.A. Eberhardt, A. Proctor, M. Houalla, D.M. Hercules, *J. Catal.* **1996** 160 27 and references therein.
- [5.14] C. Hess, R. Schlögl, *Chem. Phys. Lett.* **2006** 432 139.
- [5.15] Z. Wu, H.S. Kim, P.C. Stair, S. Rugmini, S.D. Jackson, *J. Phys. Chem. B* **2005** 109 2793.
- [5.16] C. Sanchez, J. Livage, G. Lucazeau, *J. Raman Spec.* **1982** 12 68.
- [5.17] S. Xie, E. Iglesia, A.T. Bell, *Langmuir* **2000** 16 7162.
- [5.18] M.D. Argyle, K. Chen, A.T. Bell, E. Iglesia, *J. Catal.* **2002** 208 139.
- [5.19] X. Gao, I.E. Wachs, *J. Phys. Chem. B* **2000** 104 1261.
- [5.20] N. Steinfeldt, D. Müller, H. Berndt, *Appl. Catal. A* **2004** 272 201.
- [5.21] F. Klose, T. Wolff, H. Lorenz, A. Seidel-Morgenstern, Y. Suchorski, M. Piórkowska, H. Weiss, *J. Catal.* **2007** 247 176.
- [5.22] J. Kanervo, PhD Thesis, Helsinki University of Technology, Espoo, **2003**.
- [5.23] M.D. Argyle, K. Chen, A.T. Bell, E. Iglesia, *J. Catal.* **2002** 208 139.
- [5.24] E.V. Kondratenko, M. Cherian, M. Baerns, *Catal. Today* **2005** 99 59.
- [5.25] O. Schwarz, B. Frank, C. Hess, R. Schomäcker, *Catal. Commun.* **2007** (accepted), DOI: 10.1016/j.catcom.2007.06.009.
- [5.26] A. Bottino, G. Capannelli, A. Comite, S. Storace, R. Di Felice, *Chem. Eng. J.* **2003** 94 11.

- [5.27] VDI-Gesellschaft Verfahrenstechnik und Chemieingenieurwesen (GVC), VDI-Wärmeatlas, Karlsruhe and Düsseldorf, **1977**.
- [5.28] H. Purnama, T. Ressler, R.E. Jentoft, H. Soerijanto, R. Schlögl, R. Schomäcker, *Appl. Catal. A* **2004** 259 83.
- [5.29] E.V. Kondratenko, N. Steinfeldt, M. Baerns, *Phys. Chem. Chem. Phys.* **2006** 8 1624.
- [5.30] J. B. Peri, *J. Phys. Chem.* **1965** 69 211.
- [5.31] O. Dewaele, G.F. Froment, *Appl. Catal. A Gen.* **1999** 185 203.
- [5.32] C. Doornkamp, M. Clement, X. Gao, G. Deo, I.E. Wachs, V. Poncet, *J. Catal.* **1999** 185 415.
- [5.33] M. Mellor, A. Burrows, S. Coluccia, J.S.J. Hargreaves, R.W. Joyner, C.J. Kiely, G. Martra, M. Stockenhuber, W.M. Tang, *J. Catal.* **2005** 234 14.
- [5.34] M. Cabrejas Manchado, J. M. Guil, A. Pérez Masiá, A. Ruiz Paniego, J.M. Trejo Menayo, *Langmuir* **1994** 10 685.
- [5.35] J. Chen, R.D. Cortright, Y. Shen, J.A. Dumesic, *J. Phys. Chem.* **1994** 98 8067.
- [5.36] C. Monterra, G. Magnacca, *Catal. Today* **1996** 27 497.
- [5.37] G.K. Boreskov, V.S. Muzykantov, *Ann. N.Y. Acad. Sci.* **1973** 213 137.
- [5.38] A. Pantazidis, S.A. Buchholz, H.W. Zanthoff, Y. Schuurman, C. Mirodatos, *Catal. Today* **1998** 40 207.
- [5.39] J.R. Anderson, M. Boudart, *Catalysis Science and Technology*, Vol. 3, Springer, Berlin, **1982**.
- [5.40] R. Grabowski, J. Słoczyński, N.M. Grzesik, *Appl. Catal. A* **2003** 242 297.
- [5.41] E.V. Kondratenko, X. Rozanska, O. Ovsitser, R. Fortrie, U. Dingerdissen, J. Sauer, *J. Catal.* **2007**, submitted.
- [5.42] B. Frank, E.V. Kondratenko, in preparation
- [5.44] I.E. Wachs, *Catal. Today* **2005** 100 79.
- [5.45] Z. Wu, H.S. Kim, P.C. Stair, S. Rugmini, S.D. Jackson, *J. Phys. Chem. B* **2005** 109 2793.
- [5.46] A.D. McNaught, A. Wilkinson, *Compendium of Chemical Terminology. The Gold Book*, 2nd ed., Blackwell Science, Oxford, **1997**.
- [5.47] M. Digne, P. Sautet, P. Raybaud, P. Euzen, H. Toulhoat, *J. Catal.* **2002** 211 1.
- [5.48] K. Chen, E. Iglesia, A.T. Bell, *J. Catal.* **2000** 192 197.
- [5.49] X. Rozanska, R. Fortrie, J. Sauer, *J. Phys. Chem. C* **2007** 111 6041.
- [5.50] W. Turek, J. Haber, A. Krowiak, *Appl. Surf. Sci.* **2005** 252 823.
- [5.51] F.M. Bautista, J.M. Campelo, A. García, D. Luna, J.M. Marinas, A.A. Romero, M.T. Siles, *Catal. Today* **2003** 78 269.
- [5.52] M.I. Zaki, N. Sheppard, *J. Catal.* **1983** 80 114.
- [5.53] D. Haffad, A. Chambellan, J.C. Lavalley, *J. Mol. Catal. A* **2001** 168 153.
- [5.54] J.E. Rekoske, M.A. Barteau, *J. Catal.* **1997** 165 57.
- [5.55] J.D. Butler, *J. Chem. Soc. B* **1968** 905.
- [5.56] C. Lahousse, F. Maugé, J. Bachelier, J.-C. Lavalley, *J. Chem. Soc. Faraday Trans.* **1995** 91 2907.
- [5.57] J. Cunningham, B.K. Hodnett, M. Ilyas, J. Tobin, E.L. Leahy, J.L.G. Fierro, *Faraday Discuss. Chem. Soc.* **1981** 283.

6 Concluding Remarks

The present study aimed at getting insight into mechanistic characteristics of two heterogeneously catalyzed reactions: (i) steam reforming of methanol (SRM), and (ii) oxidative dehydrogenation of propane (ODP). SRM has already been investigated for several years in the research group of Prof. Schomäcker, the experimental program could thus begin immediately with a microkinetic study. Against that, the ODP and oxidation reactions at all are a relatively new field of research in this group. A novel experimental set-up had to be developed and built up. The experimental study here required knowledge and experience in basic topics as catalyst preparation and their characterization, get in touch with problems like mass and heat transfer, and pinpointing optimal operation conditions. Although a similar microkinetic modeling of ODP was aspired as done for SRM, the mass and quality of experimental results from basic studies on mass and heat transfer, reoxidation kinetics, TAP study and investigation of the dehydration of 2-propanol already fulfilled the scope of this thesis.

The reaction mechanism of SRM was investigated in detail by means of a kinetic study based on the differential method. The proposed reaction mechanism, based on previous studies, was supported by a DRIFTS study. Microkinetic measurements were conducted, taking the elimination of mass transfer limitation, as well as experimental errors and result falsification due to catalyst aging, into account. The elementary reaction steps occurring on the surfaces of copper catalysts during SRM were found to be similar and independent of the catalyst support. As reported by several authors, the dehydrogenation of methoxy groups was found to be the RDS of this reaction over Cu/ZnO/Al₂O₃ catalysts. This insight was extended to Cu/SiO₂ and Cu/ZrO₂/CeO₂ systems, which showed identical reaction rate dependence on the feed composition. Kinetic constants were found to be in the same order of magnitude for each catalyst. The surfaces of all catalysts were covered predominantly by methoxy and formate groups; the intermediates formaldehyde, dioxomethylene, and methyl formate were not observed. Because methyl formate appeared in the product spectrum only at high methanol surplus, a change in the reaction pathway from the dioxomethylene to the methyl formate route is assumed, depending on the water content in the feed. A strong signal of formate groups in the DRIFT spectrum indicates relatively slow decomposition of these species into the reaction products. This does not affect the reaction rate over the Cu/ZnO/Al₂O₃, Cu/SiO₂, and Cu/ZrO₂/CeO₂ catalysts investigated. With regard to the Cu/Cr₂O₃/Fe₂O₃ catalyst, this step was indeed found to decrease the overall reaction rate, and a combined rate was proposed considering methoxy and formate dehydrogenation as the two slowest elementary reaction steps. This significant finding was confirmed by a thorough evaluation of the corresponding band areas in the DRIFT spectra, as well as by the higher formation of the by-product CO over this catalyst, which is probably formed by the

decomposition of methyl formate, the surface intermediate preliminary to formate in the supposed catalysis cycle. A particularly low apparent SRM activation energy over CCF compared with CZA, CZC, and CS also confirms the assumption of a change in the RDS on this catalyst.

For the investigation of ODP, a low loaded $\text{VO}_x/\gamma\text{-Al}_2\text{O}_3$ catalyst (VA-200) has been prepared by a saturation-impregnation method and characterized by XRD, UV-Vis, TPR, TEM, XPS and Raman spectroscopy, as well as oxygen titration. These methods confirm the presence of dispersed VO_x species on the surface, which are all accessible for gas phase oxygen. Crystalline V_2O_5 has not been detected. Recent results show that this method, if applied repeatedly on the same sample and thereby achieve higher loadings, is suitable for the deposition of dispersed VO_x species even in a range of vanadia loadings, where common incipient wetness methods inevitably lead to the formation of crystalline V_2O_5 . A microkinetic study on these samples is planned for the near future.

Macrokinetic aspects of the ODP have been studied over this catalyst in the temperature range of 673–773 K using catalyst particles of different size (0.1–2.5 mm). In the studied range of catalyst particle sizes, it was found that the higher the particle size, the lower the propene selectivity at similar degrees of propane conversion. This is due to the appearance of mass transport limitations, which lead to product accumulation in the catalyst pores resulting in consecutive propene oxidation to CO_x . These limitations do not play significant role for catalyst particles up to 0.3 mm and temperatures up to 773 K. Since the ODP selectivity and the mass transport limitations increase with reaction temperature, it appears desirable to perform the reaction at highest possible reaction temperature using smallest possible catalyst particles. Taking this into account, microstructured reactors are suggested to be suitable candidates for such studies, because mass transport in these reactors has lower influence on the intrinsic kinetic as compared to conventional fixed bed reactor.

The kinetic parameters of the ODP reaction were determined under thorough exclusion of mass transport and heat effects, using a PFTR model and a power-law kinetic approach. The simplified model included propene formation from propane and a consecutive combustion of propene with a resulting ratio of CO to CO_2 of 2. This ratio was found to be nearly constant under the chosen reaction conditions. The model predicts the axial temperature profile of the reactor by inclusion of the heat transfer over the reactor wall. Moreover, the negative effects of particle size on the propene selectivity could be predicted nearly quantitatively with the kinetic model if applied in the material balance of a single catalyst particle with spherical geometry. This excellent agreement make this model a powerful tool to design microkinetic investigations in a gradient less Berty-type reactor.

Although the applied catalyst was of relatively low activity as compared to most of the catalytic systems discussed in literature, it could not be completely excluded that the propene selectivity at 773 K was not affected by the mass transport limitations even at the smallest particle diameter (0.1–0.3 mm) investigated in this study. This knowledge may serve as a guideline for performing further ODP tests over more active catalysts. Moreover, by comparing literature data on various catalytic materials, it is highly important to critically analyze, whether the results reported in literature may be influenced by the mass transport limitations, if these aspects have not been explicitly discussed.

The reaction network of ODP has also been investigated by the TAP method. As experiments under ambient pressure indicated the CO_x formation mainly stems from secondary propene combustion, these findings could be confirmed from transient experiments under vacuum. During propene combustion, the release of CO_x was found to be rather slow. This is referred to the low vanadia loading of the catalyst and the resulting time-delay which is needed for the surface-adsorbed oxygenates to collect enough lattice oxygen for deep oxidation. Consequently a higher loaded $\text{VO}_x/\gamma\text{-Al}_2\text{O}_3$ catalyst is expected to provide sharper CO_x responses. Corresponding experiments with multiple impregnated catalysts as described above are in progress. The rate constant of CO oxidation is in the same order of magnitude than that of the ODP but this reaction can be neglected since significant concentrations of CO are normally reached not until O_2 is consumed. However, a rudimentary mechanistic model of CO oxidation has been developed and, with moderate accuracy, fitted to the experimental data.

The process of reoxidation of highly dispersed VO_x species supported on a $\gamma\text{-Al}_2\text{O}_3$ surface has here been successfully interpreted thanks to a novel microkinetic model that involves water as a key intermediate, whose presence, in catalytic amount, increases the overall rate of the reoxidation reaction. Transient experiments have been performed introducing oxygen into an ideally-mixed Berty-type reactor containing reduced VA-200 catalyst. The complex transient response to oxygen step-marking indicates a strong influence of the water which remains from the reduction using hydrogen. However, when water is added to the feed in higher concentrations, its inhibiting effect on the overall reaction is prevailing, and the details of the complex response curve disappear. It is thereby concluded, that only trace amounts of water can affect the reoxidation of surface VO_x species positively. The presence of water in the catalytic system may furthermore stem from the highly hydrophilic $\gamma\text{-Al}_2\text{O}_3$ surface, which prevents or minimizes the loss of water with the product stream leaving the reactor system. However, strong interactions of water with this $\gamma\text{-Al}_2\text{O}_3$ surface during the reoxidation experiments allowed only for a qualitative experimental description of the water response.

The microkinetic analysis of these response curves indicate a reoxidation pathway which mainly proceeds via the oxidation of hydroxylated and hydrated VO_x species, whereas the reaction of gas phase oxygen with naked $[\text{V}^{\text{III}}]$ sites appears to be negligible. The proposed reaction pathways have been tested for their thermodynamic relevance by theoretical calculation of reaction Gibbs free energies of selected reactions. The results are consistent with the proposed reaction network. The calculations, however, give no answer to the question why direct $[\text{V}^{\text{III}}]$ oxidation appears to be slower than that of $[\text{V}^{\text{III}}\text{OH}_2]$ species. A microkinetic evaluation based on quantum chemical calculations could answer this question.

Although the microkinetic model contains several elementary reactions, a reaction order of 1 for oxygen in reoxidation rate laws was found to be most accurate for data fitting. This indicates a consecutive reoxidation pathway with molecular addition of O_2 on $[\text{V}^{\text{III}}\text{OH}_2]$ sites or the dissociation of resulting peroxo-species as the rate determining step. Transferring these results to steady-state conditions in selective oxidation reactions, e.g., the oxidative dehydrogenation of propane where water is present as a reaction product, the following rate law is derived for catalyst reoxidation. The role and activity of intermediate peroxo species has to be investigated in (selective) oxidation experiments.

Rate constants and activation energies for this reaction have been determined from the fit of experimental data. They are reported in the supporting information since the experimental data have only been described qualitatively. Experimentally derived water concentrations turned out to be too low for mathematical modeling with the available methods. However, the general shape of water response is reflected in a sufficient manner so that the determined rate constants suffer from a systematic deviation rather than from a statistical error. Inclusion of water sorption processes on alumina as well as proposed migration of water molecules on the catalyst surface between vanadia and alumina sites is projected for future research.

The amount of oxygen consumed during one reoxidation experiment depends on the reaction temperature and corresponds to a change in the average oxidation degree of vanadia of $\Delta = +2$ at temperatures above 400 °C. Below this temperature a smaller oxygen consumption indicates an incomplete oxidation, which could not be enhanced by variation of the oxygen concentration in the feed. If referred to a kinetic barrier this is not in contradiction to the theoretical calculations. They show that the oxidation of VO_x species is favoured over the whole range of temperatures investigated and independent from water adsorption or hydroxylation. On the other hand a surface structure substantially different from that one used for DFT calculations may be present on the surface of VA-200, e.g., polymeric species as proposed recently even for extremely low loaded $\text{VO}_x/\gamma\text{-Al}_2\text{O}_3$ and $\text{VO}_x/\text{SBA-15}$ catalysts.

7 Appendices

7.1 Supporting Information

(A) Program for TPR profile fitting with a 2-site model by means of Berkeley Madonna

```
A_1 = k0_1 * exp(-EA_1 / R / T) * nV_1  
rxn_1 = 1 / (1 / A_1 / cH2 + 0.5 / dVdt / cH2_0)
```

```
k0_1 = 192  
EA_1 = 117000
```

```
A_2 = k0_2 * exp(-EA_2 / R / T) * nV_2  
rxn_2 = 1 / (1 / A_2 / cH2 + 0.5 / dVdt / cH2_0)
```

```
k0_2 = 192  
EA_2 = 117000
```

```
rxn = rxn_1 + rxn_2
```

```
p = 101300  
R = 8.314  
T0 = 298  
T = 273.15 + 26 + dTdt * TIME
```

```
dTdt = 8,4  
m_kat = 0,750  
wV = 0.014  
MV = 50.942
```

```
xV_1 = 0.99  
xV_2 = 1 - xV_1
```

```
dVdt = 50e-6  
xH2 = 0.05
```

```
cH2 = xH2 * p / R / T
```

```
cH2_0 = xH2 * p / R / T0
```

```
INIT nV_1 = m_kat * wV / MV * xV_1  
d/dt(nV_1) = -rxn_1
```

```
INIT nV_2 = m_kat * wV / MV * xV_2  
d/dt(nV_2) = -rxn_2
```

```
xH2_TPR = xH2 * (1 - rxn / dVdt / cH2_0)
```

```
METHOD RK4
```

```
STARTTIME = 0  
STOPTIME = 100  
DT = 0.01
```

(B) Program for modeling of the tubular reactor by means of Berkeley Madonna

```
rxn_1 = k0_1 * exp(-EA_1 / R / T) * C3H8^n1 * O2^n2
rxn_2 = k0_2 * exp(-EA_2 / R / T) * C3H6^n3 * O2^n4

k0_1 = 80.4
k0_2 = 134

EA_1 = 111000
EA_2 = 102000

p = 101300
R = 8.314

n1 = 0.65
n2 = 0.10
n3 = 0.70
n4 = 1.00

INIT C3H8 = 0.291 * p / R / 673
INIT O2 = 0.145 * p / R / 673
INIT C3H6 = 0

d/dt(C3H8) = -rxn_1
d/dt(C3H6) = rxn_1 - rxn_2
d/dt(O2) = -0.5 * rxn_1 - 3.5 * rxn_2

INIT T = 673
d/dt(T) = (rxn_1 * dH_1 + rxn_2 * (dH_2 - dH_1)) / cp / (p / R / T) - (T - 673) * kw

dH_1 = 120000
dH_2 = 1480000
cp = 65.4
kw = 2.53

METHOD RK4

STARTTIME = 0
STOPTIME = 60
DT = 0.01
```

(C) Program for modeling of intraparticle gradients by means of Berkeley Madonna

```
rename time = r

{A = Propan; B = Propen; C = Sauerstoff}

R = 8.314

epsilon = 0,7
tau = 3.5
dp = 17.3e-9

D_AK = epsilon / tau * dp / 3 * (8 * R * T / Pi / 44 * 1000)^0.5
D_BK = epsilon / tau * dp / 3 * (8 * R * T / Pi / 42 * 1000)^0.5
D_CK = epsilon / tau * dp / 3 * (8 * R * T / Pi / 32 * 1000)^0.5

rho = 250

rxn_1 = rho * 197371 * exp(-111000 / R / T) * c_A^0.65 * c_C^0.10
rxn_2 = rho * 94284 * exp(-102000 / R_gas / T) * c_B^0.70 * c_C^1.00

INIT c_A = 4.5
INIT z_A = 0
d/dt(c_A) = z_A
d/dt(z_A) = -2 / (r + 1e-100) * z_A - (-rxn_1) / D_AK
dn_Adt = z_A * D_AK

INIT c_B = 1.4
INIT z_B = 0
d/dt(c_B) = z_B
d/dt(z_B) = -2 / (r + 1e-100) * z_B - (rxn_1 - rxn_2) / D_BK
dn_Bdt = z_B * D_BK

INIT c_C = 0.01
INIT z_C = 0
d/dt(c_C) = z_C
d/dt(z_C) = -2 / (r + 1e-100) * z_C - (-0.5 * rxn_1 - 3,5 * rxn_2) / D_CK
dn_Cdt = z_C * D_CK

INIT T = 773
INIT TZ = 0
d/dt(T) = TZ
d/dt(TZ) = -2 / (r + 1e-100) * TZ - (rxn_1 * drH_1 + rxn_2 * drH_2) / lambda

lambda = 0.2
drH_1 = 120000
drH_2 = 1480000 - 120000

INIT rxn = 0
d/dt(rxn) = rxn_1 * 4 * Pi * r^2
S = -z_B / (z_A + 1e-10)
eta = rxn / (rho * 197371 * exp(-111000 / R / T) * c_A^0.65 * c_C^0.10) / (4 / 3 * Pi * (1e-3)^3)

METHOD RK4

STARTTIME = 0
STOPTIME = 0.626e-3
DT = 0.001
```

(D) Program for modeling of transient oxygen responses by means of Berkeley Madonna

```

r1 = k1 * O2 * a^2          {O2 + 2 * => 2 O*}
r2 = k2 * a * H2O           { H2O + * => H2O*}
r3 = k3 * O2 * aOH2^2       { 0.5 O2 + H2O* => H2O2*}
r4 = k4 * aO2H2             {H2O2* => H2OO*}
r5 = k5 * aOOH2             {H2OO* => O* + H2O}
r6 = k6 * aOH2 * aO         {H2O* + O* => 2 HO*}
r7 = k7 * O2 * aOH^2        {0.5 O2 + HO* => HOO*}
r8 = k8 * aOOH * aOH        {HOO* + HO* => H2OO* + O*}

a = aTOT - aO - aOH - aOH2 - aO2H2 - aOOH2 - aOOH
aTOT = 15

k1 = 1
k2 = 1
k3 = 1
k4 = 1
k5 = 1
k6 = 1
k7 = 1
k8 = 1

V_R = 11.3
F = 4.306
tau = V / F

p0 = 101300
R = 8.314
T = 206
X_O2 = 0.03

O2_0 = p0 / R / (T + 273.15) * xO2
N2_0 = O2_0 / xO2 * (1 - xO2)
H2O_0 = 0

INIT O2 =
INIT H2O = 0
INIT N2 = 0

INIT aO = 0
INIT aOH = 0
INIT aOH2 = 0
INIT aO2H2 = 0
INIT aOOH2 = 0
INIT aOOH = 0

d/dt(O2) = 1 / tau * (O2_0 - O2)      - r1      - r3      - r7
d/dt(H2O) = 1 / tau * (H2O_0 - H2O)    - r2      + r5
d/dt(N2) = 1 / tau * (N2_0 - N2)

d/dt(aO)      =      + 2*r1      + r5      - r6      + r8
d/dt(aOH)     =      + 2*r6      - 2*r7      - r8
d/dt(aOH2)    =      + r2      - 2*r3      - r6
d/dt(aO2H2)   =      + 2*r3      - r4
d/dt(aOOH2)   =      + r4      - r5      + r8
d/dt(aOOH)    =      + 2*r7      - r8

```

{3-Kessel-Kaskade, welche die Rückvermischung in Partikelfilter und MS-Ventilblock beschreibt}

$$\tau_K = 1.15 / 3$$

$$\text{INIT } O2_K1 = 0$$

$$d/dt(O2_K1) = 1 / \tau_K * (O2 - O2_K1)$$

$$\text{INIT } O2_K2 = 0$$

$$d/dt(O2_K2) = 1 / \tau_K * (O2_K1 - O2_K2)$$

$$\text{INIT } O2_K3 = 0$$

$$d/dt(O2_K3) = 1 / \tau_K * (O2_K2 - O2_K3)$$

$$\text{INIT } N2_K1 = 0$$

$$d/dt(N2_K1) = 1 / \tau_K * (N2 - N2_K1)$$

$$\text{INIT } N2_K2 = 0$$

$$d/dt(N2_K2) = 1 / \tau_K * (N2_K1 - N2_K2)$$

$$\text{INIT } N2_K3 = 0$$

$$d/dt(N2_K3) = 1 / \tau_K * (N2_K2 - N2_K3)$$

$$\text{INIT } H2O_K1 = 0$$

$$d/dt(H2O_K1) = 1 / \tau_K * (H2O - H2O_K1)$$

$$\text{INIT } H2O_K2 = 0$$

$$d/dt(H2O_K2) = 1 / \tau_K * (H2O_K1 - H2O_K2)$$

$$\text{INIT } H2O_K3 = 0$$

$$d/dt(H2O_K3) = 1 / \tau_K * (H2O_K2 - H2O_K3)$$

METHOD RK4

$$\text{STARTTIME} = 0$$

$$\text{STOPTIME} = 100$$

$$DT = 0.02$$

Fitted parameters for the reoxidation of 1.0 g VA-200 at 479 K:

$$k_1 = 0 \text{ s}^{-1} (\text{m}^3 \text{ mol}^{-1})^2$$

$$k_2 = 4.2 \text{ s}^{-1} (\text{m}^3 \text{ mol}^{-1})$$

$$k_3 = 8.9 \text{ s}^{-1} (\text{m}^3 \text{ mol}^{-1})^2$$

$$k_4 > 100 \text{ s}^{-1} \text{ (indeterminable)}$$

$$k_5 > 100 \text{ s}^{-1} \text{ (indeterminable)}$$

$$k_6 = 0.27 \text{ s}^{-1} (\text{m}^3 \text{ mol}^{-1})$$

$$k_7 = 0.39 \text{ s}^{-1} (\text{m}^3 \text{ mol}^{-1})^2$$

$$k_8 > 100 \text{ s}^{-1} (\text{m}^3 \text{ mol}^{-1}) \text{ (indeterminable)}$$

$$a_{\text{TOT}} = 12.3 \text{ mol m}^{-3}$$

$$\text{INIT } a_{\text{O}} = 0 \text{ mol m}^{-3}$$

$$\text{INIT } a_{\text{OH}} = 0.10 \text{ mol m}^{-3}$$

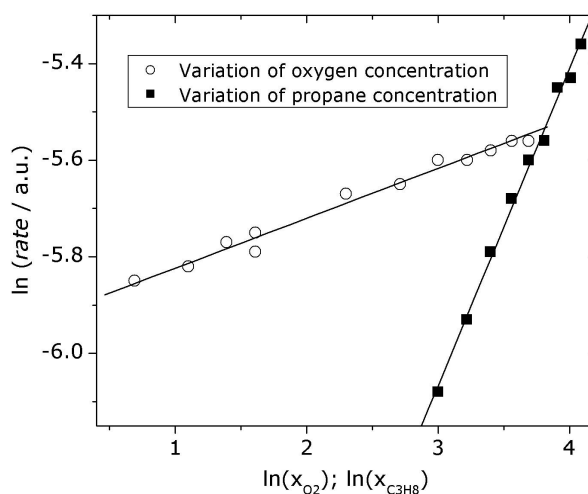
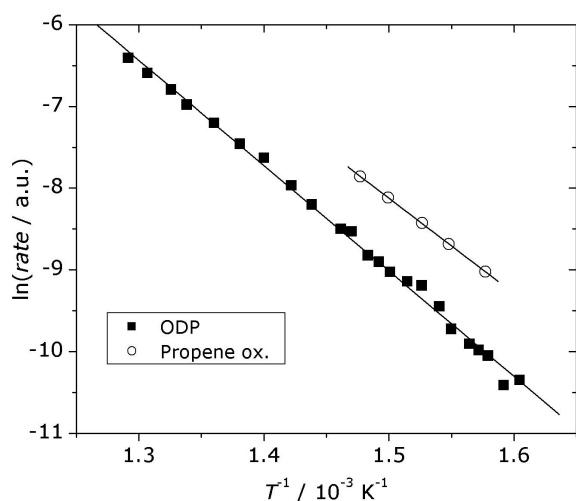
$$\text{INIT } a_{\text{OH}_2} = 0.39 \text{ mol m}^{-3}$$

$$\text{INIT } a_{\text{O}_2\text{H}_2} = 0 \text{ mol m}^{-3}$$

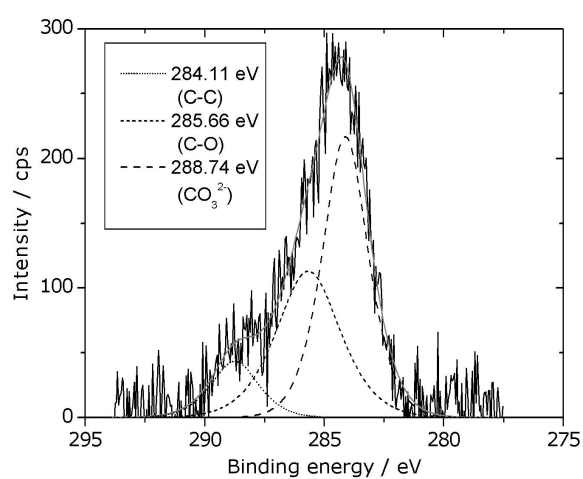
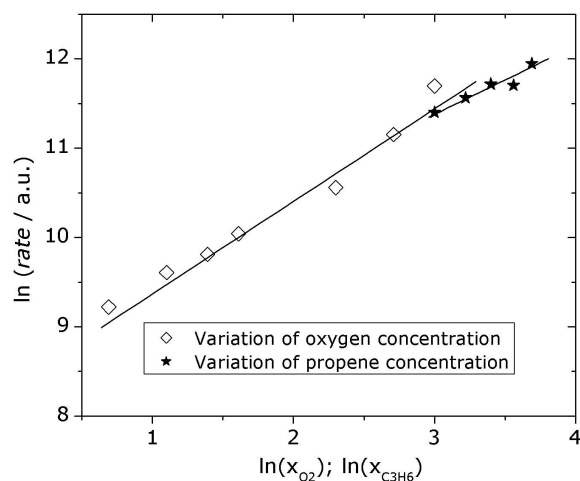
$$\text{INIT } a_{\text{OOH}_2} = 0 \text{ mol m}^{-3}$$

$$\text{INIT } a_{\text{OOH}} = 0 \text{ mol m}^{-3}$$

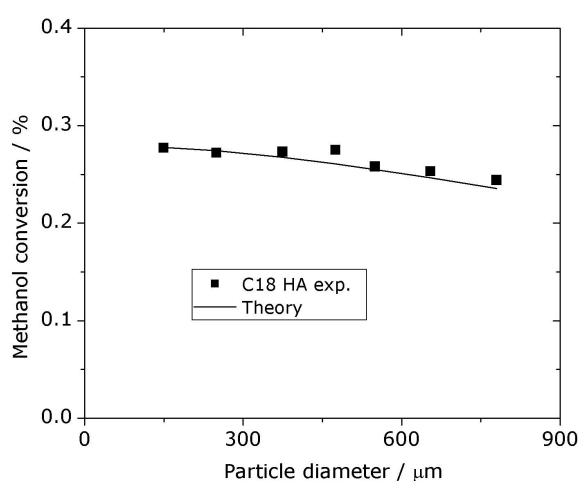
(E) Various diagrams



Determination of activation energies of ODP and propene combustion (top left), reaction orders of oxygen and propane in ODP (top right), and reaction orders of oxygen and propene in propene combustion (right).



C 1s XPS spectrum of VA-200



Mass transport limitation of SRM over C18 HA

(F) Acknowledgements for permission to reprint published material

- Substantial part of this PhD Thesis is reprinted from (a) *Journal of Catalysis*, Vol. 246, pp. 177, B. Frank, F.C. Jentoft, H. Soerijanto, J. Kröhnert, R. Schlögl, R. Schomäcker, *Steam reforming of methanol over copper-containing catalysts: influence of support material on microkinetics*, Copyright (2007), (b) *Applied Catalysis A*, Vol. 323, pp. 66, B. Frank, A. Dinse, O. Ovsitser, E.V. Kondratenko, R. Schomäcker, *Mass and heat transfer effects on the oxidative dehydrogenation of propane (ODP) over a low loaded $\text{VO}_x/\text{Al}_2\text{O}_3$ catalyst*, Copyright (2007), and (c) *Journal of Catalysis*, submitted, B. Frank, R. Fortrie, X. Rozanska, J. Sauer, C. Hess, R. Schlögl, R. Schomäcker, *Reoxidation kinetics of a low loaded $\text{VO}_x/\text{Al}_2\text{O}_3$ catalyst under "non-ideal" conditions - a mechanistic approach*, Copyright (2007), with permission from Elsevier
- Figure 2.8 (a-d) is reprinted from *Catalysis Today*, Vol. 78, pp. 25, B.M. Weckhuysen, D.E. Keller, *Chemistry, spectroscopy and the role of supported vanadium oxides in heterogeneous catalysis*, Fig. 4, Copyright (2003), with permission from Elsevier
- Figure 2.8 (e) is reprinted from *Journal of Catalysis*, Vol. 247, pp. 176, F. Klose, T. Wolff, H. Lorenz, A. Seidel-Morgenstern, Y. Suchorski, M. Piórkowska, H. Weiss, *Active species on γ -alumina-supported vanadia catalysts: Nature and reducibility*, Fig. 12 (a), Copyright (2007), with permission from Elsevier
- Figure 5.14 is reprinted from *Physical Chemistry Chemical Physics*, Vol. 8, pp. 1624, E.V. Kondratenko, N. Steinfeldt, M. Baerns, *Transient and steady state investigation of selective and non-selective reaction pathways in the oxidative dehydrogenation of propane over supported vanadia catalysts*, Fig. 2 (b), Copyright (2006), reproduced by permission of the PCCP Owner Societies
- Figure 5.29 is reprinted from *Journal of Molecular Catalysis A*, Vol. 168, pp. 153, D. Haffad, A. Chambellan, J.C. Lavalley, *Active species on γ -alumina-supported vanadia catalysts: Nature and reducibility*, Fig. 6, Copyright (1997), with permission from Elsevier

7.2 Curriculum Vitae

Personal Information

Name Benjamin Frank
Day and Place of Birth 06.04.1979, Aachen

Email benjamin.frank@chem.tu-berlin.de



Education

8/2007 PhD Thesis "Contributions to a Microkinetic Understanding of the Steam Reforming of Methanol (SRM) and the Oxidative Dehydrogenation of Propane (ODP)" at the TU Berlin
4/2004–8/2007 Scientific Assistant at the TU Berlin (Prof. Schomäcker)
2/2002–4/2002 Internship at Bayer AG, Leverkusen
3/2004 Diploma Thesis "Investigation of Novel Catalysts for the Steam Reforming of Methanol in Fixed Bed and Membrane Reactors"
9/1999–3/2004 Study of Chemistry at the TU Berlin, Grade 1.1 (Distinction)
(1998–1999 Civil Service)
1991–1998 Secondary School; Abitur, Grade 2.0

Teaching and Administration

- Supervision of Lab Courses *Technical Chemistry I* and *Reaction Engineering* (WS 2004/05–SS 2007)
- Supervision of Diploma Students A. Yildiz (2005) and A. Ruch (2007)
- Development and Maintenance of the Research Group's Web site

Language and Software Skills

- German (mother tongue), english (fluent)
- MS Office, Visual Basic, Maple, Origin, Berkeley Madonna, Dreamweaver, Fireworks

Awards and Scholarships

- Doctoral Scholarships of the FCI (2004–2006, Chemiefonds-Scholarship) and the DFG (2004, GRK 352)
- DECHEMA Student Award 2005 (Technical Chemistry)
- Klaus Koch-Scholarship of the TU Berlin

Publications

- (10) B. FRANK, R. FORTRIE, X. ROZANSKA, J. SAUER, C. HESS, R. SCHLÖGL, R. SCHOMÄCKER, Reoxidation kinetics of a low loaded $\text{VO}_x/\text{Al}_2\text{O}_3$ catalyst under "non-ideal" conditions - a mechanistic approach, *J. Catal.*, submitted
- (9) O. SCHWARZ, B. FRANK, C. HESS, R. SCHOMÄCKER, Characterisation and catalytic testing of $\text{VO}_x/\text{Al}_2\text{O}_3$ catalysts for microstructured reactors, *Catal. Commun.* **2007**, accepted
- (8) Á. MASTALIR, Á. PATZKÓ, B. FRANK, R. SCHOMÄCKER, T. RESSLER, R. SCHLÖGL, Steam reforming of methanol over $\text{Cu}/\text{ZnO}/\text{Al}_2\text{O}_3$ modified with hydrotalcites, *Catal. Commun.* **2007**, accepted
- (7) B. FRANK, A. DINSE, O. OVSITSER, E.V. KONDRATENKO, R. SCHOMÄCKER, Mass and heat transfer effects on the oxidative dehydrogenation of propane (ODP) over a low loaded $\text{VO}_x/\text{Al}_2\text{O}_3$ catalyst, *Appl. Catal. A* **2007** 323 66.
- (6) B. FRANK, F.C. JENTOFT, H. SOERIJANTO, J. KRÖHNERT, R. SCHLÖGL, R. SCHOMÄCKER, Steam reforming of methanol over copper-containing catalysts: influence of support material on microkinetics, *J. Catal.* **2007** 246 177
- (5) B. FRANK, A. YILDIZ, E. FEIKE, H. SCHUBERT, R. SCHOMÄCKER, Preparation and characterization of a solid acid catalyst from commercial niobia hydrate, *Chem. Eng. Technol.* **2006** 29 519, Verwendung eines kommerziell erhältlichen Nioboxid-Hydrates als Katalysator für feststoffsäurekatalysierte Reaktionen, *Chem. Ing. Tech.* **2006** 78 39
- (4) L. GRÖSCHEL, R. HAIDAR, A. BEYER, H. CÖLFEN, B. FRANK, R. SCHOMÄCKER, Hydrogenation of propyne in palladium-containing polyacrylic acid membranes and its characterization, *Ind. Eng. Chem. Res.* **2005** 44 9064
- (3) R. SCHOMÄCKER, A. SCHMIDT, B. FRANK, R. HAIDAR, A. SEIDEL-MORGENSTERN, Membranen als Katalysatorträger, *Chem. Ing. Tech.* **2005** 77 549
- (2) B. FRANK, D. HABEL, R. SCHOMÄCKER, *N*-alkylation of aniline with ethanol over an industrial niobic acid catalyst - influence of water formation on kinetics and selectivity, *Catal. Lett.* **2005** 100 181
- (1) Á. MASTALIR, B. FRANK, A. SZIZYBALSKI, H. SOERIJANTO, A. DESHPANDE, M. NIEDERBERGER, R. SCHOMÄCKER, R. SCHLÖGL, T. RESSLER, Steam reforming of methanol over $\text{Cu}/\text{ZrO}_2/\text{CeO}_2$ catalysts: a kinetic study, *J. Catal.* **2005** 230 464

